ISSN 1344-6320

PHOTON FACTORY ACTIVITY REPORT

1998

PART A

HIGH LIGHTS
AND
FACILITY REPORT

#16

High Energy Accelerator Research Organization, KEK

KEK Progress Report 99-2
November 1999
A/M

KEK Reports are available from:

Information Resources Division
High Energy Accelerator Research Organization (KEK)
1-1 Oho, Tsukuba-shi,
Ibaraki-ken, 305-0801
JAPAN

Phone : 0298-64-5137
Fax : 0298-64-2801
Cable : KEK OHO
E-mail : adm-jouhoushiryou1@ccgemail.kek.jp
Internet: http://www.kek.jp

Photon Factory Activity Report

1998

Staff members and visitors of the Photon Factory

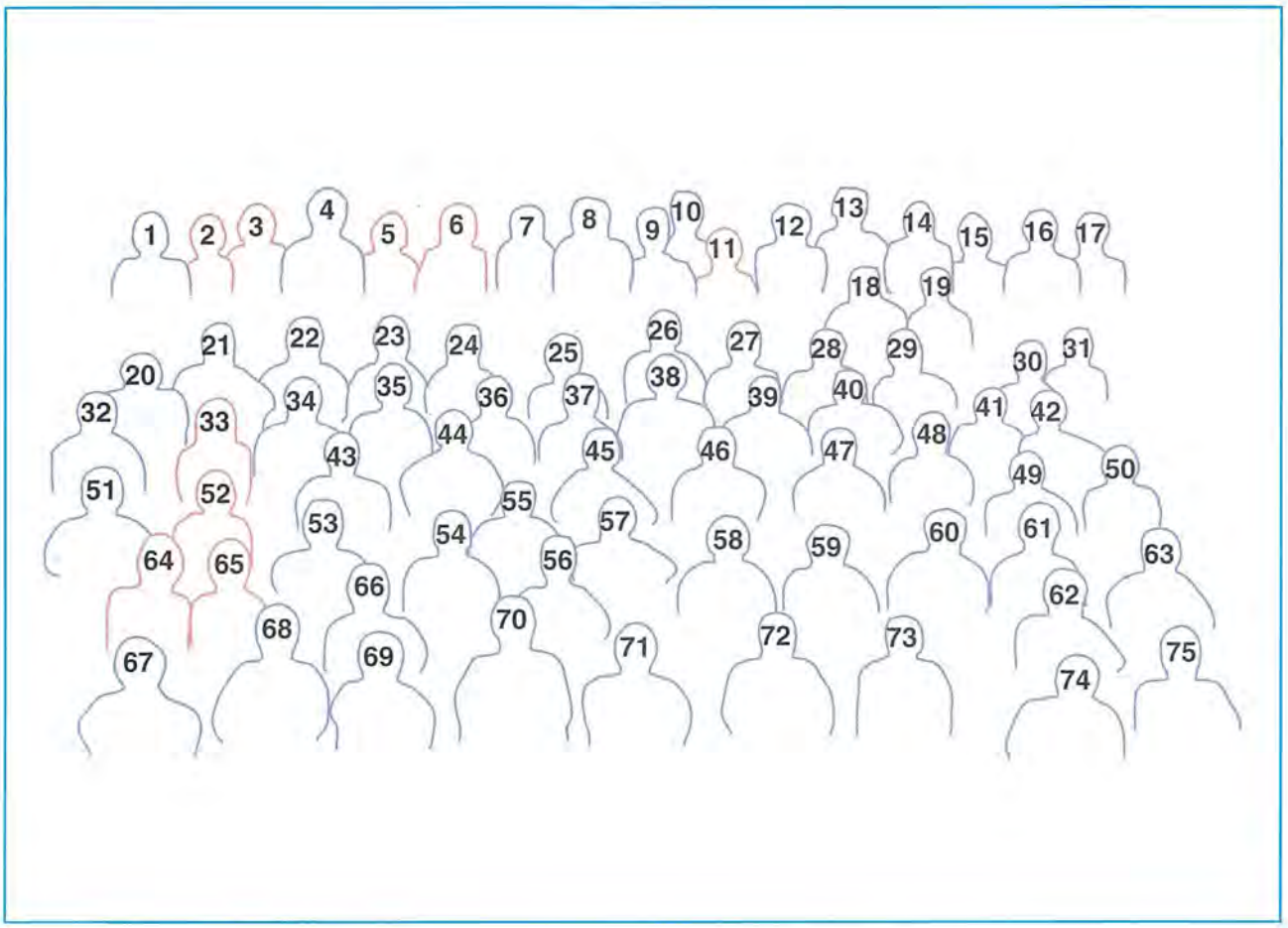

1. M. O. Rahman
2. K. Kojo
3. H. Furubayashi
4. R. F. Garrett
5. S. Isoyama
6. M. Kimura
7. T. Kikuchi
8. Y. Uchida
9. N. Tomita
10. A. Mishina
11. Visitor
12. T. Iwazumi
13. Y. Kitajima
14. M. T. Huang
15. K. Ohmi
16. M. Ando
17. A. Yagishita
18. A. Koyama
19. K. Tanaka
20. H. Nakao
21. K. Tsuchiya
22. G. J. Foran
23. Y. Hori
24. T. Honda
25. H. Sugiyama
26. N. Tomita
27. Visitor
28. Visitor
29. Y. Azuma
30. K. Ono
31. M. Kato
32. S. Sakanaka
33. A. Kikuchi
34. Y. Wakabayashi
35. T. Kiyama
36. T. Miyajima
37. A. Mochihashi
38. Y. Kobayashi
39. T. Nogami
40. K. Haga
41. T. Uchiyama
42. M. Nomura
43. Y. Murakami
44. M. Watanabe
45. T. Obina
46. C. Pak
47. M. Isawa
48. T. Kasuga
49. Y. Tanimoto
50. S. Asaoka
51. M. Suzuki
52. S. Takano
53. H. Kamikuba
54. T. Saitoh
55. Y. Sakamoto
56. H. W. Yeom
57. N. Watanabe
58. N. Igarashi
59. T. Kosuge
60. K. Kobayashi
61. K. Nasu
62. T. Takahashi
63. H. Hashimoto
64. F. Mori
65. K. Ishii
66. A. Iida
67. H. Mizouchi
68. M. Tanaka
69. T. Kurihara
70. H. Kawata
71. T. Matsushita
72. Y. Kimura
(Director of IMSS)
73. A. Mikuni
74. I. Matsumoto
75. A. Kakizaki

You can jump to the article by clicking its title.

CONTENTS

CONTENTS

Introduction

The fiscal year 1998 (from April 1998 to March 1999) was a memorable one both to users and the Photon Factory staff members. Following the re-commissioning of the 2.5 GeV ring and machine study made in FY 1997, the Photon Factory started a routine low emittance (36 nmrad) operation of the 2.5 GeV ring for users experiments in May 1998. The initial current has still been kept as high as 400 mA, the same as that of the previous operational mode (130 nm rad). The typical life time of the electron beam is 25 hours. The low emittance operation gives a smaller source size, typically one-third of the previous one. A 3 GeV operation of the ring with the low emittance optics was also successfully tested in December 1998 giving a beam current of 200 mA and a beam life time of 60 hours.

In FY 1998, the 2.5 GeV ring was operated for 4564 hours which is increased by 940 hours compared with that in FY 1997. Users experimental run of the ring logged 3560 hours and the rest was assigned to machine studies and start-up tuning of the machine at every run. It is expected that the operational hours of the 2.5 GeV ring will be increased by 10-15 % in FY 1999. On the other hand, the PF-AR (6.5 GeV ring) was operated only in April-June period of 1998 resulting in accumulated hours of 900 hours. The fall run of the PF-AR was not scheduled because the operation of PF-AR might have caused an interference with the commissioning of KEK-B rings. In addition, the operation scheduled in March,1999 has been cancelled because the injection of e-beam to PF-AR interfered with the operation of KEK-B rings. This situation will greatly be improved in FY 1999.

Thanks to the low emittance operation, higher intensity at sample positions and higher resolution data are being obtained on many beam lines having focusing or non-focusing optics. Beamlines commissioned in last year are now fully open to users as described in EXPERIMENTAL FACILITY section. BL-1B is used for powder diffractometory of exotic materials. The optics on BL-1C covering 20-250 eV region attained a resolution better than 10,000 and is now supplying a beam for angle resolved high resolution photoelectron spectroscopy of quantum nano-structure materials. The 5 m long undulator on BL-2 is able to deliver soft X-ray beams as brilliant as that obtained on typical third generation VUV/Soft X-ray rings. Soft X-ray emission spectrometer on BL-2C is producing high resolution data. The new fully automated Weissenberg camera for protein crystallography

was installed on BL-6C and are now under commissioning.

In FY 1998, there was a significant increase in the number of experimental proposals compared with that in FY 1997. During the 9 month long shut down for emiitance up-grade in 1997, the number of active proposals dropped to approximately 590 from 670. It recovered almost to 670 in FY 1998. We continue encouraging users to make project-type experimental proposals(S1 and S2 categories) in which users can receive special support in budget and beam time allocation.

The construction and its use for high resolution electron spectroscopy of BL-1C is one of very good examples of S1 category experimental proposals in which users groups are responsible for the construction and commissioning of beamlines and further supporting users after commissioning. In FY 1988, ten of such S1 and S2 proposals have been active.

As we reported in our last activity report, the Photon Factory has been proposing an upgrade of PF-AR to a dedicated single bunch X-ray machine. In this proposal, we propose building a new experimental floor building in the north west corner of the ring with 4 more insertion device beamlines. Although we are not yet successful in obtaining full approval of the project, we made an effort to prepare for the future construction of a new insertion beamline on PF-AR. In the north building of PF-AR where there is a deep hall adjacent to the straight section of the ring. We constructed a floor which has an equal level to that of the ring tunnel in order to make it possible to construct one more insertion device beamline even without a large scale building construction. A design study is under way to install a protein crystallography station on this beamline. On the 2.5 GeV ring, a straight section between the bending magnets 5 and 6 is still left vacant for installation of an insertion device. A design study is being made to inst all a beamline for utilizing soft X-rays of alternating circular polarization. In addition to the routine operation of the low emittance optics of the 2.5 GeV ring, we also plan to increase the initial current of the ring up to 500 mA and also to increase operational hours of the ring up to 5000 hours in FY 1999. With those efforts, we believe that the Photon Factory will be able to continue providing users with better experimental opportunities.

Buildings

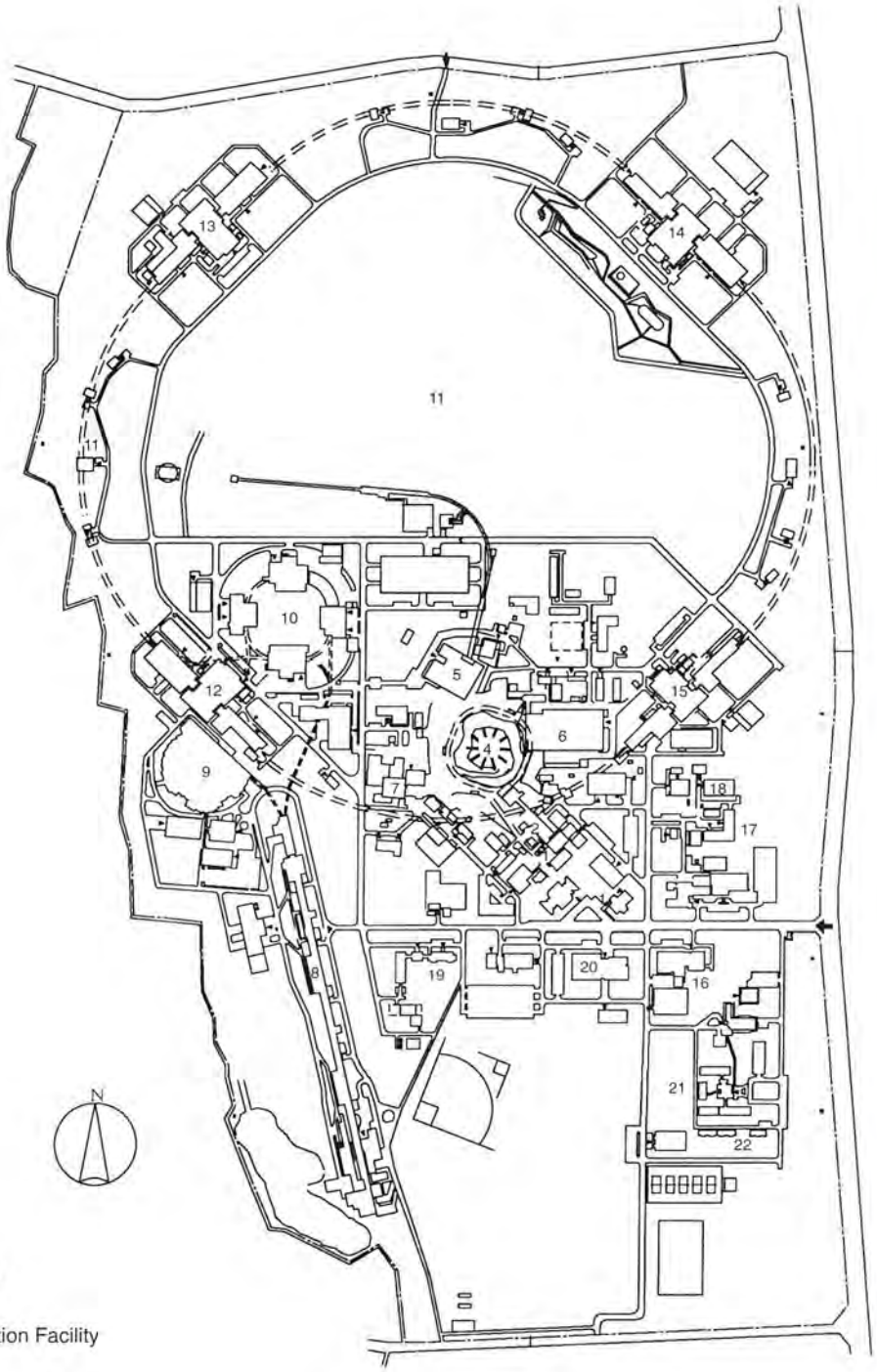

1. PS Preinjector
2. PS Injector Linac
3. PS Booster
4. PS Main Ring
5. PS North Experimental Hall
6. PS East Experimental Hall
7. Booster Synchrotron Utilization Facility
8. PF Injector Linac
9. PF Light Source/Experimental Hall
10. TRISTAN Accumulation Ring
11. TRISTAN Electron-Positron Colliding Ring
12. TRISTAN Experimental Hall: Fuji
13. TRISTAN Experimental Hall: Nikko
14. TRISTAN Experimental Hall: Tsukuba
15. TRISTAN Experimetal Hall: Oho
16. Computing Center
17. Cryogenics Center
18. Mechanical Engineering Center
19. Radiation Safety Control Center
20. Library
21. Dormitory
22. Guest House

PF 2.5GeV Ring and Beam Lines

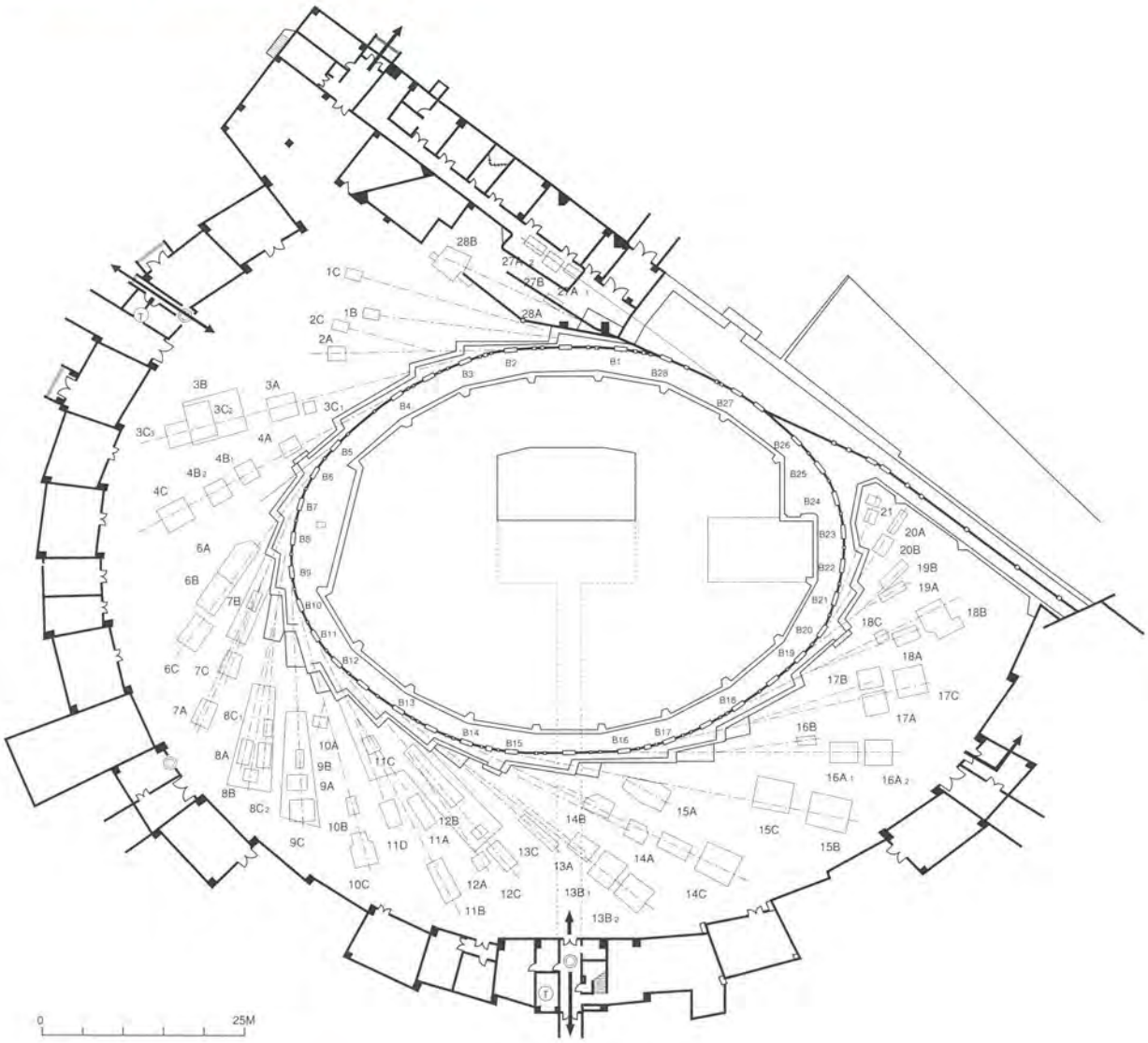

PF-AR (6.5GeV) Beam Lines

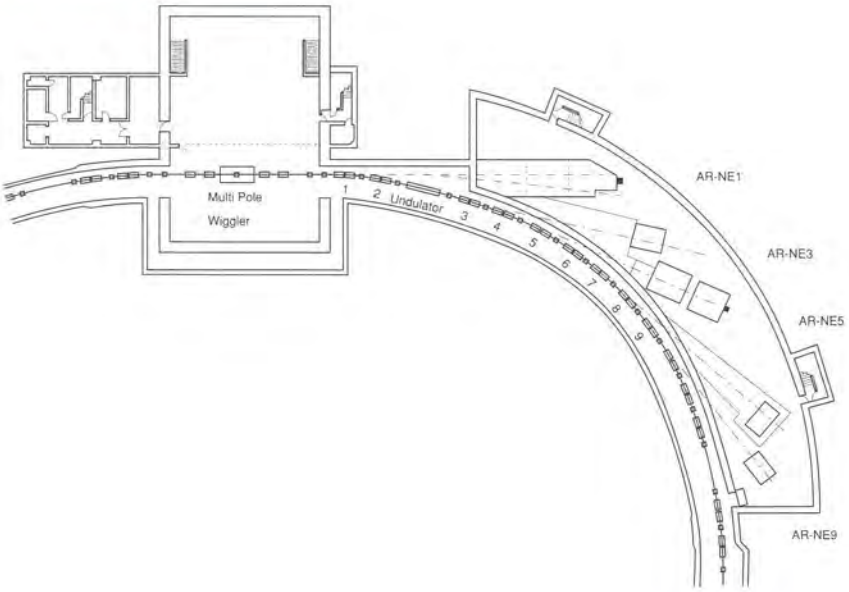

Members of Board of Councilors

CHIKAWA, Junichi	CAST Hyogo
ESAKI, Leo	University of Tsukuba
HIRASA, Takao	University of Osaka Prefecture
HIROTA, Eiji	The Graduate University for Advanced Studies
INOKUCHI, Hiroo	Okazaki National Research Institutes
ISHI, Susumu	National Museum of Japanese History
KAMITSUBO, Hiromichi	The Institute of Physical and Chemical Research
KURODA, Haruo**	The Science University of Tokyo
KYOGOKU, Yoshimasa	Osaka University
LANG, Roy	NEC Corporation
NAGAOKA, Yosuke*	Kansai University
OKUSHIMA, Takayasu	Waseda University
SASAKI, Kazuo	Okazaki National Research Institutes
SHINJO, Teruya	Kyoto University
SUGANO, Takuo	Toyo University
SUZUKI, Kennji	Tohoku University
TAKAYANAGI, Kazuo	The University of Tokyo
YAMADA, Yasusada	Waseda University
YASUOKA, Hiroshi	The University of Tokyo
YONEZAWA, Tomiko	Keio Unversity

Members of Advisory Council for Scientific Policy & Management

ARAI, Masatoshi	Neutron Science Lab., IMSS
ENDO, Yasuo	Tohoku University
FUJII, Yasuhiko	The University of Tokyo
GO, Nobuhiro	Kyoto University
HIEDA, Kotaro	Rikkyo University
IIDA, Atsuo	Photon Factory , IMSS
IKEDA, Hironobu	Neutron Science Lab., IMSS
IKEDA, Susumu	Neutron Science Lab., IMSS
KIKUTA, Seishi	The University of Tokyo
KOBAYASHI, Masanori	Photon Factory, IMSS
KUROKAWA, Shinichi	Accelerator Lab., KEK
MATSUSHITA, Tadashi**	Photon Factory, IMSS
NAGAMINE, Kanetada	Meson Science Lab., IMSS
NISHIDA, Nobuhiko	Tokyo Institute and Technology
OHTA, Toshiaki	The University of Tokyo
SATO, Shigeru	Tohoku University
SHIBATA, Tokushi	Applied Research Lab., KEK
SUEMATSU, Hiroyoshi*	The University of Tokyo
TAKATA, Koji	Accelerator Lab., KEK
YAGISHITA, Akira	Photon Factory , IMSS
YOSHIWARA, Keitaro	Japan Advanced Institute of Science and Technology, Hokuriku

** Chairman * Vice-Chairman

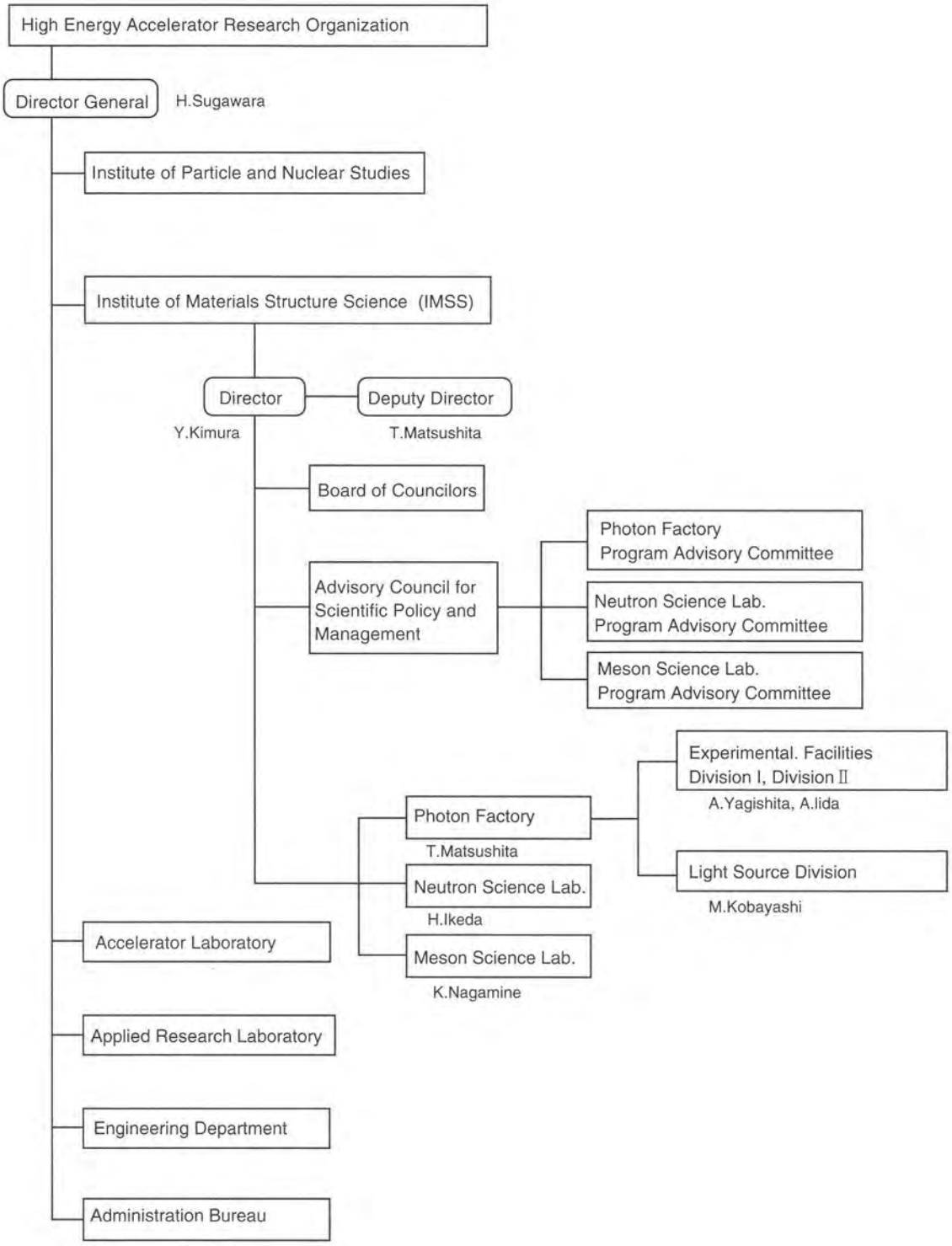
High Energy Accelerator Research Organization
Director General
H.Sugawara
Institute of Particle and Nuclear Studies
Institute of Materials Structure Science (IMSS)
Director
Y.Kimura
Deputy Director
T.Matsushita
Board of Councilors
Advisory Council for Scientific Policy and Management
Photon Factory Program Advisory Committee
Neutron Science Lab. Program Advisory Committee
Meson Science Lab. Program Advisory Committee
Photon Factory
T.Matsushita
Neutron Science Lab.
H.Ikeda
Meson Science Lab.
K.Nagamine
Experimental. Facilities Division I, Division II
A.Yagishita, A.Iida
Light Source Division
M.Kobayashi
Accelerator Laboratory
Applied Research Laboratory
Engineering Department
Administration Bureau

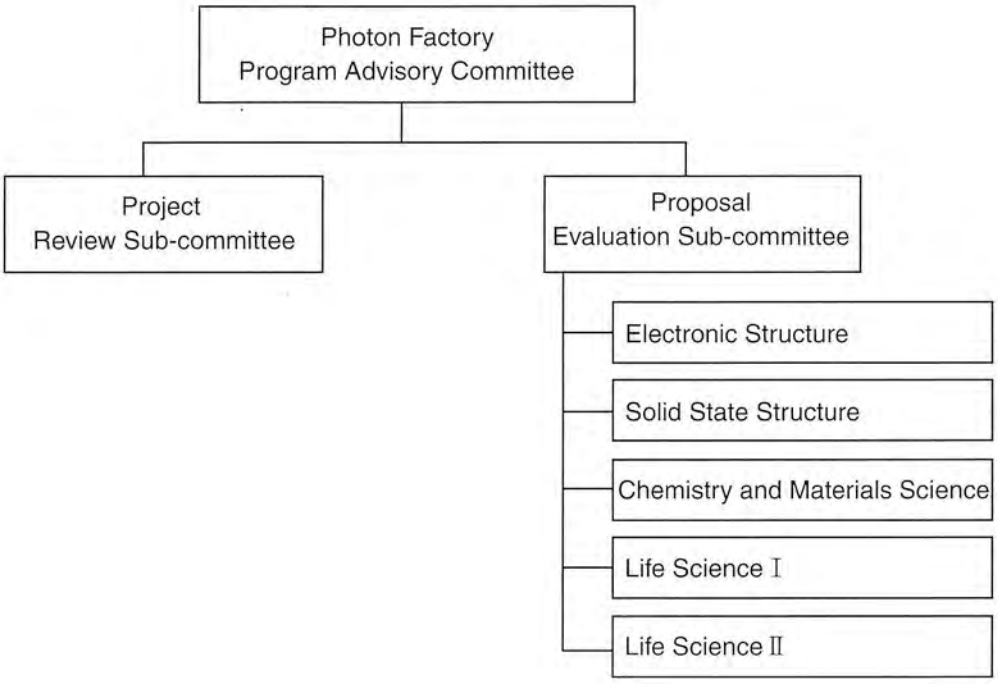
Photon Factory
Program Advisory Committee
Project
Review Sub-committee
Proposal
Evaluation Sub-committee
Electronic Structure
Solid State Structure
Chemistry and Materials Science
Life Science I
Life Science II

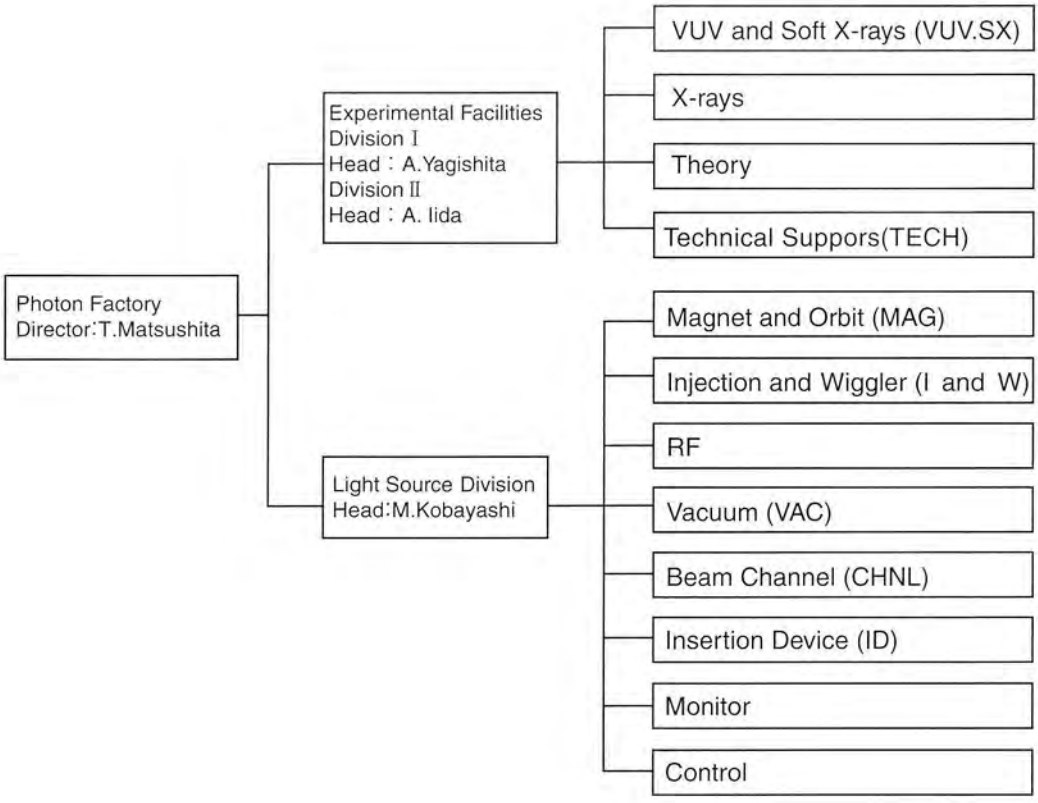
Photon Factory
Director:T.Matsushita
Experimental Facilities
Division I
Head : A.Yagishita
Division II
Head : A. Iida
VUV and Soft X-rays (VUV.SX)
X-rays
Theory
Technical Suppors(TECH)
Light Source Division
Head:M.Kobayashi
Magnet and Orbit (MAG)
Injection and Wiggler (I and W)
RF
Vacuum (VAC)
Beam Channel (CHNL)
Insertion Device (ID)
Monitor
Control

Staff members of the Photon Factory

Name	Responsibility	e-mail address
Research Staff		
MATSUSHITA, Tadashi	Deputy Director	tadashi.matsushita@kek.jp
Experimental Facilities Division I & II		
ADACHI, Hiromichi	X-rays	hiromichi.adachi@kek.jp
ANDO, Masami	X-rays	masami.ando@kek.jp
AZUMA, Yoshiro	VUV-SX	yoshiro.azuma@kek.jp
HIRANO, Keiichi	X-rays	hirano@ccpfmail.kek.jp
HYODO, Kazuyuki	X-rays	kazuyuki.hyodo@kek.jp
IGARASHI, Noriyuki	X-rays	noriyuki.igarashi@kek.jp
IIDA, Atsuo	X-rays	atsuo.iida@kek.jp
ITO, Kenji	VUV-SX	ito@ccpfmail.kek.jp
IWANO, Kaoru	Theory	iwano@nasuws1.kek.jp
IWAZUMI, Toshiaki	X-rays	toshiaki.iwazumi@kek.jp
KAKIZAKI, Akito	VUV-SX	akito.kakizaki@kek.jp
KAMIKUBO, Hironari	X-rays	hironari.kamikubo@kek.jp
KAWATA, Hiroshi	X-rays	hiroshi.kawata@kek.jp
KIKEGAWA, Takumi	X-rays	takumi.kikegawa@kek.jp
KISHIMOTO, Syunji	X-rays	syunji.kisimoto@kek.jp
KITAJIMA, Yoshinori	X-rays	yoshinori.kitajima@kek.jp
KOBAYASHI, Katsumi	X-rays	katsumi.kobayashi@kek.jp
KOIDE, Tsuneharu	VUV-SX	tkoide@ccpfmail.kek.jp
KURIHARA, Toshikazu	VUV-SX	toshikazu.kurihara@kek.jp
MURAKAMI, Youichi	X-rays	myouichi@ccpfmail.kek.jp
NASU, Keiichiro	Theory	knasu@nasuws4.kek.jp
NOMURA, Masaharu	X-rays	masaharu.nomura@kek.jp
OHSUMI, Kazumasa	X-rays	kazumasa.ohsumi@kek.jp
SAITOH, Tomohiko	VUV-SX	tomohiko.saitoh@kek.jp
SUGIYAMA, Hiroshi	X-rays	hiroshis@mail.kek.jp
SUZUKI, Mamoru	X-rays	mamoru.suzuki@kek.jp
TANAKA, Masahiko	X-rays	masahiko.tanaka@kek.jp
TOMITA, Norikazu	Theory	tomita@nasuws4.kek.jp
USAMI, Noriko	X-rays	noriko.usami@kek.jp
WATANABE, Masamitsu	VUV-SX	masamitsu.watanabe@kek.jp
WATANABE, Nobuhisa	X-rays	
YAGISHITA, Akira	VUV-SX	akira.yagishita@kek.jp
YAMAMOTO, Shigeru	X-rays	shigeru.yamamoto@kek.jp
ZHANG, Xiaowei	X-rays	xiaowei@mail.kek.jp

Name	Responsibility	e-mail address
Light Source Division		
HAGA, Kaiichi	MONITOR	haga@mail.kek.jp
HONDA, Tohru	MONITOR	tohru.honda@kek.jp
HORI, Yoichiro	VAC	hori@mail.kek.jp
ISAWA, Masaaki	RF	isawa@mail.kek.jp
KANAYA, Noriichi	CHNL	noriichi.kanaya@kek.jp
KASUGA, Toshio	MAG	kasugat@post.kek.jp
KATOH, Masahiro	MAG	katohm@mail.kek.jp
KATSURA, Tomotaro	MONITOR	tomotaro.katsura@kek.jp
KOBAYASHI, Masanori	VAC	masanori.kobyashi@kek.jp
KOBAYASHI, Yukinori	MAG	yukinori.kobayashi@kek.jp
MAEZAWA, Hideki	CHNL	maezawah@mail.kek.jp
MITSUHASHI, Toshiyuki	I&W	toshiyuki.mitsuhashi@kek.jp
OBINA, Takashi	CONTROL	obina@mail.kek.jp
OHMI, Kazuhito	I&W	ohmi@post.kek.jp
PAK, Cheol On	CONTROL	cheol-on.pak@kek.jp
SAKANAKA, Shyogo	RF	shogo.sakanaka@kek.jp
TANIMOTO, Yasunori	VAC	yasunori.tanimoto@kek.jp
TSUCHIYA, Kimichika	ID	tsuchiya@mail.kek.jp
Supporting Staff		
Experimental Facilities Division I & II		
KIKUCHI, Takashi	TECH	takashi.kikuchi@kek.jp
KOSUGE, Takashi	TECH	takashi.kosuge@kek.jp
KOYAMA, Atsushi	TECH	atsushi.koyama@kek.jp
MIKUNI, Akira	TECH	akira.mikuni@kek.jp
MORI, Takeharu	TECH	takeharu.mori@kek.jp
OKAMOTO, Wataru	TECH	wataru.okamoto@kek.jp
SAITO, Yuuki	TECH	yuuki.saito@kek.jp
SATHO, Masato	TECH	masato.satoh@kek.jp
TOYOSHIMA, Akio	TECH	akio.toyoshima@kek.jp
UCHIDA, Yoshinori	TECH	yoshinori.uchida@kek.jp
Light Source Division		
ASAOKA, Seiji	CHNL	asaoka@mail.kek.jp
MISHINA, Atsushi	CONTROL	Atsushi.MISHINA@kek.ac.jp
NOGAMI, Takashi	I&W	takashi.nogami@kek.jp
SATO, Yoshihiro	CONTROL	yoshihiro.sato@kek.jp
SHIOYA, Tatsuro	ID	tatsuro.shioya@kek.jp
TADANO, Mikito	MONITOR	takano@cccemail.kek.jp
TAKAHASHI, Takeshi	RF	takeshi.takahash@kek.jp
UCHIYAMA, Takashi	VAC	takashi.uchiyama@kek.jp
UEDA, Akira	I&W	ueda@mail.kek.jp

Name		Resposibility	e-mail address
Guest Professor			
GO, Nobuhiro	(Kyoto Univ.)		
HYODO, Toshio	(The Univ. of Tokyo)		
ITOH, Masahisa	(Himeji Inst. of Tech.)		
KATAOKA, Mikio	(Nara Inst. Sci. Tech.)		
MIYAHARA, Tsuneaki	(Tokyo Metro. Univ.)		
OHTA, Masaharu	(The Univ. of Tokyo)		
SHIN, Shik	(The Univ. of Tokyo)		
TAKAHASHI, Toshio	(The Univ. of Tokyo)		
COE Staff			
AN, Ki-Seok 1)		VUV-SX	ksan@post.kek.jp
HUANG, Ming-Tie		VUV-SX	
KOYAMA, Ichiro		X-rays	ikoyama@ccpfmail.kek.jp
MAMIYA, Kazutoshi 2)		VUV-SX	mamiya@ccpfmail.kek.jp
MIZOUCHI, Hideo 3)		Theory	mizouchi@nasuws4.kek.jp
SAITOH, Akihiro 4)		X-rays	akihiros@mail.kek.jp
The Graduate University for Advanced Studies			
HASANUZZAMAN, Sheikh, Md.			
HUAI, Ping			
MATSUMOTO, Isao			
RAHMAN Md. Obaidur 5)			
SAITOH, Tazuko			
TAI,-Renzhong			
TAKAHASHI, Yumiko 5)			
UEJI, Yoshinori			
YAMAZAKI, Masahiro 5)			

1) Feb. 16, '99 joined 2) Aug. 31, '98 left 3) Dec. 16, '98 joined 4) Sep. 16, '98 joined 5) Apr. 1,'98 joined

Highlights

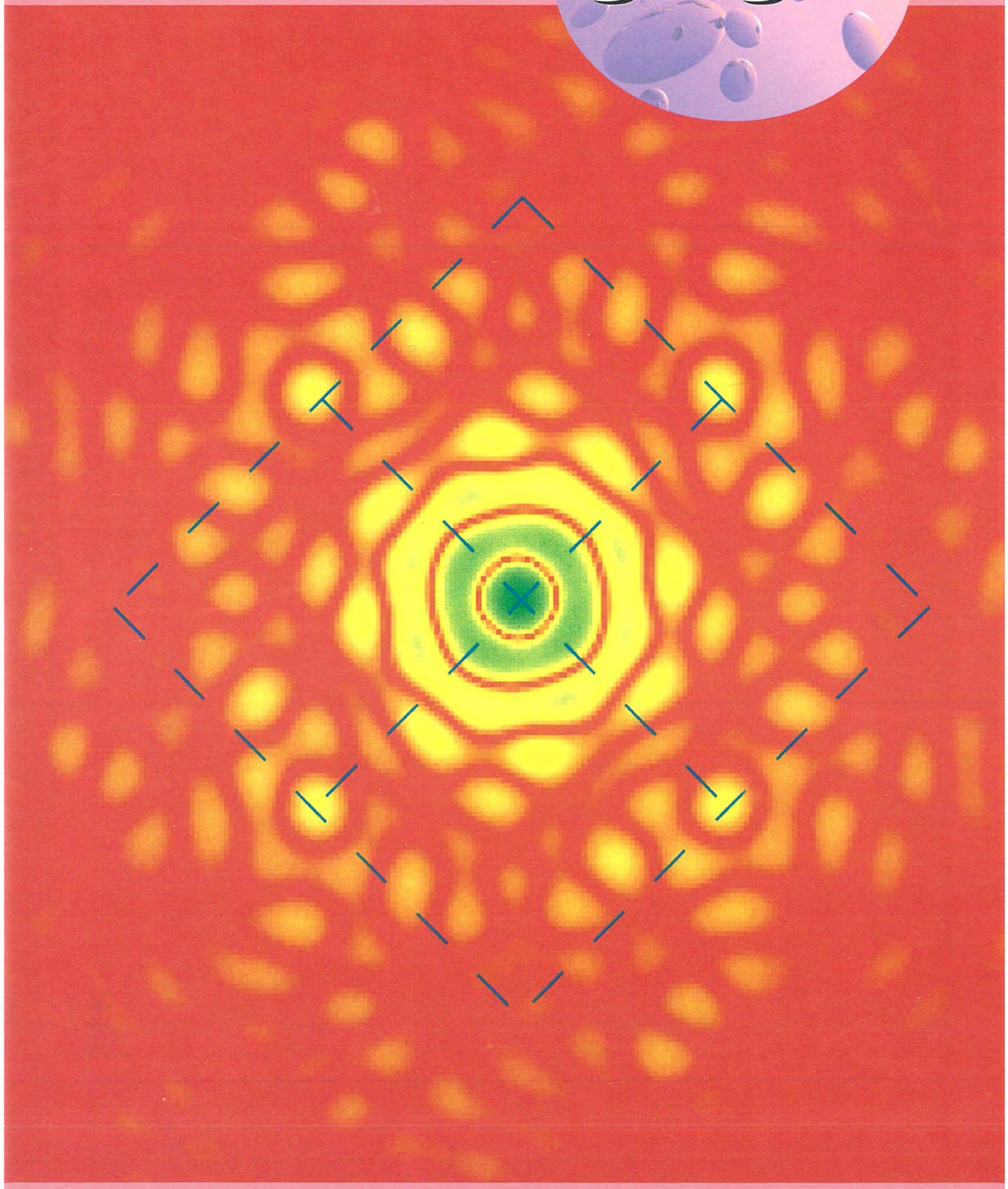

1

Atomic and Molecular Science

1 Atomic and Molecular Science

1-1 Symmetry-resolved S1s Photoabsorption Spectra of SO_2

Within the axial-recoil approximation, the angular distribution of fragment ions is directly related to the orientaion of molecules which absorb linearly polarized soft x-rays. This is because the lifetime of the molecular K-shell excited state is dominated by Auger decay to antibonding states with a repulsive force, like the Coulomb explosion, and is much shorter than the molecular rotation period. Then one can distinguish paralell (the change of angular momentum projection on the molecular axis is 0) and perpendicular transitions (the change is + 1) of diatomic molecues by measuring the fragment ions in the parallel and perpendicular direction to the electric field vector of incoming light.

For a bent triatomic molecule, like SO_2, the situation is not very simple. However, one can obtain information on the symmetries of core-excited states of the bent triatomic molecules by angle-resolved fragment-ion measurements. To give definitive assignments for the core-excited states, Adachi et al. measured the angle-resolved ion-yield S_{1S} spectra of SO_2 at the soft x-ray undulator beamline BL-2A. Figure 4 shows the spectra, where fragment-ions having energies higher than 3eV were detected. The lowest photoabsorption peak (A) at 2473.33eV is the strongest in the bound-state absorption, and is observed only in the perpendicular direction (I_{90}) to the electric vector. This means that the excited state arises in the S_{1S}-$3b_1^*$ transition, where the $3b_1^*$ orbital is of $3p_X$ (out-of-plane π) character, as shown in Figure 4. The second and third features (B and C) are strongly observed at both the perpendicular (I_{90}) and parallel direction(I_0). Based on a simple crystal-field picture, Adachi et al. have assigned those features; peaks B and C correspond to transitions from S_{1S} to

$9a_1^*$ and to $6b_1^*$, respectively. To confirm their assignments, they measured the fragment-ion energy dependence of the angle-resolved ion-yield spectra. Although those are not shown here, the spectra showed a strong and opposite energy dependence for the $9a_1^*$ and $6b_1^*$ states. This pendence mainly comes from the detection efficiency for the heviest sulfur ions having the lowest kinetic energy, which are produced by three bond-breaking reactions. Therefore, one can know the preferential molecular axes for the $9a_1^*$ and $6b_1^*$ states from the energy dependence, because the sulfur ions are ejected along the molecular axes. The experimental data on the preferential molecular axes led their assignments for peaks B and C to definitive ones.

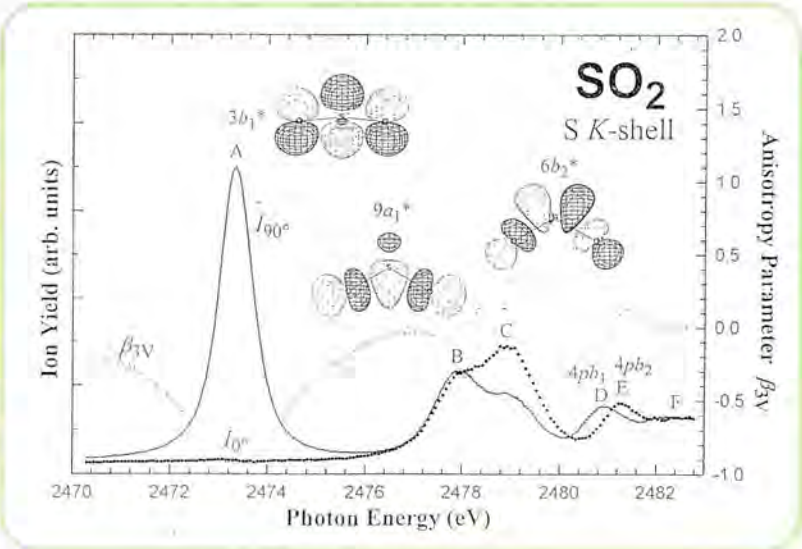

Figure 4.
Angle-resolved ion-yield spectra and the angular distribution of fragment ions with kinetic energies larger than 3eV for the S1s excited states of SO_2. The dotted and solid lines denote the I_0 and I_{90} ion yield, respectively. The thin broken line denotes the observed anisotropy parameter (β_{3V}). The singly-excited molecular orbitals, $3b_1^*$, $9a_1^*$, and $6b_2^*$, are plotted for the lowest three transitions of the valence character.

References
J. Adachi et al., Chem. Phys. Lett., 294(1998)559-564.

1-2 Near-Threshold Triple Photoionization of Lithium

The multiple-photoionization cross sections of atoms are very sensitive for interactions among the outgoing photoelectrons. Of particular importance is the multiple-ionization threshold region where the electrons leave the ion slowly and electron correlations play an important role. Thus, near-threshold multiple photoionization attracts much interest from theoretical and experimental aspects. However one must overcome any experimental difficulty to measure the multiple photoionization cross sections. That is, the cross sections are very small, especially in the threshold region.

Thanks to the intense photon flux from the soft x-ray undulator beamline BL-16B, Wehlitz et al. have succeeded in measuring the triple photoionization cross sections in the threshold region. Figure 2 shows their results concerning the near-threshold triple photoionization cross sections of lithium. As it is well known that the

multiple-ionization cross sections are expressed by a power of the excess energy above the threshold, the cross sections are plotted on a log-log scale. Although only a few data points were taken below 5eV, because of the very small cross sections, one can clearly see that the two regions are those expressed by different exponents. Below 5eV the exponent of 2.05 is consistent with the power law for the triple-photoionization cross sections. However, above 5eV the experimental data bend over to a weaker energy dependence. To explain this energy dependence, Wehlitz et al. have proposed a new mechanism of the triple photoionization of lithium. Namely, the outer 2S electron of lithium is shaken off when the core two 1s electrons are ejected simultaneously by absorbing one photon. Based on this model, they have derived a simple expression of the triple photoionization cross sections above 5eV. The theoretical predictions are shown by the solid curve in Figure 2. In a comparison of the theory with experiment, one can say that this model explains the experimental data fairly well.

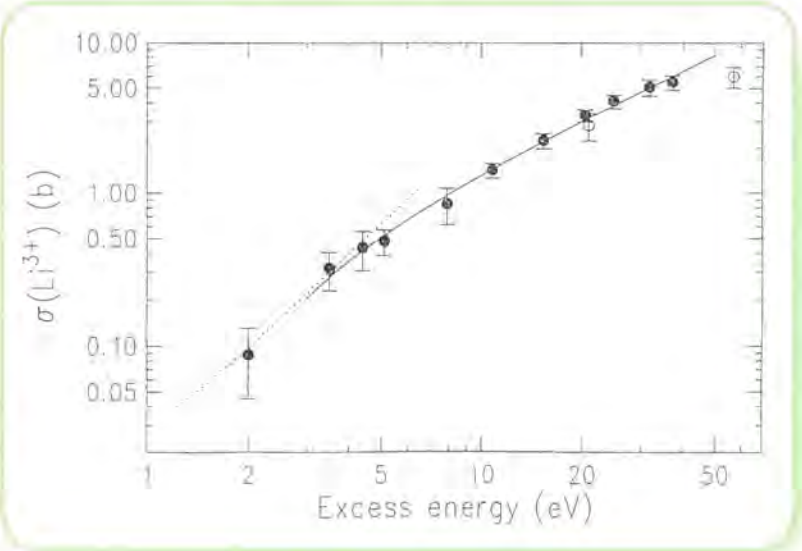

Figure 2.
Triple photoionization cross section of Li as a function of the excess energy (E) on a log-log scale. The solid line is a fit according to the theoretical model, while the dotted line corresponds to $\sigma \propto E^{2.05}$

References
R. Wehlitz et al., Phys. Rev. Lett., submitted.

1-3 Dynamic Properties of Shape Resonances in N_2 and CO_2 Molecules

K-shell excitations in N_2 and CO_2 molecules are of particular interest as prototypes of resonance phenomena in x-ray absorption and ionization of polyatomic systems. Intramolecular interference between emitted and multiply scattered photoelectron waves results in resonance features above the K-edge. These features, which are observed in the channel from the σ-to-σ transition, are regarded as either being associated with temporary trapping of ejected electrons by the molecular potential or with the promotion of core electrons into σ^*

molecular orbitals embedded in the K-shell continuum. The equivalence of atomic sites in a polyatomic system implies their equal probability of excitation. This means that one-photon absorption of the quasidegenerate K-shell levels occurs in one of the equivalent atoms of a molecule, and the relevant molecular photoelectron wave function should be presented as a symmetry-adopted linear combination of atomic wavefunctions. Now a question arises; are the equivalent atoms in the molecule the coherent or incoherent sources of photoelectron waves?

Pavlychev et al. have studied the above-mentioned fundamental problem both theoretically and experimentally. From an analysis of the 1s-photoelectron angular distributions from fixed-in-space N_2 and CO_2 molecules, it has became clear that at the σ^*_u shape resonance the angular distributions behave coherently in N_2 and incoherently in CO_2 (see Figure 3). To understand the difference, Pavlychev et al. have taken the core-hole molecular relaxation into account. Because it is known that the O 1S photolines are dominated by the antisymmetric streching mode, one can distinguish the right and left oxygen atom in CO_2 with an O 1S hole. However, one can not distinguish the right and left nitrogen atom in the N_2 with a N 1S hole. On this basis, the correlation of photoelectron emission with molecular relaxation (in other words, molecular symmetry of the excited molecule) becomes important for describing the photoelectron angular distributions. Then, Pavlychev et al. expressed the photoelectron angular distributions by a mix of the incoherent (inversion symmetry being broken) and coherent (inversion symmetry being held) distributions. In Figure 3, theoretical

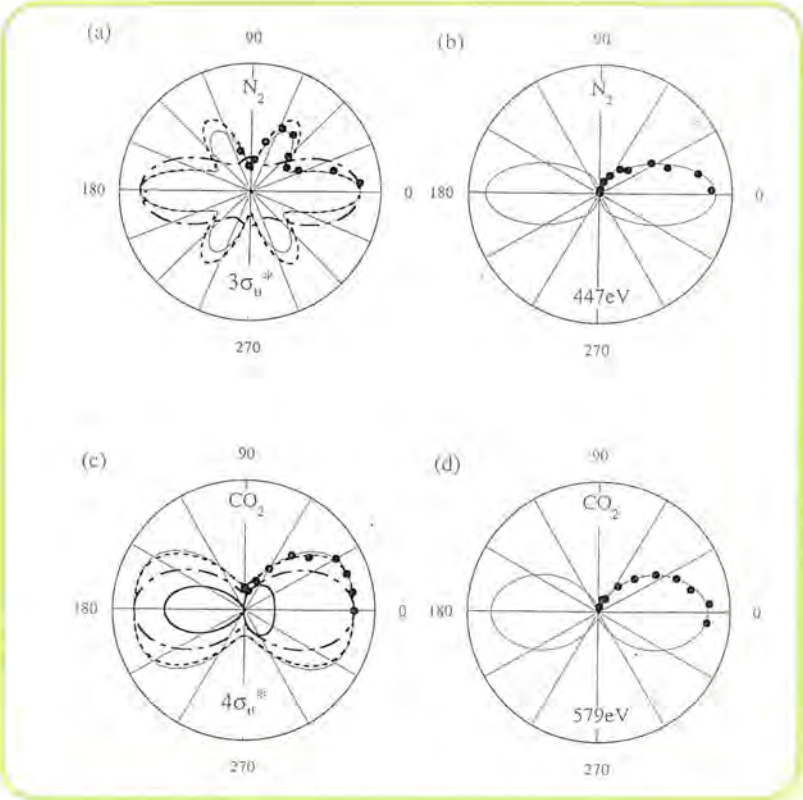

Figure 3.
Angular distributions of 1s photoelectrons at the σ^*_u resonance in N_2 (a) and above it (447eV), and at the σ^*_u resonance in CO_2 and above it (579eV). The molecules are aligned along the 0-180 axis. Filled circles, experimental data; thin solid curves, their fitting results; dash-dotted line, theoretical results for the incoherent case; dashed line, theoretical results for the sum of the coherent and incoherent parts.

results are shown with experimental data. By theoretical analyses of the experimental data, it has been revealed that the coherent intramolecular interference of *pf*-hybridized photoelectron waves is dominate for N_2, and that the incoherent interference of *spd*-hybridized waves is dominate for CO_2.

References

A. A. Pavlychev et al., Phys. Rev. Lett., 81(1998)3623-3626.

1-4 Circular Dichroism in Helium Double Photoionization

The one-photon two-electron ionization of a helium atom occurs through correlation motions of the electron pair of the helium, because the dipole operator is a single-particle type. Therefore, the helium is an ideal sample to elucidate three-body breakup in double photoionization. The double photoionization of a randomly oriented free atom by circularly polarized light produces photoelectron pairs with the ability to distinguish a right-handed coordinate frame from a left-handed one. This chirality, a new manifestation of electron correlations, causes a circular dichroism, i.e., the energy and angle resolved triply differential cross sections different for left- and right-circular polarization.

Soejima et al. have challenged measurements of circular dichroism in triply differential cross sections. To lead them to their success, they selected the helical undulator beamline BL-28A for their experiments, which provides high-intensity XUV radiation with a high degree of circular polarization. It should be emphasized that the use of undulator radiation for the experiments is essential, because the double-photoionization cross sections are two orders of magnitude smaller than those of the single ones. Furthermore, a high degree of

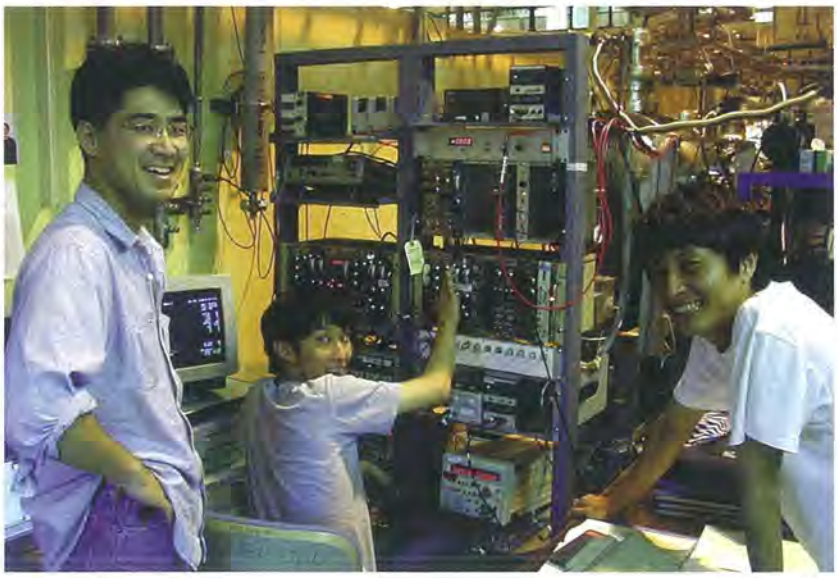

polarization of undulator radiation is inevitable to obtain reliable data. The remarkable results on circular dichroism successfully obtained by Soejima et al. are shown in Figure 1. The triply differential cross sections, i.e., coincidence rates between outgoing photoelectrons as a function of their mutual angles are shown in polar plots for the right- and left- circularly polarized light, where the propagation direction of the light is the z-axis. The ejection direction for one (e_1) of the electrons with 1eV kinetic energy is shown by the arrow. The other electron with 8eV kinetic energy was detected by a rotatable electron analyzer around the z-axis to change the mutual angles. The difference between the triply differential cross sections of Figures 1 (a) and (b), which have mirror symmetry relative to the e_1 direction, is the so- called circular dichroism. The dipole matrix element for double photoionization includes a portion being antisymmetric with respect to the angular and energy exchange of the two electrons. This portion is responsible for the origin of the dichroism. By analyzing the experimental data, Soejima et al. have determined the magnitudes of the symmetric and antisymmetric dipole matrix element separately, and also the phase difference between them. This is a great step towards a deep understanding of circular dichroism in triply differential cross sections.

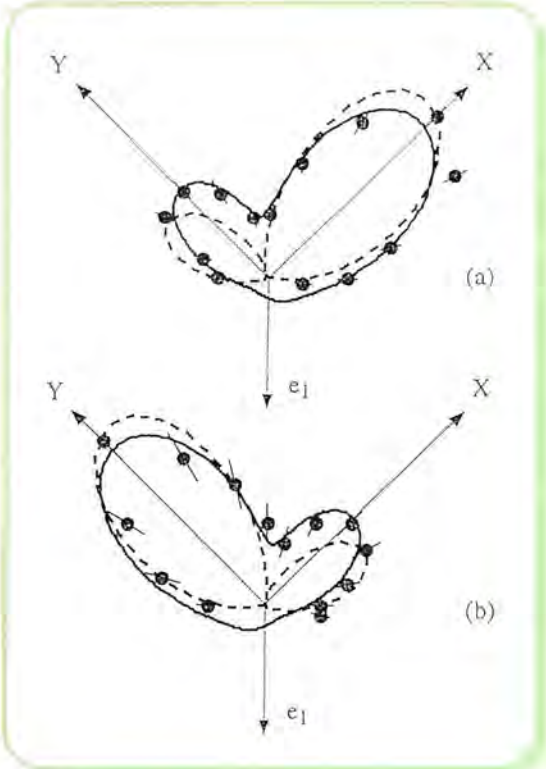

Figure 1.
Polar plots of TDCS(R) and TDCS(L) deduced by the S_1 contribution from the measured TDCS. (a) TDCS(R)(S_3=+0.95) for right-circular polarization, and (b)TDCS(L)(S_3=-0.95) for left-circular polarization. The full curves express the best-fitted curves. The dashed curves present theoretical results of Kheifets and Bray. Both the experimental and theoretical results are arbitrarily scaled for a comparison.

References

K. Soejima et al., Phys. Rev. Lett., 83(1999)1546-1549.

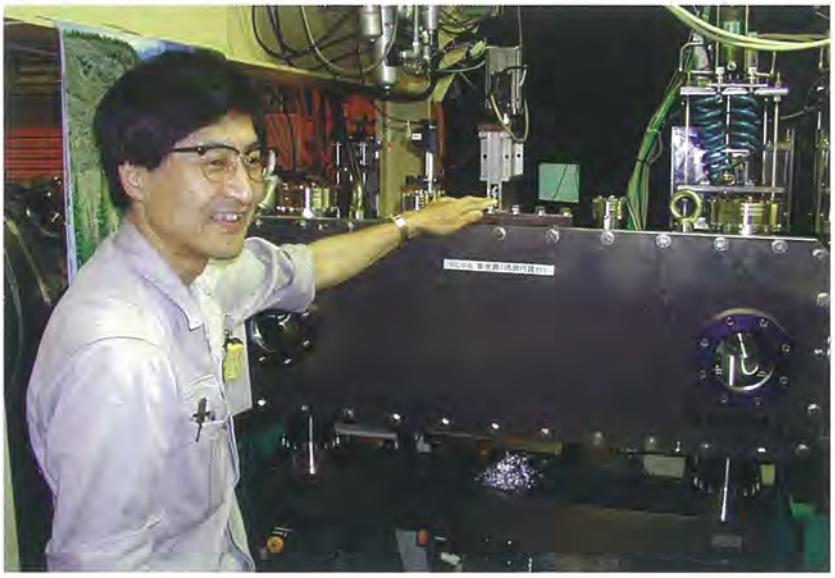

2

Chemistry

2 Chemistry

Since the characteristics of a gate insulator, silicon dioxide, determines the performance of metal-oxide semiconductor field-effect transistors (MOSFETs) in VLSI, a great number of studies on the oxide structure and the oxidation process of silicon have been performed. Enta and co-workers have investigated the initial thermal oxidation on Si (100) 2x1 surfaces with time-resolved ultraviolet and synchrotron-radiation photoelectron spectroscopies. Experiments were conducted on a beam-line BL-3B for O 2*p* UPS measurements ($h\nu$ =23eV), and a beam-line BL-3B,11D ($h\nu$ =135eV) for Si 2*p*. They measured the chemically shifted Si 2*p* core level (Si^{4+}) in real time during the initial thermal oxidation (Fig.1) and found that the time evolution of the Si^{4+} intensities (Fig.2) showed identical behaviors to those of the O 2*p* intensities. The growth mode of the oxidation was found to be separated into two modes; the Langmuir-Hinshelwood mode in the low-T-high-P region and the 2D-island growth mode in the high-T-low-P region. They have concluded, however, that the two modes were unifiedly and almost completely described by a single rate equation (autocatalytic equation) for the oxide coverage (θ), which was derived from the DOS model together with the number of density of islands that scale with $\theta(1-\theta)^2$ as

$$\frac{d\theta}{dt} = \frac{1}{\tau_0 \theta_0}(1-\theta)(\theta_0+\theta)$$

The equation can be solved analytically as

$$\theta = \theta_0 \frac{1 - e^{-\kappa t/\tau_0}}{\theta_0 + e^{-\kappa t/\tau_0}}$$

with $\kappa = (\theta_0+1)/\theta_0$. With its analytical solution containing only two parameters, the autocatalytic equation may help in forthcoming studies to obtain a deeper insight into the Si oxidation process.

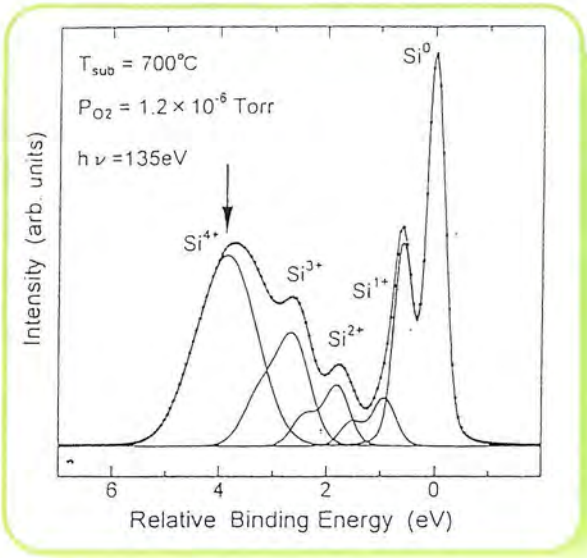

Figure 1.
Typical Si 2*p* core-level spectrum (dots) from ultrathin SiO_2 on Si(100) recorded at 135 eV photon energy. Solid lines denote the curve fitting. The oxide layer was grown with 1.2×10^{-6} Torr O_2 at 700℃ for 12 min.

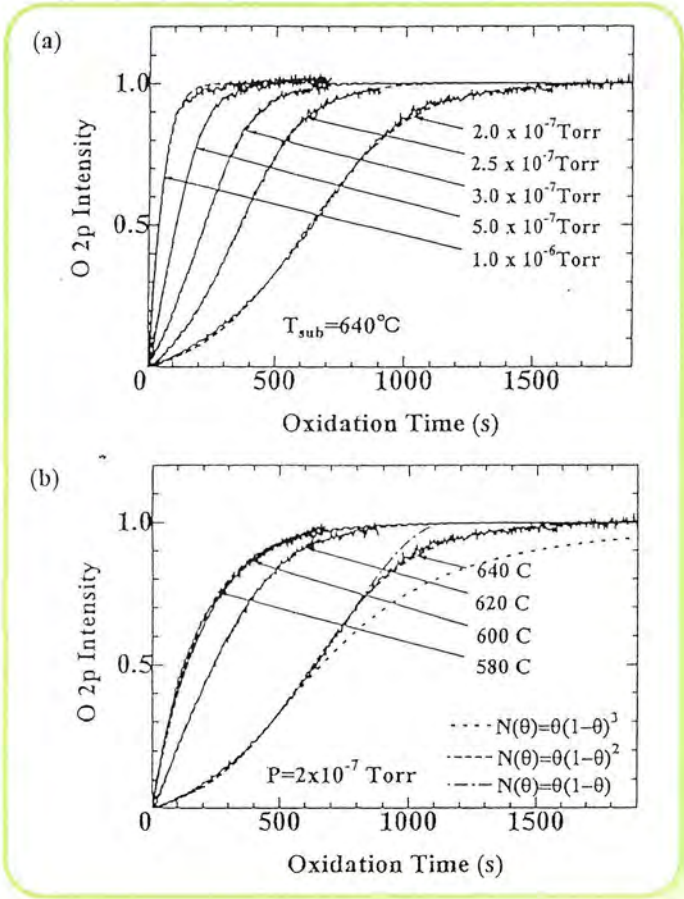

Figure 2.
Time evolutions of O 2*p* UPS intensity for (a) P = 2-10×10^{-7} Torr at T = 640℃ and (b) T = 580-640℃ at P=2× 10^{-7}Torr, respectively. The dashed lines are a fitting with (a), whereas the dotted and the dash-dotted lines in (b) are calculated with the functional forms for $N(\theta)$ as shown in the figure.

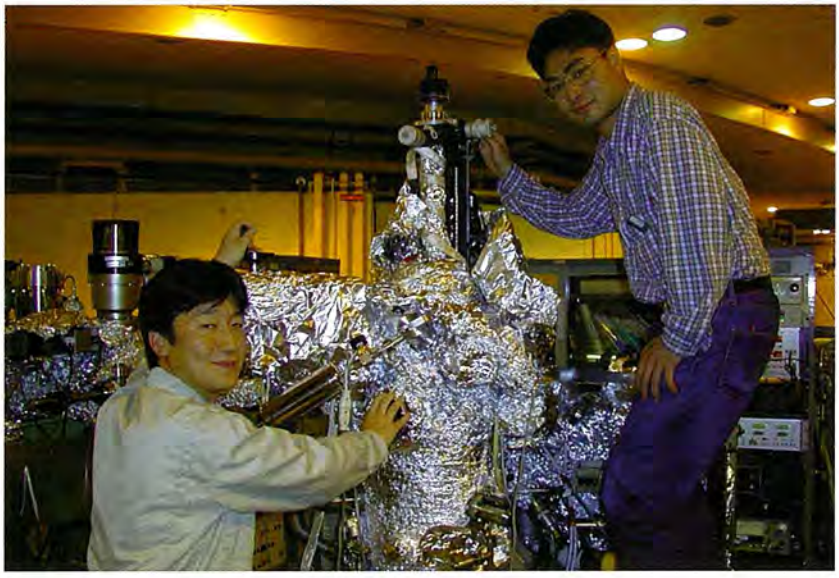

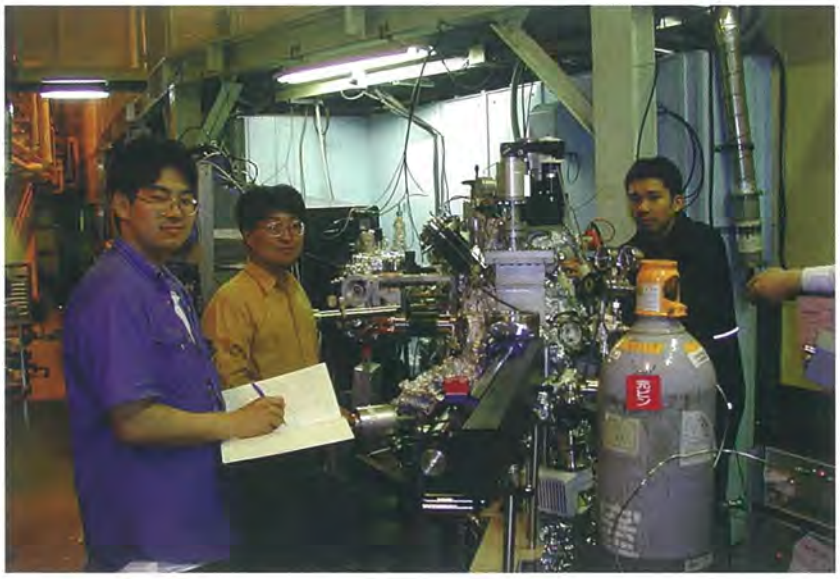

Structure of Surfaces and Interfaces

3 Structure of Surfaces and Interfaces

3-1 Strain Analysis of the SiO_2/Si Interface and Si(111)7×7 Surface

We have developed a new technique of X-ray diffraction in order to measure strain fields near to a semiconductor surface and interface in an ultra-high vacuum chamber [1]. The diffraction geometry involves the extremely asymmetric Bragg-case bulk reflection of a small incident angle to the surface and a large angle, exiting from the surface. The incident angle of the X-rays is set near to the critical angle of the total reflection by tuning the X-ray energy of the synchrotron radiation.

The X-ray intensity of the silicon substrate 311 reflection has been measured to study a Si(111) surface and an oxide/Si(111) interface in

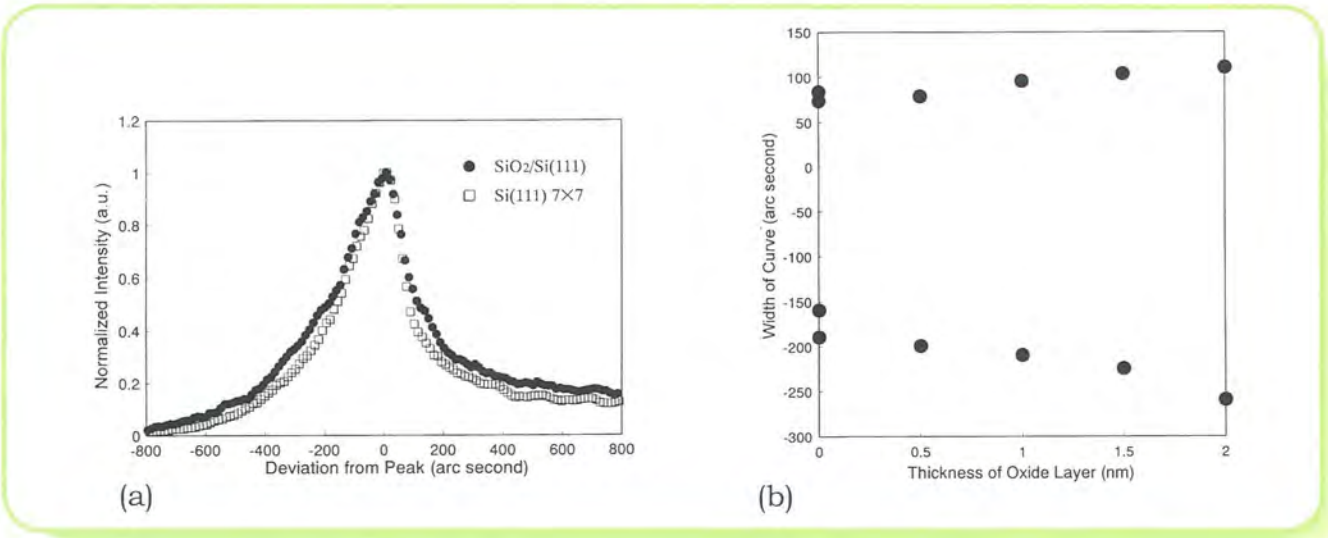

Figure 1.
(a) Rocking curve for the SiO_2/Si(111) interface (solid circles) and that for the Si(111)7×7 surface (open squares).
(b) Oxide-layer thickness dependence of the intrinsic rocking curve width.

an ultra-high vacuum chamber [1]. A clean Si(111) 7×7 surface gives a sharper X-ray diffraction peak than that of the native oxide/Si(111) system, as shown in Figure 1(a). By a theoretical consideration using dynamical theory, we have succeeded to eliminate any absorption effect of SiO_2 layers from the obtained rocking curve [2]. As a result, it was concluded that the strain field near to the interface relaxes for a thinning the oxide layer, as shown in Figure 1(b). The strain field near to the Si(111)7×7 surface is concluded to be smaller than that of the SiO_2/Si(111) interface.

References

[1] T. Emoto, K. Akimoto, and A. Ichimiya, J. Synchrotron Rad. 5 (1998) 964.

[2] T. Emoto, K. Akimoto, and A. Ichimiya, Surf. Sci., (1999) in press.

3-2 X-ray Interference and CTR Observation of GaN and GaInN Layers Grown on Sapphire with AlN Buffer Layer

Group-III nitrides have been attracting great interest as materials for short-wavelength light sources and detectors. However, it has been considered to be difficult to grow nitride crystals, since substrate crystals whose lattice constants and thermal expansion coefficients are close to nitride crystals do not exist. This problem has been solved by using a technique to grow a low-temperature (LT) deposited thin buffer layer on a sapphire substrate.

In this work, X-ray crystal truncation rod (CTR) measurement was conducted for a GaInN samples grown on sapphire substrates with LT-deposited AlN buffer layers in order to study the crystalline structure of GaInN and/or GaN layers formed on the sapphire substrates with the buffer layers. The X-ray CTR measurement is based on the fact that the shapes of X-ray diffraction spots are sensitively modified as the near-surface structure is changed.

Samples were prepared by OMVPE (organometallic vapor phase epitaxy). The sapphire (0001) substrate was treated in a hydrogen atmosphere at 1150℃ for 10 min, and then a 30nm-thick AlN layer was grown at 400℃. The AlN layer (which is called a low-temperature grown buffer layer) is considered to improve the crystalline quality of the overlayers. Then, a 2 μm-thick GaN layer and 40-nm thick GaInN layer were grown on an AlN buffer layer. The GaN and GaInN layers were grown at 750℃.

Figure 2 shows a measured X-ray CTR image recorded on an imaging plate. By analyzing the data obtained by the X-ray CTR spectra, we obtained following results [1]:

1) the GaN and GaInN/GaN layers on the sapphire substrates with the low-temperature grown AlN bufferlayers had the Al

polarity ((0001)A),

2) The surfaces were found to be covered with N,

3) The thicknesses of the GaInN layers were measured accurately to be 4.02nm and 40.5nm for samples designed to have 4nm-and 40nm-thick GaInN layers, respectively,

4) The indium compositions for 4nm-and 40nm-thick GaInN layers were determined to be 8.8% and 11%, respectively.

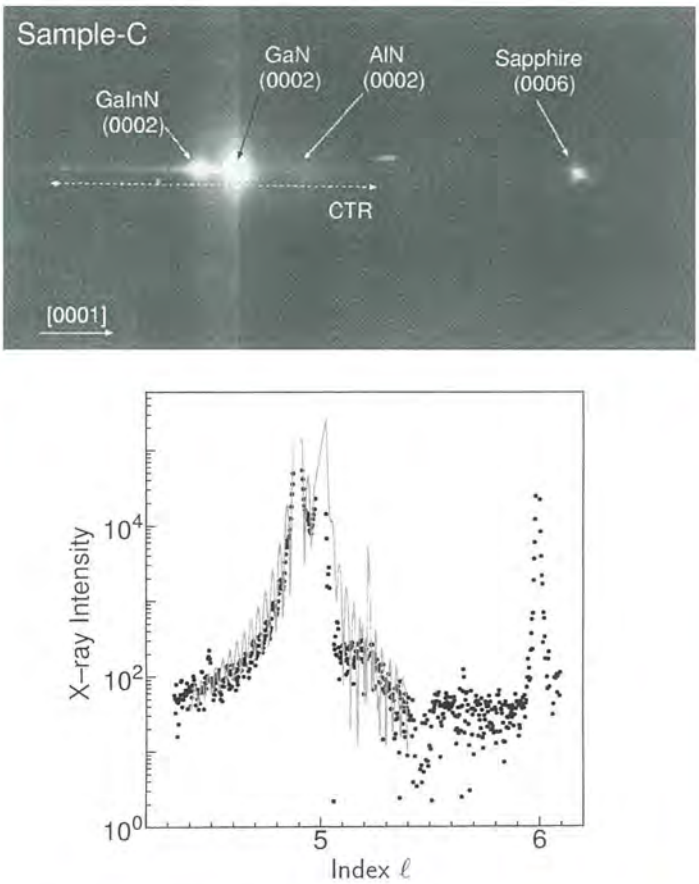

Figure 2.
Measured X-ray CTR image recorded on an imaging plate and analyzing the data obtained by the X-ray CTR spectra.

References

[1] M. Tabuchi, Y. Takeda, N. Matsumoto, H. Amano and I. Akasaki, Jpn. J. Appl. Phys., (1999) in press.

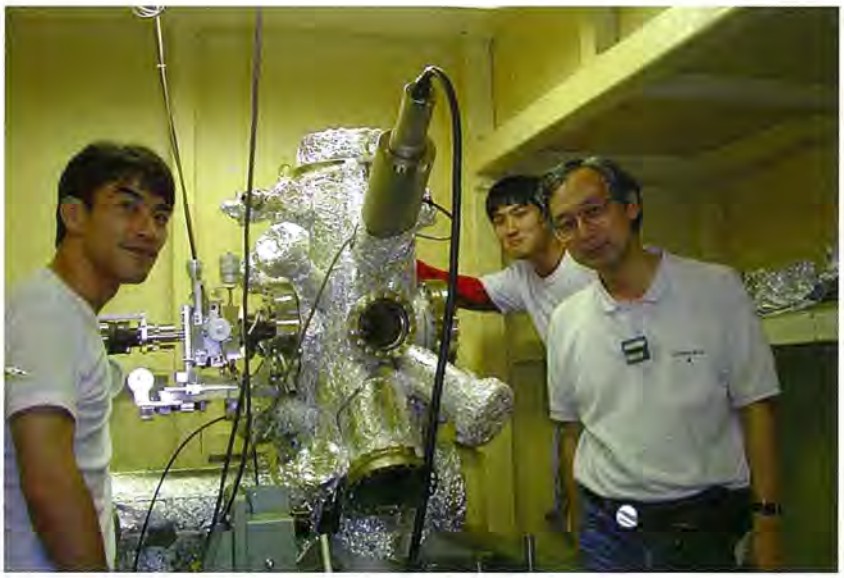

3-3 Interface Structure and Preferred Orientation of Ag/Si(111)

We studied buried interface structures of Ag/Si(111) $\sqrt{3}$ -Ag and Ag/Si(111)7×7 samples using grazing-incidence X-ray diffraction with synchrotron radiation. We also measured the crystal orientation of the Ag overlayers of the samples. Of the numerous $\sqrt{3}$ structures, only a boron-induced $\sqrt{3}$ structure has been detected in buried interfaces. We studied the buried interface superstructure of Ag(26 nm thick)/Si(111) $\sqrt{3}$ -Ag, and detected a $\sqrt{3}$ fractional-order reflection peak. This means that the $\sqrt{3}$ structure remained at the interface. Our experimental results [1] differ from previously reported measurements [2] in which Ag films were deposited at about 320K. One possible reason for the contradiction is the difference in the substrate temperatures for the Ag deposition (320K vs. 290K). To confirm this, we prepared several samples at various substrate temperatures (290 ~370K). We plotted the intensity versus substrate temperature. A plot of the intensity of the (4/3, 1/3) rod versus substrate temperature (Figure 3(a)) shows that the (4/3, 1/3) peak intensity decreased drastically at the 290~310K interval, and became very weak at 370K [1]. This result confirms that the difference in the substrate temperature is the reason for the contradicting results between different studies.

Figure 3(b) shows that the 111, 200, and 220 reflections are the in-plane reflections in a sample with 26-nm-Ag deposition on a $\sqrt{3}$ surface at 290K. Our results for the crystal orientation of the Ag overlayers of Ag/Si(111) $\sqrt{3}$ -Ag showed that Ag{110}, Ag{100}, and Ag{111} planes were grown on the surface [1]. By measuring several samples prepared at various substrate temperatures (290~370K), we found a strong correlation between the appearance of the interface $\sqrt{3}$ structure and the growth of the Ag{110} plane. In contrast, our results for the crystal orientation of the Ag overlayers of Ag(26 nm

thick)/Si(111)7×7 showed that only the Ag{111} plane was grown on the surface [1].

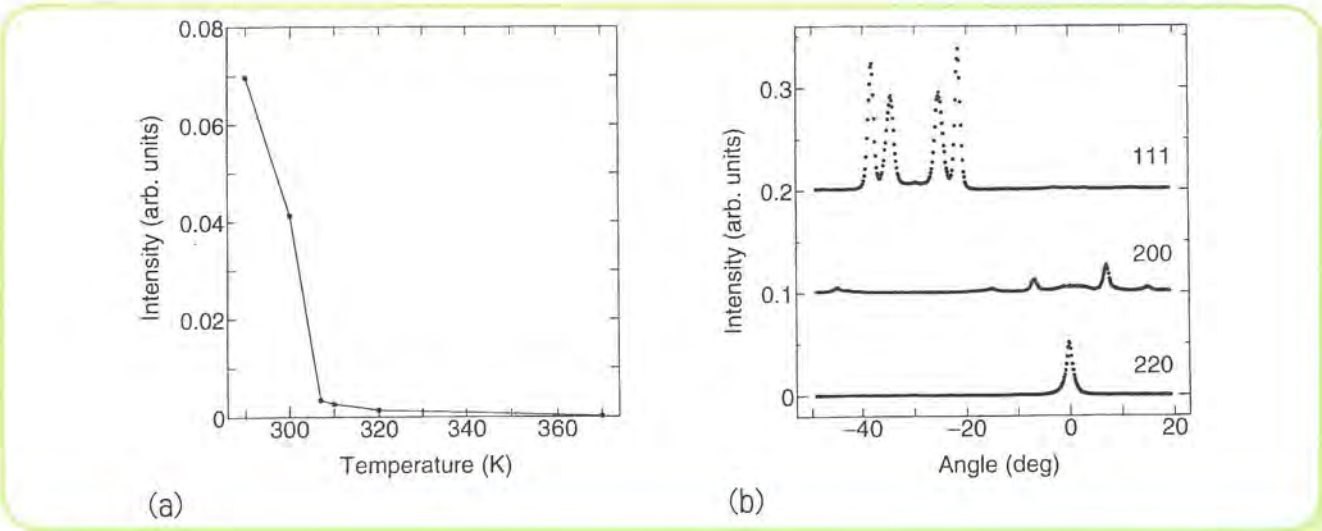

Figure 3.
(a) Intensity profile of a (4/3, 1/3) rod versus the substrate temperature for the deposition of Ag overlayers in Ag/Si(111) $\sqrt{3}$ -Ag. (b) Intensity profiles of Ag bulk rods (220, 200, 111 reflections) for Ag/Si(111) $\sqrt{3}$ -Ag.

References
[1] K.Akimoto, M.Lijadi, S.Ito, and A.Ichimiya, Surf. Rev. Lett., 5 (1998) 719.
[2] H. Hong, R.D.Aburano, D.-S.Lin, H. Chen, T.-C.Chiang, P.Zschack, and E.D.Specht, Phys. Rev. Lett. 68 (1992) 507.

3-4 Surface Band Structures of Ag and Pb Quantum Chain Structures on the Si(001) Surface

The initial growth of metals on semiconductor surfaces often results in very anisotropic structures (self-organized quantum chains), which may feature exotic 1D properties and can also have great implications for future nano-scale device technology. We have studied the electronic band structures of well-ordered surface phases of such quantum chains; especially for Ag and Pb on Si(001).

Several submonolayer surface phases were extensively studied, such as 2×1 [1], 2×3 [2], c(6×2) [3] for Ag/Si(001) and 2×2, 2×1 for Pb/Si(001). For example, Figure 4 shows the surface-state band structures within the bulk band gap measured for the 2×3- and c(6×2)-Ag surfaces. These studies made clear (1) that the two surfaces are semiconducting with ~ 1 eV band gaps and (2) that there are three characteristic and very similar surface states bands (S1—S3). This result denies the present structure model of a 2×3 surface [2], which yields a metallic surface, and elucidates the structural proximity of the 2×3 and c(6×2) phases [3]. Although these surface-state bands

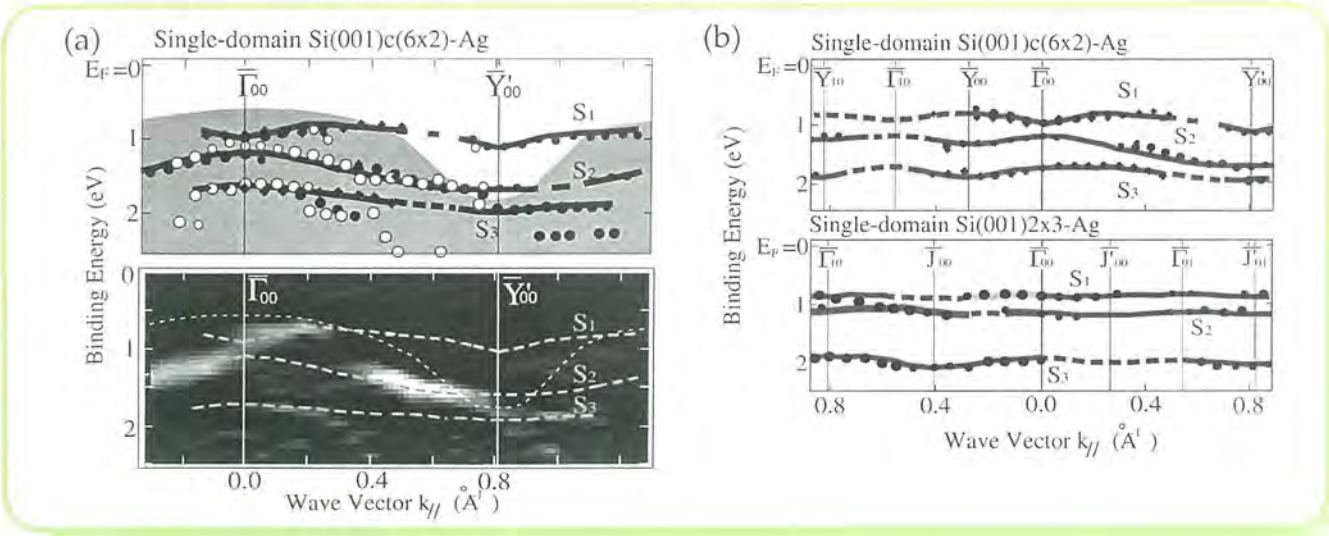

Figure 4.

(a) Gray-scale E_B - $k_{//}$ diagrams for the single-domain Si(001)c(6×2)-Ag surface. (b) Summary of the surface-state dispersion of single-domain Si(001)c(6×2)-Ag and Si(001)(2×3)-Ag surfaces within the bulk band gap.

show no significant anisotropy or dispersions, a further angle-resolved photoemission (ARP) study for the Ag 4d levels has shown that only the 2×3 phase has anomalous 4d bands with a prominent anisotropy along the chains reflecting a 1D interaction along the Ag linear chains. Similar ARP studies for the 2×2-Pb have suggested that the surface-state electrons are well-localized to form strong covalent bonds within the linear chains. This result is consistent with the very similar 2×2 linear chain structures of the Al, Ga and In adsorbates on Si(001). However, we found an interesting surface metalization for the 1 ML 2×1-Pb phase, whose origin is still unclear.

References

[1] I. Matsuda, H. W. Yeom, K. Tono, and T. Ohta, Surf. Sci. (1999) in press.

[2] H. W. Yeom, I. Matsuda, K. Tono and T. Ohta, Phys. Rev. B 57 (1998) 3949.

[3] I. Matsuda, H. W. Yeom, K. Tono, and T. Ohta, Phys. Rev. B 59(1999)15784.

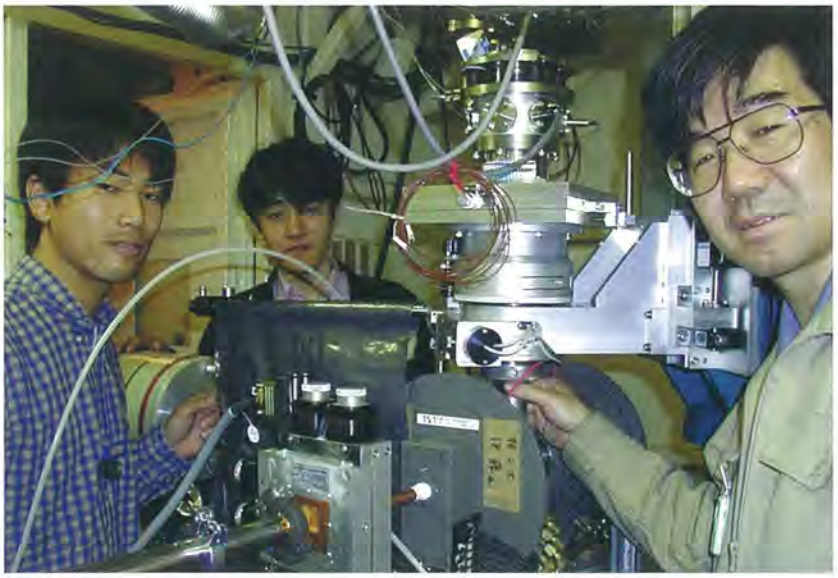

Materials Science

4 Materials Science

4-1 Transition between Two Ferromagnetic States Driven by Orbital Ordering

It has been widely accepted that the orbital degree of freedom plays a central role in the electric and magnetic properties of some strongly correlated electron systems. For example, the colossal magneto-resistance (CMR) effect in manganites is attributed to the role of the orbital on the coupled system of the charge-spin-lattice. By utilizing the resonant x-ray scattering technique, [1] this study has uncovered the role of the orbital in the metal-insulator transition in lightly doped manganites. [2]

A lightly doped perovskite manganite, $La_{0.88}Sr_{0.12}MnO_3$, exhibits a phase transiton at T_{OO}=145 K from a ferromagnetic metal (T_C=172 K) to a novel ferromagnetic insulator. We have identified that the key parameter in the transition is the orbital degree of freedom in eg electrons of Mn^{3+}. Figure 1(a) shows the incident energy dependence of the (030) peak, which is structurally forbidden, at T=12 K. The peak exhibits a sharp enhancement at the Mn K-edge, determined experimentally from fluorescence. Figure 2(b) shows the azimuthal scan, clearly revealing the square of the sinusoidal angle dependence of two-fold symmetry. Note that the origin of the azimuthal angle is defined where the c-axis is within the scattering plane. These results directly indicate that orbital ordering occurs at T = 12 K. Figure 1(c) shows the temperature dependence of the resonant peak intensity. It is clear that the orbital ordering appears only below T_{OO}=145 K. Recently, neutron-diffraction experiments have revealed that the cooperative Jahn-Teller (JT) distortion disappears, or significantly decreases, in this phase (T < 145 K), though this appearance of orbital ordering in the phase without JT-distortion is counter-intuitive. [2] Besides, it is theoretically suggested that this type of orbital ordering

can drive the super-exchange process under a strong electron correlation together with ferromangetic ordering. [2]

Thus, the present investigation shows a novel role of the orbital degree of freedom as a hidden parameter in the ferromangetic metallic to the ferromangetic insulating phases in lightly doped CMR manganites.

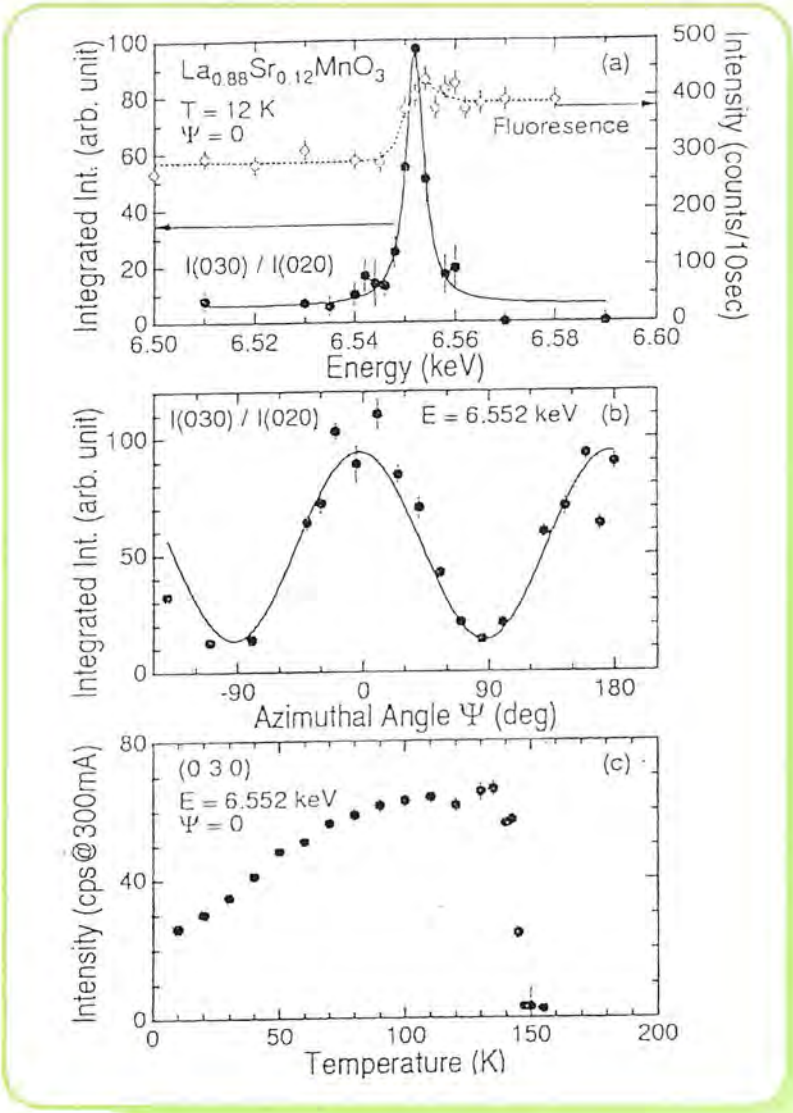

Figure 1.
(a) Energy dependence of the intensity of the orbital ordering reflection (030) at T=12 K. The dashed curve represents fluorescence showing the resonant energy (6.552 keV) corresponding the Mn K-edge.
(b) Azimuthal-angle dependence of (030). The solid line is a two-fold squared sine curve of the angular dependence.
(c) Temperature dependence of the (030) peak intensity.

References

[1] Y. Murakami et al., Phys. Rev. Lett. 80, 1932 (1998), and Phys. Rev. Lett. 81, 582 (1998).

[2] Y. Endoh et al., Phys. Rev. Lett. 82, 4328 (1999).

4-2 Exotic Phase Transition of NaV_2O_5

The inorganic compound α'-NaV_2O_5 [1] has an exciting-phase transition at Tc=35K associated with its spin, charge and lattice systems. The spin-gap formation at (1,1/2,0) [2] and the atomic displacements with its modulation vector, q=(1/2, 1/2, 1/4), [2] and charge ordering of vanadium ions (V^{4+} and V^{5+}) [3] take place

simultaneously at T_C.

An X-ray anomalous scattering study of NaV_2O_5 to clarify this charge ordering pattern of the vanadium ions has been performed. [4] Using the X-ray energy near to the vanadium K-absorption edge (~ 5.465keV) to enhance the difference of f' and f" between V^{4+} and V^{5+}, selective information about the vanadium atoms can be obtained.

The energy dependence of the superlattice intensity at (15/2 1/2 1/4) has been observed, as shown in Fig.2(a). Near to the absorption energy, a large energy modulation relevant to the charge-ordered state is clearly observed. This result is explained by a *zigzag*-type charge-ordered state, [5] instead of the *chain* type. [6] The temperature dependence of the order parameters of the atomic displacement and charge-ordered state can be observed at such energies, E=5.41KeV and 5.47keV, as shown in Fig.2(b). These intensities, normalized at T = 7K, indicate a similar temperature

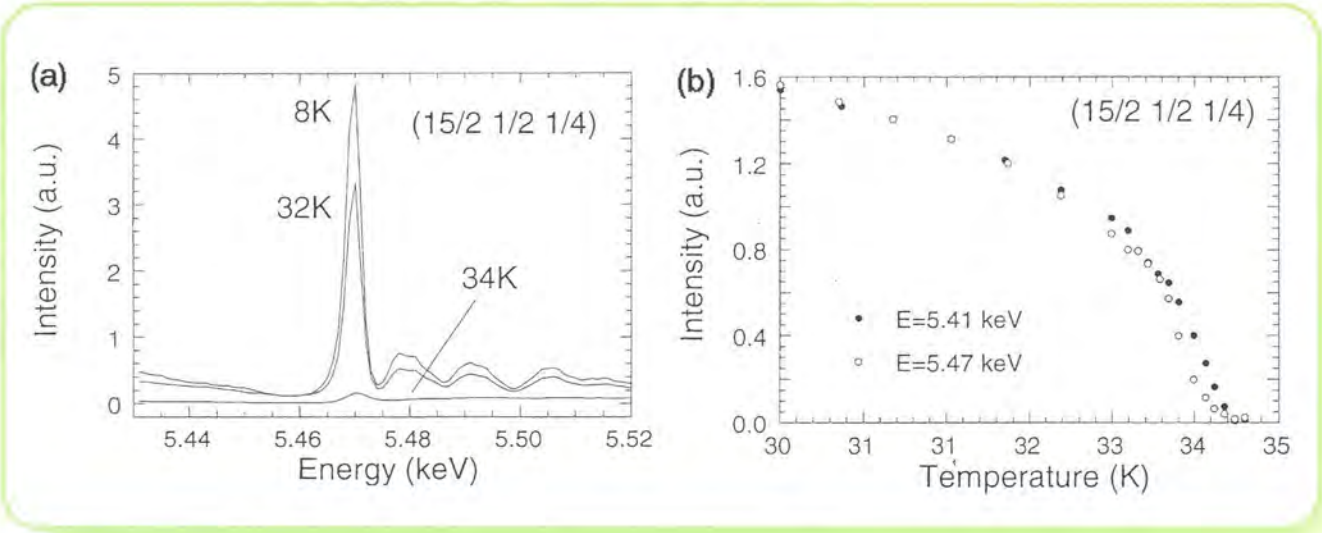

Figure 2.

(a) Energy dependence of the superlattice intensity at (15/2 1/2 1/4). (b) Temperature dependence of the order parameters of the atomic displacement and charge-ordered state.

dependence over the whole temperature region. Therefore, this charge-ordered state does not immediately appear at T_C, but gradually grows while accompanying the atomic displacement below T_C. This aspect of charge disproportionation has been first identified.

References

[1] M. Isobe and Y. Ueda, J. Phys. Soc. Jpn. 65 (1996) 1178.

[2] Y. Fujii et al., J. Phys. Soc. Jpn. 66 (1997) 326.

[3] T. Ohama et al., Phys. Rev. B59 (1999) 3299.

[4] H. Nakao, Doctor thesis (Univ. of Tokyo, 1998).

[5] H. Seo and H. Fukuyama, J. Phys. Soc. Jpn. 67, 2602 (1998); M. V. Mostovoy and D. I. Khomskii, cond-mat/9806215.

[6] P. Thalmeier and P. Fulde, Europhys. Lett. 44 (1998) 242.

4-3 Resonant Inelastic X-Ray Scattering in Ni Compounds

Resonant inelastic x-ray scattering (RIXS) at the Ni *K*-edge in NiO, $NiSO_4$, NiF_2, $NiCl_2$ and $NiBr_2$ were measured at BL-9C. [1] It is known that profiles of the Ni $K\beta_{1,3}$ x-ray fluorescence spectra of Ni compounds can be interpreted by a charge-transfer effect from the ligand field to Ni. However, the charge-transfer energy is derived from fitting to the XPS spectra indirectly. By using RIXS measurements, we investigated the charge-transfer energy directly and the correlation between the charge-transfer energy and the Ni $K\beta_{1,3}$ spectra.

All of the samples were powder and made into pellets. The scattered radiation was analyzed by a Ge (444) crystal for the energy range around the Ni $K\beta$ fluorescence lines. The analyzed x-rays were detected by a position-sensitive proportional counter. The $K\beta_{1,3}$ and the elastic scattering were measured at the same time. The total energy resolution is about 2.5eV around the Ni $K\beta_{1,3}$ line.

About 5 ~ 9 eV below the elastic peaks, we observed charge-transfer satellites. From the energy differences between the elastic and inelastic scattering, we could estimate the charge-transfer energies more directly than from a 2*p*-XPS fitting calculation. The sample dependence of the present charge-transfer energies agrees roughly with the result of the calculation. Figure.3 shows the relationship between the charge-transfer energy and the intensity ratio of the shoulder to the main peak of the Ni $K\beta_{1,3}$ emission spectra. A negative correlation can be clearly observed. Kawai *et al.* have pointed out that the intensity ratio of the shoulder to the main peak becomes larger with increasing the mixing ratio of the $3d^9\underline{L}$ and $3d^{10}\underline{L}^2$ configurations due to a charge-transfer effect, where $\underline{L}$ represents a ligand hole. [2] Therefore, Figure.3 shows that the charge-transfer from the ligand electrons to the Ni 3*d* states is depressed with increasing the charge-transfer energy.

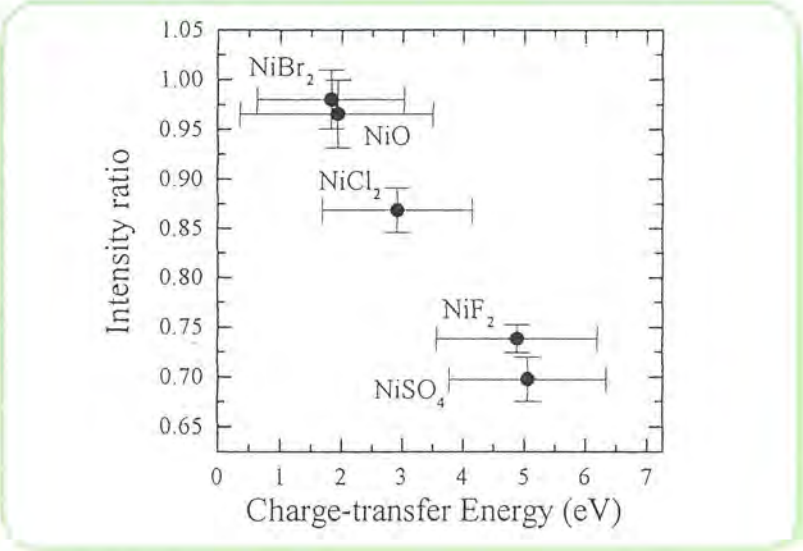

Figure 3.
Relationship between the charge-transfer energy and the intensity ratio of the shoulder to the main peak of Ni $K\beta_{1,3}$

References

[1] H. Shoji, K. Kobayashi, T. Iwazumi, R. Katano, Y. Isozumi, S. Kishimoto and S. Nanao, Japan. J. Appl. Phy5. Supl. 38-1, 592 (1999).

[2] J. Kawai, M. Takami and C. Satoko, Phys. Rev. Lett., 65 (1990) 2193

4-4 Direct Determination of Purely Interfacial Magnetic Moments and Ferromagnetism-to-Superparamagnetism Transition in Au/Co Nanoclusters/Au(111)

Studies of magnetism of nanoclusters are expected to shed new light on the evolution of magnetic order from the Hund's-rule-derived atomic spin to the macroscopic, long-range, spin-ordered ferromagnetism, because of their bridge character between 0-dimensional isolated atoms and 3-dimensional condensed systems. A direct and separate determination of the spin (m_{spin}) and orbital (m_{orb}) moments of purely surface or interface atoms remains to be a challenge for experimentalists. Direct experimental evidence is still lacking for superparamagnetism (SPM) in nanoclusters. To study these problems, we have performed angle-, field-, and temperature-dependent Co $L_{2,3}$-edge MCXD measurements including a magic angle of 54.7° on self-assembled Au/2-ML Co nanoclusters/Au(111), with simultaneous nano-structural confirmation using STM [1].

Figure 4 shows the sample structure, MCXD experimental arrangements, typical remnant (B=±0T) and ±3-T Co $L_{2,3}$-edge XAS and MCXD spectra, and the field (H) dependence of the normal-incidence Co L_3 MCXD (hysteresis curve). We emphasize that almost all the Co atoms can be regarded as interfacial ones with a small number of perimeter atoms in Co nanoclusters, because the clusters

have a constant 2-ML height and they are interposed between Au films. A sharp rectangular MCXD hysteresis was observed for the 5-ML film at room temperature (RT), showing complete ferromagnetism (FM). The Co nanoclusters with $\theta_{Co}\simeq$1.6ML ($D_{av}\simeq$6nm) and $\theta_{Co}\simeq$ 1.2ML ($D_{av}\simeq$5.3ML) also showed a remnant MCXD and a clear MCXD hysteresis at RT. This shows that those Co clusters are FM at RT. In contrast, no remnant MCXD was seen at RT for Co clusters with θ_{Co} $\simeq$0.4ML ($D_{av}\simeq$3.5nm) and the MCXD intensity depends strongly on the field strength. The same behavior was observed for Co clusters with $\theta_{Co}\simeq$0.8ML ($D_{av}\simeq$4.5nm) and $\theta_{Co}\simeq$1.1ML ($D_{av}\simeq$5nm). The field-dependent MCXD can be fitted approximately by a Langevin function. These results indicate SPM of independent Co clusters with $\theta_{Co}\simeq$1.1ML ($D_{av}\simeq$5nm). The T-dependent MCXD for H=$\pm$0Oe revealed that a clear remnant MCXD appeared at T$\lesssim$70K with lowering T for $\theta_{Co}\simeq$0.4ML, whereas no remnant MCXD was seen for T$\gtrsim$85K. The blocking temperature, T_B is thus determined to be $T_B\simeq$ 70-80K for $\theta_{Co}\simeq$0.4ML. A similar T-dependent remnant MCXD for θ_{Co} $\simeq$0.8ML yielded $T_B\simeq$100-120K. The H-dependent MCXD at T=30K for $\theta_{Co}\simeq$0.4ML shows that the MCXD intensity for B=$\pm$5T at 30K is almost equal to that at T=300K. The large saturation MCXD at 300K can not be explained by usual paramagnetism. We thus conclude that independent Co nanoclusters with $\theta_{Co}\lesssim$1.1ML ($D_{av}\lesssim$5nm) are essentially SPM and that a phase transition takes place from FM to SPM around $\theta_{Co}\simeq$1.1-1.2 ML with decreasing cluster size [1].

Figure 5 (a) shows the angle (γ)-dependent XAS and MCXD spectra for the SPM Co clusters $\theta_{Co}\simeq$1.1ML ($D_{av}\simeq$5nm). The MCXD orbital [2] and spin [3] sum rules, as applied to the angle-dependent mode [4,5], state that $[\Delta A_{L3}+\Delta A_{L2}]_\gamma = -C\cdot m^\gamma_{orb}/2\mu_B$ and $[\Delta A_{L3}-2\cdot\Delta A_{L2}]_\gamma = -C\cdot(m_{spin}-7\cdot m^\gamma_T)/3\mu_B$. We further note that use of $m^\perp_T+2m^\parallel_T=0$ leads to $m^\gamma_T=1/2\cdot m^\perp_T\cdot(3\cos^2\gamma-1)=0$ at $\gamma=54.7^\circ$ (magic angle). Thus, the spin sum rule for $\gamma=54.7^\circ$ reduces to $[\Delta A_{L3}-2\cdot\Delta A_{L2}]_{\gamma=54.7^\circ}$ $=-C\cdot m_{spin}/3\mu_B$, allowing a direct determination of m_{spin} by a single

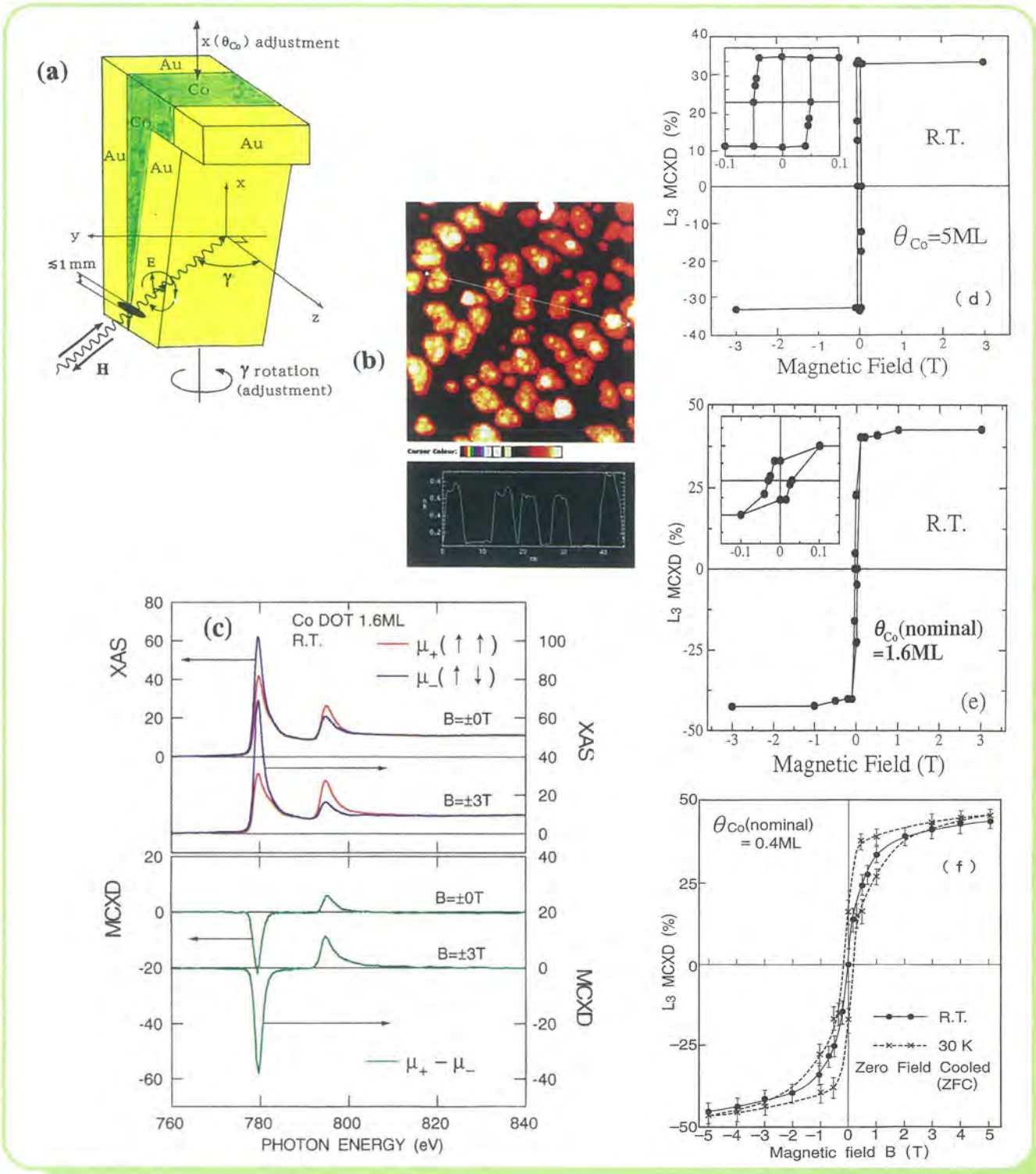

Figure 4.

(a) Schematic view of the sample and MCXD experimental arrangement. (b) STM observation of the wedge-shaped Co part with nominal coverage (θ_{Co}), showing nanoclusters with a constant 2-ML height. Note that no bulk-like Co atoms exist and almost all Co atoms can be regarded as interfacial ones in Au/2-ML Co/Au(111). The average in-plane diameter (D_{av}) of nanoclusters is proportional to the root-mean square θ_{Co}. (c) Remnant (H=±0Oe) and ±3-T Co $L_{2,3}$ MCXD taken at 300K in normal incidence for nanoclusters with $\theta_{Co}\simeq$1.6ML ($D_{av}\simeq$6nm). (d) Normal-incidence L_3 MCXD hysteresis at 300K for the 5-ML Co film. (e) Normal-incidence L_3 MCXD hysteresis at 300K for nanoclusters with $\theta_{Co}\simeq$1.6ML ($D_{av}\simeq$6nm). (f) Field-dependent normal-incidence L_3 MCXD at 300K and L_3 MCXD hysteresis at 30K for nanoclusters with $\theta_{Co}\simeq$0.4ML ($D_{av}\simeq$3.5nm).

magic-angle MCXD measurement, as originally suggested in ref.[4]. We have determined the constant C by a magic-angle MCXD measurement on a single-crystalline hcp Co film and the known values of m_{spin} and m_{orb} for bulk hcp Co. By applying the sum rules to the data at $\gamma=0^\circ$ and 54.7°, we have determined m_{spin}, out-of-plane ($m^{\perp}_{orb}$) and in-plane ($m^{\parallel}_{orb}$) orbital, and out-of-plane ($m^{\perp}_{T}$) and in-plane ($m^{\parallel}_{T}$) magnetic dipole moments of almost purely interfacial Co atoms. The total moment, $m_{total}=m_{spin}+1/3\cdot(m^{\perp}_{orb}+2m^{\parallel}_{orb})$, has also been obtained. The self-consistency of the analyses was confirmed by the combined use of the data for $\gamma=0^\circ$ and 65°. The results are shown in Fig.2(b) as a function of θ_{Co} [1]. The m_{spin} and $m^{\perp}_{orb}$ of purely interfacial Co atoms are remarkably enhanced as compared to those in bulk, directly verifying recent theoretical predictions. The m_{total} values of $\cong$2.3-2.5 μ_B for clusters with $\theta_{Co}\lesssim$1.2ML agree surprisingly well with $m_{tot}\cong$2.4-2.5 μ_B of free Co clusters in the range of the smallest number of atoms, obtained by recent Stern-Gerlach-deflection experiments [6]. The magnetic anisotropy energy calculated using the $m^{\perp}_{orb}$ and $m^{\parallel}_{orb}$ values shows a strong

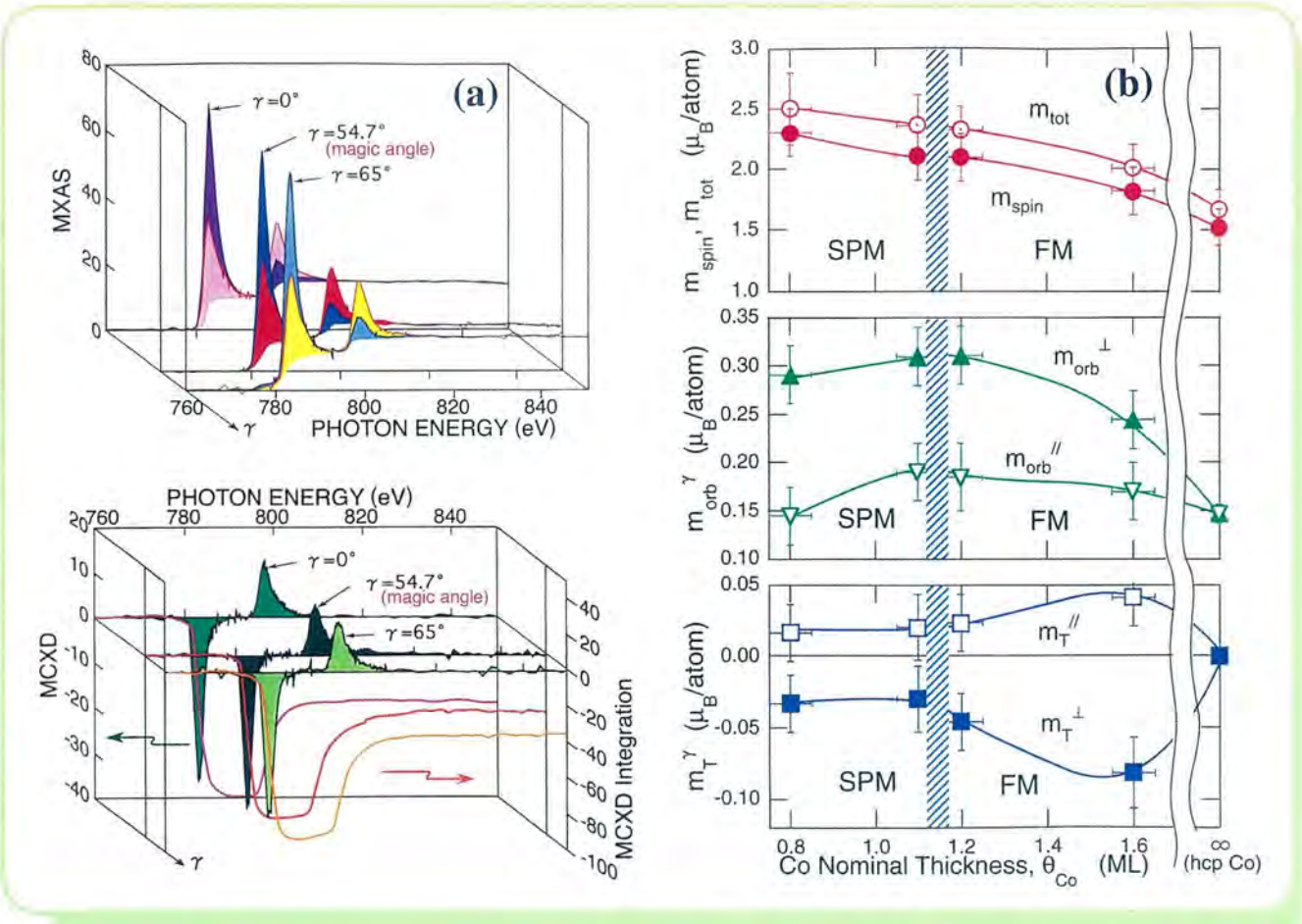

Figure 5.

(a) Angle (γ)- and polarization-dependent XAS spectra (upper panel), and MCXD and its energy-integrated spectra (lower panel) of the SPM Co nanoclusters with $\theta_{Co}\simeq$1.1ML ($D_{av}\simeq$5nm). (b) θ_{Co} dependence of m_{spin}, $m^{\perp}_{orb}$, $m^{\parallel}_{orb}$, $m^{\perp}_{T}$, and $m^{\parallel}_{T}$ of almost purely interfacial Co atoms, determined by the angle-dependent sum rules. $m_{total}=m_{spin}+1/3\cdot(m^{\perp}_{orb}+2m^{\parallel}_{orb})$, is also shown. The hutched area denotes the FM-to-SPM transition region.

perpendicular magnetic anisotropy for the single-domain FM clusters, providing promise for technological applications for nano-scale magnetic bits operating at room temperature. The details of the results and discussion will be reported elsewhere [1].

References

[1] T. Koide, H. Miyauchi, J. Okamoto, T. Shidara, A. Fujimori, H. Fukutani, K. Amemiya, H. Takeshita, T. Katayama, S. Yuasa, and Y. Suzuki, Science (submitted).
[2] B.T. Thole et al., Phys. Rev. Lett. 68, 1943 (1992).
[3] P. Carra et al., Phys. Rev. Lett. 70, 694 (1993).
[4] Stöhr and König, Phys. Rev. Lett. 75, 3748 (1995).
[5] D. Weller et al., Phys. Rev. Lett. 75, 3752 (1995).
[6] I. M. L. Billas et al., Science 265, 1682 (1994).

4-5 Electric Dipole Ordering and Phase Transitions in a Metallofullerene Crystal

The endohedral metallofullerene ($M@C_n$) has a novel molecular structure consisting of a fullerene cage and a metal atom inside the cage, and can be regarded as being a "superatom" having additional degrees of freedom in electronic and spin structures of the molecule. In the $M@C_{82}$ molecule, charge transfer from the metal atom to the cage brings about a large electric-dipole (ED) moment of the molecule. The dipole-dipole interaction between the molecules has an important role for the stability of the crystal structure as well as the elastic interaction in usual "empty" fullerene crystals, which depends on the molecular form and the Van der Waals interaction between the molecules. In most cases, however, the metal atom is positioned out of the center of the molecule, and the ED direction is different from the symmetric axis of the molecule, so that the dipole-dipole interaction competes with the elastic one for determining the orientation of the molecules in the crystal.

In a recent x-ray diffraction study using single crystals of $La@C_{82}$ [1] we observed complicated successive phase transitions, that is, the face-centered-cubic (FCC, T >180 K), rhombohedral (RH, 140<T<180 K), triclinic (TC) and simple cubic (SC) structures below 140 K. The FCC phase is known to be in the merohedral disorder of molecules; i.e., the molecule randomly directs to one of the preferred orientations. The phase transition at low temperatures from RH to TC or SC depends on the cooling rate, and a slow-cooling TC phase appears, while the SC phase appears upon fast cooling. The TC phase seems to be a structure in which a long axis of molecules aligns in the same direction, but metal atoms distribute randomly on one of the equivalent positions in a cage, namely a state of the cage ordering, but ED

disordering. On the other hand, the SC phase has an opposite structure of the ED ordering, but cage disordering. We consider that the low-temperature structure is determined by a delicate balance of the elastic and dipole interactions.

A most remarkable phenomenon of low-temperature phases is that the phase transition from TC to SC occurs due to intense x-ray irradiation. The stable position of the metal atom in the cage depends on the valence of the metal, and this novel transition is considered to be related to the positional relaxation of the metal atom in the cage brought about by x-ray irradiation.

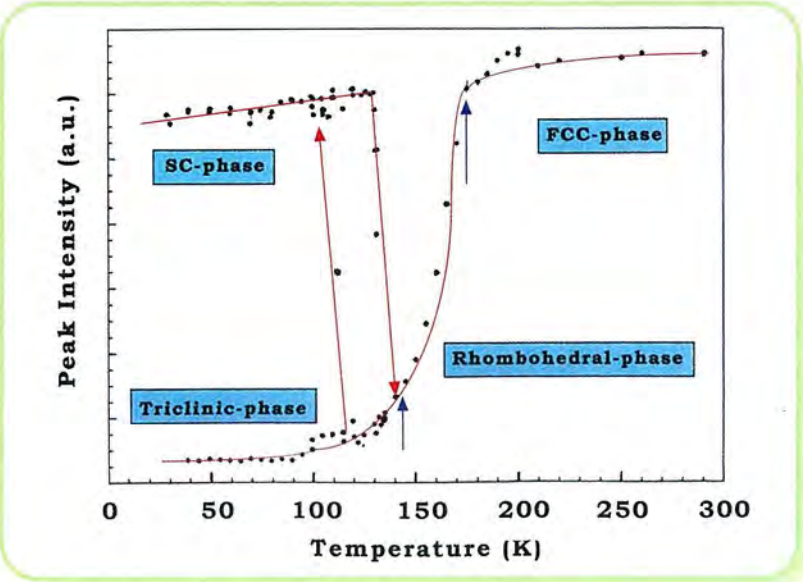

Figure 6.
Temperature dependence of the (022) diffraction peak intensity.
The triclinic phase, which appears upon slow cooling, has a cage ordering structure with no electronic dipole ordering, while the single cubic (SC) phase has a dipole ordering structure. A most interesting feature is that the phase transition from TR- to SC-phase is induced by intensive x-ray irradiation.

References

[1] T.Watanuki et al.: *Proceed. 13th Intern. Winterschool on Electronic Properties of Novel Materials,* Austria, 1999.

Crystallography

5 Crystallography

Crystallographic studies, on inorganic materials including minerals, biominerals and semiconductor materials, using SR have been continuously promoted at the Photon Factory in the fields of structure refinements to obtain accurate structures, the application of anomalous scattering to elucidate the site occupancies of solid solutions, phase transition and so on. From these studies, four topics are introduced below.

5-1 Domain Structure of Gamma Al_2O_3

A aluminum hydroxide, gibbsite $Al(OH)_3$, dehydrates to alpha alumina, Al_2O_3, upon heating via many metastable and transition phases. All of these phases exhibit very poor crystallinity and like amorphous in the diffraction pattern. Abnormal broadening in the powder diffraction patterns reported in references can be clearly elucidated by a single-crystal diffraction study using synchrotron radiation.

Among the metastable phases, gamma alulmina, Al_2O_3, is the most common. Gamma alumina has been described as being a defect spinel-type structure (Fd3m and a=7.9Å) with 32 oxygen atoms and 64/3 aluminum atoms occupying tetrahedral and octahedral sites formed by oxygen atoms.To clarify the aspects ofÅ@the diffraction patterns of gamma alumina, single-crystal photographs were taken. In the Laue photograph, every diffraction spot is abnormally broad and elongated due to the finite size of the reciprocal-lattice point expected due to poor crystallinitt(Fig.1). Therefore a monochromatic beam with λ = 1.0Å was selected by double Si(111) crystals and the size of the beam was limited to 0.5mmÉ" by a collimator. A whole-rotation photograph was taken using a small crystal with a size of

0.1x0.1x0.01mm³. In the rotation photograph around the [110], it is clear that two types of reflections are observed: one exhibits isotropic broadening without a sharp maximum, and the other exhibits a relatively sharp maximum and a broadened base. The former is with all odd indices, e.g. 311 and 511 reflections. The latter is with all even indices, e.g. the 400 and 440 reflections with weak powder streaks. All of the reflections are indexed based on the cubic face-centered spinel-type lattice. The powder patterns expected from the results of the rotation photograph taken with the single crystal agree with the observed powder patterns.

The aspects of the reflections are more clearly shown in an oscillation photograph around the [110] direction taken using a large crystal as a size of 2x1.5x0.75mm³ (Fig.2). X-rays were irradiated to a part of the crystal. The basic aspects are the same with those of the rotation photograph. However, the two types of reflections are more clearly distinguished in the oscillation photograph: one exhibits a sharp maximum and a powder streak(abbreviated to s-reflection hereafter); the other exhibits abnormal broadening, but no powder streak. (abbreviated as b-reflection hereafter). If we assume that both types of reflections are from the same part of the crystal, that is, from the same domain, both types of reflections must exhibit the same shape in the diffraction photograph, even if they are broad or sharp. The different aspects of both reflection shapes indicate that gamma alumina consists of at least two domains: one gives the s-reflection with a sharp maximum, and the other lives the b-reflection with a

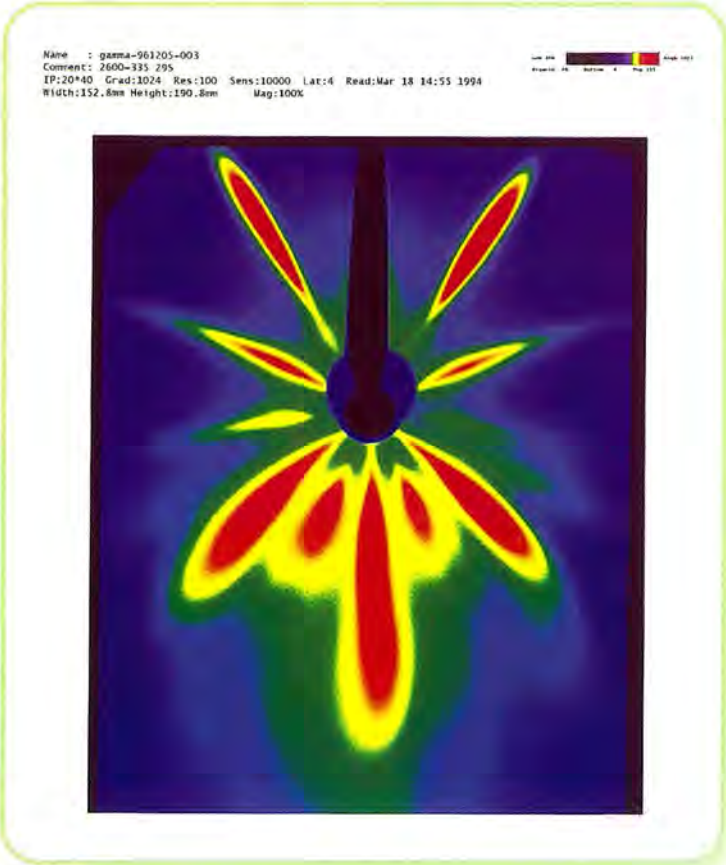

Figure 1.
Laue photograph of gamma alumina taken with continuous
X-rays within a range of $\lambda = 0.7 \sim 1.3$ Å.

broadened shape.

The jamma alumina crystal studied in this work exhibits a spinel twinning. Some reflections of both twin individuals are superimposed, but some are not. The 004 reflection from an individual of spinel twinning exhibits an overlapping of the s-reflection and the b-reflection. On the other hand, the 400 reflection from the other individual indicated by the bold arrow in Fig.2 exhibits only a sharp maximum without a broadened base. If both types of reflections are from the same domain, the 400 reflection from the other individual should also exhibit a sharp maximum with a broadened base. This fact lends additional credibility to the assumption that gamma alumina consists of two domains.

The structure of gamma alulmina has been described as a defect spinel-type structure with aluminum vacancies. All of the structures proposed so far were determined based on the assumption that the diffraction patterns came from the single coherent domain. All of the indices of the s-reflections are even, indicating that the unit cell of the s-reflections is half of the unit cell of the cubic face-centered spinel-type structure. One of the possible candidates for the structure of the s-reflections is a defect rock-salt-type structure, where aluminum atoms randomly occupy the octahedral interstices of the cubic face-centered lattice of oxygen atoms. In this structure all aluminum atoms may essentially have favorite six coordination to oxygen atoms. However, some aluminum atoms may be displaced from the ideal octahedral sites, or the structure may be deformed from the ideal rock salt-type because the intensity of the reflections, such as 222 and 440, is more intense than that of the reflection, 400, which is the most intense reflection for the rock salt-type structure. Here, the indices are according to the spinel-type structure.

On the other hand the structure of the b-reflections has the cell dimensions of the spinel-type structure, and is considered to be a defect spinel-type structure, as proposed so far where aluminum

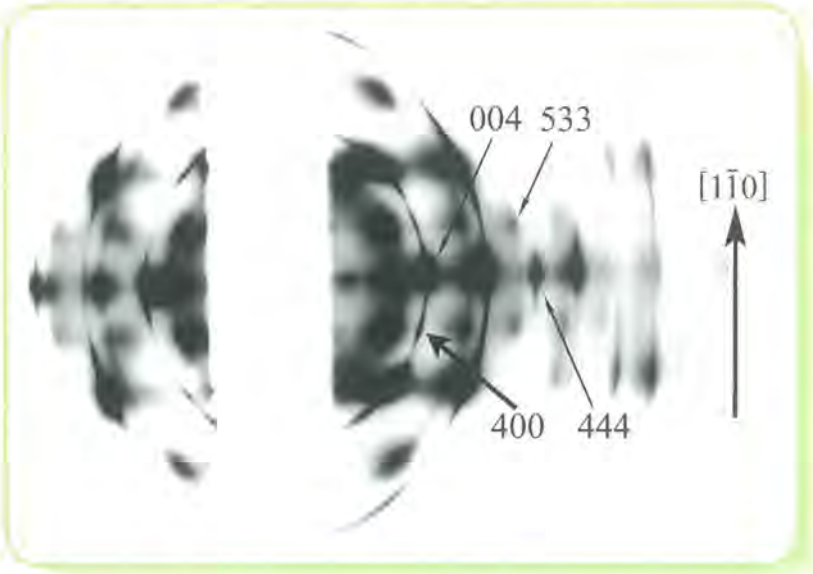

Figure 2.
Oscillation photograph with an oscillation range of 60° around the [110] directiev of gamma alumina.

atoms occupy both the tetrahedral and octahedral interstices of oxygen atoms. As all of the structures proposed so far, however, were determined using powder data, that is, the overlapping data of the s- and b-reflections, the spinel-type structure should be re-determined based on measurements of intensity data of the b-reflections. In conclusion, gamma alumina consists of two domains: one has the spinel-type structure with a small domain size giving broadening of b-reflections, the other has half of the unit cell of the spinel-type structure with a larger domain size suggested from the sharp s-reflections.

5-2 Diffraction from Intermediate State on AuCd Martensitic Transformation

Martensite was originally named for a microstructure of quenched steel. The microstructure has been utilized for steel hardening. The nature of the microstructure of steel was studied and became better known, and the term "martensite" was extended for other alloys systems. The process of obtaining martensite is a martensitic transformation. There days the product phase is called martensite and the high-temperature phase is called a the parent phase.

The characteristics of a martensitic transformation from a macroscopic pint of view are described well by the phenomenological theory of martensite.[1-4] The phenomenological theory of martensite was derived by assuming an undistorted and unrotated plane called the habit plane. Several materials were examined and revealed that the theory described the characteristics of the transformation well. However, the phenomenological theory does not explain the mechanism of the transformation from a microscopic point of view.

From a microscopic point of view, a martensitic transformation is characterized to be a displacive, shear-like transformation in a solid, in which atoms move cooperatively. Phonon sroftening is an attractive picture for describing the martensitic transformation. Meutron inelastic-scattering experiments are a useful way to observe the dynamical aspect of transformations; they were performed to observe phonon softening in several alloys.

A theoretical approach has been made to understand the mechanism of a martensitic transformation. Clapp discussed the stresses and strain around defects which could induce a local mechanical instability and led to the concept of a 'local-soft-mode'.[5-6] Yamada proposed the MLR (Modulated Lattice Relaxation) model for a martensitic transformation.[7-8] Those models attribute the transformation to defects or impurities. On the other hand, a continuum model was developed by Falk[9] in one dimension. It was extended by Barsch and Krumhansl[10] to the two-dimensional case.

AuCd is a one of typical alloys which show a martensitic

transformation. The parent phase has the B2 (CsCl) type structure and the martensite phases have two different structures, ζ_2' and γ_2', depending on the composition. ζ_2' appears at around $Au_{50}Cd_{50}$ and γ_2' appears at around $Au_{52.5}Cd_{47.4}$. Although ζ_2' martensite was known to exist, the crystal structure was not solved for more than 50 years. The crystal structure was recently solved, and the relationship between the crystal structure of the parent and martensite was proposed.[11] A structure study revealed that the superposition of three transverse waves whose wave vector is <110> and whose polarization vector is $<1\bar{1}0>$ produce the ζ_2' martensite. Phonon dispersion relations were observed, overcoming the difficulty of strong absorption.[12] A precursor phenomenon of the transformation provides information about the mechanism of the transformation. A static approach is reported in this paper.

Single crystals of $Au_{50.5}Cd_{49.5}$ were grown. Small fragments of approximately 100 μm in diameter of crystals were electro-polished. Those fragments were picked up and mounted on glass fibers.

A four-circle diffractometer of BL-10A at the Photon Factory of KEK was utilized for two-dimensional mesh-scan measurements at around 1/3 of $[1\bar{1}0]^*$ using a wavelength of 1.050 Å. The monochromater was Si(111) crystal. N_2 gas blower was employed for temperature control. Counting time for one step was 10 s and the interval was 0.01 in index.

Figure 1 shows the 1/3 peak observed 2 K above the transformation-temperature Ms. When the temperature was decreased to below Ms, this reflection split into Bragg reflections of martensite variants. Figure 1 shows a single reflection; it is obvious

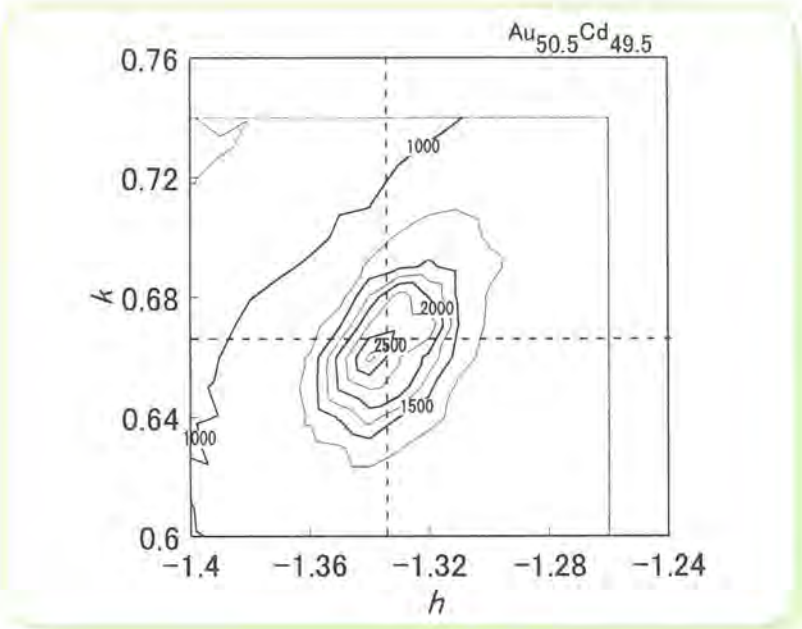

Figure 1.
Intensity distribution around 1/3 position observed at Photon Factory which was measured 2 K above Ms. Contours are drawn every 500 counts for 10 seconds. Dashed lines represent h =2/3 and k =5/3, respectively.

evidence that a transitional (intermediate) state exists prior to the transformation.

Transitional (intermediate) states were recently reported by several researchers in other systems. Zheludev et al.[13] reported that there was a temperature (T_1 in their paper) at which the soft-mode energy increased; they suggested that between temperature T_1 and Ms (T_M in their paper) another phase may be developed which coexists with the parent phase in the Ni_2MnGa system. Mañosa et al.[14] measured several physical properties and concluded that in the Ni_2MnGa system a 'micromodulated structure' exists.

Further discussion is necessary to understand the role of an intermediate state in the martensitic transformation.

References

[1] M. S. Wechsler, D. S. Lieberman and T. A. Read: Trans. AIME, 197(1953), 1503.
[2] D. S. Leiberman, M. S. Wechsler and R. T. Read: J. Appl. Phys., 26(1955), 473.
[3] J. Bowles and J. K. Mackenzie: Acta Metall., 2(1954), 129, 138, 224.
[4] K. Otsuka and C. W. Wayman Ed., Shape Memory Alloys, Cambridge University Press, 1998.
[5] P. Clapp: Materials Science and Engineering, A127(1990), 189.
[6] P. Clapp: Phys. Stat. Sol., (b)57,(1973), 561.
[7] Y. Yamada, Y. Noda and M. Takimoto: Solid State Commun., 55(1985), 1003.
[8] Y. Yamada: Proc. of International Conference on Martensitic Transformations, The Japan Institute of Metals, (1986), 89.
[9] F. Falk: Z.Physik B51(1983), 177.
[10] G. B. Barsch and J. A. Krumhansl: Metall. Trans. 19A(1988), 761.
[11] T. Ohba, Y. Emura and K. Otsuka: Materials Trans. JIM, Vol. 33(1992), 29.
[12] T. Ohba, S. M. Shapiro, S. Aoki and K. Otsuka: Jpn. J. Appl. Phys. Vol.33, 1994, L1631.
[13] A. Zheludev, S. M. Shapiro, P. Wochner, A. Schwartz, M. Wall and L. E. Tanner: Phys. Rev. B51(1995), 11310.
[14] L. Mañosa, A. González-Comas, E. Obrado, A. Planes, V. A. Chernenko, V. V. Kokorin and E. Cesari: Phys. Rev., B55(1997), 11068.

5-3 Experimenally Determined Charge Density of MnS_2 in the Light of Molecular Orbital Calculations

MnS_2 is a paramagnetic semiconductor with a pyrite-type structure. The crystal undergoes an antiferromagnetic phase transition

at 48.2 K. [1] The Mn atom has an oxidation state of +2, with the $3d^5$ electron configuration in the high-spin state. Subsequently, the electron-density distribution around Mn in MnS_2 was expected to be spherical. An experimental charge-density study of the compound by single-crystal synchrotron X-ray diffraction, however, revealed a different topography. [2] Molecular-orbital calculations based on first principles were thus carried out, which justified the experimentally determined charge density. [3]

A diffraction experiment was carried out using a horizontal-type high-speed four-circle diffractometer [4] at the beamline 14A, Photon Factory. An octahedrally shaped natural crystal of MnS_2 (hauerite) from Osorezan, Aomori, was ground into a sphere of 36 micron by the Bond method. In all, 14921 reflection data were collected in the range $2\theta < 138^\circ$ with a wavelength of 0.75 Å. The starting atomic coordinates for the least-squares procedure were taken from those given by Chattopadhyay et al. [5,6] A refinement employing atomic-scattering factors of neutral atoms [7] yielded a final R/Rw value of 0.0119/0.0122 for 539 independent reflections. No significant extinction was detected in the course of refinement based on the Becker and Coppens formalism [8,9] The difference Fourier map of the section including Mn and the nearest S-S dumbbell is shown in Fig. 1 with a contour interval of 0.1 $e\text{Å}^{-3}$. Positive residual peaks with a height of 0.49 $e\text{Å}^{-3}$ were found at a distance of approximately 0.5 Å apart from the Mn atom. These peaks lie in-between the lines connecting Mn, and the first and second nearest

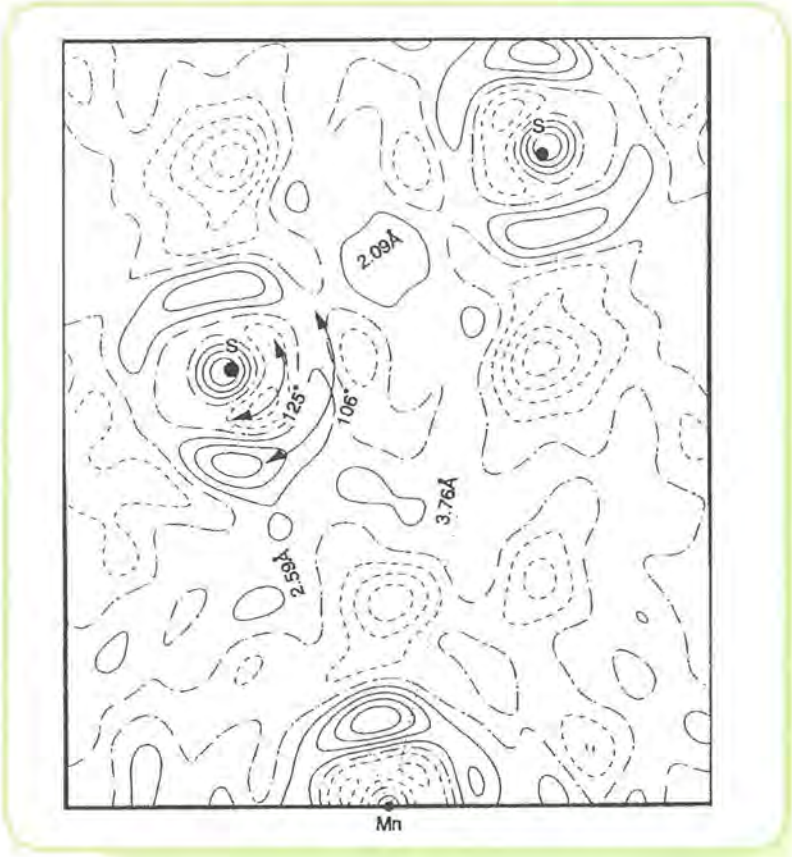

Figure 1.
Experimentally determined deformation density of MnS_2 in the section including Mn and S-S bond. Positive and negative regions are indicated by solid and broken contours.

sulphur atoms. It was beyond expectation to observe lesser excess electrons in the middle of S-S bond because the bonding was thought to be typically covalent.

Molecular-orbital calculations were thus carried out for an $Mn(S_2)_6$ cluster using the SCAT program packagee [10] based on the DV-Xα method [11] All of the 217 electrons, including their spin orientations in the cluster, were taken into consideration for the self-consistent field calculation. The results suggest that the occupied Mn 3*d* atomic orbitals and the 3*p* orbitals of the first and second neighbour sulphur atoms were intricately admixed together to form the valence band. The final calculated electron density and the initial promolecular density of the section containing Mn and S_2 dumbbell are shown in Figs. 2 and 3, respectively, with contour intervals of 0.1 e$Å^{-3}$. In Fig. 2, we can see the electron-density cross-section around the S atoms deformed into an oval-like shape, the lobes extending towards the Mn neighbours. A similar tendency, though subtle, can be found for Mn. Furthermore, a decrease in the charge density was observed near the middle of S-S bond compared to that in the promolecule. This can be ascribed to the flow of valence electrons into the bonds between Mn and sulphur. It is also observed that some electrons around Mn are squeezed out toward the open space of the octahedral environment. All of these features are essentially in good agreement with those observed by the X-ray diffraction study. The theoretically expected deformation density is shown in Fig. 4 with a 0.025 e$Å^{-3}$ contour interval, obtained by subtracting the promolecule density shown in Fig. 3 from the calculated charge density shown in Fig. 2. The heights of the excess electron peaks near Mn were the same within the estimated uncertainties between the observed and calculated deformation density maps.

This study is an example that can assure us of the accuracy and precision of the experimentally determined charge density by single-crystal synchrotron X-ray diffraction at 14A. The collection of virtually extinction-free diffraction data is indispensable for these sorts of studies. The accurate electron density in crystals determined by this technique will serve as an assessment for various approximations used in the theoretical approach.

References

[1] T. Chattopadhyay, H. G. Schnering and H. A. Graf : Solid State Comm. 50, 865 (1984).

[2] M. Ueki, N. Ishizawa and F. Marumo: Abstracts of the second AsCA Meeting, Bangkok, Thailand, 1P14 (1995)

[3] S. Kuze, N. Ishizawa and M. Ueki: Abstracts of the XVIIIth IUCr congress, Glasgow, Scotland, 519 (1999).

[4] Y. Satow and Y. Iitaka: Rev. Sci. Instrum., 60, 2390 (1989).

[5] T. Chattopadhyay, Th. Bruckel and P. Burlet: Phys. Rev. B, 44, 7394 (1991).

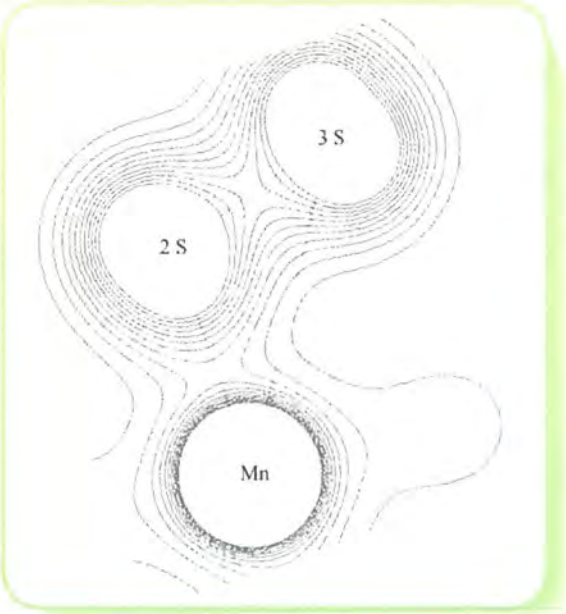

Figure 2.
Calculated charge density for the $Mn(S_2)_6$ cluster in the section including Mn and S-S bond.

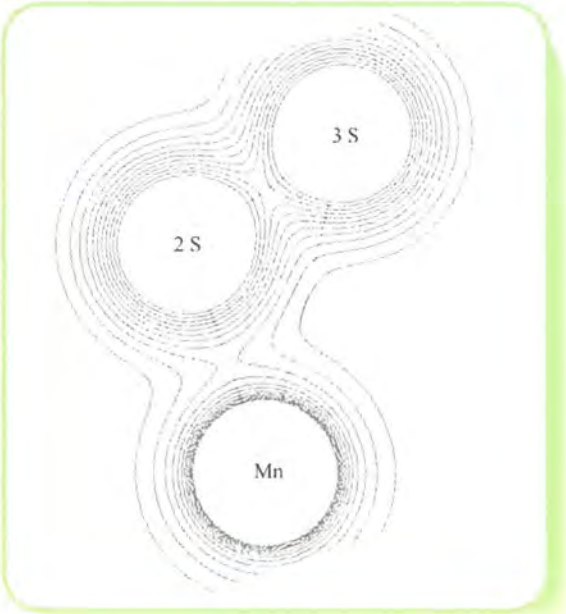

Figure 3.
Promolecule charge density for the $Mn(S_2)_6$ cluster in the section including Mn and S-S bond.

Figure 4.
Calculated deformation density for $Mn(S_2)_6$ cluster in the section including Mn and S-S bond. Positive and negative regions are indicated by solid and broken contours.

[6] T. Chattopadhyay, H. G. Schnering, R. F. D. Stansfield and G. J. McIntyre: Z. Kristallogr., 119, 13 (1992).
[7] International Tables for X-ray Crystallography, Vol. IV (1974) Kynoch Press, Birmingham, England.
[8] P. J. Becker and P. Coppens: Acta Cryst., A30, 129 (1974a)
[9] P. J. Becker and P. Coppens: Acta Cryst., A30, 148 (1974b)
[10] H. Adachi, M. Tsukada, and C. Satoko: J. Phys. Soc. Jpn., 45, 875 (1978)
[11] D. E. Ellis and G. S. Painter: Phys. Rev. B, 2, 2887 (1970)

5-4 Surface-melting of Si:In situ x-ray Reflectivity Study on Si(001) Surface up to the Melting Temperature [1]

The melting of metal and semiconductor surfaces has attracted much attention recently, because surface melting is one of the best examples of fundamental issues : the stability and evolution of a liquid/solid interface. Surfaces experience roughening and/or melting transitions upon heating at temperatures below the bulk melting temperature ($T_{m;b}$). Surface melting can generally be understood as a state in which a liquid film is formed and wets the solid/vapor interface.

Surface melting of Si has attracted special attention in a recent few years; it is not only interesting in terms of fundamental issues but is deeply related with the liquid/solid interface of Si, which is essential for contrcling the growth-process of a Si single crystal.

However, most work on the Si surfaces has focused on their behavior at low and intermediate temperatures, [2] and little information has been obtained near $T_{m;b}$. One of the reasons is experimental difficulties; $T_{m;b}$ =1683K is rather high.

An in situ system was newly designed for measurements of the x-ray reflectivity of Si surfaces at high temperatures. A surface of a block specimen was heated with a carbon heater under an atmosphere of He-gas flow. The reflectivity of the surface could be measured up to the bulk melting temperature ($T_{m;b}$).

In situ measurements of reflectivity were carried out at a beam line BL-3A [3] at Photon Factory, KEK, in Tsukuba, Japan. In this beam line, an x-ray beam from a bending magnet is monochromated by Si (111) double crystal. The size of beam is about 8^{W} x 0.8^{H} mm^2 at the position of a specimen. The energy of x-ray beam (E) is E = 6812 eV, which is 500 eV below Fe K_-edge; this was determined considering an accuracy measuring the reflection angle and eliminating possible noise caused by Fe-fluorescence from the chamber.

Reflectivity curves obtained at each temperature were analyzed; the obtained values of the density : ρ of Si(001) surface are plotted as a function of temperature in Fig 1. In Fig., the results of this study

("surface" density) are shown by larger symbols with the reported values of the "bulk" solid and liquid. [4] Errors in determination of _ and _, which mainly comes from the measurements of the angle and the fitting procedure, are also shown in Fig.

It has been shown that Si (001) surface experience the surface pseudo-melting in a range of 1473 K< $T_{m;s}$ < 1573 K. This temperature is about 20-50 K higher than the temperature rage where the atomic disordering was reported to occur; it has been reported that the order of Si (001) suddenly decreases at T > 1400 K by reflection electron microscopy (REM) [5] and X-ray photo electron diffraction (XPD), [6] , and crystallographic anisotropy in the plane becomes almost zero at T=1500 K, [5] As shown by the value of surface density, the coordination number around a Si atom of the surface-melting layer in a range of $T_{m;b}$ > T > $T_{m;s}$ is expected to be that of the bulk liquid. [7]

References

[1] M. Kimura, A. Ikari, T. Suzuki, Physia B , (1999) (submitted).

[2] V. G. Lifshits, A. A. Saranin, A. Z. Zotov, *Surface Phase on Silicon: Preparation, Strucutres, and Properties* (John Wiley & Sons, Chichester, 1994).

[3] S. Sasaki, T. Mori, M. Akira, H. Iwasaki, K. Kawasaki, Y. Takagi, K. Nose, Rev. Sci. Instrum 63, 1047-1050 (1992).

[4] Y. Tatsumi, H. Ohsaki, in Properties of SILICON T. H. Ning, Eds. (INSPEC, The Institution of Electrical Engineers, New York, 1987), vol. EMIS Datareviews Series No.4, pp. 1-6.

[5] J. J. Metois, D. E. Wolf, Surf. Sci. 298, 71-78 (1993).

[6] J. Fraxedas, S. Ferrer, F. Comin, Europhys. Lett. 25, 119-124 (1994).

[7] K. Omote, Y. Waseda, Jpn J Appl Phys Part 1 35, 151-155 (1996).

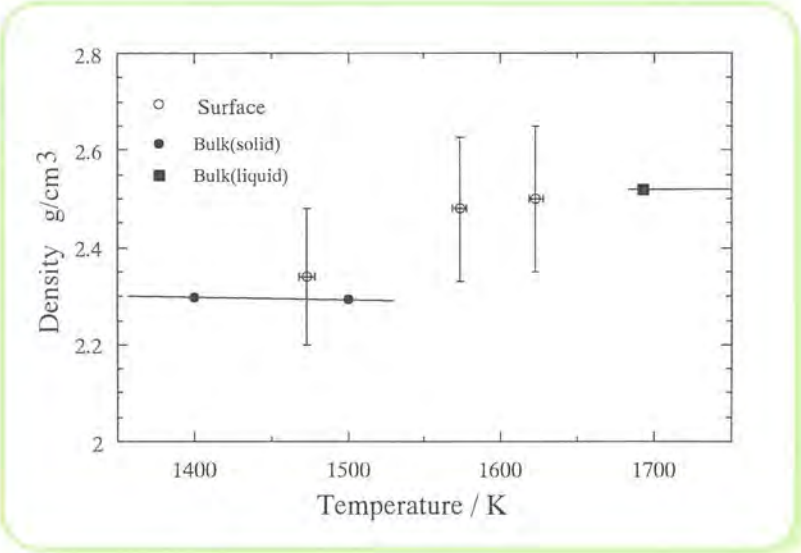

Figure 1.
Temperature dependence of density of Si (001) surface. Open symbols for this study (heated in the patterns of B and C), and closed ones for the bulk. The line is a guide for eye.

6

High Pressure Science

6 High-Pressure Science

Two different types of high-pressure apparatuses are working at Photon Factory. One is a diamond anvil cell (DAC) and the other is a multi-anvil device. At BL13B2, a system for high pressure and high temperature in situ X-ray diffraction has been constructed using DAC combined with a laser heating system. After several improvements, the system now consists of a 150 W YAG laser combined with an IP detector, and it covers the condition corresponding to the Earth's lower mantle (140 GPa and 3000 K). The behaviors of various silicates and oxides have been intensively studied using this system. Very unique behaviors is found in simple oxides, such as MnO[1] and CoO[2]. Both of them have a rock-salt (B1) structure at the ambient condition and transform into various high-pressure phases with increasing pressure. The nature of the high-pressure phases is discussed in conjunction with their electronic structures. Another interesting topic is the behavior of $LiNbO_3$. The existence of a high-pressure phase above about 35 GPa has been known, but its structure remains

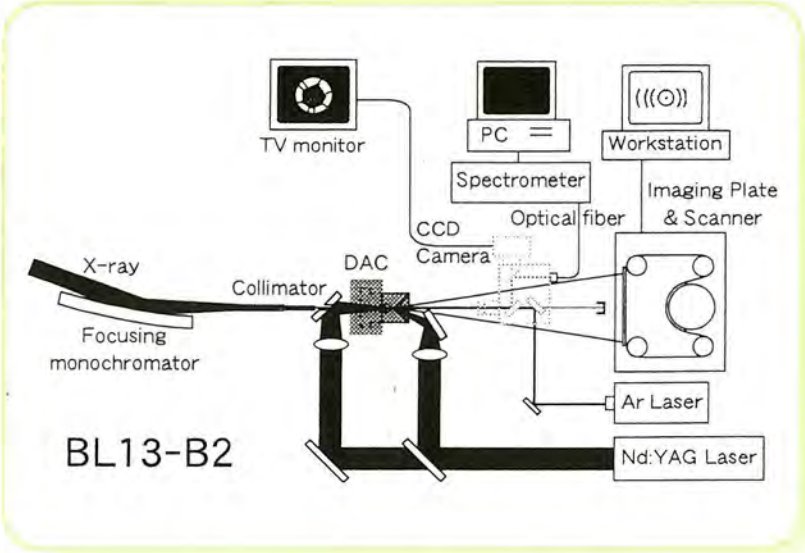

Figure 1.
Block diagram of the laser-heated DAC system for high pressure and temperature in situ X-ray diffraction measurement at BL13-B2.

unsolved. High-quality diffraction data obtained by this system enable us to determine its-structure as a $NaIO_3$-type structure[3]. Furthermore, the existence of quenchable high-pressure and temperature phase was found upon heating the sample above 30 GPa. Detailed analysis of this structure is in progress now and it is likely that this is a new structure type formed only at elevated pressure. These results will greatly contribute to advance our understandings of high-pressure crystal chemistry. At BL-18C, high-pressure and room-temperature or low-temperature experiments are carried out on up to megabar pressures using DAC. The most exciting topic is a structure analysis of various elements, such as oxygen and niobiu above megabar.

The multi-anvil apparatus has the advantage to achieve well-controlled and uniform pressure and temperature conditions, although the pressure range is limited compared to that of DAC. Using this advantage, the detailed behavior of materials is studied using MAX80 (at AR-NE5C) and MAX90 (at BL-14C) systems. Breakdown reactions are studied in detail for garnets of various compositions up

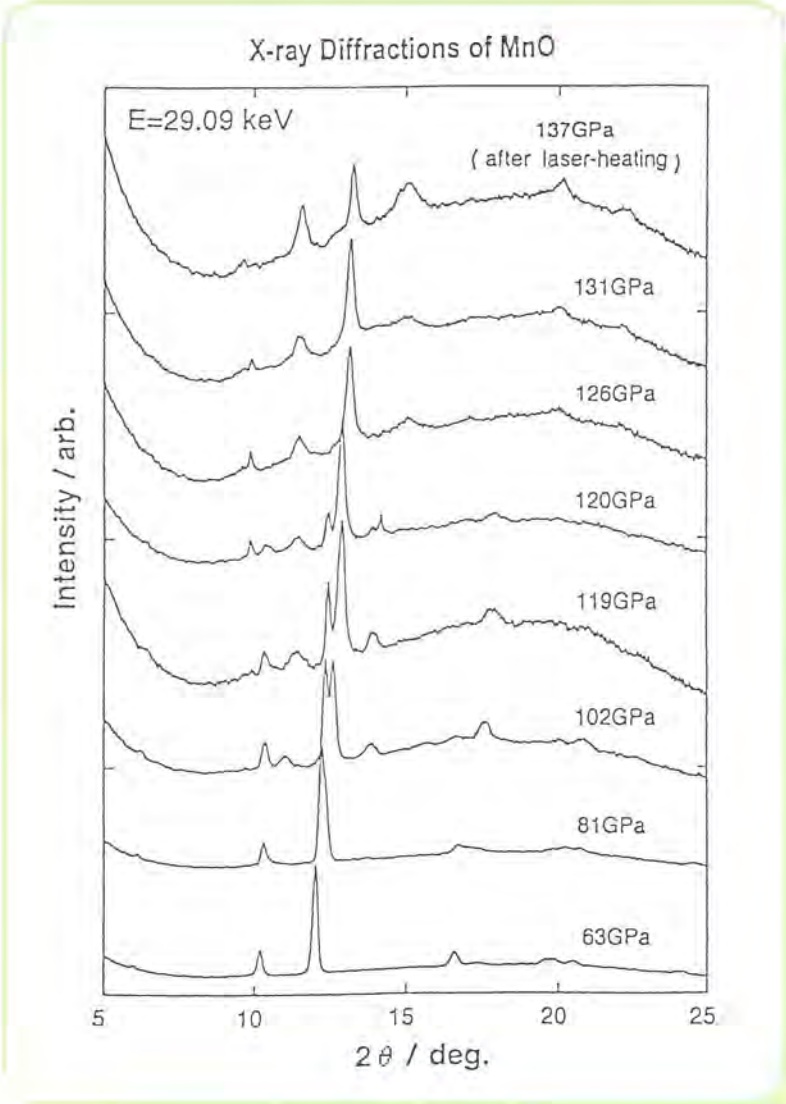

Figure 2.
Powder X-ray diffraction profiles of MnO. The structure changes from B1 structure - distorted B1 structure - unknown phase - NiAs-type structure, with increasing pressure[1].

to about 30 GPa. Many other crystal chemical studies have been carried out using these systems.

References

[1] T. Yagi, T. Kondo, and Y. Syono, AIP Conference Proceedings 429, (1998) 159; T. Kondo et al., J. Appl. Phys. in press.
[2] Y. Noguchi et al., Jpn. J. Appl. Phys. 38 (1999) L7.
[3] T. Mukaide et al., Phys. Rev. B, submitted.

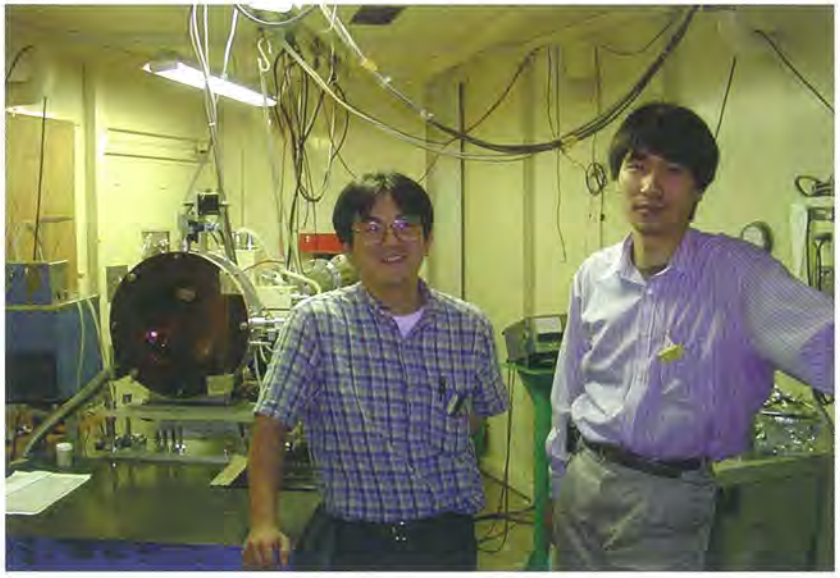

7

Biological Science

7 Biological Science

Synchrotron radiation is widely utilized in the field of biological science. Typical applications are shown in X-ray crystallography, X-ray small-angle diffraction and scattering and X-ray spectroscopy. Another important field is radiation biology. As is previous years, substantial progresses in these fields have been observed, some of which will be introduced here. One significant aspect of the last 2 years is the fact that SPring-8 has been open to public and is producing remarkable results. The beam properties of the Photon Factory are different from those of SPring-8. Investigators are required to understand the difference and to utilize them them properly.

In the field of X-ray crystallography, many new structures of biological macromolecules have been solved to the atomic resolution. With the rapid development of the genom project, many putative proteins with unknown function and structure have been discovered. It should be a necessary consequence to solve these structures, as well as to do functional analyses. The DNA recombinant technique makes the expression of a large amount of such a protein possible. We expect that the necessity of X-ray crystal structure analysis of proteins (and other biological macromolecules) wiee still be increasing from now.

In the field of small-angle diffraction and scattering, the mechanisms of biological function and structure formation are the main targets, rather than studies of the structure itself, Crystallography gives us precise structural information of a protein, but not the molecular mechanism of its function or the folding mechanism. Small-angle diffraction and scattering is useful to study the structure of a transient state, which gives us deep insight into function and structure formation, when the crystal structure is available. As an example, a small-angle diffraction study of muscle fiber is introduced here.

The highlights presented here do not intend to cover all of the

major results obtained in the Photon Factory in the last couple of years. Readers should refer to volume B of this series to take a look for the activities of the Photon Factory in the field of biological science.

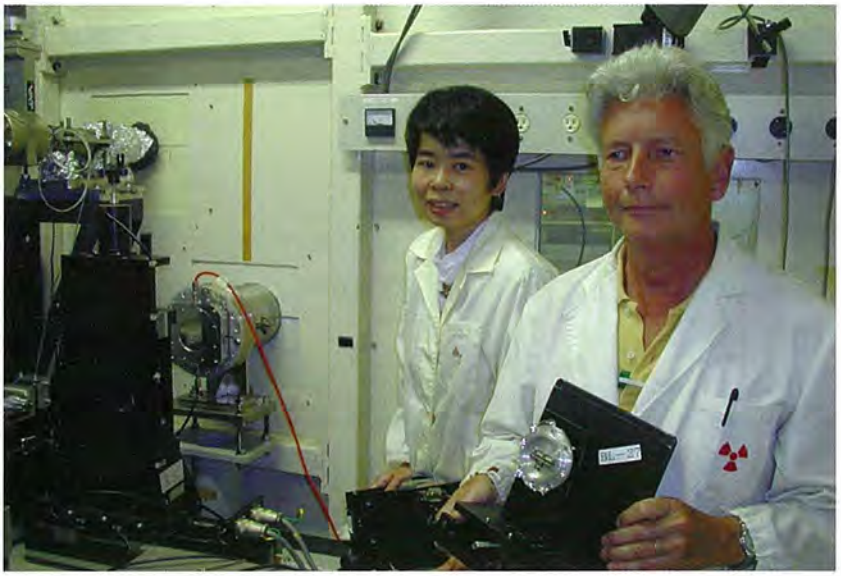

7-1 X-ray Spectroscopy Raises a Question about the Life History of Fresh-water Eels [1]

It is widely accepted that fresh-water eels migrate from fresh-water streams to the sea to spawn, which is called catadromous migration. However, the detailed life history of the fresh-water eel remains unknown. The proportion of time spent in fresh-water and ocean habitats can be determined by the ratio of strontium (Sr) and calcium (Ca) in the otoliths (ear stones) of the eels. Tsukamoto et al. used synchrotron X-ray fluorescence analysis to examine the Sr/Ca

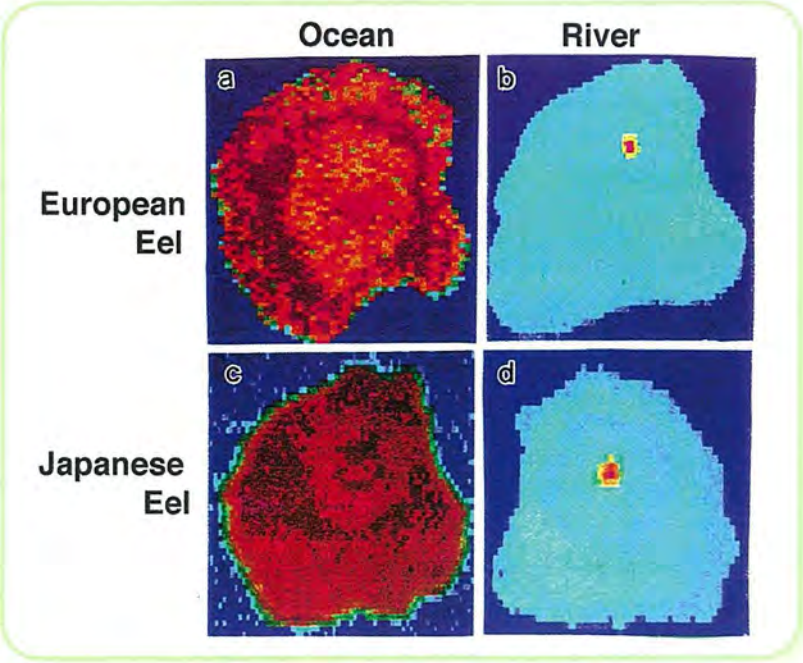

Figure 1.
Two-dimensional images of the otoliths of European eels *Anguilla anguilla* and Japanese eels A.*japonica*. a: European eel from North Sea, b; European eel from River Elbe, c: Japanese eel from East China Sea, d: Japanese eel from River Tone.

ratios in individual eel otoliths. Eels were collected from both fresh-water (from the River Elbe and the River Tone) and ocean habitats (from the North Sea and the East China Sea) for both Atlantic and Pacific species. Two-dimensional images showed a remarkable difference in Sr/Ca between ocean and river samples (Fig. 1). Red indicates high Sr/Ca intensity. Apparently, ocean eel has the high Sr/Ca ratio, while fresh-water eel shows little Sr. They reconstructed a life-history transect of individual ontogeny (Fig. 2). All river smaples contained a small region of high Sr ratio in the center of their otoliths. This indicates the migration from the sea in the stage of leptocephalus to a fresh-water habitat where they grew. On the other hand, all specimens collected in an ocean habitat had no evidence of fresh-water history regardless of the species, sex or developmental stage. Based on the results, they suggested that catadromous migration is not an obligatory migratory pathway of eels, and that eels would have a facultative catadromy with ocean residents. They also considered that a relatively small number of fresh water eels are back to the ocean and the spawning grounds.

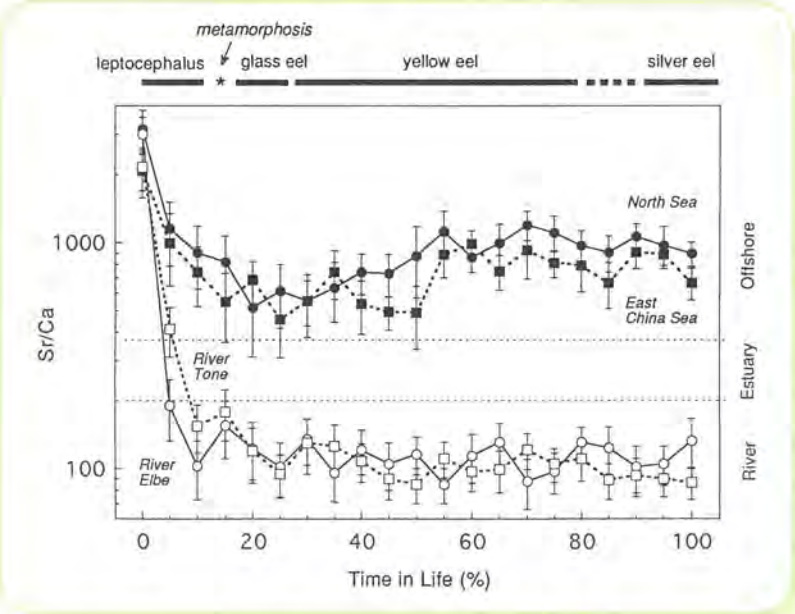

Figure 2.
Pattern of Sr/Ca ratio across the life of silver eels for both Atlantic and Pacific species. Atlantic species captured in North Sea(●) and in River Elbe(○), and Pacific species, in East China Sea(■) and in River Tone(□). Otolith's longest radius representing all life history transect of an individual was expressed as time in life(%).

7-2 X-ray Diffraction Casts Light on the Mechanism of Muscle Contraction

Muscle contraction takes place by relative sliding between the thin (actin) and thick (myosin) filaments without changing their lengths in the structural unit called a sarcomere. The widely accepted model is the "rotating or tilting crossbridge (myosin head)" model. In this model, the thick filament changes its structure while the thin filament remains unchanged. The thin filament has been thought to have the role of a rigid rail for thick filament sliding. X-ray diffraction patterns recorded

from a contracting muscle taken by Wakabayashi et al. indicated, however, that the structure of the thin filaments is altered by an asynchronous interaction of the myosin heads with actin, and that this structural change involves elastic elongation and twisting of the helical filaments [2]. This finding leads to the conclusion that thin filaments are flexible and very compliant. Further, Wakabayashi et al. revealed a conformational change of the myosin head upon ATP hydrolysis by X-ray solution scattering [3,4], also indicating a coupling between the force generation and structural changes occurred in the myosin heads. Based on these results, they proposed a sophisticated model in a combination of specific structural changes of actin and myosin heads, as described in Fig. 3 [5], instead of the current mechanism of the rotating or tilting of the crossbridge as the main constituents. In active muscle, the myosin heads first bind ATP, hydrolyzes it and a deformed myosin head having ADP and Pi interacts weakly with actin. In this process the structure of the actin filaments is altered. As the force develops, the actin filaments could be elongated, possibly by reverse conformational changes of the attached myosin heads upon the release of Pi and then ADP. It seems possible that a cranking action in a myosin head could be combined with the lever action, applying a torque to explain the unscrewing motion of the actin filaments as observed.

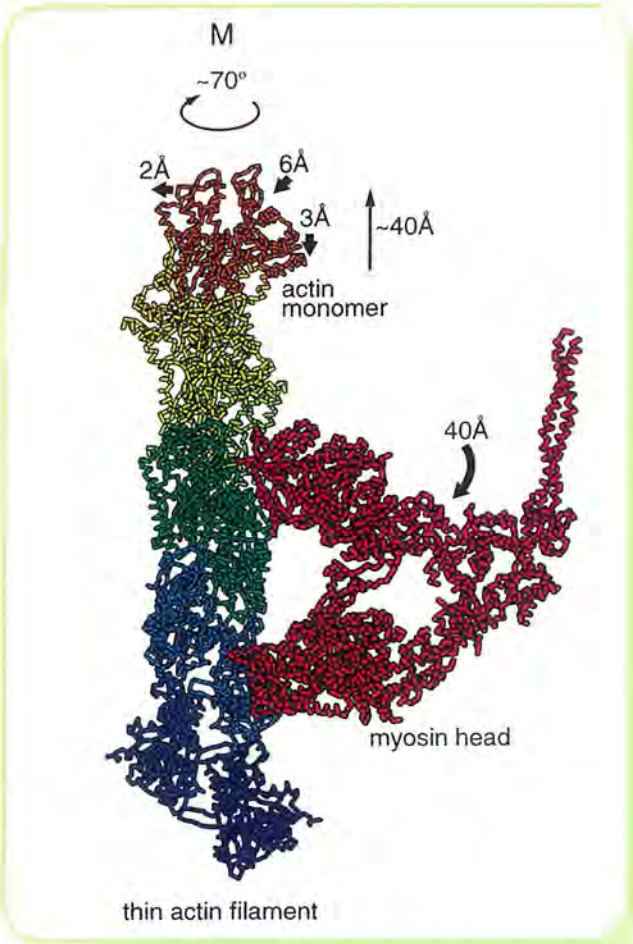

Figure 3.
Molecular interaction of the actin and myosin heads to generate a contractile force in muscle using their atomic structures.

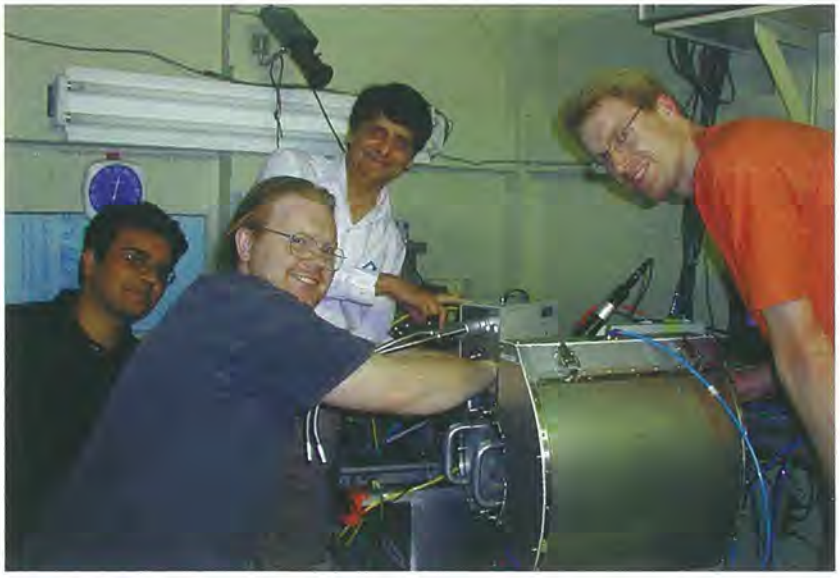

7-3 New Crystal Structures Determined by X-ray Crystallography give Deep Insights into the Molecular Mechanisms of Biologically Important Reactions.

a. Crystal Tructure of Mitrile Hydratase [6]

The 1998 Nobel Prize in physiology and medicine was awarded for discoveries concerning nitric oxide (NO) as a signalling molecule in the cardiovascular system. The mechanism of regulation by NO is, thus, a hot topic in life science. The crystal structure of nitrile hydratase (Nhase) revealed by Nagashima *et al.* would provide new insights into a mechanism utilizing NO molecules in biological systems. NHase is a soluble enzyme catalyzing the hydration of various nitrile compounds to their corresponding amides ($RCN + H_2O \rightarrow RCONH_2$). The enzyme consists of two subunits (the α- and the β-subunits). The active center of the enzyme is composed of non-heme iron (Fe-type) or non-corrinoid cobalt atom (Co-type) chelating to the a-subunit. Some Fe-type NHases show an extraordinary characteristic in that the activities of the enzyme regulated by light. The light-regulated binding and releasing of an endogenous nitric oxide (NO) molecule in the active center is the cause for the photo-reactivation. The crystal structure of the Fe-type NHase from Rhodococcus sp. N-771 revealed an unprecedented coordination sphere of non-heme iron atom at the active center (Fig. 4). The photo-reactive catalytic center consists of the non-heme iron atom coordinated to the sulfur atoms from three cysteine residues (Cys109A, Cys112A and Cys114A) and two amide nitrogen atoms from the main chains of Ser113A and Cys114A. In particular, two of the three cystein residues are post-translationally modified into cysteine sulfinic ($CysSO_2$-112A) and cysteine sulfenic (CysSO-114A) acids. The two oxygen atoms of the side chains in the modified cysteine residues form a claw setting structure with the OG atom from

Ser113A. The modifications were further verified by using Fourier-transform mass spectrometry. In addition, 20 hydration water molecules confined in the interface between the subunits have important roles to stabilize the claw setting structure. The present structure may provide an excellent model for designing photo-controllable chelate complexes and proteins.

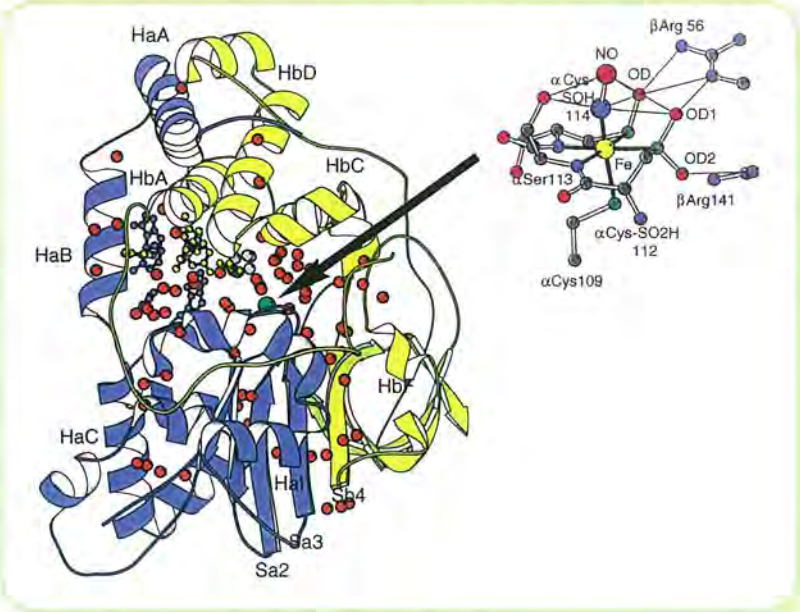

Figure 4.
Ribbon model of nitrile hydratase and the detailed structure of the photo-reactive catalytic center.

b. Three-dimensional Tructure of Phosphoenolpyruvate Carboxylase: A Proposed Novel Mechanism for Allosteric Inhibition [7]

Phosphoenolpyruvate carboxylase (PEPC) catalyzes the irreversible carboxylation of phosphoenolpyruvate to form oxaloacetate and inorganic phosphate using Mg^{2+} as a cofactor. The enzyme is widespread in all plants and some species of bacteria playing a central role in CO_2 fixation in photosynthesis. PEPCs from various sources are usually composed of four identical subunits whose molecular masses are 95 to 110 kD. Kai *et al.* reported the first crystal structure of PEPC by X-ray diffraction methods at 2.8 Å resolution using *Escherichia coli* PEPC complexed with L-aspartate, an allosteric inhibitor of all known PEPCs (Fig. 5). The four subunits are arranged in a "dimer-of-dimers" form with respect to subunit contact, resulting in an overall square arrangement. The contents of α- helices and β-strands are 65% and 5%, respectively. All of the eight β-strands, which are widely dispersed in the primary structure, participate in the formation of a single β-barrel. Replacement of a conserved Arg residue (Arg438) in this linkage with Cys increased the tendency of the enzyme to dissociate into dimers. The location of the catalytic site is suggested to be near the C-terminal side of the β-barrel. The binding site for L-aspartate is located about 20 Å away from the catalytic site and four residues (Lys773, Arg832, Arg587 and Asn881)

are involved in effector binding. The participation of Arg587 is unexpected because it is known to be catalytically essential. Considering that this residue is in a highly conserved glycine-rich loop, which is characteristic of PEPC, it seems that L-aspartate causes inhibition by removing this glycine-rich loop from the catalytic site. There is another mobile loop from Lys702 to Gly708 that is missing in the crystal structure. The importance of this loop in catalytic activity was also demonstrated. Thus, a crystal-structure determination of PEPC revealed two mobile loops bearing the enzymatic functions and accompanying allosteric inhibition by L-aspartate.

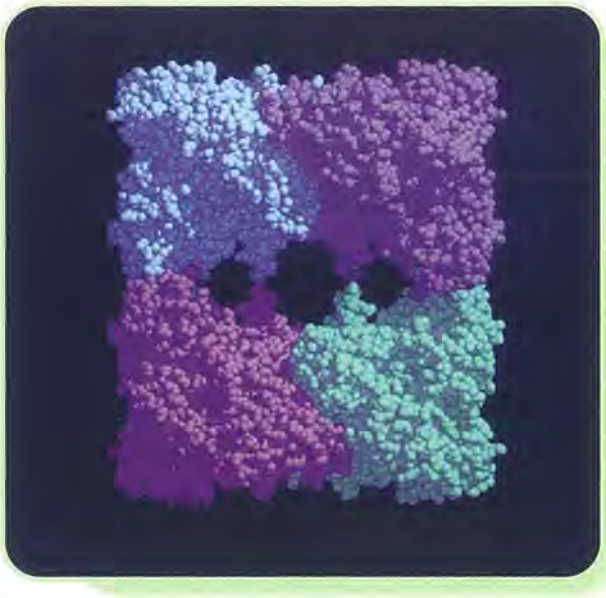

Figure 5.
Overall views of phosphoenolpyruvate carboxylase from *E. coli*, in which the four identical subunits are related by the crystallographic 222 symmetrey.

c. Crystal Tructure of DNA Photolyase from *Anacystis nidulans* [8]

Photolyases (photoreactivating enzymes) repair a major type of UV-induced lesion, that is, a cyclobutane type dimer formed from adjacent pyrimidine bases. Photoreactivation comprises several steps: damage recognition and binding of photolyase to DNA, photon absorption, interchromophoric energy transfer and electron transfer from chromophore to DNA, resulting in the reversal of UV-induced pyrimidine dimers into monomers. Miki and coworkers reported on the crystal structure of photolyase from a cyanobacterium, *Anacystis nidulans* at 1.8 Å resolution, and compared it with that of *E. coli* photolyase.

The structure is composed of an α/β and a helical domain, which provides binding sites for the 8-HDF (light-harvesting cofactor) and FAD (catalytic cofactor) chromophores, respectively (Fig. 6). The backbone structure of *A. nidulans* photolyase (A-PLase) could be superimposed with that of *E. coli* photolyase (E-PLase) for both α/β and helical domains, showing a high similarity in overall folding. The cofactor FAD is a common chromophore for both types of photolyases. In A-PLase FAD is located between four-helix bundles and accessible

through a hole in the surface of the helical domain. This hole is also of the right size to admit a pyrimidine dimer. FAD is bound in the same position and binding-mode as in E-PLase. In contrast to the conserved position of FAD it should be emphasized that 8-HDF is bound at a quite different position compared to the corresponding MTHF cofactor in E-PLase. Nevertheless, the overall tertiary structure of the α/β domain is quite similar for both photolyases, even in the region which recognizes the two light-harvesting cofactors.

Elucidation of the crystal structure of A-PLase showed a high degree of conservation for the three-dimensional structure of 8-HDF and MTHF photolyases. In addition, this is a first example that homologous primary and tertiary structures in closely related proteins recognize two different types of cofactors at different binding sites by a limited number of amino acid replacements.

Figure 6.
Ribbon model overall structure of A. *nidulans* photolyase.

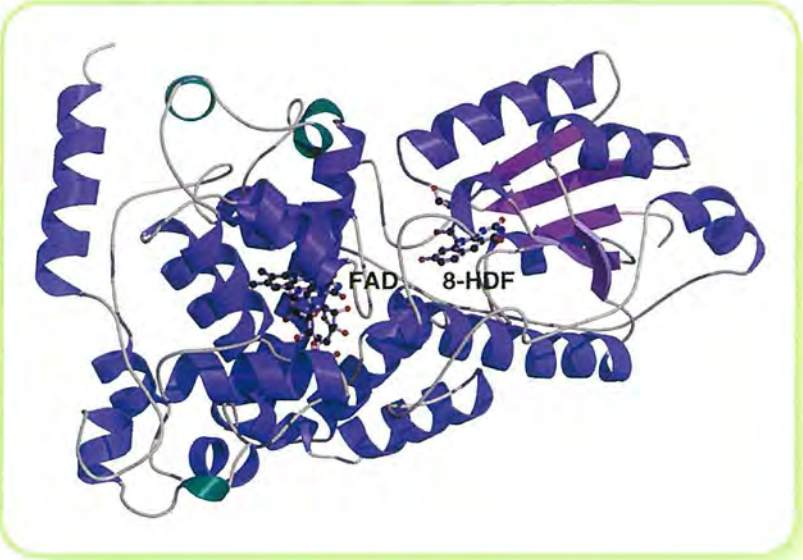

d. The Three-Dimensional Tructure of the RNA-binding Domain of Ribosomal Protein L2; a Protein at the Peptidyl Transferase Center of the Ribosome [9]

In all living cells, protein synthesis is carried out in cellular organelles called ribosomes. These large ribonucleoprotein complexes are generally organized in two subunits of unequal size. Each subunit of the ribosome is responsible for each of two important activities, as which have been localized by immunoelectron microscopy. While the decoding property resides in the small subunit, the peptidyl transferase activity is in the large subunit. A number of experiments have been carried out to elucidate the responsive elements for the ribosome activities, and particularly for the peptidyl transferase activity. Such experiments have shown that some ribosomal proteins are implicated in peptidyl transferase activity. Among them, the protein L2 is known to be most important constituent of the peptidyl transferase center.

Ribosomal protein L2 is the largest protein component in the ribosome. It is located at or near the peptidyl transferase center and has been a prime candidate for the peptidyl transferase activity. It binds directly to 23S rRNA and plays a crucial role in its assembly. Tanaka and coworkers reported the crystal structure of the RNA-binding domain of L2 from Bacillus stearothermophilus at 2.3 Å by means of the Se-Met MAD method (Fig. 7). The RNA-binding domain of L2 consists of two recurring motifs of about 70 residues each. The N-terminal half domain (pos. 60 ~ 130) is homologous to the OB-fold and the C-terminal half (pos. 131 ~ 201) is homologous to the SH3-like barrel. The residues Arg86 and Arg155, which have been identified by mutation experiments to be involved in the 23S rRNA binding, are located at the gate of the interface region between the

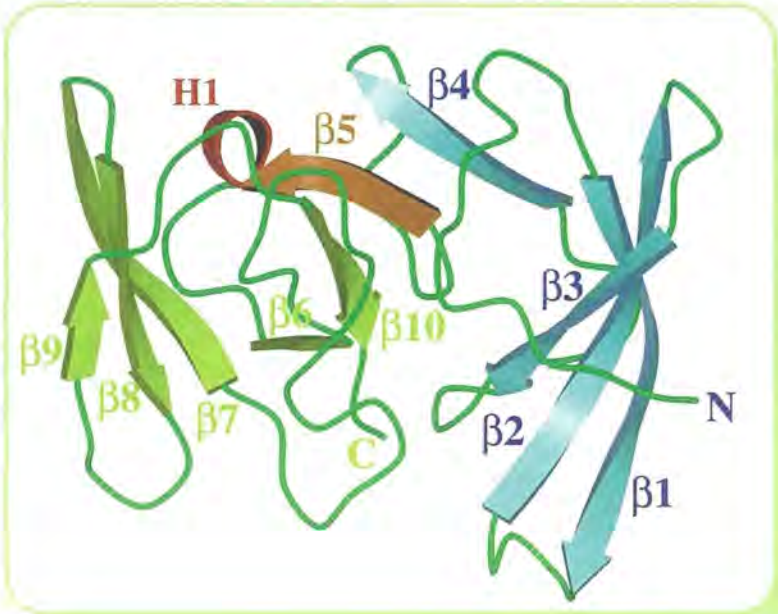

Figure 7.
Ribbon model of the RNA-binding domain of L2 from *Bacillus stearothermophilus*.

two domains. The molecular architecture suggests how this important protein has evolved from the ancient nucleic acid binding proteins to create a 23S rRNA-binding domain in the very remote past.

References

[1] K. Tsukamoto, I. Nakai & W.-V. Tesch, Nature 396, 635 (1998)

[2] Wakabayashi, K. Sugimoto, Y. Tanaka, H. Ueno, Y. Takezawa, Y. and Amemiya, Y. Biophys. J., 67, 2422-2435 (1994).

[3] Wakabayashi, K. Tokunaga, M. Kohno, I. Sugimoto, Y. Takezawa, Y. Wakabayashi, T. and Amemiya, Y. Science, 258, 443-447 (1992).

[4] Sugimoto, Y. Tokunaga, M. Takezawa, Y. Ikebe, M. and Wakabayashi, K. Biophys. J. 68, 29-34 (1995).

[5] Wakabayashi, K. and Yagi, N. J. Synchrotron Rad., 6 (1999). In press.

[6] S. Nagashima, M. Nakasako, N. Dohame, M. Stujimura, K. Takio, M. Odaka, M. Yohda, N. Kamiya and I. Endo, Nature Structural Biology 5, 347- 351. (1998)

[7] Y. Kai, H. Matsumura, T. Inoue, K. Terada, Y. Nagara, T. Yoshinaga, A. Kihara, K. Tsumura and K. Izui, Proc. Natl. Acad. Sci. USA 96, 823-828 (1999)

[8] T. Tamada, K. Kitadokoro, Y. Higuchi, K. Inaka, A. Yasui, P. E. de Ruiter, A. P. M. Eker and K. Miki, Nature Struct. Biol. 4, 887-891 (1997)

[9] A. Nakagawa, T. Nakashima, M. Taniguchi, H. Hosaka, M. Kimura and I. Tanaka, EMBO J. 18, 1459-1467, (1999)

Medical Applications

8 Medical Applications

Phase-contrast X-ray imaging has also been studied while aiming at medical applications. Using an X-ray interferometer, imaging of nonstained soft tissues can be performed with a sensitivity of about one thousand-times higher than that of the conventional absorption-contrast imaging. Phase-contrast X-ray computed tomography, which reconstructs three-dimensional images using X-ray phase information obtained with the X-ray interferometer, was carried out to observe human cancerous tissues. Figure 1 shows a phase-contrast X-ray CT image of a sample cut out from a human cancerous kidney [1]. It was demonstrated that cancer could be depicted without the need for staining. From an instrumental point of view, a separated-type X-ray interferometer has been developed to observe larger objects *in vivo*. Currently, 2.5 cm x 1.5 cm interference patterns can be generated with this device. If the observation area is broadened up to 10 cm x 10 cm, phase-contrast mammography might be carried out.

Figure 1.
Phase-contrast X-ray CT image of a sample of human kidney (cortex). The dark part in the right half of the image is a cancer lesion.

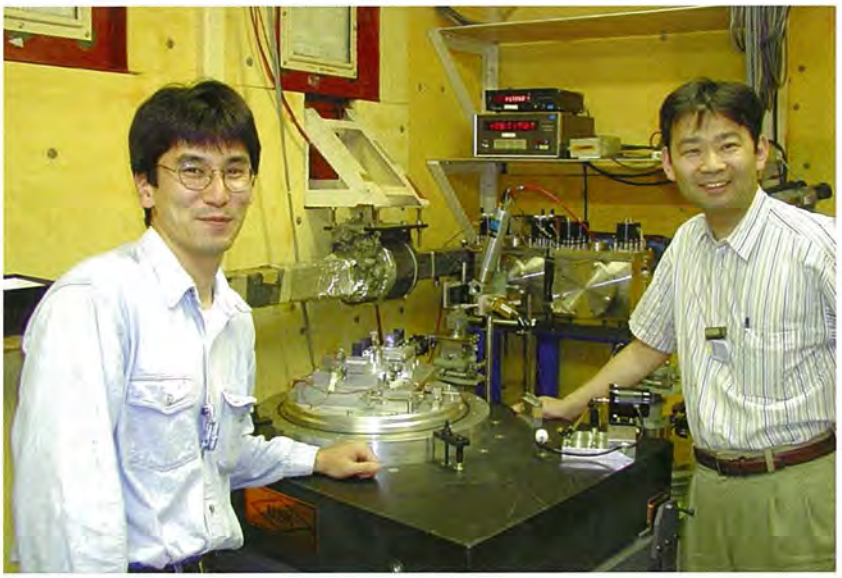

Table 1: Correlation of breast cancer with hair structure.

Breast cancer diagnosed ?	Samples	Samples with changed structure	Familial history of cancer (pathologic *BRCA1* mutation)	Hair origin
Yes	15	15	Yes (positive)	Scalp
Yes	8	8	None	Pubic
No	3	3	Yes (positive)	Scalp
No	2	Partial 2	Yes (positive)	Scalp
No	8	1	Yes (negative)	Scalp
No	16	3	None	Scalp
No	4	0	None	Pubic

References

[1] A. Momose, T. Takeda, Y. Itai, J. Tu, and K. Hirano, *SPIE Proc.* 3659 (1999) in press.

Applied Science

9 Applied Science

There have been excellent results on the materials science of low-resistive $TiSi_2$ contact and gate SiO_2 oxide for Si-ULSI with BL-17 Fujitsu beam-lines. The techniques are Grazing Incidence X-ray Diffraction (GIXD) for contact metals and X-ray Reflectivity [1] and Crystal Truncation Rod analysis for oxide films [2]. We introduce $TiSi_2$ in this short review.

Low-resistive silicide contact $TiSi_2$ is fabricated with two-step annealing; the formation of the high-resistive C49 phase at low temperature and a phase transition from the C49 to the low-resistive C54 phase at high temperature. However, the resistivity tends to rise for severe conditions, such as increase in ion implantation into a Si substrate or a decrease in the line width and/or film thickness.

The influence of BF_2^+ implantation on silicidation is summarized in the figure[3]. After the 1st annealing, only the C49-$TiSi_2$ is formed on both low- and high-dosed Si, but the rocking curve shows that the epitaxial grains preferentially oriented to Si are formed on high-dosed Si. After the 2nd annealing, all C49 grains are transformed to C54 on low-dosed Si, but not on high-dosed Si. Furthermore, the rocking curve of residual C49 is the same. An epitaxial relationship between C49 and Si was finely determined from other rocking curves[4]. Then, the cause of the high resistivity could be explained as follows; epitaxial C49 grains grow from the interface during Ti/Si inter diffusion and segregation of silicides; these thermally stable epitaxial C49 grains remain after the 2nd annealing, and the contact resistivity becomes high.

Pre-amorphizing As-implantation for formation of amorphous surface layer of Si was effective to suppress the epitaxial growth during silicidation. Then, the epitaxial grains decrease along with an increase in the amorphous layer after the 1st annealing, and the phase transition to C54 is finished after the 2nd annealing and a low-resistive contact is formed [5].

References

[1] N.Awaji, S.Ohkubo, T.Nakanishi, Y.Sugita, K.Takasaki and S.Komiya: J. J. Appl. Phys. 35 (1996) L67.

[2] N.Awaji, Y.Sugita, Y.Horii and I.Takahashi: Appl. Phys. Lett. 74 (1999) 2669.

[3] H.Tomita, S.Komiya, Y.Horii and T.Nakamura: J. J. Appl. Phys. 34 (1995) L876.

[4] S.Komiya, H.Tomita, K.Ikeda, Y.Horii and T.Nakamura: J. J. Appl. Phys. 35 (1996) 242.

[5] K.Ikeda, H.Tomita, S.Komiya and T.Nakamura: thin solid films 330 (1998) 206.

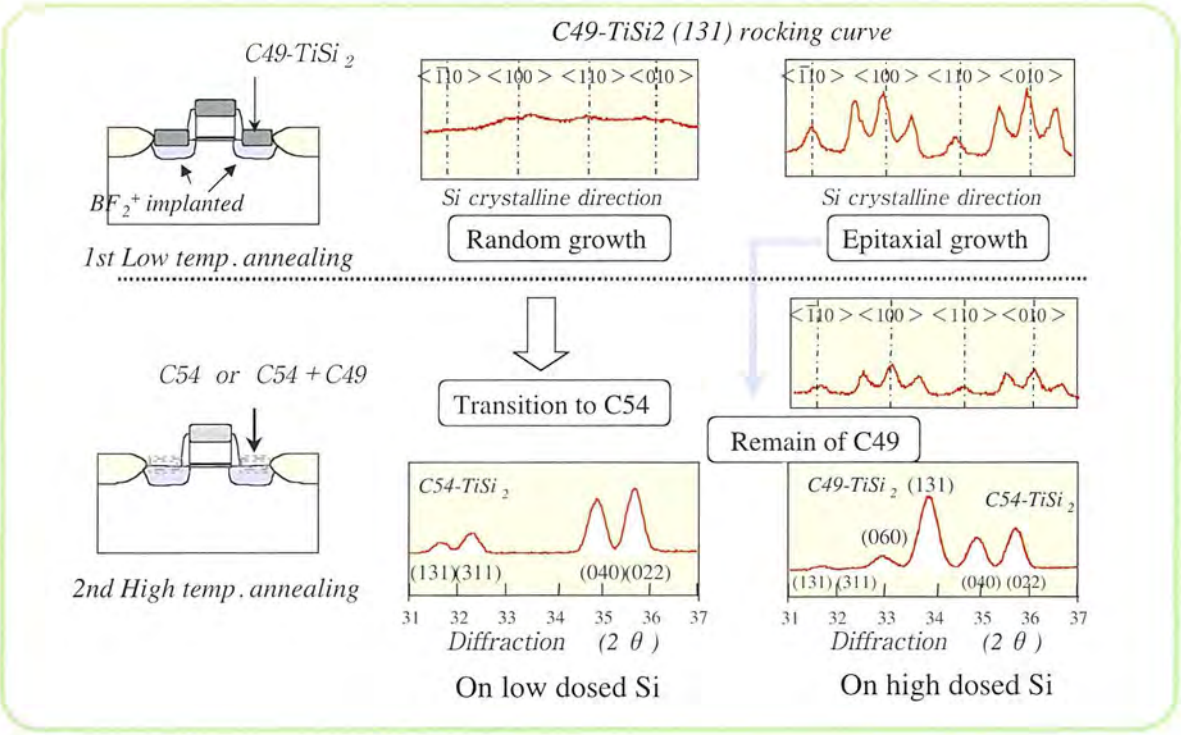

Figure 1.

Mechanism of resistivity rise by high-dose ion implantation Epitaxial C49 grains grow on high-dosed Si after the 1st annealing and their grains remain after the 2nd annealing, and then the resistivity rises.

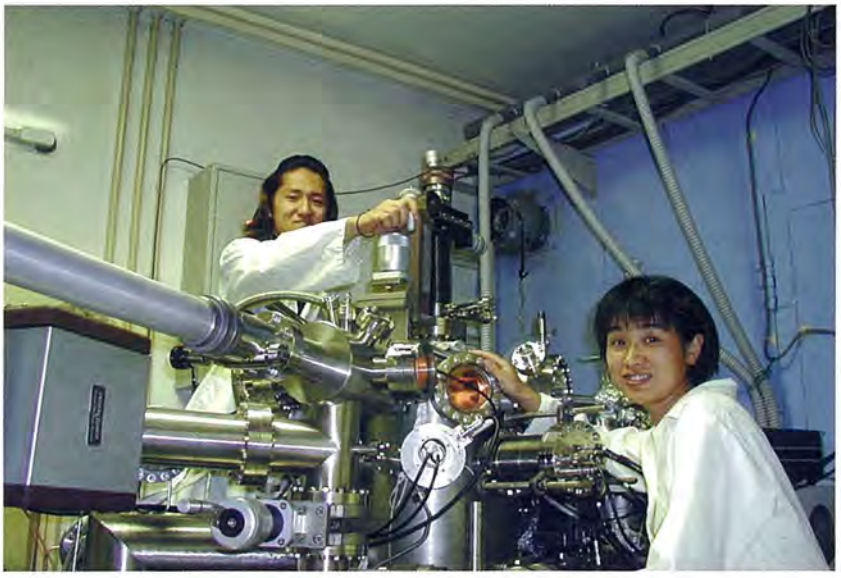

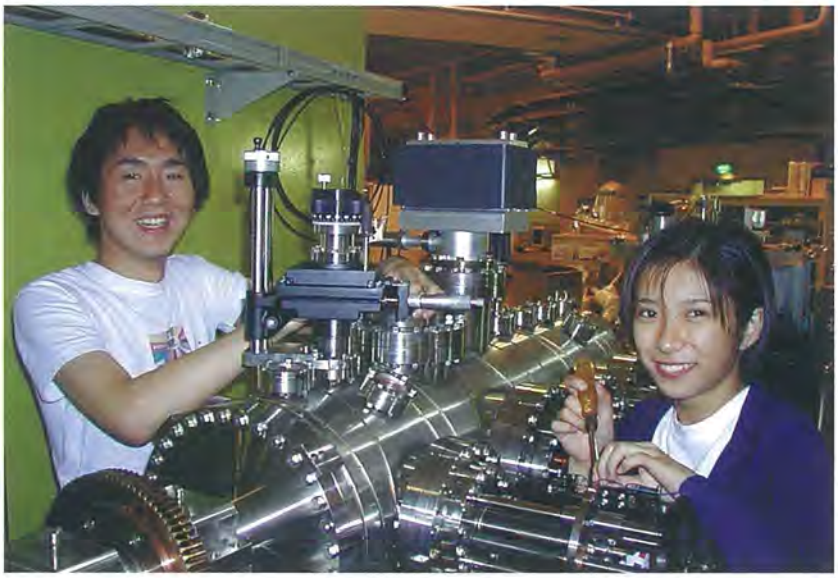

10

Instrumentation and Technique

10 Instrumentation and Technique

10-1 Automated Angle-Scanned Photoemission Spectrometer with MBE at BL-1C

Bending magnet beamline BL-1C is operated by the S1 project (97S1-002) for "Quantum nanostructure spectroscopy" represented by Prof. Oshima's group of the University of Tokyo. The main subject of the project is an electronic structure of quantum nanostructure, such as quantum dots (0D), quantum wires (1D), quantum wells (2D) and other low-dimensional materials. For studying the electronic structure of quantum nanostructures, photoemission with high energy and momentum resolution is indispensable. It is also noted that the state-of-the-art photoemission techniques, such as Fermi surface mapping, requires on automated angle scanning system.

For this purpose, a high-energy and-angular resolution angle-resolved photoemission spectrometer, VG Microtech ARUPS10, was installed at the end station. This spectrometer has an entrance lens, which allows the entrance angle of the emitted photoelectrons to be electronically varied from $\pm 0.4^\circ$ to $\pm 2.0^\circ$ and makes high-momentum resolution possible. The photoelectron analyzer is a 75mm radius hemispherical analyzer and photoelectron detection is done using a multi-channel detector. Up to now, a total resolution of 31meV at 60eV of photon energy has been achieved. For the automated angle-scanned photoemission, the in-vacuum two-axis goniometer of the spectrometer can be moved by the computer controlled stepping motors. This system was developed in collaboration withs Dr. Aiura of the Electrotechnical Laboratory. This automated angle-scanning system opens the way to do the Fermi-surface mapping, x-ray photoelectron diffraction (XPD), and so on much more easily and faster.

Another distinctive feature of this spectrometer is that it is

connected to the molecular beam epitaxy (MBE) chamber in ulta high vacuum (UHV). MBE is one of the most powerful technique for fabricating quantum nanostructures. In this system, MBE-grown samples can be transferred to the photoemission chamber without breaking the UHV.

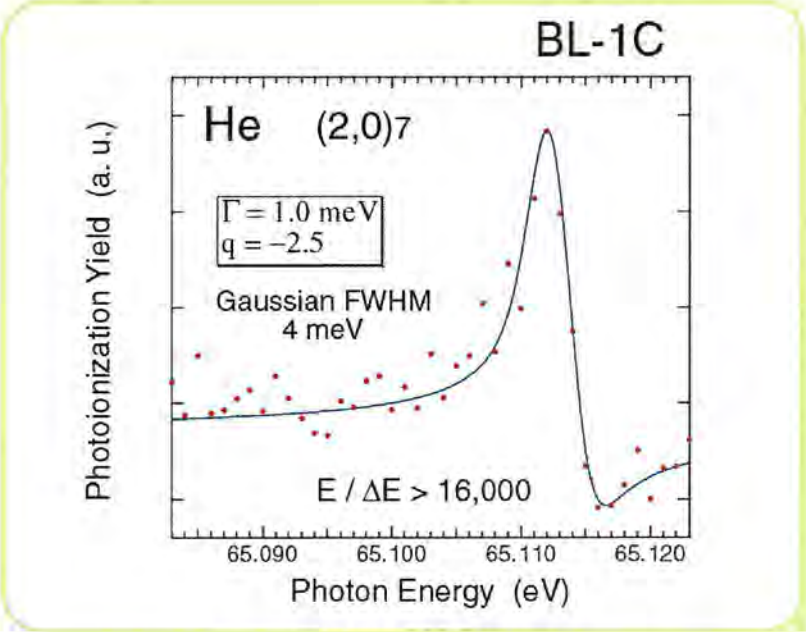

Figure 1.
Photoionization yield rpecdvum of doubly excited He.

10-2 X-ray Natural Circular/Linear Dichroism and Birefringence Measured with the X-ray Ellipsometer

We have developed an x-ray ellipsometer which consists of an x-ray polarizer, quadruple phase retarders and polarization. This x-ray ellipsometer enables us to create an x-ray beam having a high degree (about 98 %) of linear or circular polarization state in x-ray energy range (7-10 keV). It also enables us to analyze precisely the polarization states of the beam transmitted by the specimen.

With this x-ray ellipsometer, we successfully measured the spectra of both natural circular dichroism (NCD) and natural circular birefringence (NCB) simultaneously at Ni K-edge (8.333 keV) with a NiSO4-6H2O crystal (P41212) whose c-axis was aligned in parallel to the x-ray beam. The NCD spectrum was obtained from the spectrum of polarization ellipticity of the transmitted x-ray beam, whereas the NCB spectrum was obtained from the polarization rotation (6 mrad at maximum) spectrum (Figure). It was found that the Kramers-Kronig relations hold between the spectra of NCB and NCD.

The NCD spectra of the same crystal were also measured by switching the helicity of circular polarization of the incident beam with the x-ray polarizer and quadruple x-ray phase retarders. These NCD spectra agreed with the above NCD spectra obtained from a polarization analysis.

Linear dichroism (LD) and linear birefringence (LB) were measured simultaneously by polarizations analysis of the transmitted beam with the same crystal whose c-axis was aligned at 45 degree with respect to the polarization direction in the plane of the crystal foil. It was found that the Kramers-Kronig relations hold between the spectra of LD and LB. The LD spectra were also measured by switching the linear polarization of the incident x-ray beam between horizontal and vertical directions. These LD spectra were in good agreement with those measured by the polarization analysis of the transmitted beam.

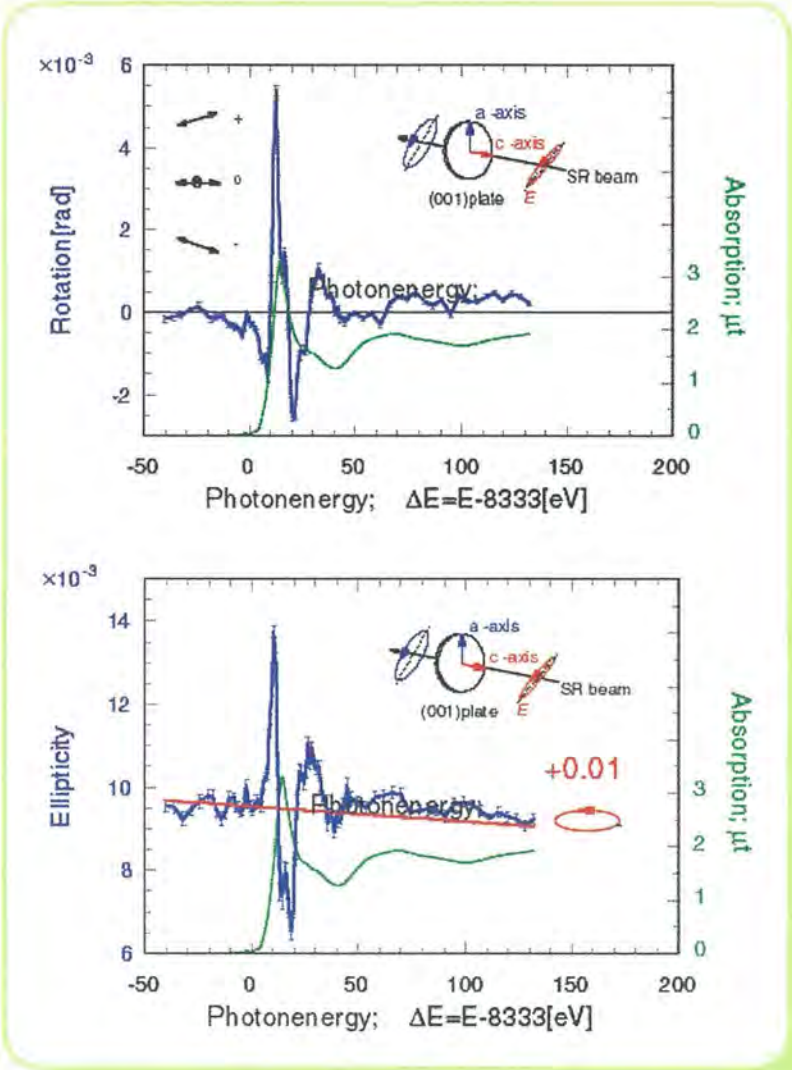

Figure 2.
Polarization analysis of x-ray beam transmitted by a $NiSO_4$-$6H_2O$ crystal ($P4_12_12$) whose c-axis is aligned in parallel to the x-ray beam.
(a) Spectrum of polarization rotation, which corresponds to the natural circular birefringence (NCB) spectrum.
(b) Spectrum of polarization ellipticity, which corresponds to the natural circular dichroism (NCD) spectrum.

10-3 Rotated-inclined Focusing Monochromator for Protein Crystallography

Many beamlines for protein crystallography use single, bent, asymmetric-cut silicon or germanium crystals to achieve a focused monochromatic beam. The demagnification rate of a beam passing through an asymmetric cut crystal monochromator depends on the angle between the beam and the crystal surface with the asymmetry

factor. If one uses this type of monochromator, the asymmetry factor or beam demagnification rate alters with the Bragg angle (θ_B) when the crystal is rotated to change the wavelength. Therefore, five or more monochromator crystals of different asymmetric angle, (α,) would be necessary to cover a wide wavelength range. A new single-crystal focusing monochromator for protein crystallography has been developed at BL-6B [1]. The monochromator allows tuning of the asymmetry factor, or beam demagnification rate, and the radius of curvature of the crystal simultaneously through rotation about the azimuthal angle only. In order to achieve simultaneous tuning of the two parameters over a wide wavelength range, the surface of an inclined monochromator was cylindrically bent. The monochromator is able to tune these two parameters simultaneously with a single rotation of the crystal about the azimuthal axis. The monochromator was designed for use in the wavelength range 0.87 to 1.90 Å, and beam focusing was tested at wavelengths of 1.04, 1.38 and 1.74 Å. A well compressed and focused beam was obtained at all three wavelength by rotation about the azimuthal axis only. An example of the two-dimensional intensity profile of the focused beam at several ϕ angles recorded using imaging plates is shown in Figare 3. The monochromator could focus the x-ray beam to less than 0.8 mm FWHM in the horizontal direction.

References

[1] N. Watanabe et al. J. Synchrodvon Rad.6(1998)64.

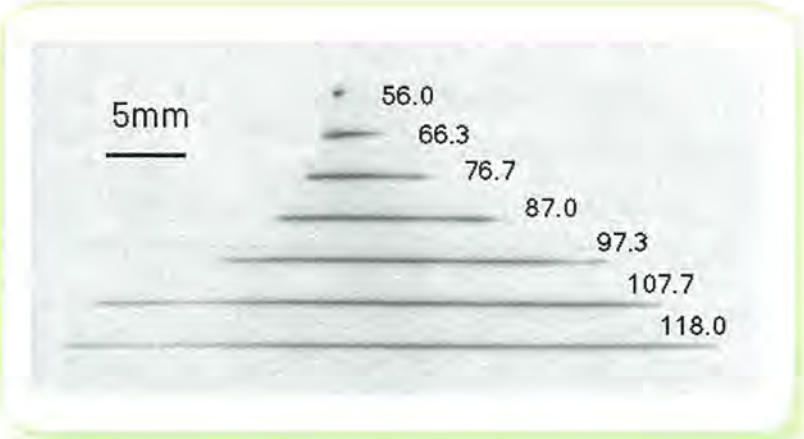

Figure 3.
Observed image of the focused beam at 1.38 Å. From lower to upper, ϕ axis was rotated from 118.0°, where the surface of the monochromator is nearly flat, to 56.0° in 10.3° steps.6 mm of aluminum plate was used as an attenuator.

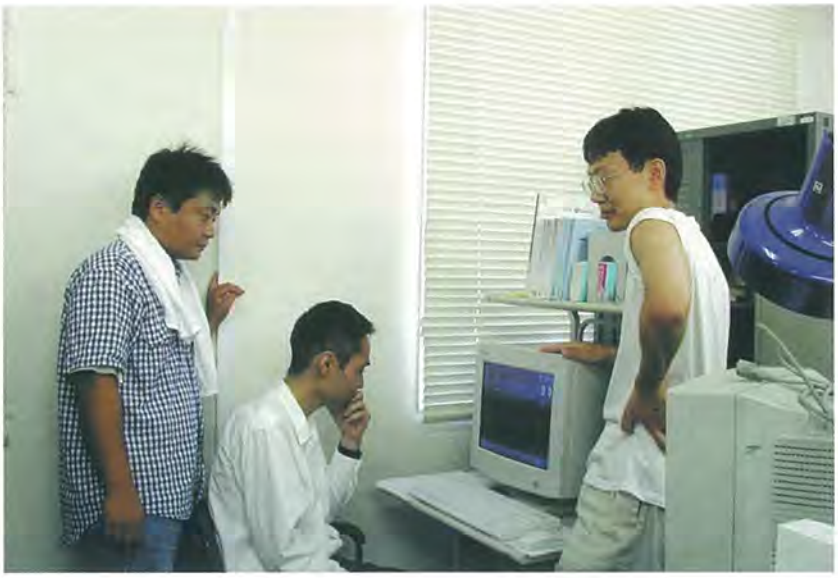

Theory

11 Theory

The theory group has been conducting research on many subjects, such as strongly correlated electron systems, second-order optical processes in the x-ray region, and photo-induced phase transitions. Here, we briefly introduce a few results.

11-1 A small One-electron Gap Versus a Large Optical Gap in 1-, 2-, and 3-Dimensional Half-filled Hubbard Models

We have shown that in the insulating state caused by a strong Coulomb repulsion, the one-electron density of state has only a small gap, while the light-absorption spectrum has a relatively large gap[1]. In Fig.1, we show the one-electron density of states and the light-absorption spectra of 1-, 2-, and 3-dimensional half-filled Hubbard systems calculated by means of a quantum Monte-Carlo simulation. We can see that the one-electron gap is at most half as large as the optical gap. Such an apparent difference between two kinds of gaps has actually been observed for metal-oxide systems, and it should be a characteristic of such exotic insulating systems with large quantum fluctuations.

11-2 Electronic Relaxation Dynamics of x-ray Radiation from a Shallow Core Level to a Deep Core Level in Insulators

We have studied the electronic relaxation dynamics of x-ray radiation in wide-gap insulators[2]. A four-band system, comprising dispersionless deep and shallow core bands and conduction and valence bands, is taken as our model. The Coulomb interactions

among conduction electrons and valence holes are treated by perturbation theory. We focus on the following process. First, an electron is excited from a deep core level to the conduction band by an incident x-ray. Then, another x-ray is radiated by a subsequent transition of an electron from a shallow core level to a deep one. When the energy of the incident x-ray is larger than the energy difference between the upper edge of the conduction band and the deep core level, the radiation spectrum has two peaks(Fig.2a). One peak depends linearly on the incident x-ray, while the other peak is fixed at the energy difference between the two core levels. The former peak is due to Raman scattering, while the latter peak is a characteristic luminescence. The electron excited by the incident x-ray is relaxed into the conduction band by creating pairs of a conduction electron and a valence hole through a Coulomb interaction. After such an electronic relaxation, the x-ray is radiated with the energy, irrespective of the incident x-ray (plateaus in Fig.2b and 2c). This electron-hole pair creation also occurs in the Raman process to make an extra peak(Fig.2c). Such a multi-peak structure in the x-ray radiation spectrum has been actually observed for YF_3.

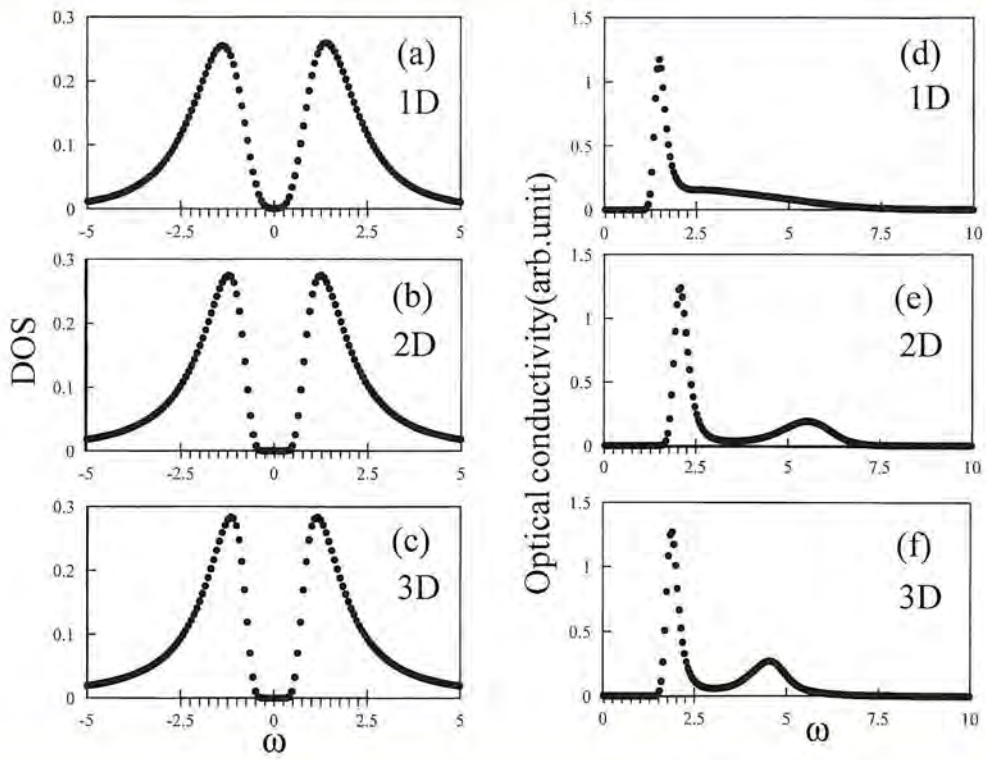

Figure 1.

Density of states for 1D(a), 2D(b), and 3D(c) systems and light-absorption spectra for 1D(d), 2D(e), and 3D(f) systems. The parameters are (t,U)=(1,4), (0.7,4), and (0.6,4) for the 1D , 2D, and 3D systems, respectively.

References
[1] N.Tomita and K.Nasu, Solid State Commun. 111(1999)175.
[2] H.Mizouchi, Phys.Rev.B58(1998),15557.

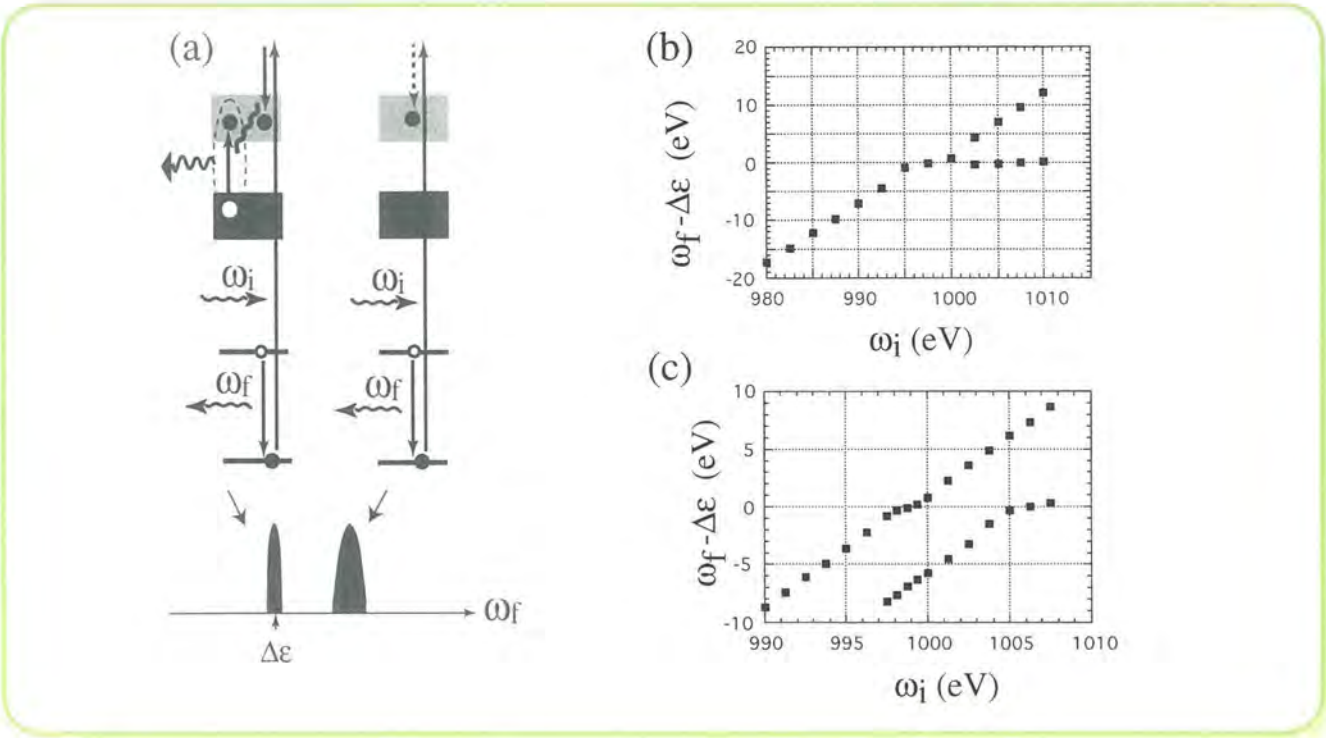

Figure 2.
Schematic representation of the second-order optical processes in the four-band electronic system(a) and the peak positions of x-ray radiation spectra of these systems with different band widths, (b) and (c).

List of Photon Factory Seminars

Carra, P. (ESRF, France) Core-level spectroscopies of magnetic systems	April 3, 1998
Yan, Y. M. (Institute of Low Energy Nuclear Physics, Beijing Radiation Center) X-ray capillary lens and its application	April 15, 1998
Kabachnik, N. M. (Moscow State University) Angular correlation between photoelectron and auger electrons	May 15, 1998
Mase, K. (Experimental Facilities Division I, IMSS, KEK) Study of mechanism of ion desorption induced by core-electron excitations using electron ion coincidence spectroscopy	May 15, 1998
Kamikubo, H. (Experimental Facilities Division II, IMSS, KEK) Structure and function of light driven proton pump, bacteriorhodopsin	May 29, 1998
Stroxov, V.N. (Universitaet des Saarlandes, Saarbruecken, Germany, and Chalmers University of Technology, Goteborg, Sweden) Very-low-energy electron diffraction as a direct probe for unoccupied bandstructure above the vacuum level : principles, results, implications in photoemission	June 8, 1998
Chen, J. H. (Center for High Pressure Research, SUNY) High pressure and temperature research at the X17B of NSLS	June 25, 1998
Saitoh, T. (Experimental Facilities Division I, IMSS, KEK) Angle-resolved photoemission study on the layered perovskite-type manganese oxides	June 26, 1998
Hikosaka, Y. (Experimental Facilities Division I, IMSS, KEK) Dynamics of superexcited molecules	July 16, 1998
Yamanouchi, K. (Graduate School of Science, Univ. of Tokyo) Ultrafast nuclear dynamics of molecules in intense laser fields	July 24, 1998
Hodgson, K. (Stanford Synchrotron Radiation Laboratory, Stanford University) Protein crystallography with synchrotron radiation-from the early days to recent developments	August 25, 1998
Fujimori, A. (Graduate School of Frontier Sciences, Univ. of Tokyo) Photoemission spectra of high-temperature superconductors and related materials	August 11, 1998
Tröger, L. (HASYLAB, Germany) Nanocrystals and chemical reactions as studied by XAFS	October 2, 1998
Hall, R. (DIAM, University Pierre & Marie Curie, France) New method for the study of dissociation dynamics of state-selected doubly charged ions: application to CO_2^{+}	October 9, 1998
Kamimura, H. (Graduate School of Science, Science Univ. of Tokyo) Theory of high temperature superconductivity in underdoped cuprates unusual electronic-spin states	October 20, 1998
Soejima, K. (Graduate School of Science and Technology, Niigata Univ.) Circular dichroism in the double photoionization of helium	October 22, 1998
Nahon, L. (LURE and CEA/DRECAM/SPAM, France) The SU5 high resolution/high flux VUV beamline with exotic polarizations at super-ACO :Why ? How ? and first results	October 26, 1998
Liu, N. Q. (Tsinghua Univ., China) Status of the TESLA project	October 30, 1998
Hansen, J. E. (Dept. of Physics and Astronomy, University of Amsterdam) Photoionization in the iron group elements	November 13, 1998
Koide, T. (Experimental Facilities Division I, IMSS, KEK) A phase transition from ferromagnetism to superparamagnetism and direct determination of interfacial magnetic moments in two-dimensional Co nanoclusters on Au(111) surface	December 4, 1998
Ikegami, H. (Uppsala Univ.) Coherent molecular system psn and scanning clustering microscopy	February 10, 1999
Takatsuka, K. (Graduate School of Arts and Science, Univ. of Tokyo) Ultra fast dynamics of ionized states studies by angle-resolved pump-probe photoelectron spectroscopy	February 19, 1999
Ishihara, S. (Institute for Materials Research, Tohoku Univ.) Theory of orbital degree of freedom and its observation by x-ray scattering in magnetites	March 12, 1999

EXPERIMENTAL FACILITIES

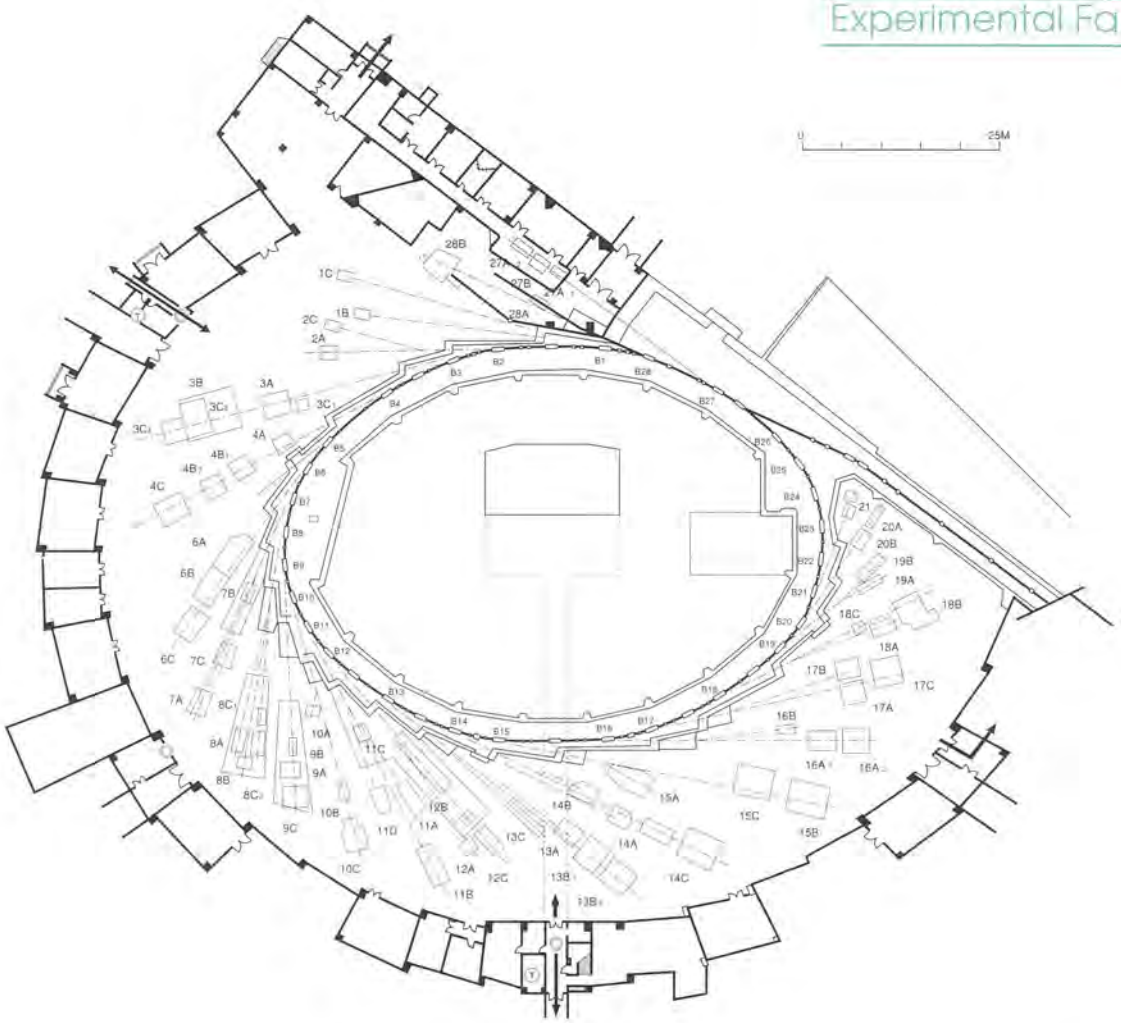

Plan view of the experimental hall of PF storage ring.

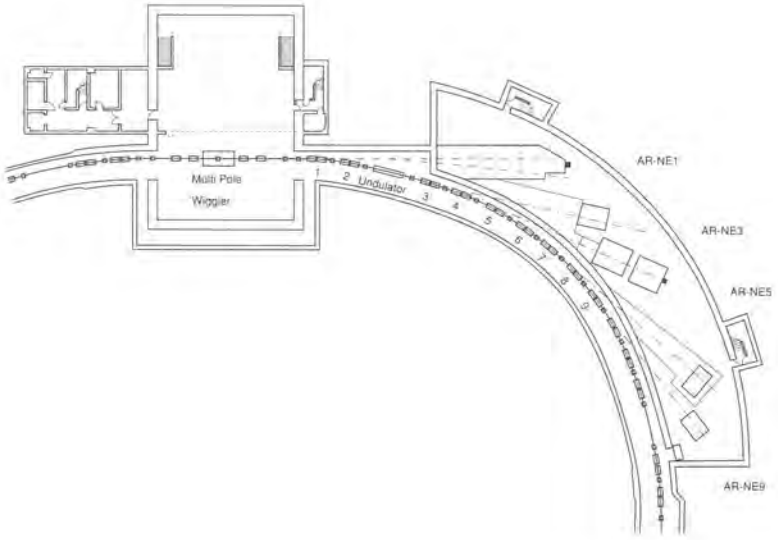

Plan view of the experimental hall of PF-AR.

Summary of Experimental Stations

1

Table 1 List of Experimental Stations at PF Storage Ring

Experimental Station			Spokesperson
BL-1			
	A	[NTT] Solid surface analysis	Y. Watanabe [NTT], A. Kakizaki
	B	X-ray powder diffraction under extreme condition	Y.Murakami
	C	Soft X-ray photoelectron spectroscopy (under construction)	A.Kakizaki
BL-2		(Undulator)	
	A	Soft X-ray spectroscopy	Y.Kitajima
	C	Soft X-ray spectroscopy	M.Watanabe
BL-3			
	A	X-ray diffraction and scattering	M.Tanaka
	B	VUV and soft X-ray spectroscopy	Y.Azuma
	C1	X-ray diffraction	H.Adachi, H.Kawata
	C2	Characterization of X-ray optical elements	M.Ando
	C3	X-ray magnetic Bragg scattering by means of white X-rays	H.Adachi, H.Kawata
BL-4			
	A	Trace element analysis, X-ray microprobe	A.Iida
	B1	Micro-crystal and -area structure analysis	K.Ohsumi
	B2	Powder diffraction	M.Tanaka, K.Ohsumi
	C	X-ray diffraction and scattering	Y.Murakami
BL-6			
	A	Macromolecular crystallography by Weissenberg camera	N.Igarashi
	B	[TARA] Macromolecular crystallography by Weissenberg camera	N.Sakabe [TARA], M.Suzuki
	C	[TARA] Macromolecular crystallography by Weissenberg camera	N.Sakabe [TARA], M.Suzuki
BL-7			
	A	[RCS] Soft X-ray photoelectron spectroscopy	H.W.Yeom [RCS], K.Ito
	B	[RCS] Surface photochemical reaction and angle resolved photoelectron spectroscopy	H.W.Yeom [RCS], K.Ito
	C	X-ray spectroscopy and diffraction	M.Nomura
BL-8			
	A	[Hitachi] Soft X-ray spectroscopy	Y.Hirai [Hitachi], A.Yagishita
	B	[Hitachi] EXAFS	Y.Hirai [Hitachi], A.Yagishita
	C1	[Hitachi] X-ray lithography	Y.Hirai [Hitachi], A.Yagishita
	C2	[Hitachi] X-ray tomography and X-ray microscopy	Y.Hirai [Hitachi], A.Yagishita

Experimental Station		Spokesperson
BL-9		
A	XAFS(under construction)	M.Nomura
B	[NEC] Photochemical reaction	I.Nishiyama [NEC], M.Nomura
C	[NEC] EXAFS and X-ray toptgraphy/diffraction	H.Kimura [NEC], M.Nomura
BL-10		
A	X-ray diffraction/scattering, crystal structure analysis	M.Tanaka
B	XAFS	N.Usami
C	Small-angle X-ray scattering of solution sample	K.Kobayashi
BL-11		
A	Soft X-ray spectroscopy	Y.Kitajima
B	Surface EXAFS, soft X-ray spectroscopy	Y.Kitajima
C	VUV spectroscopy(solid state)	A.Kakizaki
D	Angle-resolved photoelectron spectroscopy(under construction)	A.Kakizaki, T.Saitoh
BL-12		
A	Characterization of VUV-SX optical elements, soft X-ray spectroscopy	A.Kakizaki
B	VUV high-resolution spectroscopy	K.Ito
C	XAFS	M.Nomura
BL-13	(Multipole weiggler/Undulator)	
A	High pressure(under construction)	T.Kikegawa
B1	Surface-sensitive XAFS, X-ray diffraction	T.Kikegawa
B2	High pressure & high temperature X-ray diffraction	T.Kikegawa
C	Soft X-ray photoemission spectroscopy and XAFS	E.Shigemasa
BL-14	(Vertical wiggler)	
A	Crystal structure analysis, EXAFS	S.Kishimoto
B	High-precision X-ray optics	K.Hirano
C	General purpose(X-rays)	K.Hyodo
BL-15		
A	Small-angle X-ray scattering of muscle and alloys	H.Kamikubo
B1	White X-ray topography and X-ray magnetic Bragg scattering	H.Kawata
B2	Surface and interface diffraction	H.Sugiyama, H.Kawata
C	High-resolution X-ray diffraction	K.Hirano
BL-16	(Multipole wiggler/Undulator)	
A1	General purpose (X-ray)	H.Kawata
A2	X-ray diffraction and scattering	Y.Murakami
B	Soft X-ray spectroscopy	E.Shigemasa
BL-17		
A	[Fujitsu] XAFS	S.Komiya [Fujitsu], A.Iida
B	[Fujitsu] Photochemical vapor deposition	S.Komiya [Fujitsu], A.Iida
C	[Fujitsu] Grazing incident X-ray diffraction, X-ray fluorescence analysis	S.Komiya [Fujitsu], A.Iida
BL-18		
A	[ISSP] Angle-resolved photoelectron spectroscopy of surfaces and interfaces	A.Kimura [ISSP], A.Kakizaki
B	Macromolecular crystallography(Weissenberg and Laue)	N.Watanabe
C	High pressure X-ray powder diffraction	T.Kikegawa

Experimental Station		Spokesperson
BL-19	(Revolver undulator)	
A	[ISSP] Spin-resolved photoelectron spectroscopy(Mott detector)	A.Kimura [ISSP], A.Kakizaki
B	[ISSP] Spin-resolved photoelectron spectroscopy (SPLEED)	S.Shin [ISSP], A.Kakizaki
	[ISSP] Soft X-ray emission spectroscopy	
BL-20		
A	VUV spectroscopy	K.Ito
B	[ANBF] White and monochromatic beam general purpose X-ray station	G.Foran [ANBF], K.Ohsumi
BL-21	[Light Source Division] Beam position monitoring	T.Katsura [Light Source Div.]
BL-27	(Beamline for experiments using radioisotopes)	
A	Radiation biology, soft X-ray photoelectron spectroscopy	K.Kobayashi
B	Radiation biology, X-ray diffuse scattering	K.Kobayashi
BL-28	(Elliptical multipole wiggler/Undulator)	
A	VUV and soft X-ray spectroscopy with circularly polarized undulator radiation	T.Koide
B	Spectroscopy and scattering with polarized X-rays	T.Iwazumi
NTT	Nippon Telegraph and Telephone Corporation	
TARA	Tsukuba Advanced Research Alliance	
RCS	Research Center for Spectrochemistry, University of Tokyo	
ISSP	Institute for Solid State Physics, University of Tokyo	
ANBF	Australian National Beamline Facility	

Table 2 List of Experimental Stations at PF-AR

Experimental Station		Spokesperson
AR-NE1	(Elliptical multipole wiggler/Undulator)	
A1	High resolution Compton and magnetic Compton scattering	H.Kawata
A2	Spectroscopy and scattering with circularly polarized X-rays	T.Iwazumi
B	Spectroscopy with circularly polarized soft X-rays	T.Koide
AR-NE3	(Undulator)	
A	Nuclear resonant scattering	X.Zhang
AR-NE5		
A	Angiography and X-ray computed tomography	K.Hyodo
C	High pressure and high temperature X-ray diffraction	T.Kikegawa
AR-NE9		
B	[Accelerator Department] Vacuum science and technology	K.Kanazawa [Acc.Dept.]

Table 3 X-Ray Beamline Optics

Branch Beamline	Acceptance Horiz. (mrad)	Type of Monochromator	Mirror	Photon Energy (keV)	Beam Size (H × V) (mm)	Photon Flux at Sample Position	Energy Resolution ($\Delta E/E$) $\times 10^{-4}$	Reference
BL-4B1	2	Flat Double Crystal Si(111)	Bent Cylinder	6 ~ 21	0.5 × 0.3	8×10^{10}/4mm^2 (8.3 keV, 300 mA)	~ 5	
BL-3A	4	Double Crystal Si(111) Sagittal Focusing	Collimating Focusing Mirrors (Fused Quartz)	6 ~ 20	100 × 5 2 × 1		~ 2	1 - 3
BL-3C2/C3	2	Double Crystal Si(111)						4, 5
BL-4A	6	Double Crystal Sagittal Focusing	None	4 ~ 20	50 × 4 4 × 1		~ 2	6
BL-4B1	4.5	Double Crystal Si(111)	None	6 ~ 20	13 × 2		~ 2	7
BL-4B2	4.5	Double Crystal Si(111)	Bent Cylinder	4 ~ 35	15 × 3		~2	
BL-4C	2	Flat Double Crystal Si (111)	Bent Cylinder	6 ~ 21	1.0 × 0.6		~5	9, 10
BL-6A	1.2	Bent Si(111) (a = 0, 6.0°, 7.8°, 9.5°, 11.4°, 13.7°, 16.5°)	Bent Plane Fused Quartz	5 ~ 25	2.5 × 1			11
BL-6B	1	Bent Si(111)	Bent Plane Si Pt-coated	7 ~ 14	1.7 × 0.2			12, 13
BL-6C2	0.5	Bent Crystal Si (111)	Bent Plane Si Pt-coated	8 ~33	5 × 5			4, 5, 12
BL-7C	4	Double Crystal Si (111) Sagittal Focusing	Double Mirror Fused Quartz Focusing	4 ~ 20 (4 ~ 13)	8 × 1	1×10^{10}/6mm^2 (8 keV, 300 mA) (1×10^{11} when focused)	~ 2	15 - 17
BL-8C1/C2	5	Channel-Cut Si(220), Si(111), Si(400)	None	5 ~ 40	50 × 5	6×10^{8}/mm^2 (10 keV, 300 mA)	~2	
BL-9C	5	Double Crystal Si(111), Si(311)	None	5 ~ 25 4 ~ 23 or white	1 × 1		~ 2	
BL-10A	1	Si(111), Si(311) Quartz(100), PG(002) Curved Si(111) (α ~ 4°, 8°)	None	5 ~ 25	10 × 3		50 ~ 5	18

Branch Beamline	Acceptance Horiz. (mrad)	Type of Monochromator	Mirror	Photon Enegy (keV)	Beam Size (H×V) (mm)	Photon Flux at Sample Position	Energy Resolution (ΔE/E) ×10⁻⁴	Reference
BL-10B	2	Channel-Cut Si(311)	None	5 ~ 30	5×1	1×10^{9}/7mm² (10 keV, 300 mA)	1	
BL-10C	4	Double Crystal Si(111)	Bent Cylinder	4 ~ 10	2.4×0.6	10^{11}/1.5mm² (8 keV, 400 mA)	2	
BL-12C	2	Double Crystal Si(111) Si(311)	Bent Cylinder	6 ~ 23	0.65×0.4	5×10^{10} (8.0 keV, 300mA) w.Si(111)	~ 2	19
BL-13A	1	Double Crystal Si(220)	None	4 ~ 30			~ 0.1	20
BL-13B1/B2	4	Double Crystal Si(111), Si(220) Sagittal Focusing	Bent Plane Fused Quartz	4 ~ 30	4×1		~ 2	20
BL-14A	1.28 (Vertical)	Double Crystal Si (111) Si (311) Si (553)	Bent Cylinder Pt-coated Fused Quartz	5.1 ~ 19.1 9.9 ~ 35.6 22.7 ~ 84.5	2×1 5×38 5×38		2	21
BL-14B	2.2 (Vertical)	Double Crystal Si(111),	None	10 ~ 57	5×14		2	
BL-14C	1.3 (Vertical)	Double Crystal Si(111), Si(220)	None	5.5 ~ 70 or white	6×90		2	
BL-15A	2	Bent Crystal Ge(111) (α = 8.0°)	Bent Plane, Fused Quartz	8.0 (fixed)	0.5×0.25	9×10^{10}/6mm² (8.0 keV, 150 mA)	~ 10	22
BL-15B1/B2	2	Double Crystal Si (111)	Bent Cylinder	5 ~ 20 or white	0.6×0.4	10^{11}/1mm² (8.0keV, 350mA)	~ 2	
BL-15C	2	Double Crystal Si (111)	None	4 ~ 30	60×6			
BL-16A	1	Double Crystal Si(111) Sagittal Focusing	Bent Plane (Pt on SiC) for Vertical Collimating Bent Plane (Pt on SiO_2) for Vertical Focusing	4 ~ 25	1.3×0.4	$\sim1\times10^{13}$ (8.3 keV, 300 mA)	~ 1	23
BL-17A	4	Double Crystal Si(111)	None	5 ~ 13	100×10		~ 2	24
BL-17C	1	Double Crystal Si(111)	None	5 ~ 13	20×5		~ 2	25

Branch Beamline	Acceptance Horiz. (mrad)	Type of Monochromator	Mirror	Photon Enegy (keV)	Beam Size (H×V) (mm)	Photon Flux at Sample Position	Energy Resolution (ΔE/E) ×10^{-4}	Reference
BL-18B	2	Double Crystal Si(111) Si(220) Ge(111) Ge(220)	Bent Cylinder Fused Quartz, Pt-coated	6 ~ 30	0.6×0.4	1.1×10^{10} (12.4 keV, 300 mA) Si(111)	~ 2	26
BL-18C	1	Double Crystal Si(111)	Cylinder Fused Quartz, Pt-coated	6~25	0.07×0.04		~2	
BL-20B	2	①Channel Cut Si(111) ②Double Crystal Sagittal focusing Si(111)	None	4 ~ 25	26×3		~ 2	27
BL-27B	4	Double Crystal Si(111)	None	4 ~ 20	100×6		~ 2	28
BL-28B	H: 4 V:0.2	Double Crystal Si(111) Si (220) InSb(111)	Pre-mirror Bent Cylinder Si Pt- & Ni-coated Post-mirror Bent Plane Fused Quartz Pt- & Ni-coated	2 ~ 10	2.4×0.3	1.9 Si(111)	3 (at 6.3 keV)	29
AR-NE1A1	2	Double Bent (at 60 keV) Crystal Si(111)	None	40 ~ 180	2×0.5	5×10^{12} (60 keV, 35mA)	8	28, 29
AR-NE3A1	H:0.3 V:0.03	Double Crystal Si(111) High-resolution Monochromator Nuclear Monochromator of Single Crystal $^{57}Fe_2O_3$(777)	None	5 ~ 295 8 ~ 26 14.4	15×2	4×10^{9} (14.4 keV30mA)	2 5×10^{-3} 1×10^{-7}	32
AR-NE5A	10	Asym.Cut Single Crystal Si(311), Si(511) (α = 4° ~ 6°) Double Crystal Si (311), Si(111)	None	33, 52 20 ~ 60	150×150 (33.2 keV) 150×3	5×10^{8}	60 2	33, 34
AR-NE5C	3	Double Crystal Si (111)	None	30~ 100	60×5		1	35

References

[1] S. Sasaki et al., Rev. Sci. Instrum. 63 (1992) 1047.
[2] K. Kawasaki et al., Rev. Sci. Instrum. 63 (1992) 1023.
[3] T. Mori and S. Sasaki, Rev. Sci. Instrum. 66 (1995) 2171.
[4] T. Nakajima et al., Nucl. Instrum. Meth. A261 (1987) 308.
[5] T. Nakajima et al., Rev. Sci. Instrum. 66 (1995) 1440.
[6] A. Iida et al., Rev. Sci. Instrum. 66 (1995) 1373.
[7] K. Ohsumi et al., Rev. Sci. Instrum. 66 (1995) 1448.
[8] H. Toraya et al., J. Synch. Rad. 3 (1996) 75.
[9] H. Iwasaki et al., Rev. Sci. Instum. 60 (1989) 2406.
[10] Photon Factory Activity Report 1995 #13 (1996) E-1.
[11] K. Sakabe et al., Rev. Sci. Instrum. 66 (1995) 1276.
[12] K. Sakabe et al., J. Synch. Rad. 4 (1997) 136.
[13] N. Watanabe et al., J. Synch. Rad. 5 (1998) 500.
[14] Photon Factory Activity Report 1982/83 (1984) V-25.
[15] M. Nomura and A.Koyama, KEK Internal 93-1 (1993) .
[16] M. Nomura et al., KEK Report 91-1 (1991).
[17] M. Nomura and A. Koyama, in "X-ray Absorption Fine Structure", ed. by S. S. Hasnain, Ellis Horwood, Chichester, 1991, p.667.
[18] S. Sasaki, Rev. Sci. Instrum. 60 (1989) 2417.
[19] M. Nomura and A. Koyama, KEK Report 95-15 (1996).
[20] K. Nakayama et al., J. Synchr. Rad. 5 (1998) 527.
[21] Y. Satow and Y. Iitaka, Rev. Sci. Instrum. 60 (1989) 2390.
[22] Y. Amemiya et al., Nucl. Instrum. Meth. 208 (1983) 471.
[23] Photon Factory Activity Report 1994 #12 (1995) E-3.
[24] Photon Factory Activity Report 1988 #6 (1988) I-15.
[25] Y. Horii et al., Rev. Sci. Instrum. 66 (1995) 1370.
[26] N. Watanabe et al., Rev. Sci. Instrum. 66 (1995) 1824.
[27] G. J. Foran et al., J. Synch. Rad. 5 (1998) 500.
[28] H. Konoshi et al., Nucl. Insrtum. Meth. A 372 (1996) 322.
[29] T. Iwazumi et al., Rev. Sci. Instrum. 66 (1995) 1691.
[30] H. Kawata et al., J. Synchr. Rad. 5 (1998) 673.
[31] Photon Factory Activity Report 1994 #12 (1995) E-4.
[32] X. Zhang et al., Rev. Sci. Instrum. 63 (1992) 404.
[33] K. Hyodo et al., Handbook on SR IV, (1991) 55.
[34] Y. Itai et al., Rev. Sci. Instrum. 66 (1995) 1385.
[35] T. Kikegawa et al., Rev. Sci. Instrum. 66 (1995) 1335.

Table 4 VUV and Soft X-ray Beamline Optics

Branch Beamline	Acceptance Horiz. (mrad)	0Type of Monochromator	Grating Groove Density (l/mm)	Photon Enegy (eV)	Beam Size (mm)	Typical Resolving Power (E/ΔE) and Photon Flux (/s)	Reference
BL-2A Undulator	K = 0.5 ~ 2.2 λ_u = 6cm	Double Crystal InSb (111), Si (111)	——	1740 ~ 5000	< 1 ϕ	2000,8000 10^{10}	1 - 4
BL-2C Undulator	K = 0.55 ~ 2.2 λ_u = 6 cm	Varied-Space Plane Grating	1000 2200	250 ~ 1400	< 0.9 × 0.1	5000 ~ 10000 10^{11} ~ 10^{10}	5, 6
BL-3B	10 2	Grazing Incidence R = 24 m $\alpha+\beta$ = 165°	200 600 1800	10 ~ 280	< 2 ϕ	200 ~ 3000 10^{12} ~ 10^{9}	7, 8
BL-7A (RCS)	6 1	Plane Grating	1200 2400	10 ~ 1000	2 × 1	500	9
BL-7B (RCS)	6 4	1m Seya-Namioka	1200 2400	5 ~ 50	1 × 1	1000	10
BL-8A (Hitachi)	0.5 1	SX700 Plane Grating	1221	38 ~ 2300	5 × 1	2000 10^{10}	
BL-8B (Hitachi)	3 0.5	Double Crystal InSb (111), Si (311)	——	1700 ~ 14000	1.9 × 0.5	5000	11
BL-9B (NEC)	10	Plane + Toroidal Mirrors	——	——	15 × 20	——	12
BL-11A	5 1	Varied-Line-Space Plane Grating	300 800	70 ~ 1900	2 × 1	500 ~ 5000 10^{12} ~ 10^{9}	13 - 16
BL-11B	4 0.6	Double Crystal InSb (111), Ge (111)	——	1760 ~ 3910	5 × 2	2000 10^{10}	17, 18
BL-11C	4.8 3	1m Seya-Namioka	1200	4 ~ 35	~1 ϕ	1000	19
BL-11D	4 2	Grazing Incidence On-blaze Mount R_1 = 52.5 m R_2 = 22.5 m	2400	G_3 20~280 G_1 200~1200			
BL-12A	2.2 0.34	Grazing Incidence R = 2 m α = 88°	1200	30 ~ 1000	2 × 3	1000 10^{9}	20
BL-12B	5 3.6	6.65 m Off-Plane Eagle	1200 4800	5 ~ 30	——	2.5 × 10^{5} 10^{4}	21 - 23
BL-13C Undulator	K = 0.3 ~ 4.2 λ_u = 18 cm	Grazing Incidence R = 50 m $\alpha+\beta$ = 173.2°	250	70 ~ 500	5 × 1	1000 ~ 6000 10^{12} ~ 10^{10}	24, 25
BL-16B Undulator	K = 0.5 ~ 5.75 λ_u = 12 cm	Grazing Incidence R = 24 m $\alpha+\beta$ = 168.6°	400 900 2000	40 ~ 550	< 1 ϕ	1000 ~ 10000 10^{12} ~ 10^{10}	26 - 28
BL-17B (Fujitsu)	8 1	Toroidal Mirror	——	——	10 × 1	——	——

Branch Beamline	Acceptance Horiz. (mrad)	Type of Monochromator	Grating Groove Density (l/mm)	Photon Enegy (eV)	Beam Size (mm)	Typical Resolving Power (E/ΔE) and Photon Flux (/s)	Reference
BL-18A (ISSP)	2 2	Grazing Incidence R = 3 m $\alpha+\beta = 160^\circ$ R = 6.65 m $\alpha+\beta = 167.5^\circ$	300 600 1200 500	7 ~ 150	< 1 ϕ	1000~2000 10^{11} ~10^{9}	29
BL-19A Revolver Undulator (ISSP)	K = 1.0 ~ 9.0 λ_u = 16.4 cm K = 0.5 ~ 1.25 λ_u = 5 cm K = 0.5 ~ 2.5	Grazing Incidence R = 2 m $\alpha+\beta = 160^\circ$ R= 4 m $\alpha+\beta = 170^\circ$	600 1200 600 1200	12 ~ 250	< 0.7 ϕ	1000 10^{12}	30, 31
BL-19B Revolver Undulator (ISSP)	λ_u = 7.2 cm K = 1.0 ~ 5.0 λ_u = 10 cm	Varied-space Plane Grating	800 2400	10 ~ 1200	< 0.5 ϕ	400~4000 10^{12} ~10^{11}	32
BL-20A	28 5	3m Normal Incidence	1200 2400	5 ~ 40	2 × 1 10^{12} ~ 10^{9}	300 ~ 30000 10^{12} ~ 10^{6}	33
BL-27A	5 0.5	Double Crystal InSb (111)	——	1800 ~ 6000		2000	34
BL-28A Helical Undulator	Kx = 0.23 ~ 3 Ky = 0.23 ~6 λ_u = 16 cm	Grazing Incidence R = 2 m $\alpha+\beta = 160^\circ$ R = 4 m $\alpha+\beta = 170^\circ$	600 1200 600 1200	30 ~ 250	< 0.5 ϕ	1000 10^{10}	35
AR-NE1B Helical Undulator	Kx = 0.2 ~ 3 Ky = 0.2 ~6 λ_u = 16 cm	Grazing Incidence R = 10m $\beta = 89^\circ$	1200 2400	250 ~ 1800	~ 0.8 × 0.2	1000~5000 10^{11} ~10^{9}	36,37

References

[1] H. Maezawa et al., Nucl. Instrum. Meth. A246 (1986) 310.
[2] Y. Kitajima et al., Rev. Sci. Instrum. 63 (1992) 886.
[3] Y. Kitajima, J. Elec. Spec. Relat. Phenom. 80 (1996) 405.
[4] Y. Kitajima, J. Synchr. Rad. 6 (1999) 167.
[5] Y. Yan and A. Yagishita, KEK Report 95-9 (1995).
[6] M. Watanabe et al., SPIE Vol. 3150 (1997) 58.
[7] A. Yagishita et al., Nucl. Instrum. Meth. A306 (1991) 578.
[8] S. Masui et al., Rev. Sci. Instrum. 63 (1992) 1330.
[9] H. Namba et al., Rev. Sci. Instrum. 60 (1989) 1909.
[10] H. Namba et al., Rev. Sci. Instrum. 60 (1989) 1917.
[11] K. Ogata et al., Photon Factory Activity Report 1994 #12 (1995) 164.
[12] Photon Factory Activity Report 1988 #6 (1989) I-13.
[13] K. Amemiya et al., J. Synchrotron Rad. 3 (1996) 282.
[14] K. Amemiya et al., SPIE 3150 (1997) 171.
[15] Y. Kitajima et al., J. Syncrotron Rad. 5 (1998) 729.
[16] Y. Kitajima J. Eleci Spectrosc. Relat. Phenom. 101-103 (1999) 927.
[17] T. Ohta et al., Nucl. Instrum. Meth. A246 (1986) 373.
[18] M. Funabashi et al., Rev. Sci. Instrum. 60 (1989) 1983.
[19] Photon Factory Activity Report 1982/1983, (1984) V-15.
[20] Photon Factory Activity Report 1992 #10 (1993) I-2.
[21] K. Ito et al., Appl. Opt. 25 (1986) 837.
[22] K. Ito et al., Appl. Opt. 28 (1989) 1813.
[23] K. Ito and T. Namioka, Rev. Sci. Instrum. 60 (1989) 1573.
[24] M. Matsubayashi et al., Rev. Sci. Instrum. 63 (1992) 1363.
[25] H. Shimada et al., Rev. Sci. Instrum. 66 (1995) 1780.
[26] E. Shigemasa et al., KEK Report 95-2 (1995).
[27] Photon Factory Activity Report 1995 #13 (1996) E-2.
[28] E. Shigemasa et al., J. Synchrotron Rad. 5 (1998) 777.
[29] S. Suzuki et al., Activity Report of SRL-ISSP 1988 (1989) 60.
[30] A. Kakizaki et al., Rev. Sci. Instrum. 60 (1989) 1893.
[31] A. Kakizaki et al., Rev. Sci. Instrum. 63 (1992) 367.
[32] M. Fujizawa et al., Rev. Sci. Instrum. 67 (1996) 345.
[33] K. Ito et al., Rev. Sci. Instrum. 66 (1995) 2119.
[34] H. Kouishi et al., Nucl. Instrum. Meth. A372 (1996) 322.
[35] Y. Kagoshima et al., Rev. Sci. Instrum. 63 (1992) 1289.
[36] Y. Kagoshima et al., Rev. Sci. Insturm. 66 (1995) 1696.
[37] Y. Kagoshima et al., Rev. Sci. Instrum. 66 (1995) 1534.

Table 5 Timetable of the Machine Operation in FY 1998.

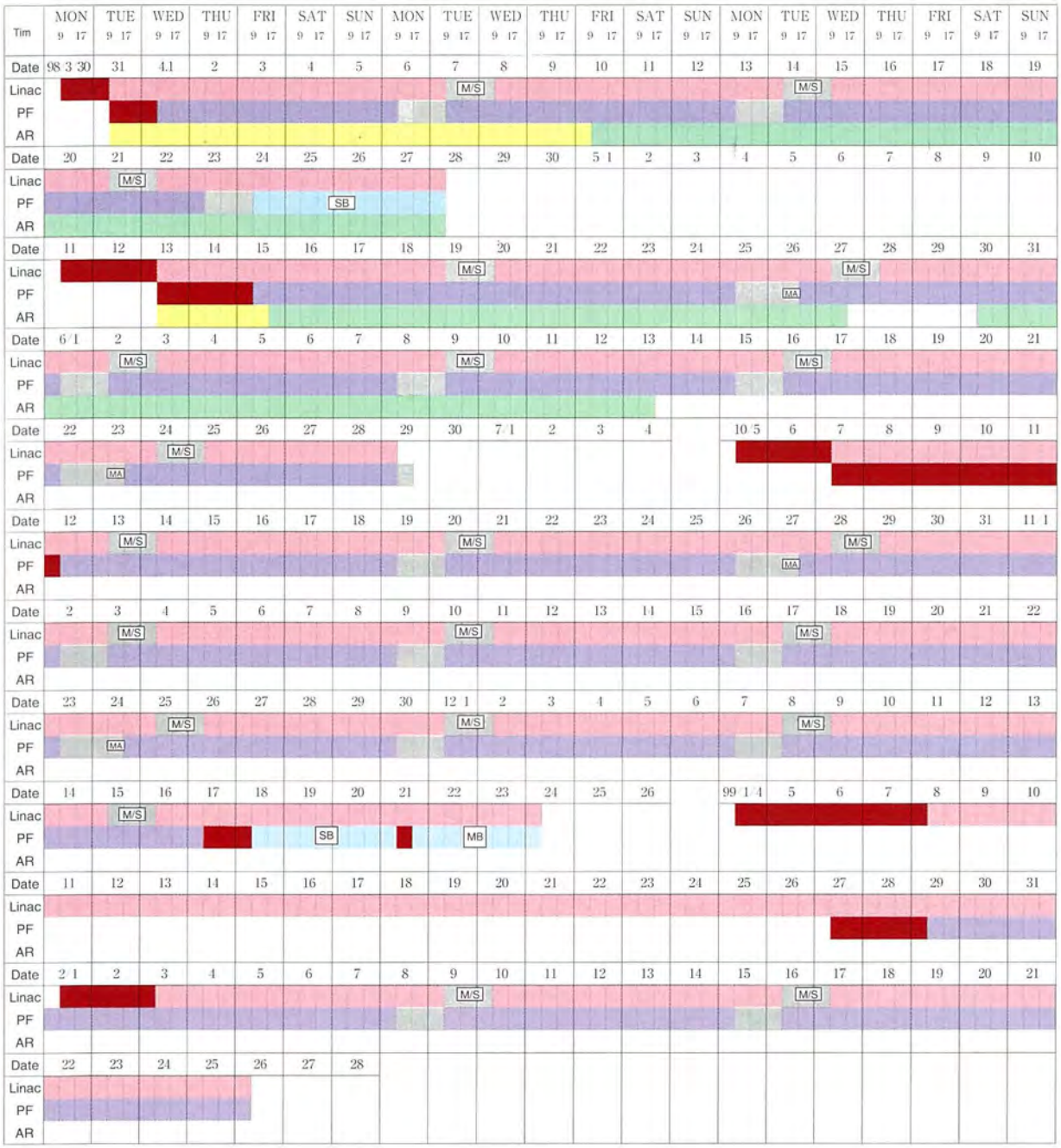

PF: PF ring

Machine Tuning
Operation Time
Machine Study
M/S: Maintenance & Study
Users Beamtime
3Gev
MA: Maintenance
SB: Single Bunch
MB: Multi Bunch

AR: PF-AR

AR-mode User Time
Mon. 21:00 ~ Fri. 11:00 (14hr/day)
Fri. 21:00 ~ Mon. 9:00 (24hr/day)
Machine Tuning & Study

Figure 1.
Operation Time of Photon Factory Ring

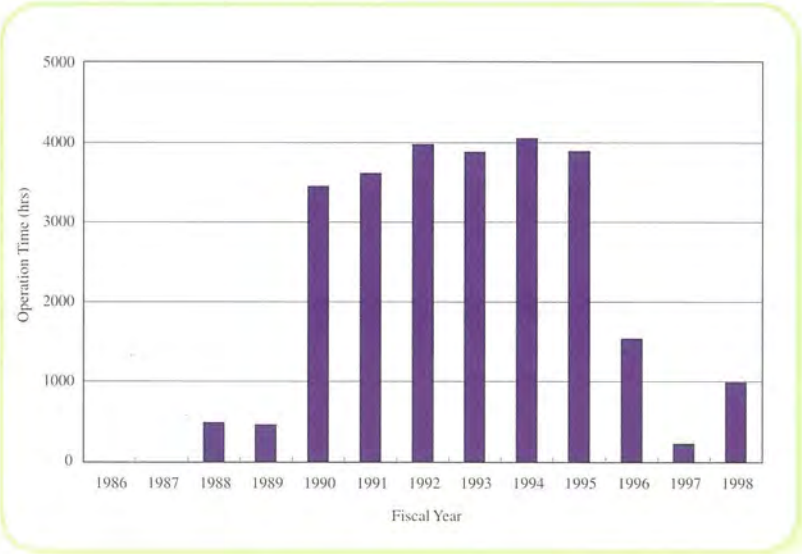

Figure 2.
Operation Time of PF-AR

2

Reconstruction and Upgrading of Beamline

2 Reconstruction and Upgrading of Beamline

2-1 BL-1B, a New Beamline for Diffraction Experiments at Low Temperature and/or High Pressure

A new beamline, BL-1B, was constructed during the summer shutdown in 1998. This beamline is designed for powder and single-crystal diffraction experiments in non-ambient conditions, such as low temperature and/or high pressure. A diffractometer with a curved imaging plate has been installed at BL-1B to carry out diffraction experiments in the field of material science. Figure 1 shows top and side views of this beamline.

The beameline consists of a monochromator and horizontal and vertical focusing mirrors. The monochromator is a fixed-exit type with double flat crystal, Si(111), which covers an energy range of 5 to 21 keV. The cylindrical mirror, which is coated by Rh on Si single crystal, is bent so as to focus the beam vertically and horizontally. The

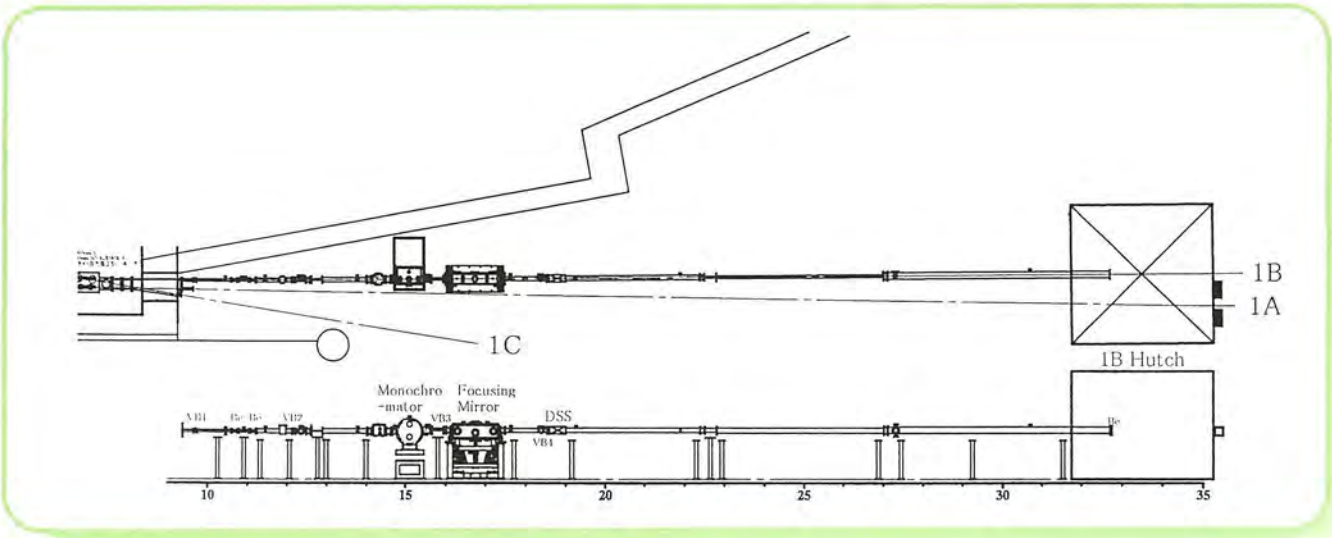

Figure 1.

focused beam size was about 0.4mm (vertical) by 0.7mm (horizontal) in FWHM at E=10 keV. The measured shift of the beam position in the energy range of 8 to 18 keV was 0.4mm and 0.1mm in the horizontal and vertical direction, respectively. The energy resolution is about $\Delta E/E = 5 \times 10^{-4}$. The total photon number was measured by a normalized photo-diode. The energy dependence is shown in Table 1.

We now have two projects in this beamline. One is for developing experiments at low temperature (10 K) and high pressure (50 GPa) in which a diamond anvil cell is installed on a cold head of a closed-cycle cryostat. The pressure at low temperature is changed by the helium gas pressure of a metal-membrane cell. The other project is a crystal-structure analysis using a very small single crystal. Both projects are now going well.

We thank the members of Suematsu and Fjii laboratory (University of Tokyo) for a collaboration in constructing of this beamline.

Table 1: Energy dependence of the total photon number

Energy (keV)	6.20	8.27	12.4	17.7
Photon number (10^{10})	2.2	7.9	7.7	2.7

2-2 BL-1C

BL-1C is the newest bending-magnet beamline of the Photon Factory, which was installed during the summer of 1998 and successfully commissioned during the fall-winter season of 1998. This beamline delivers high-resolution, high-flux photons with an energy of 20 ~ 250 eV by a varied-line-spacing-grating monochromator. The major scientific project focused on is a study of exotic quantum-scale nanostructures (PF-PAC 97S1-002 Quantum Nanostructure Project leaded by M. Oshima). The probe is based on a high-resolution angle-resolved measurement of the photoelectrons in valence bands (e.g.

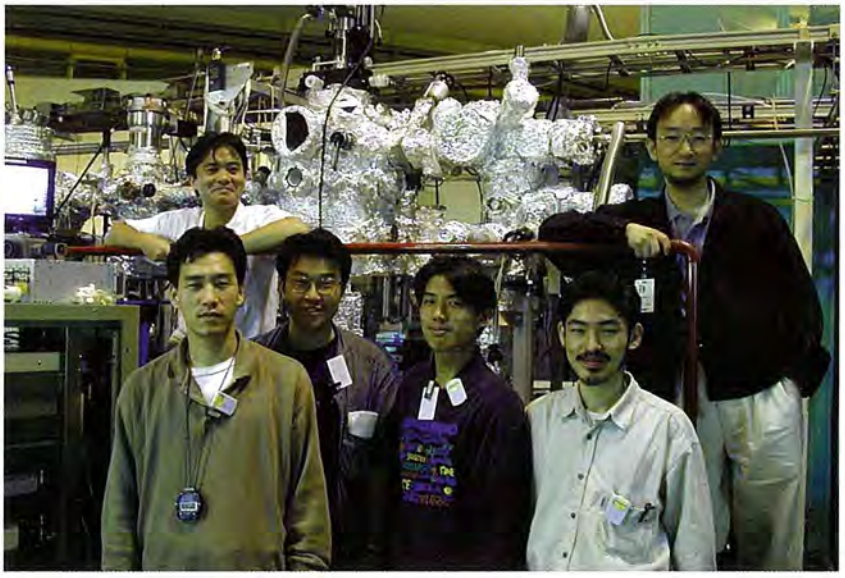

band mapping and Fermi-surface mapping) and in core levels (e.g. photoelectron diffraction). The nanostructure samples will be fabricated *in situ* by molecular-beam epitaxy systems and also by *in situ* evaporation/reaction systems.

At present, the commissioning of a high-speed automated angle-resolved photoemission system is underway along with the setting-up of a GaAs MBE system. In parallel, two preliminary photoemission projects have been undertaken; (1) a high-resolution photoemission study of the 2D charge-density-wave (CDW) phases of layered compounds 1ital-TaS_xSe_{2-x} (x = 0 ~ 2) and (2) a high-resolution photoemission and photoelectron diffraction study of the interfaces of ultrathin Si oxides and Si(001) or Si(111). One of the major physical concerns for the 2D CDW systems is the interplay between the interlayer coupling and the electron correlation in the CDW states, which also depends on the chemical composition. As shown in Fig. 1, the band dispersions of 1*T*-$TaSe_2$ in its commensurate CDW state exhibit a substantial difference from that of 1*T*-$TaSe_2$, indicating the

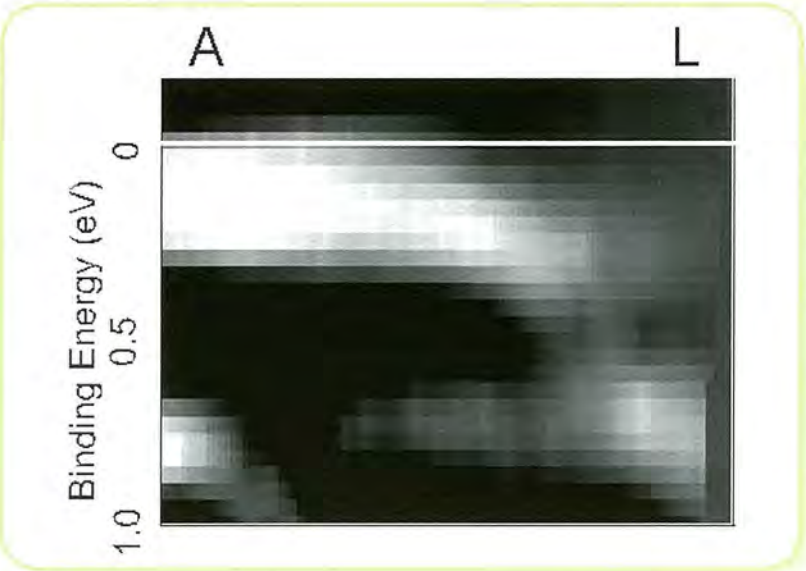

Figure 1.
Experimental band dispersions of the CDW-state 1*T*-$TaSe_2$.

absence of the Mott-Hubbard type gap for 1*T*-$TaSe_2$. Further systematic studies with detalied band- and Fermi-surface-mapping are underway together with high-resolution meassurements of site-specific screening and CDW shift in the Ta 4f core levels.

On the other hand, Fig. 2 shows high-resolution Si 2*p* core level spectra for 5 Å-thick SiO_2 oxides on Si(001) and Si(111) surfaces. These high-resolution measurements carry rich information on the chemical and structural aspects of the interface through the intensities and energy-shifts of the suboxide (Si^{1+}, Si^{2+} and Si^{3+}) components. Furthermore, the count-rate of Si 2p is an order of magnitude larger than the previous beamlines of Photon Factory, even in the angle-resolved mode. This high count rate, gained by the high photon flux and full multichannel-detector system, made possible fully angle-resolved photoelectron diffraction measurements of Si 2*p* at a component-resolved level. The detailed photoelectron diffraction patterns of the suboxide components are measured at a wide energy range of h ν = 110 ~ 270 eV, which will give quantitative information on the interface structures after proper analyses.

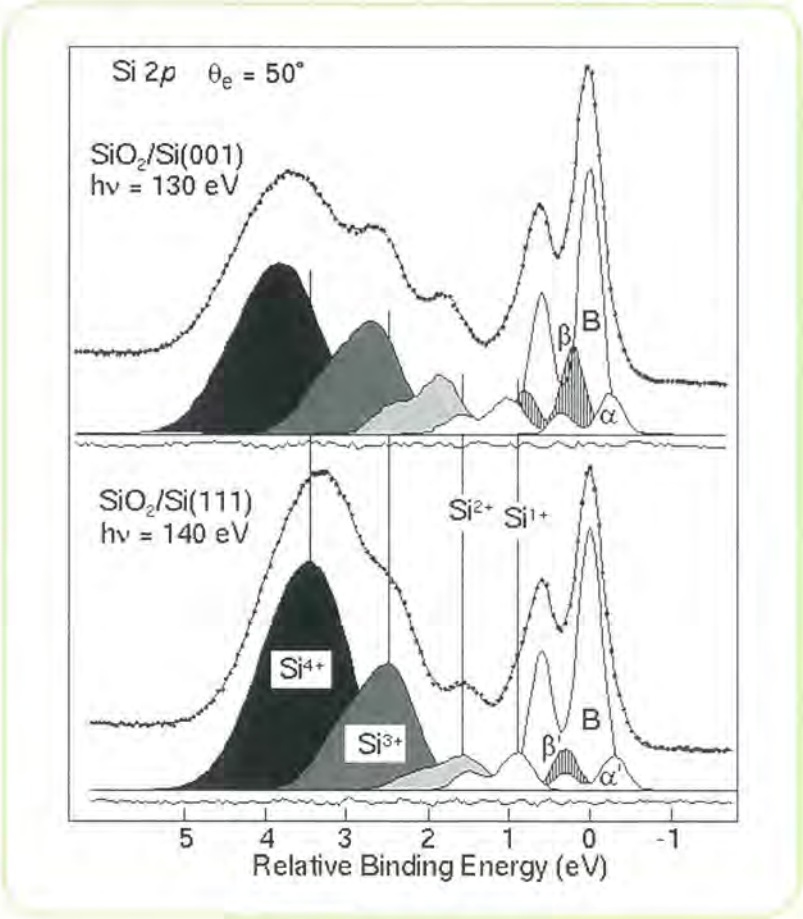

Figure 2.
High-resolution angle-resolved Si 2*p* spectra for the 5 Å-thickness SiO_2 oxides on Si(001) and Si(111) surfaces.

2-3 BL-3C2 for Characterizing X-ray Optical Elements

A new x-ray station for characterizing x-ray optical elements started activity in October, 1998. It has two major objectives: the characterization of Si crystals that are in use for almost all x-ray optical components at each x-ray beamline and station and the other development of x-ray fluorescence microscopy by means of a Wolter mirror. The first is a project to research a very small strain in a Si wafer to be measured with a precision of $Bd/d \sim 10^{-8}$. Thus one may need very high-precision goniometers and their well-conditioned atmosphere. Also, the design and fabrication of various x-ray optics capable of revealing this strain is our task. The goal is clear: the provision of x-ray optics with any desirable photon energy resolution higher than 10^{-7}, which may be very beneficial to high-energy resolution spectroscopy which can replace the Mössbauer line technique. By its product one can apply this technique to d-spacing measurements of some semiconductor materials, such as GaAs. By current x-ray fluorescent microscopy it is possible to observe the dynamic behavior of materials with a spatial resolution of a few microns in the near future.

2-4 BL-6C

BL-6C has been constructed as a beamline for monochromatic macromolecular crystallography using an automatic Weissenberg camera [1].

The beamline consists of a Platinum-coated bent-plane Si single-crystal mirror and an asymmetrically cut Si(111) monochromator (Figure 1). The mirror and the monochromator are located at 20.5 m and 26.5 m from the source, respectively. The monochromator is located in an experimental hutch.

To change the critical wavelength, the glancing angle of the mirror is tunable between 3 and 6 mrad. A rotated-inclined focusing monochromator[2] is equipped to provide a focused beam over a wide wavelength range by the simultaneous tuning of the asymmetric factor and the radius of curvature.

The specifications of the optics are as follows:

Mirror:

Type:	bent plane
Materials:	platinum-coated (1000 Å) Silicon
Size:	1000 x 100 x 50 mm
Radius of curvature:	3.66km
Glancing Angle:	3 - 6 mrad

Monochromator:

Type:	Rotated-inclined focusing monochromator
Material:	Si(111) 1mm wafer
Base:	Copper
Maximum asymmetric angle :	19.14°
Maximum radius of curvature :	45.05m
Available Wavelength:	0.9 Å -1.8 Å

Installation of the mirror was completed during the summer shutdown of 1998. Installation of an automatic Weissenberg camera and a monochromator is in progress. The beam line will be opened for general users in April, 2000.

*BL-6C was constructed as a beamline for the Tsukuba Advanced Research Alliance(TARA) .

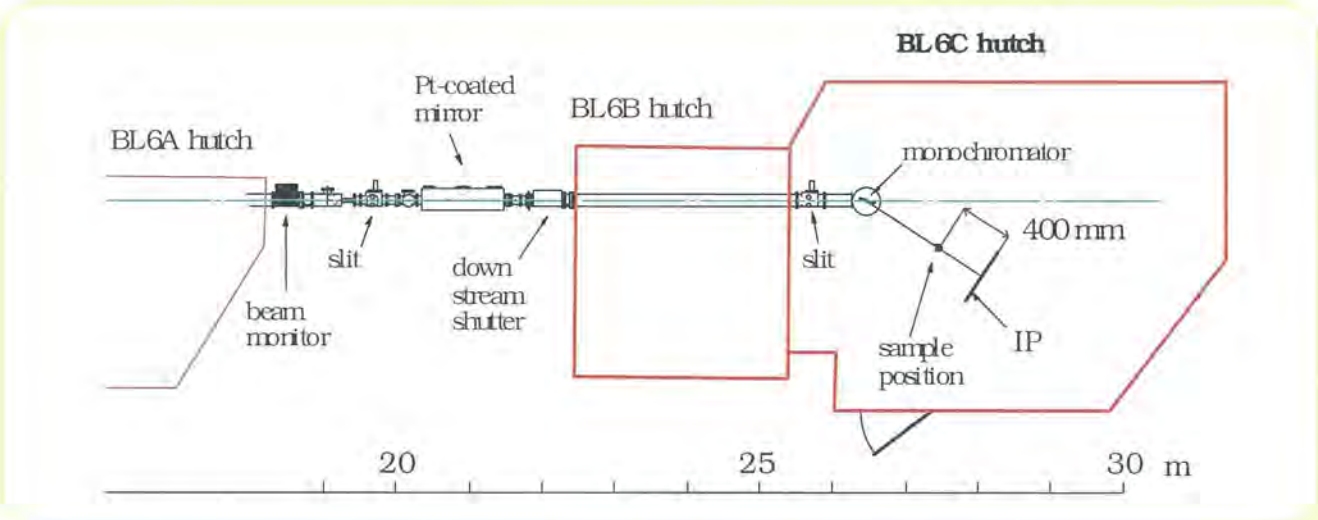

Figure 1.
Plan view of BL-6C

References

[1] K.Sakabe, K.Sasaki, N.Watanabe, M.Suzuki, Z.G.Wang, J.Miyahara and N.Sakabe, J. Synchrotron Rad. 4 (1997) 136-146.

[2] N.Watanabe, M.Suzuki, Y.Higashi and N.Sakabe, J. Synchrotron Rad. 6 (1999) 64-68.

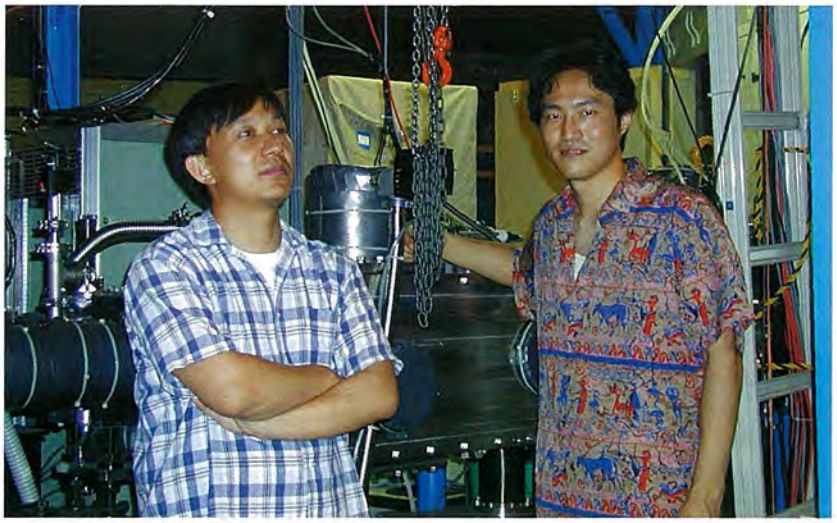

3 New Instrumentation

3-1 Soft X-ray Emission Spectrometer at BL-2C and BL-19B

Soft x-ray emission spectrometers were installed at undulator beamlines BL2C and BL19B. They are used from 350 to 1200eV at BL-2C and from 65 to 600eV at BL19B. An experimental system at BL-2C was constructed in order to measure the polarization dependence of soft X-ray Raman scattering, while that at BL-19B can be measured only at depolarized configuration. Each system consists of an analyzer chamber and a sample-preparation chamber. The analyzer chamber is equipped with a soft X-ray emission spectrometer (sxes) and a commercially available photoelectron spectrometer,

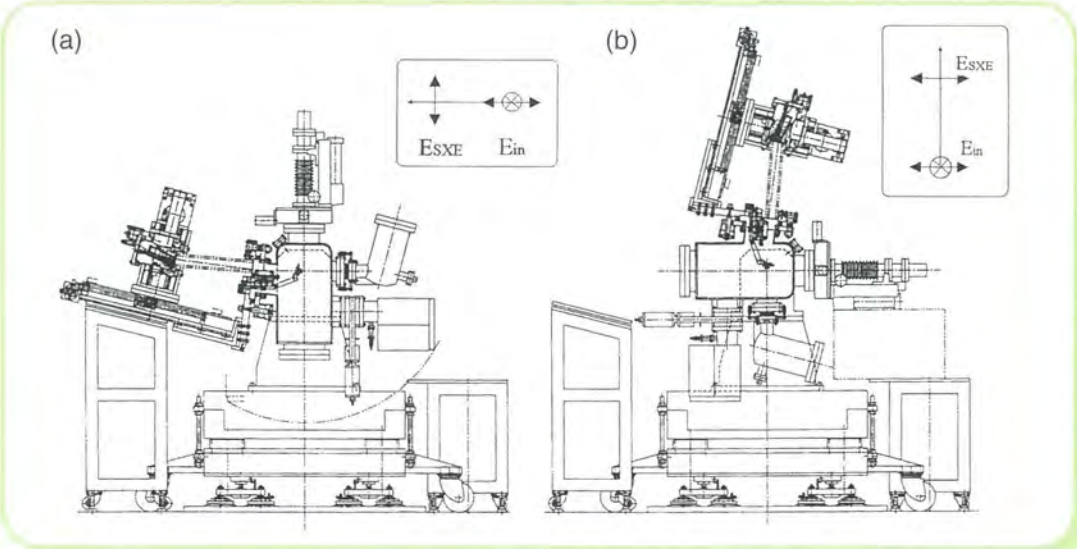

Figure 1.
Side view of the spectrometer at BL-2C. (a) In the depolarized configuration, the electric fields of SXES rotates from that of the incident light, while (b) the polarized configuration has the same polarization as that of the incident light. The insets show the polarizations of the incident photon (E_{in}) and that of the SXES (E_{SXE}).

which enables us to calibrate the incident photon energy and the SXES spectrometer. Samples can be cooled down to 15 K using a manipulator with a He-refrigerator.

Figure 1 shows a front view of the system at BL-2C. The analyzer chamber can be rotated by 90° together with the spectrometer and the photoelectron analyzer around the axis of the incident photon beam, where the rotation center is located at the sample position. The analyzer chamber is sealed with two differentially pumped rotary feed-throughs, and is connected with the sample-preparation chamber. The sample-preparation chamber has a small air-lock chamber to insert many samples from the atmosphere. In a beamline BL-2C, the electric field of the incident photon is polarized in the horizontal plane. When the SXES is measured by the 'depolarized' configuration, as shown in Fig.1(a), the polarization of the SXES rotates by 90° from the polarization of the incident light. On the other hand, when the SXES is measured by the 'polarized' configuration, as shown in Fig.1(b), the polarization of the SXES contains the same polarization as that of the incident light. The spectrometer uses the Rowland circle geometry on which an incidence slit, gratings, and a detector are located. The slit is located 10 mm apart from the sample. The available slit widths are 10, 20, 50, 100, and 300 μm. The distance between the slit and the grating is the same for each grating. The detector is positioned tangentially on the Rowland circle by the three-axis control of two translations and one rotation using pulse motors. Three laminar-type holographic spherical gratings have been prepared. We can choose two gratings according to the desired energy range in a spectrometer at once. Two gratings are changeable in a vacuum. In order to compensate for any distortion of the slit image, a two-dimensional multichannel plare (Mcp) detector is used. To increase the quantum efficiency of the detector, we have adopted a wire in front of the MCP, whose surface is coated by CsI. Figure 2

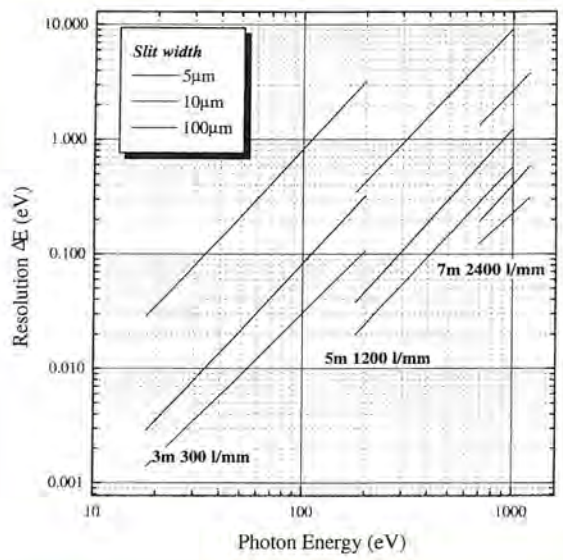

Figure 2.
Energy resolution (ΔE) for three gratings obtained by ray tracing with a 10 μm slit width. The curves are labeled with the ruling density (l/mm) and grating radii (mm).

shows the energy resolution calculated by ray tracing when a 10 μm slit width is used. The spot size on the sample is 8 μm×100 μm at BL-2C. An energy resolution of 200 meV can be reached at 700 eV by using a 7m-radius grating, and 40meV can be reached at 200eV by using a 5m-radius grating.

The experimental system at BL-19B is similar to that at BL-2C. However, the spectrometer is much longer than that of BL-2C. The dispersion at the detector is much larger by about four times. A one-dimensional and much longer position-sensitive detector is used. These differences are due to the used photon energy region and the spot size at the sample.

Figure 3 shows the V2p-SXES spectra of V_2O_3 as an example. The SXES is very sensitive to the quality of the light source. The resolution becomes improved by using a more brilliant light source from PF. By using a 20-μm slit width, a resolution of about 0.5 eV is obtained at 550 eV.

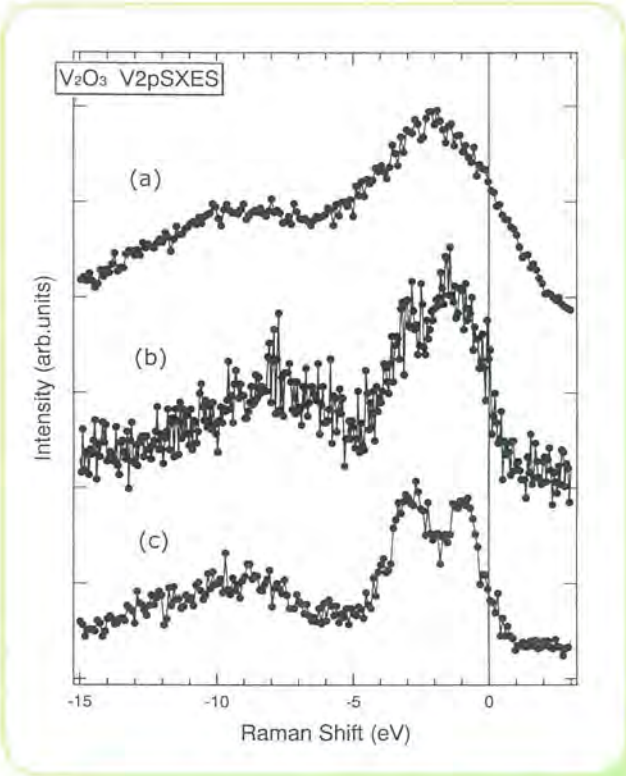

Figure 3.
Comparison of the SXES spectra of V_2O_3. (a) and (b) were measured under high-emittance operation of the PF in 1997. (b) was measured by using second-order light of the SXES spectrometer. (c) was measured under low-emittance operation of the PF in 1998.

3-2 New Powder Diffractometer with a Multiple Detector System at BL-4B2

Parallel-beam optics using synchrotron radiation enabled us to attain an angular-resolution of less than 0.01° in powder diffraction. With increasing the angular resolution, however, a serious problem occurred. It was the prolonged time required for step-scanning an entire powder pattern with a single counter. It would take, for example, ~3 days to complete a scan in a 2θ-range of 5-155° at a step interval

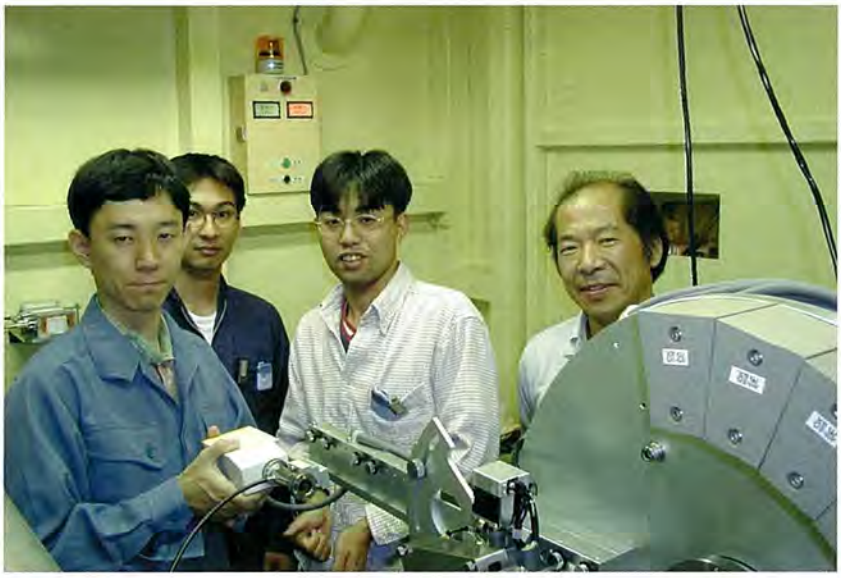

of 0.002° and a counting time of 2s at each step (plus the time required to move the counter system to the next step by 1.5s). It was therefore urgent to improve the cost-performance of synchrotron radiation experiments for high-resolution powder diffraction. One solution was to build a multiple-detector system (hereinafter called MDS).

A diffractometer design was developed for satisfying two requirements: one was to measure the profile intensity by step scanning using a point counter; the other was the capability to employ a flat-specimen reflection geometry. Step-scanning with the point counter coupled with a crystal analyzer was considered to be the best choice for obtaining high-angular resolution and a good signal-to-noise ratio. Another important thing is that we can estimate errors in a measurement based on counting statistics. The flat-specimen reflection geometry was primarily important for obtaining a high counting rate and for future applications to thin-film diffraction. This geometry could be incorporated into the MDS by adopting an asymmetric 2θ-scan mode at a fixed incident angle. Figure 1 shows a recent photograph of the MDS set on a two-axis diffractometer. Six

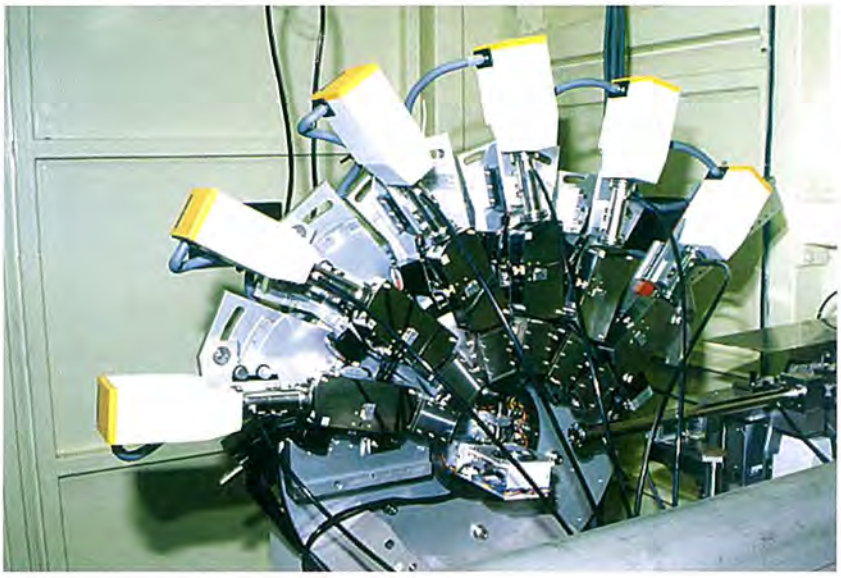

Figure 1.
Multiple detector system (MDS) at the BL-4B2 experimental station.

counter arms are attached radially at intervals of 25° to the 2θ-axis. The optical elements of the individual arms consist of Soller slits, a flat-crystal analyzer and a scintillation counter. Ge(111) or Si(111) crystals are presently available to the analyzer crystal. The sixth arm on the high-angle side has a sufficient length to equip long horizontal parallel slits with an angular aperture of 0.032 or 0.065°. A capillary specimen can also be used in place of a flat specimen holder. Six data sets are output from the MDS. Single data sets can also be output if we use the fifth or the sixth arm as a single counter system.

Beamline BL-4B consists of a bending-magnet light source, a double-crystal Si(111) monochromator, a Rh-coated cylindrical mirror for focusing the beam in the horizontal direction and the MDS. The MDS is presently installed at a distance of 29.5m from the light source in the BL-4B2 experimental station. With the aid of a computer-controlled system, a wavelength can be easily chosen by entering the value of the wavelength in the range of 0.65-2.5 Å from a key board, and a second crystal of the monochromator can be automatically tuned.

The angular-resolution of the observed diffraction pattern is our chief concern. Figure 2 shows the variations of the full-width at half-maximums (FWHM) of the observed profiles of Si powder as a function of 2θ measured with the beam at a wavelength of 0.7 Å. A compromise of the angular resolution with the diffracted intensity is unavoidable. Spending 3s at each step for scanning a whole powder pattern, however, could give the angular resolution shown in Figure 2 and the maximum counts, for example, of 80,000 for α-Si_3N_4 that is a ceramic material consisting of light elements (in this case the wavelength was 1.2 Å).

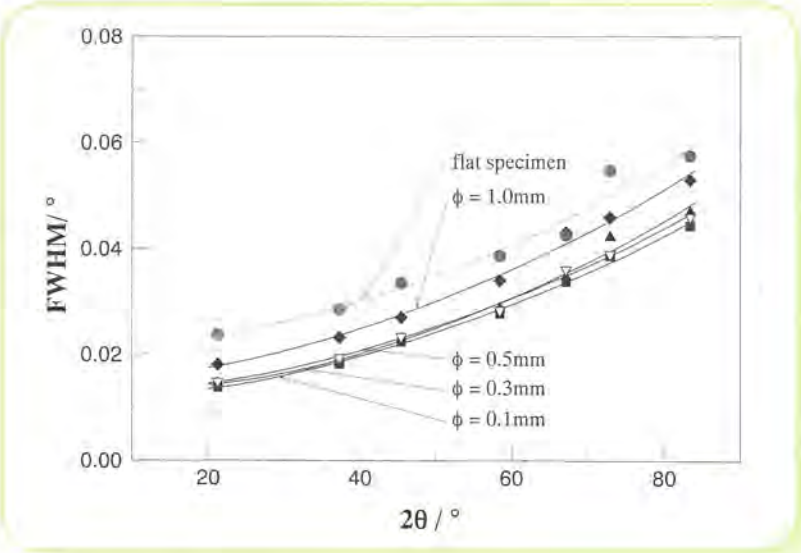

Figure 2.
Variations in the full-width at half-maximum (FWHM) of Si powder with 2θ. The plots on the top line are the FWHM measured in flat-specimen reflection geometry and the remaining ones in capillary transmission geometry (wavelength was 0.7 Å).

Data processing is an important step which transforms raw intensity data into a data set that can be used in currently available computer programs for powder data analysis, such Rietveld refinement. After data collection, it is necessary to combine the profile

intensity data sets in six blocks into a data set of the entire powder pattern. At present, we have written a computer program for least-squares fitting to combine successively two patterns in adjacent blocks. The differences in the background height, intensity scale and peak-positions between the two blocks can be adjusted.

Structure refinement is one of the goals of our experiments. The accuracy of the structural parameters derived from a Rietveld refinement is of great concern. A new weight function to be used in the minimization function for a Rietveld refinement has been proposed. It has the form $w = Y_0^e$ with $e \approx 2$ (Y_0 : observed profile intensity), and works to reduce the weights for strong and sharp peaks with high uncertainty in profile modeling and to increase relatively the weights on the weak intensities of the higher-order reflections. Recent studies have shown that 1) sufficient $\sin\theta / \lambda$-range, 2) adequate counting statistics, 3) simple profile shape for easy modeling, 4) high-resolution diffraction data and 5) proper weighting on observations are equally important for obtaining accurate structural parameters in a Rietveld refinement. Synchrotron-radiation powder diffraction has a high capability to provide the former four factors.

3-3 Fully Automated Weissenberg Camera at BL-6C

We are developing a new type of automated (on-line) data-collection system (Sakabe, et. al., J. Synchrotron Rad. 4, 136-146 (1997)). This system consists of a Weissenberg-type camera, an imaging-plate reader equipped with 5 reading heads which will be set at intervals of 90mm, an imaging-plate eraser, and a cassette transportation table, as shown in Fig.1. One large-size imaging plate (2513mm x 450mm) is fixed onto the inside of a movable cylindrical cassette. The cylindrical cassette has 36 small rectangular holes at 10 deg. intervals along the circumference of the cylinder. A primary X-ray beam passes through one of the holes and is diffracted by a sample

crystal. The exposure area on the imaging plate can be selected by adjustable screens. After the first frame has been recorded, the cassette is rotated to set the second frame recording. The exposed area can be selected from 10 deg. to 180 deg. at 10 deg. intervals. We have already made the mechanical parts and installed then at BL-6C ; however, the control parts and the data-processing software will be made in FY1999, and will be available to users in FY2000.

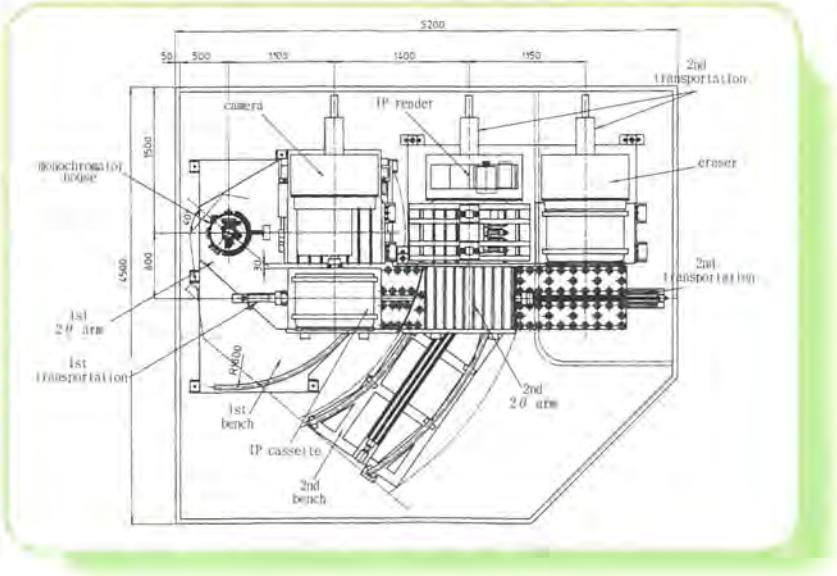

Figure 1.
Plan view of the automated data collection system in the BL-6C hutch.

3-4 New Compact Spin Detector at BL-19A

Spin- and angle-resolved photoelectron spectroscopy has been of increasing importance as a feasible experimental technique to obtain direct information on the spin-dependent electronic structures of magnetic and non-magnetic materials. These experiments are achieved in combination with two measurements: angle-resolved photoemission and electron-spin polarization. For electron spin-polarization measurements, many kinds of spin-detectors have been developed utilizing various spin-dependent electron-scattering processes. Among them, the Mott scattering process is one of the most widely used methods to measure the electron-spin polarization. In the conventional-type Mott detector, the electron detectors and the target are kept at a high voltage of about 100 kV in a vacuum to obtain a large value of the Sherman function, and hence large efficiencies of the spin detector. Since electronic equipment, e.g. amplifiers, discriminators, electron counters, etc., are preferable to be operated near to the ground potential and to be outside of the vacuum chamber, the electric insulation is strenuous, and this kind of polarimeter tends to have a large size [1]. On the other hand, in the retarding-potential Mott polarimeter, detectors for scattered electrons could be operated near to the ground potential and the entire system could be made with a very compact size. Because of its high efficiency, good stability, small size and possibility for self-calibration, the retarding-potential

Mott polarimeter has become one of the most widely used electron-spin polarimeters, and an efficiency of 1.6 x 10^{-4} has been achieved with a size of about 10 cm. In this article, we present a new compact size retarding-potential Mott polarimeter with high efficiency, which could be easily attached to an electron energy analyzer and used to measure the spin- and angle-resolved photoemission spectra [2].

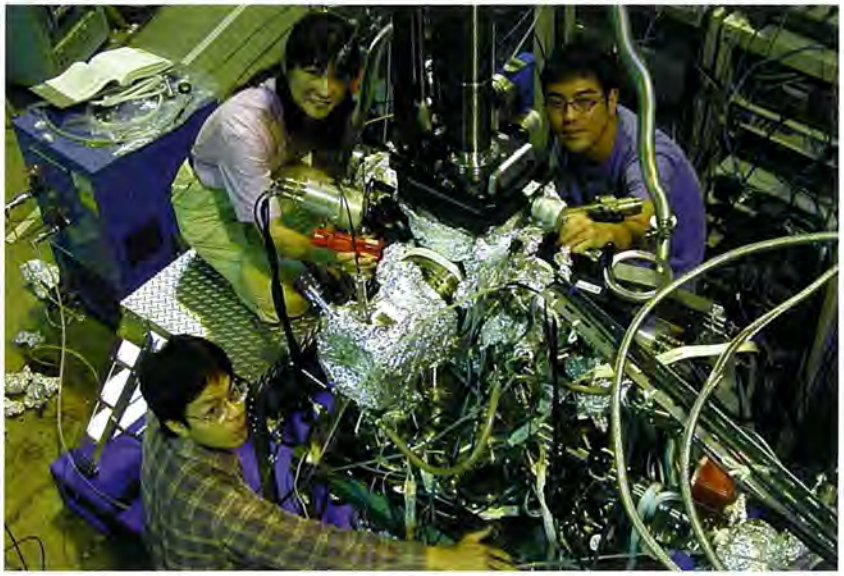

When we design a retarding-potential Mott polarimeter with high efficiency, we must know not only how the effective Sherman function and the scattering intensity depend on the target thickness and the scattering angle, but also the dependence of the effective Sherman function and the scattering intensity on the energy loss windows. The energy-loss window is the inelastic energy-loss that an electron can suffer and still reach to the electron detector. We have carried out Monte-Carlo calculations on the spin-dependent scattering process for 50 keV electrons incident on a gold target [3], and obtained the dependence of the effective Sherman function and the scattering intensity on the target thickness and inelastic energy-loss windows for various scattering angles. We have found that the scattering intensity takes its maximum at a scattering angle of about 120°, and when the inelastic energy-loss window is larger than 1200 eV the effective Sherman function is almost constant over a wide range of scattering angles. This enables us to design a Mott scattering spin detector while setting the electron detectors at a position of 120°; the larger is the collection angle for scattered electrons, the higher is the efficiency of the Mott polarimeter.

The new spin detector has been intended to be connected with a hemispherical electron energy analyzer to measure the spin- and angle-resolved photoemission spectra; also, the polarimeter consists of three parts of electron optics: a transport lens, a focus lens and retarding optics (Figure 1). The most crucial thing in designing a retarding-potential Mott polarimeter is the retarding optics for the scattered electron beam. Utilizing the electron optics-program, the

most reliable design of the retarding optics was determined. Schematics of the Mott polarimeter are shown in Fig. 2. We measured the scattering intensity of our polarimeter as a ratio of the incident electron intensity to the scattered electrons intensity counted by the detectors. The scattering intensities of different energy-loss windows at 20, 25 and 30 keV operating voltages are shown in Fig. 3(a), and the obtained efficiency of the polarimeter is shown in Fig. 3(c). A maximum efficiency of $(1.9 \pm 0.2) \times 10^{-4}$ was obtained for a 25 keV operating voltage and a 800 eV energy-loss window. The

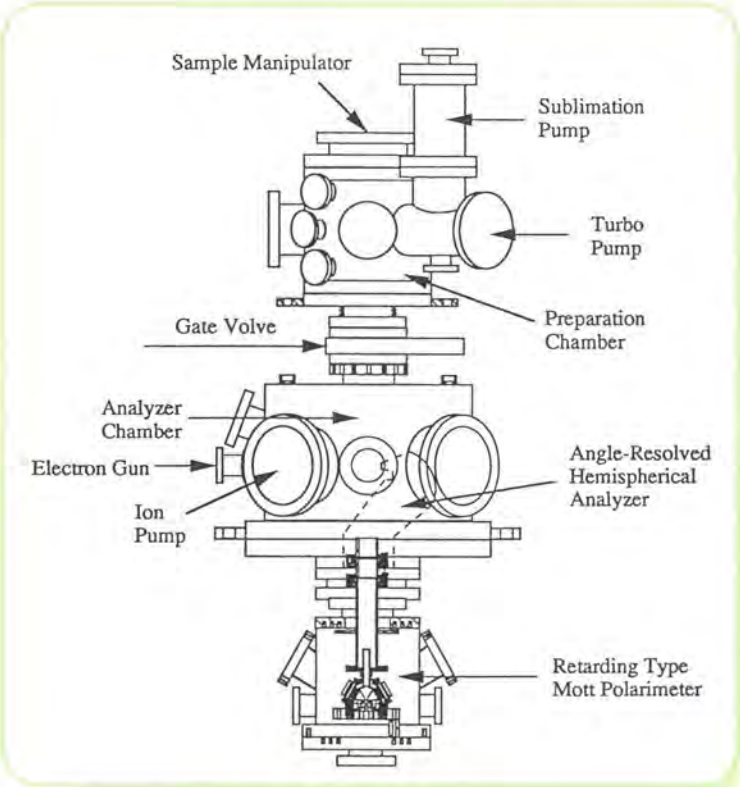

Figure 1.
Schematics of a new spin- and angle-resolved photoelectron spectrometer installed in BL19A. The new compact spin detector is connected to the hemispherical electron energy analyzer.

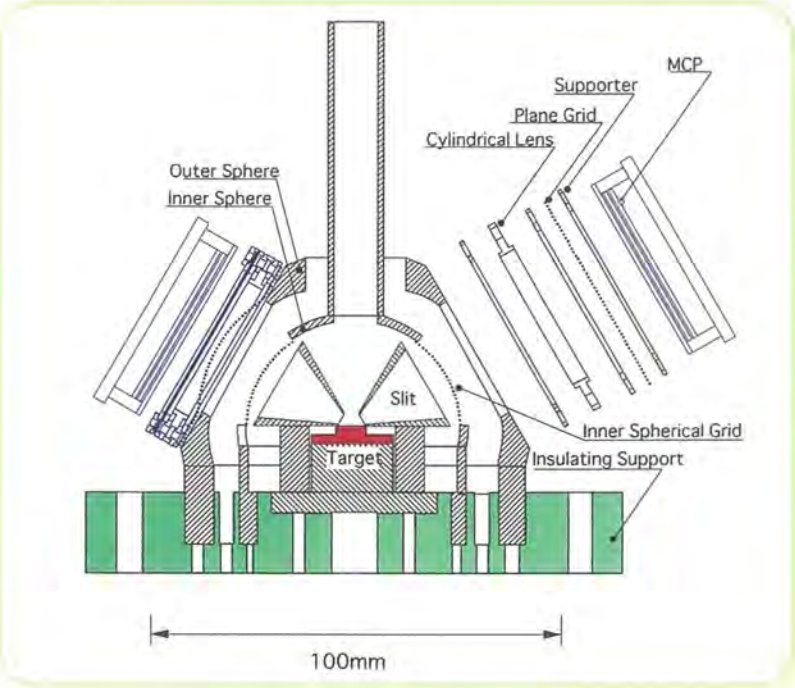

Figure 2.
Retarding electron optics of the new spin detector.

corresponding scattering intensity and the Sherman function are (9.7 ± 0.2) x 10^{-3} and 0.14 ± 0.01, respectively. Our result concerning the efficiency is slightly larger than the largest efficiency reported by using a thorium target. Since the atomic weight of thorium is greater than that of gold, by replacing the target from gold to thorium the effective Sherman function and the scattering intensity will increase by 10 - 20% and 15%, respectively. Hence, the efficiency of the new spin detector will increase to 2.9 x 10^{-4} by using a thorium target.

The new spin- and angle-resolved photoelectron spectrometer opened for general users in April 1998, and is used not only at BL 19A, but also at BL28A, utilizing undulator radiation with an elliptical polarization.

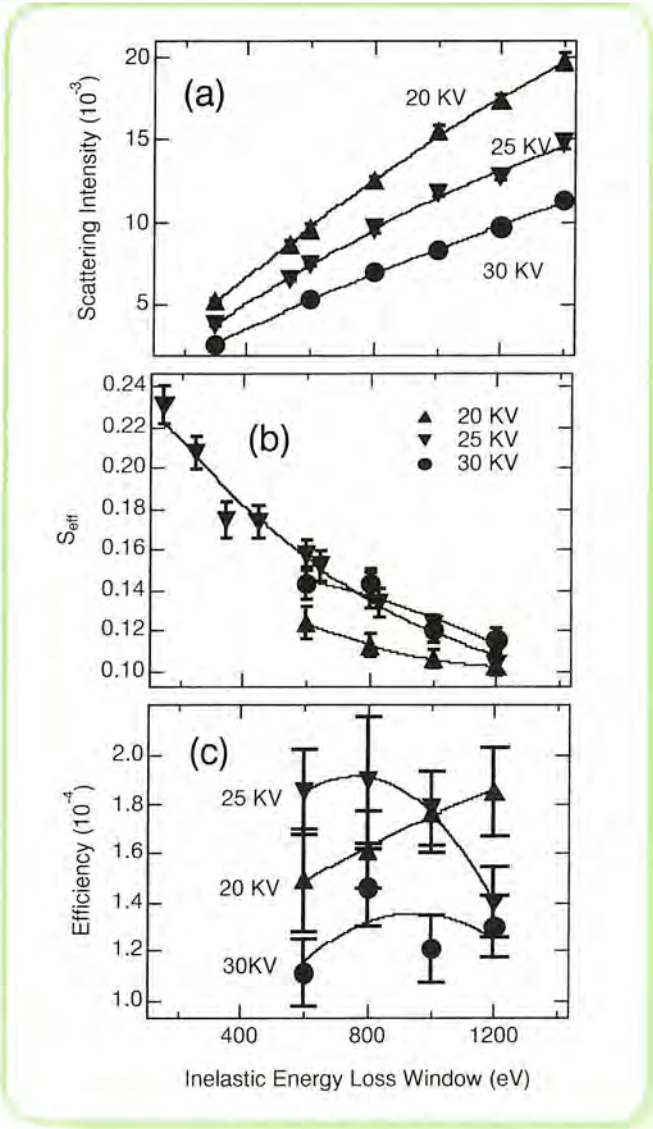

Figure 3.
Measured scattering intensities (a), effective Sherman function (b), and efficiency (c) of the Mott polarimeter for different energy-loss windows working at 20, 25 and 30 keV.

References

[1] T. J. Gay and F. B. Dunning, Rev. Sci. Instr. 63, 1635 (1992).

[2] S. Qiao, A. Kimura, A. Harasawa, M. Sawada, J. -G. Dhung and A. Kakizaki, Rev. Sci. Instr. 68, 4390 (1997).

[3] S. Qiao and A. Kakizaki, Rev. Sci. Instr. 68, 4390 (1997).

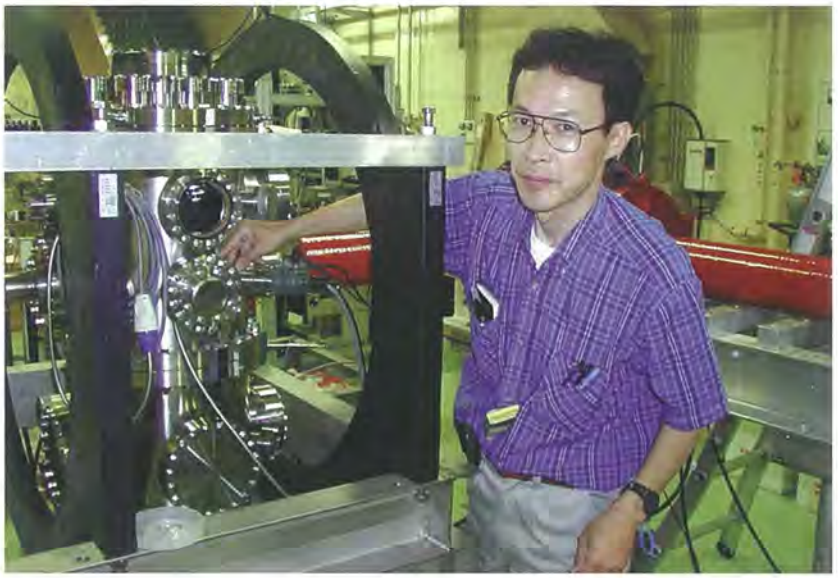

4

Slow Positron Facility

4 Slow Positron Facility

We relocated our slow-positron facility to the 1.5-GeV point of the KEKB J-linac. The slow-positron generator linac (TEST LINAC) will soon be put into commission. The new experimental hall is now in its construction period. Experiments such as 1) beam two-dimensional angular correlation of annihilation radiation (2D-ACAR) measurements, 2) beam time-of-flight (TOF) experiments and 3) positron microscope will be performed in this hall. A schematic view of the new experimental hall is shown in Fig. 1. Here we describe the new experimental method: a conventional positron-annihilation method with the newest slow-positron beam.

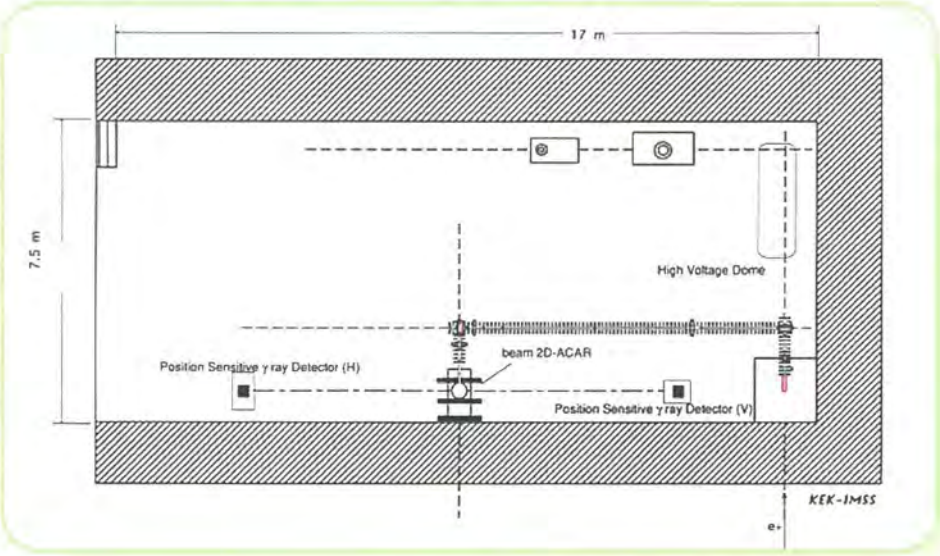

Figure 1.
Schematic view of the new experimental hall in the electron-positron linac building.

When positrons are injected into a solid, they come to rest very quickly. The momentum distribution of the electrons can be determined by observing the two annihilation γ-rays. The γ-rays emerge exactly 180 degrees apart in the frame of reference where the annihilating positron-electron pair is at rest. Since the electrons inside

the sample are moving, their moment must be carried away by the γ-rays in order to conserve the total momentum of the system. The result is that in the laboratory frame of reference the γ-rays actually emergy at an angle that deviates slightly from 180 degrees (Fig. 2). The mean angular deviation indicates the average moment of the electrons encountered by the positrons within the sample. The shape of the angular deviation, that is, the scatter of the angular values around the average deviation, reveals details of the electronic structure in the substance where the positrons are annihilated.

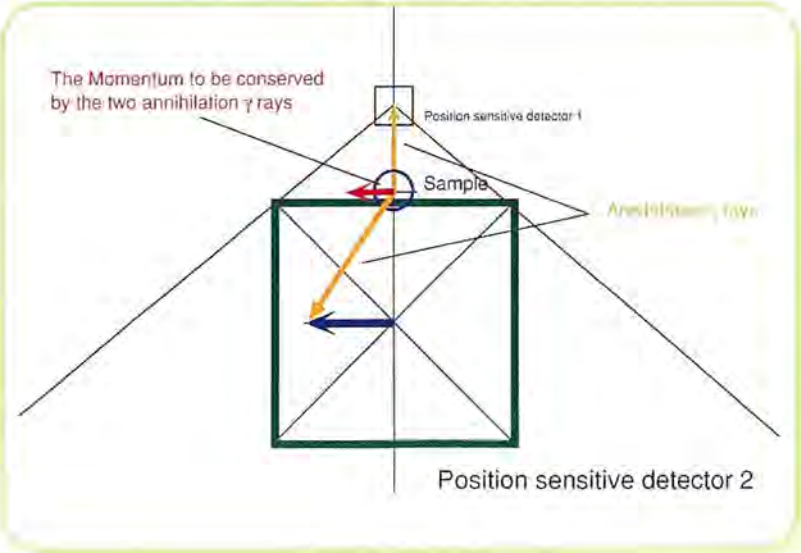

Figure 2.
Schematic of the two-dimensinal angular correlation of annihilation-radiation (2D-ACAR) measurements.

Two-dimensional angular correlation of annihilation radiation (2D-ACAR) measurements combined with the slow-positron beam technique provides us with useful information about the surface, defects near to be surface, the interface, positron and/or positronium diffusion in materials, and so on from the aspect of the momentum distribution. The essential parts in the 2D-ACAR apparatus are a pair of position-sensitive γ-ray detectors. The sizes of the small BGO crystals are 2.2 x 2.2 x 15 mm^3. The crystals of 25 x 21 pieces are arranged in 2.4 mm pitch and optically coupled to a position-sensitive photomultiplier tube (PS-PMT), a Hamamatsu R3941, which has a rectangular sensitive area of 60 mm x 55 mm. The position signals from the anodes are converted into voltage signals by preamplifiers in the photomultiplier bases, and are fed into a CAMAC 16-channel 12-bit analogue-to-digital converter (ADC) which is controlled by a personal computer (PC). The outputs from the reflecting plane (last) dinodes of the PS-PMTs, after being amplified by fast preamplifiers in the photomultiplier bases, and energy selected by the discriminators, are used to take coincidence between the two 511 keV γ-rays. The rise time of the outputs of the fast preamplifiers is ~ 30 ns. About 30 coincidence counts per second can be obtained with a momentum resolution of 1.2 x 10^{-3} mc if the 10^8 slow-positrons per second are available.

We have measured the time-of-flight (TOF) spectra of orthopositronium (o-Ps) emitted from SiO_2 surface [1], and demonstrated the surface sensitivity of positrons. The above mentioned 2D-ACAR equipment combined with positron beams will be a powerful tool to investigate surface electronic structures.

References

[1] Y. Nagashima, Y. Morinaka, T. Kurihara, Y. Nagai, T. Hyodo, T. Shidara, K. Nakahara: Origins of positronium emitted from SiO_2, Physical Review B 58, 12676-12679 (1998)

5

PF-AR Project

5 PF-AR Project

5-1 Experimental Facilities

In 1998, we constructed a new experimental hall (North-Experimental hall) for a time-resolved protein-crystallography beamline, as described in the previous Photon Factory Activity Reports. Briefly, the components of the front ends for the beamline; (fixed mask, heat absorber, beam shutter, graphite heat absorber and Be windows), are being designed and are to be prepared by the end of March, 2000.

In 1998, an operation peried for SR was carried out from April 9 to June 13. Several experiments, such as Compton scattering, development of a high-precision monochromator system using nuclear-resonant Bragg scattering, development for medical applications and X-ray diffraction under high-pressure environments were corried out. Although the operation was satisfactory for some experiments, the single-bunch purity was not satisfactory for the users of nuclear resonant Bragg scattering. The problem was caused by the following two reasons: first was the system itself for the single-bunch purifier; the other was the absence of a bunch-monitoring system. At a shut-down period, a new beamline, NE5B, the system for monitoring single-bunch purity and X-ray beam position were constructed in the North-East experimental hall. As shown in the next section, we satisfied the single-bunch purity, which was better than 10^{-6}, after these improvements.

5-2 Light Source

After recommissionig the PF-AR in March, 1998, routine operation for SR users was carried out from April 9 to June 13. In

order to ensure construction of the beam-transport line for the KEK B Factory, injection of the beam into the ring could not be performed during the time zone from 9:00 to 21:00 on weekdays. Since the PF-AR was left as it was for more than one year, we encountered several problems, especially in the vacuum system. A problem involving single-bunch operation was also serious. Although the PF-AR is planned to be a single-bunch machine, the single-bunch purity was not satisfactory for users during this period.

After shutdown of the ring, several improvements were carried out. Concrete walls and a ceiling for radiation shielding were constructed in the North experimental hall in order to ensure a higher stored beam current. The shielding between the South experimental hall and the ring tunnel was also reinforced. A new single-bunch purifier, a selective RFKO system, was tested in the 2.5-GeV PF ring and installed in the PF-AR; also a new beamline for purity measurements was constructed. The purity of a single bunch with the new system was better than 10^{-6}. Superannuated components of the vacuum system were repaired and reinforced during the shutdown period.

As described in previous Photon Factory Activity Reports, we have a plan to reconstruct the present ring, which was originally designed as a booster of TRISTAN, in order to make it suitable as a dedicated X-ray source. As improvement of the vacuum system during the FY1999 has been approved, and a task force to refine the design as well as the schedule of the project has been organized. The main parameters and the lattice of the proposed ring are given in Table 1 and Figure 1.

The authors would like to express their appreciation to members of the Accelerator Laboratory, who have been supporting us to maintain the over-age machine and to revive it.

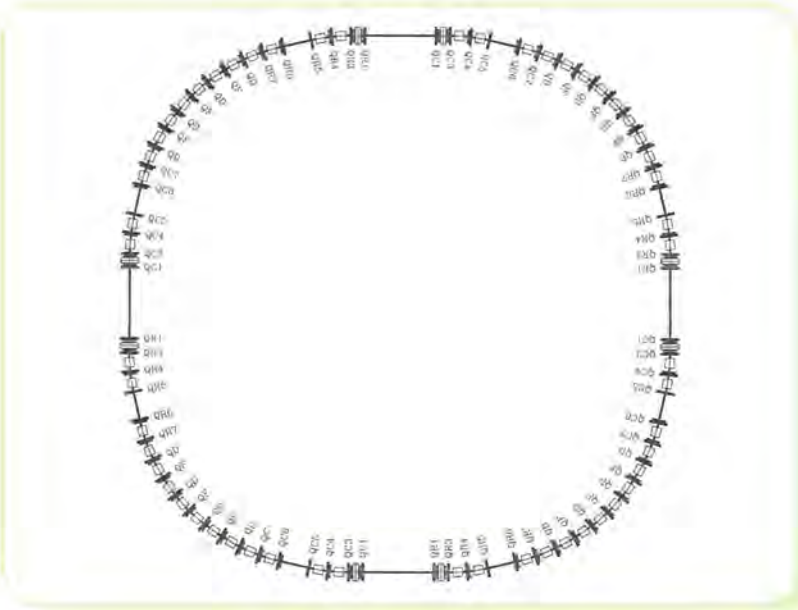

Figure 1.
Lattice of the PF-AR

Table 1 .

Main parameters of the proposed PF-AR.

		NEW OPTICS
Maximum Energy	E[GeV]	6.0
Lattice Type		FODO
Betatron Phase Advance	H/V [deg]	140/60
Superperiodicity	Ns	4
Bending Radius	ρ[m]	17.825
Bending Strength	B[T]	1.122
Circumference	C[m]	377.26
Energy Loss per Turn	U0[MeV]	6.432
Natural Emittance	ε0[nmrad]	162.9
Natural Energy Spread	σε	0.00108
Momentum Compaction	α	0.00702
Betatron Tune	νx/νy	12.45/6.30
Radiation Damping Time	τx/τy/τz[msec]	2.35/2.35/1.18
Revolution Frequency	frev [MHz]	0.794657
RF Voltage	VRF[MV]	15
RF Frequency	frf [MHz]	508.58
Harmonic Number	h	640
Synchrotron Tune	νs	0.0423
Bunch Length	σz[mm]	12.11
RF Bucket Height	(Δp/p)RF	0.0122

ACCELERATORS OPERATIONS, RESEARCH AND DEVELOPMENTS

You can jump to the article by clicking its title.

ACCELERATORS OPERATIONS, RESEARCH AND DEVELOPMENTS

1

PF Storage Ring

1 PF Storage Ring

1-1 Operations

1-1-1 Summary of the Operations

The PF electron storage ring was operated satisfactory without any serious problem according to the operation schedule through the 1998 fiscal year. On May 13 1998, we started high-brilliance operation for user runs with an emittance of 37 nm-rad. The beam lifetime increased according to the improvement of the vacuum pressure, and

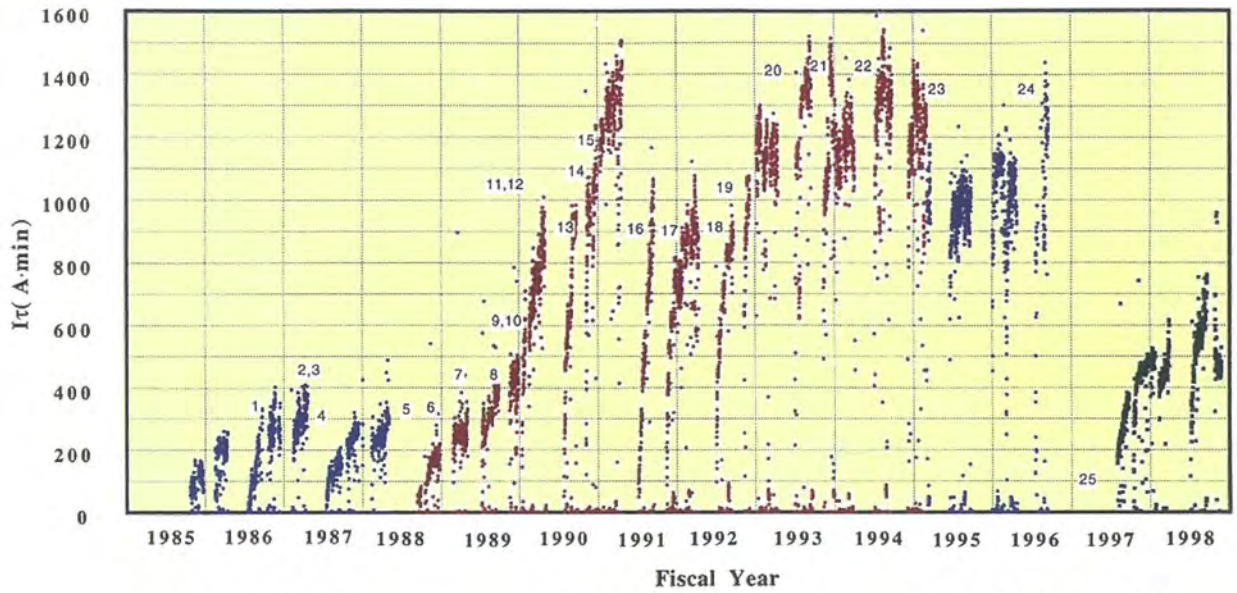

1. Vent for reduching beam emittance
   Rearramge magnet system
2. Operation with reduced emittance
3. MPW16
4. Vent for positron injection
   Renovation of the rf-cavity for reducing beam instabilities
5. Vent for insertron devices MPW13 and EMPW28
   Positron operation
6. MPW13
7. EMPW28
8. New VW14
9. New U2
10. Themal insulation
11. Low β operation
12. Single bunch run 3Gev test run
13. Vent for isolation valves, RFQ
14. New tunes
15. VW14 chamber
16. B01 chamber, Isolation valves with rf-shield
17. Water leak(absorber for VWradiation)
18. Optical klystron, Feedback system
19. B04-05 feedback cavity
20. B21 Mirror, B04-05 scraper
21. B01 crotch absorber
22. B10,11,12 crotch absorber BL6, 11 renewal
23. Electron operation
24. Damped cavity(North)
25. Improvement for low emittance

Fig. 1 Plot of I・τ

we changed beam injection from three times to two per day in an autumn run. The product of beam current and beam lifetime, $I\tau$ reached 750 A-min. in December, 1998.

We found that the beam profile was slightly twisted due to XY-coupling; a user group also pointed out that an expected vertical emittance was not obtained. We corrected the beam twist in January,1999, and the vertical beam size was reduced as expected. However this shortened the beam lifetime, $I\tau$ to about 500 A-min. The $I\tau$ trend is shown in Fig.1. In January and February runs of 1999 we experienced much trouble with the beam-injection efficiency because of a lack of reproducibility of the injecting conditions of the Injector Linac.

A new single-bunch purification scheme was tested for single-bunch operation in the high-brilliance mode and was successfully adopted in a user run. For 3.0-GeV operation, we studied the acceleration and deceleration in the high-brilliance mode. New operating conditions were used in user runs.

The control system was replaced in March, 1999. The new system comprised workstations and networks with a data-channel. It works well, and we can thus access the data-channel and use many kinds of operation data with a time stamp very easily.

The operation statistics are shown in Table 1. The total operation time was over 4464 hours and the scheduled user time for experiments was about 3560 hours. This means that the scheduled user time increased by more about 1000 hours during this fiscal year

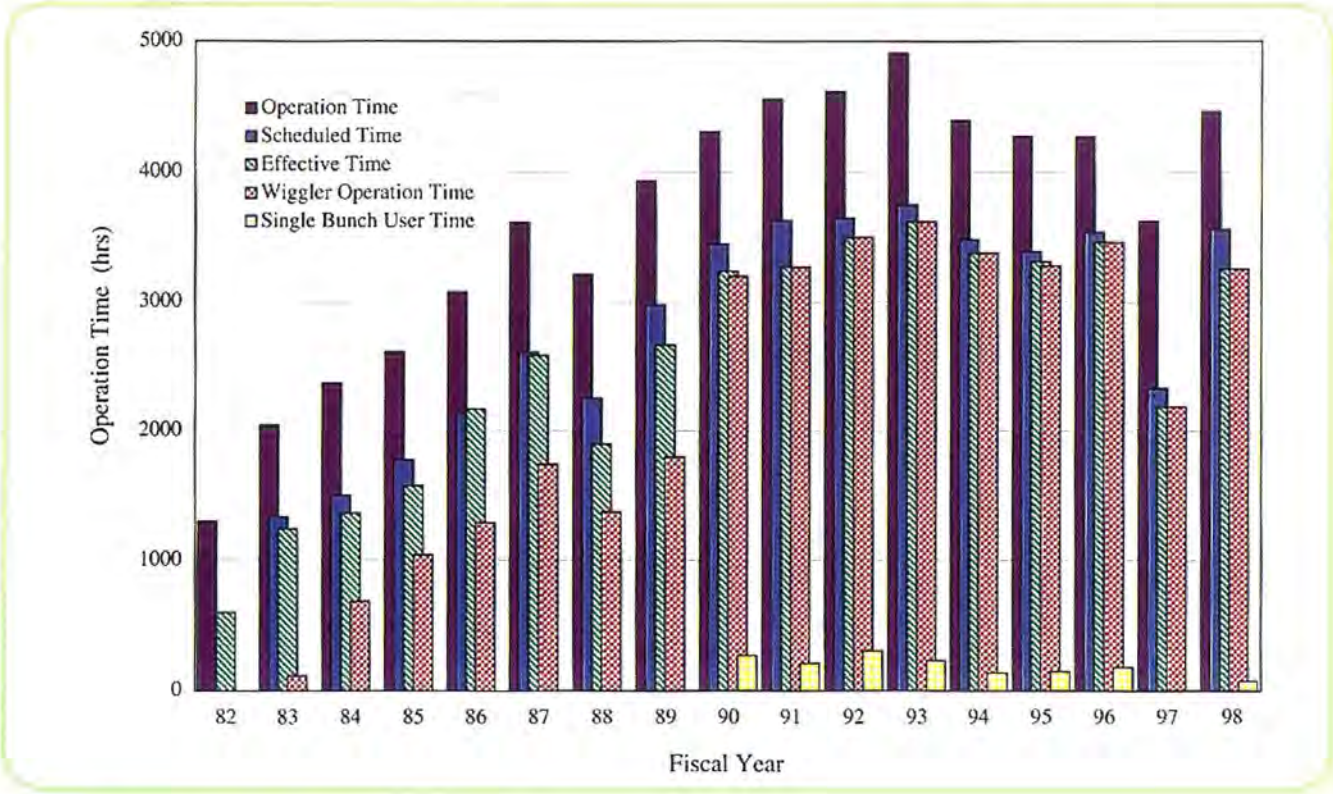

Figure 2. Operation times of the storage ring

compared to 1997 (Fig. 2). The net user time was 3254 hours. Most of the operation mode was the multi-bunch mode at 2.5 GeV with a superconducting vertical wiggler; additionally a 3.0-GeV single-bunch mode was adopted. The interval between injections was 11.7 hours for multi-bunch operation and 7 hours for single-bunch operation. The integrated beam current in the net user time was 1007 A-h, and the average beam current was 314.6 mA (Fig. 3). The failure time was about 1.2% of the total operation time (Fig. 4). The statistics show successful operations in the PF.

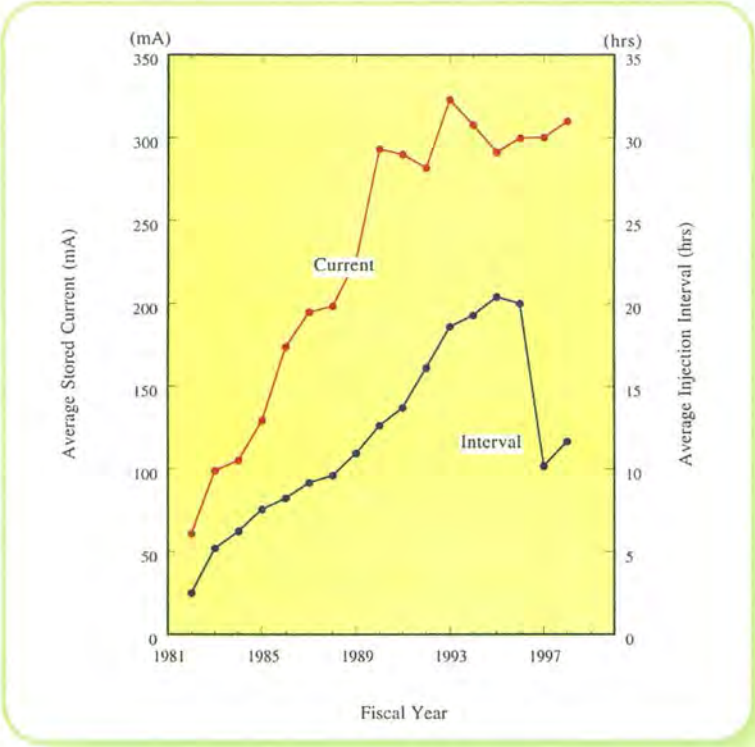

Figure 3.
Average stored currents and injection intervals.

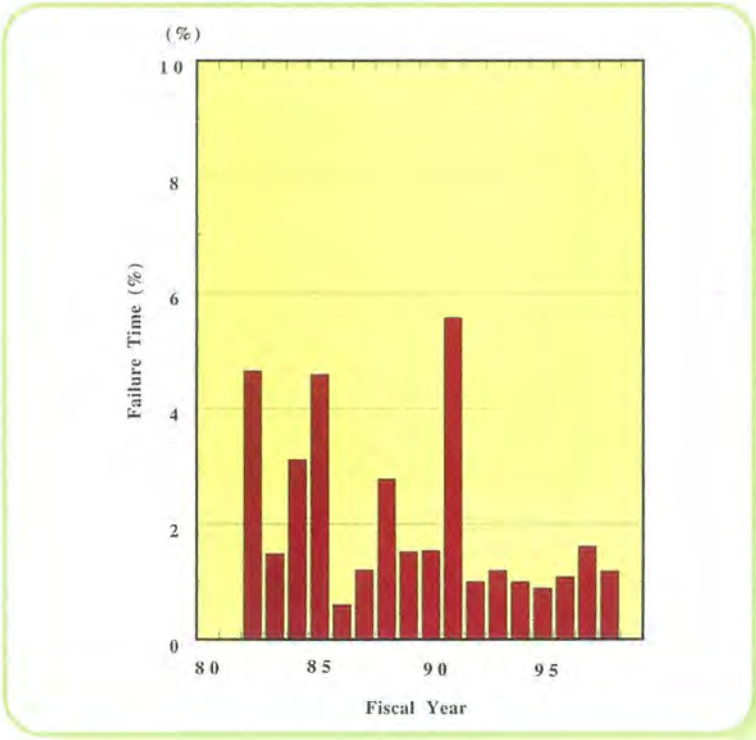

Figure 4.
Rate of failure time of the storage ring operation

Table 1 Statistics of the storage ring operation during fisical year 1997 (from Apr. 1997 to Mar. 1998)

	Multi-bunch	Single-bunch	Total
Ring Operation time (hours)	—	—	3624.0
Scheduled user time (hours)	2328.0	—	2328.0
Net user time T (hours)	2187.0	—	2187.0
Time used for injection (hours)	94.0	—	94.0
Integrated current in T (A・hours)	626.0	—	626.0
Average current in T (mA)	300.1	—	—
Number of injections	215	—	215
Interval between injections (hours)	10.2	—	—

1-1-2 Coupling Correction

The XY coupling and the vertical dispersion were corrected so as to reduce the vertical beam size and divergence by the following method developed at NSLS [1]. Additional windings on 14 sextupole magnets were utilized to produce skew quadrupole fields for the correction. The field strength of each sextupole was determined so as

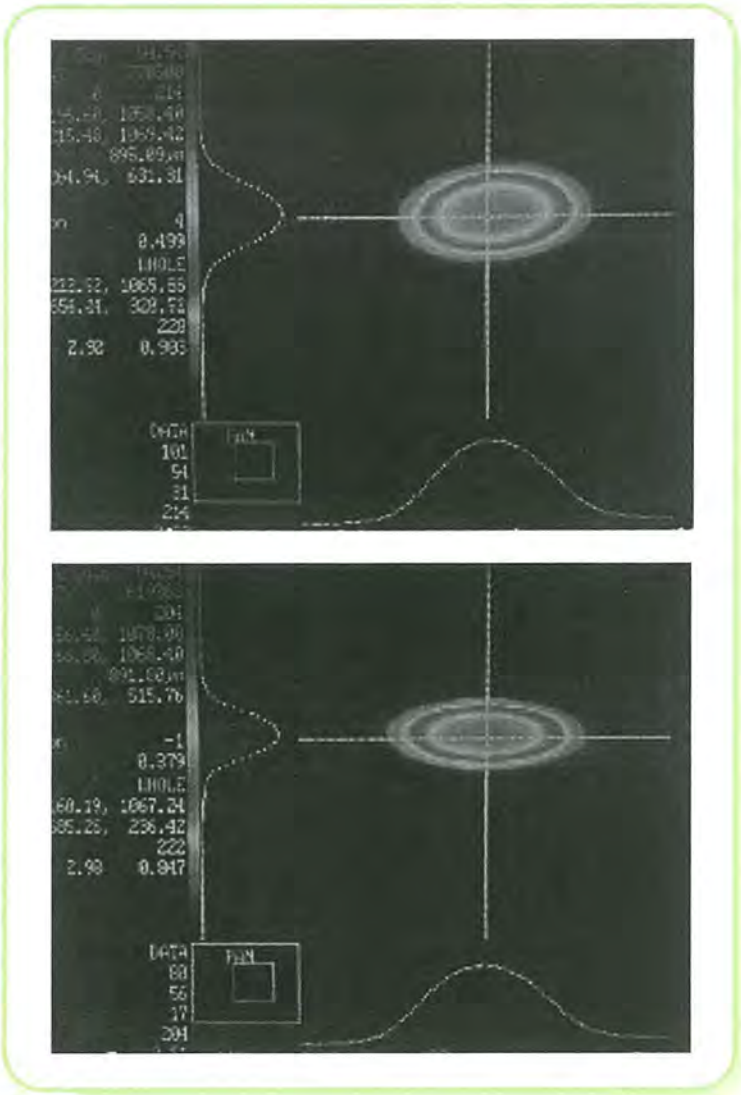

Figure 5.
Pictures of the beam profile measured at BL27 are shown. The top one is the profile before a coupling correction and the bottom after a correction.

to minimize the vertical displacements of the orbit produced by horizontal kicks of each horizontal steerer and the vertical dispersion. Reduction of the Touschek lifetime was observed, which suggested a reduction of the vertical beam size by a factor of 0.6-0.7. This was consistent with a direct measurement of the beam profile at BL27, shown in Fig. 5. In January, 1999, user runs with improved XY coupling were started. Improvements in user experiments are described elsewhere in this report.

References

[1] J. Safranek and S. Krinsky, AIP Conf. Proc. Vol. 315 (1994)

1-1-3 3.0-GeV Operation

Since last October, we have tried to accelerate beams up to 3.0 GeV in high-brilliant optics (ε_x = 50 nmrad) to supply much harder x-rays. Although we experienced 3.0 GeV operation before the high-brilliant project, the control system of the magnets was renewed and became more complex. Moreover, the operating point of the betatron tunes was different from the previous one. Thus, we needed to search a new tracking pattern of the acceleration and deceleration between 2.5 and 3.0 GeV around the new operating point of the high-brilliant optics. Using a real-time tune measurement system we found a tracking pattern which enabled us to avoid beam loss by dangerous resonance during acceleration and deceleration more easily. Figure 6 shows the measured betatron tunes of the tracking pattern on the tune

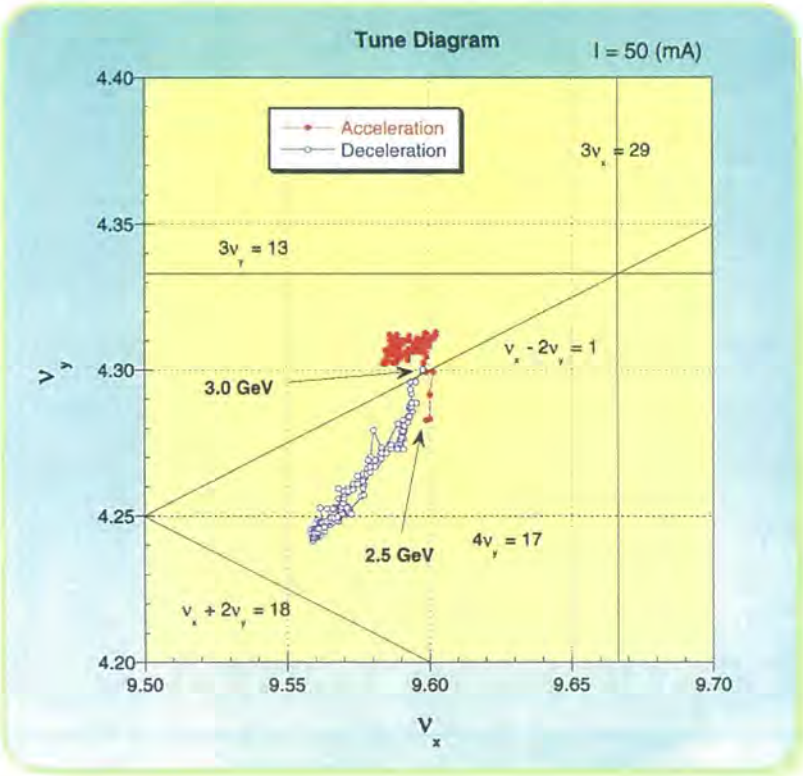

Figure 6.
Measured betatron tunes during acceleration and deceleration between 2.5 and 3.0 GeV are displayed on the tune diagram. The red closed circles are for acceleration and the blue open circles are for deceleration. The solid lines show the resonances.

diagram at a stored current of 50 mA. The strong resonances which cause the beam loss were the third resonances of $\nu_x + 2\nu_y = 18$, $3\nu_x = 29$ and $3\nu_y = 13$. We could maintain the betatron tunes inside a triangle of the strong resonances. We then succeeded to accelerate a stored beam of 200 mA in a multi-bunch mode and 70 mA in a single-bunch mode, respectively. The optical functions and beam orbit at 3.0 GeV were almost the same as those at 2.5 GeV. The lifetime was more than 60 hours at a current of 200 mA in the multi-bunch mode. As a result, 3.0 GeV user runs were smoothly performed for about one week last December.

1-1-4 Renewal of Control System

1-1-4-1 General Description

A renewal of the PF ring control system has been completed. The replacement was gradually performed for about one and half years while keeping the storage ring in operation. At first, the new control system of the magnet power supplies was commissioned in October, 1997, just in time for operation with the new low emittance optics. The new system for the RF control started operation in January, 1999. The details will be described in the next subsection. Then, replacements of several remaining systems were completed and the mini-computers of old system were entirely removed in March, 1999. Figure 7 shows an overview of the new control system. There was a need to update the control system so as to match recent computer technologies. As a guiding principle of renewal, we decided to inherit the hardware and

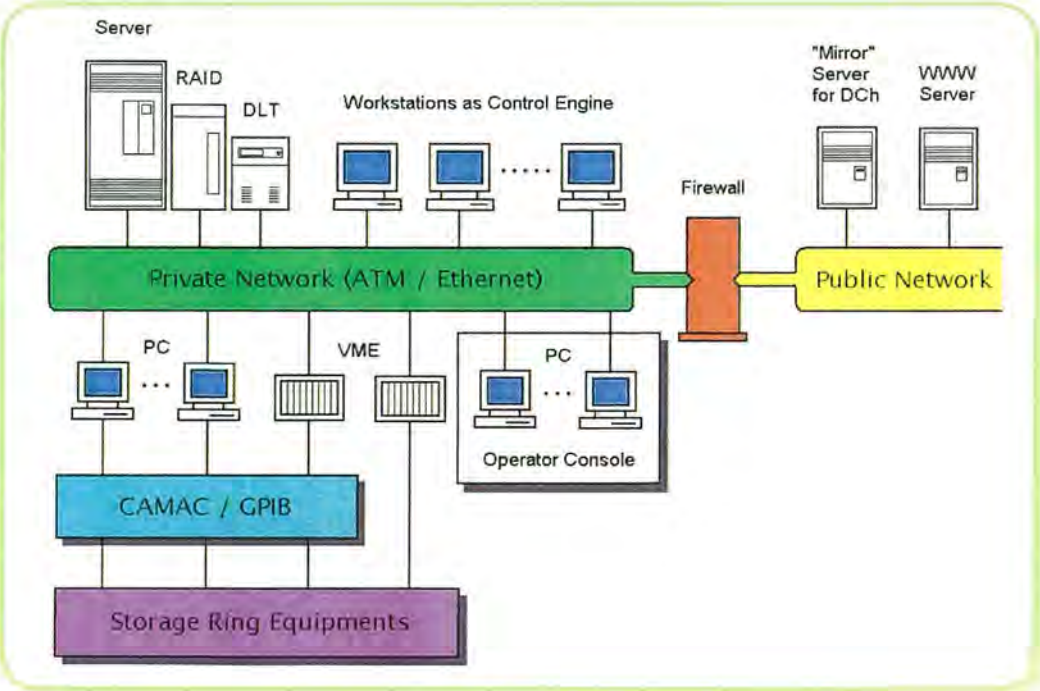

Figure 7. Overview of the new control system.

software properties from the old system as much as possible. For example, CAMAC interfaces, which were used on a large scale mainly in the RF and the magnet power supply system, were left unchanged. Also, the CAMAC server systems were newly developed using a PC (or VME) which serves network-wide access request for the CAMAC system. Service routines for the devices, such as CAMAC or GPIB, were developed while maintaining compatibilities with those of the old system. Thus, the software plugs to those devices were entirely unchanged, which was very helpful to convert programs of old system to those of the new one.

One of the key elements of the new system is a network. We constructed a private network system, which was dedicated to the control system and was separated from a public network by a firewall. A dedicated network was required to supply enough traffic capacity and to protect the control system from illegal access, which may cause serious damage to operation of the ring. The backbone of the network is an ATM (155Mbps). Twelve switching hubs, each having twelve 10BASE-T ports, are connected to an ATM switch. About 90 hosts are connected to the network at the moment.

For recent control systems, it becomes very important to realize an easy and effective communication method between the host computers widely distributed on a network. A Data channel server system (DCh) was developed as such a communication system [1]. The DCh is a kind of bulletin board with many labeled entries, each of which keeps single or dimensioned data. Application programs can access the DCh as if it were shared memories extended over a network by using few simple service routines, never minding troublesome affairs on a network. Although the DCh has no synchronization mechanism in reading or writing data, its function is sufficient in almost all control scenes. Usually about a hundred client processes maintain connection with the DCh.

One of goals of the new control system is to provide excellent HMI for operator consoles, introducing recent fruits on a GUI. New operator consoles were prepared based on an ordinary multi-window system with a screen and a mouse. Though console equipments are very different from those of the old system, a simple and easy method to handle HMIÅfs was developed [2]. Control screens are developed on a PC (or a workstation) using GUI tools independently of control processes, themselves. Mediator processes were prepared on a console PC to mediate between console processes and control processes. Thus, application programs for controls can communicate with control screens through the network, only by using several simple service routines.

References

[1] Photon Factory Activity Report#14, p.A-12, 1996
[2] Photon Factory Activity Report#15 part A, p.141, 1997

1-1-4-2 RF control system

Equipment of a RF system had been controlled by using an old minicomputer (S3500 from Fujitsu Ltd.) through CAMAC and GPIB interfaces. Incorporating modern computer technology, this system was renewed during 1998. The new control system is outlined in Fig. 8. The old software for RF control was converted into several software programs, which fit for a new workstation. Eleven such processes run

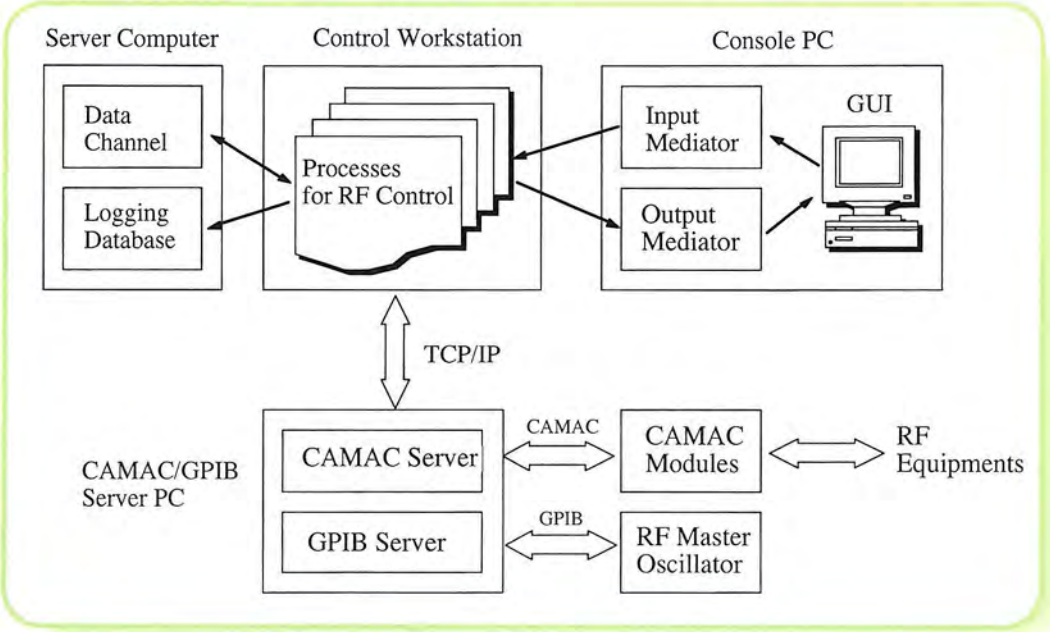

Figure 8. Configuration of the new RF control system.

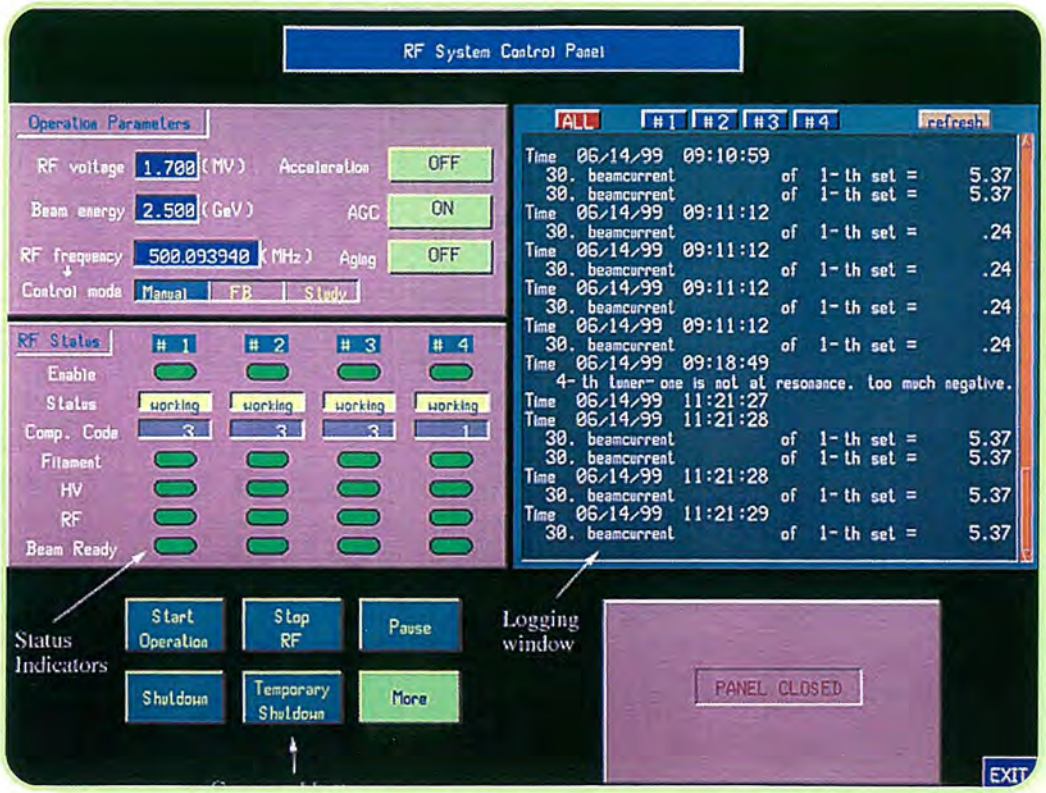

Figure 9. Typical console screen for operating the RF system.

on the control workstation. User-friendly Graphical User Interface (GUI) was prepared on a Personal Computer (PC), which serves storage-ring operators as a console. A typical console screen is shown in Fig. 9. The RF control processes can access this GUI easily by using a few console service routines. These processes also communicate to a CAMAC/GPIB server, which is connected to all of the RF equipments though CAMAC or GPIB interfaces.

A corresponding main control process, named 'rfmain' controls each of four RF stations. Using these processes, one can start up, operate and shut down all equipment. There are seven miscellaneous processes, which take charge of logging and displaying parameters, controlling the RF frequency and others. All logged parameters are written to the Data Channel (DCh) and other computers can refer them. In addition, diagnostic messages from the control processes are saved in the PF ring database system, which is very helpful to diagnose the system in the case of any problems. Most of the RF control software was written in FORTRAN, which amounts for about 15000 lines in the source code.

The new RF control system was commissioned in January, 1999, and has operated very well. Operation of the RF system has become very convenient and friendly.

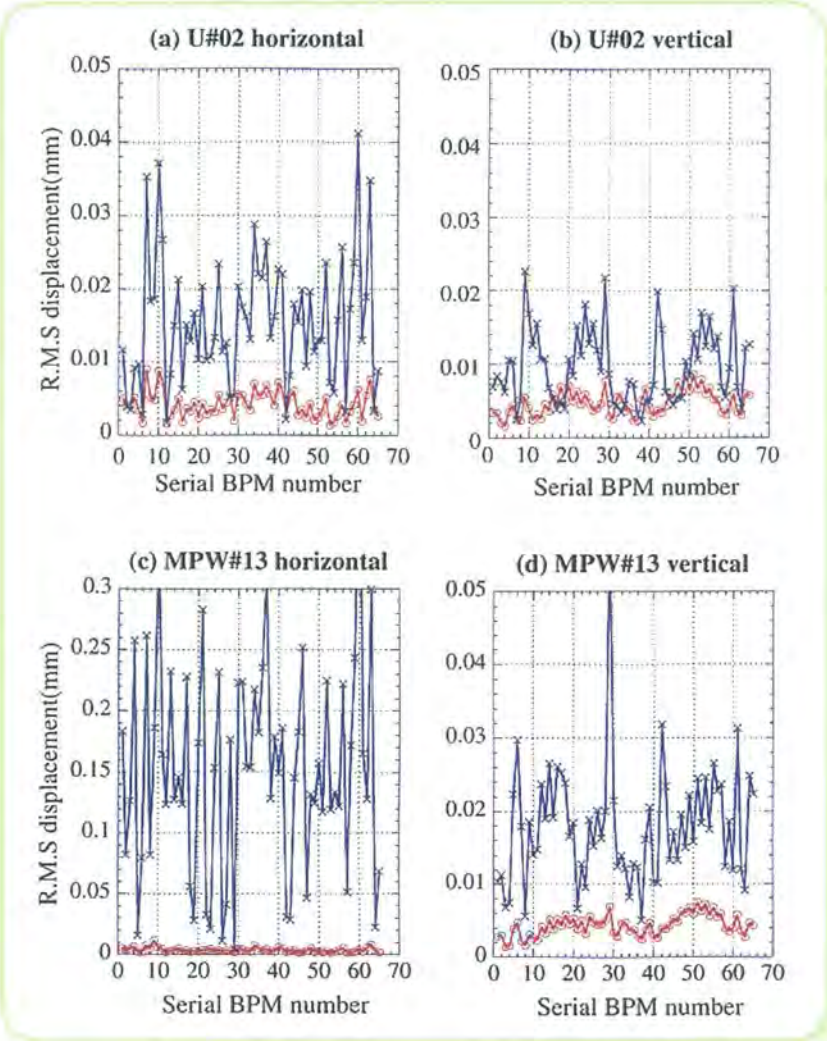

Figure 10.
Results of a COD correction for the IDs. (circles: correction ON, crosses: correction OFF)

1-1-4-3 Insertion Device Control system

Renewals of the control system for the insertion devices are performed one after another. This system was first developed in MPW#13 and its operation was started in February, 1998 [1,2]. Same control system was applied and utilized for the U#02 and the EMPW#28 during this summer shutdown. Renewals for the remaining two insertion devices (MPW#16 and Revolver #19) are underway.

For independent tuning of the insertion devices, the corrective current data for the present closed orbit with an emittance of 36 nm-rad was adjusted using a BPM system for both the vertical and horizontal directions. Figure 10 shows typical results of the COD correction during a change in the gap. The examples are for the case of the U#02 and MPW#13. The horizontal and vertical r.m.s. displacements at the BPMs are plotted during a change from the minimum gap to the maximum gap. The displacement after the correction was reduced to less than 10?m all around the ring in both directions. The results are the same in the cases of the other IDs. The reliability of the corrective data was checked using four Photon-BPMs located in beam lines BL04, 06, 12 and 21. A confirmation of the corrective data using the Photon-BPMs is always performed after a long shutdown of the PF ring.

References

[1] Photon Factory Activity Report #14, p.A-12, 1996
[2] Photon Factory Activity Report #15-A, p.140, 1997

1-2 Developments and Machine Studies

1-2-1 New Method of Single-Bunch Purification

Recently, the desire for single-bunch operation has been increasing and the restriction of the impurity, that is the rate of electrons in undesirable buckets to those in the main bunch, becomes more severe. A purification method making use of the current dependence of the betatron tune (-2×10^{-4}/mA) has been applied up to present. Namely, a RF knockout (RFKO) tuned to the betatron frequency of the weak bunches can destroy any undesirable bunches with small currents, though the main bunch with a larger current survives because its tune is slightly different. However, it requires a mastery skill to keep an impurity level better than 1×10^{-5}. Moreover, the transversal motion of the main bunch excited by the method could affect experiments of SR users. In order to overcome the situation and to improve the impurity, a new single-bunch purification method, that is essentially a "selective RFKO" , has been developed. A schematic

description of the selective RFKO is shown in Fig. 11. The RFKO signal is modulated by a rectangular pulse train with repetition of the beamÅfs revolution frequency. Since the pulse train has gaps with a width equal to the bunch spacing (~2 ns), only a selected bunch passing through the RFKO kicker on the gap timing can survive.

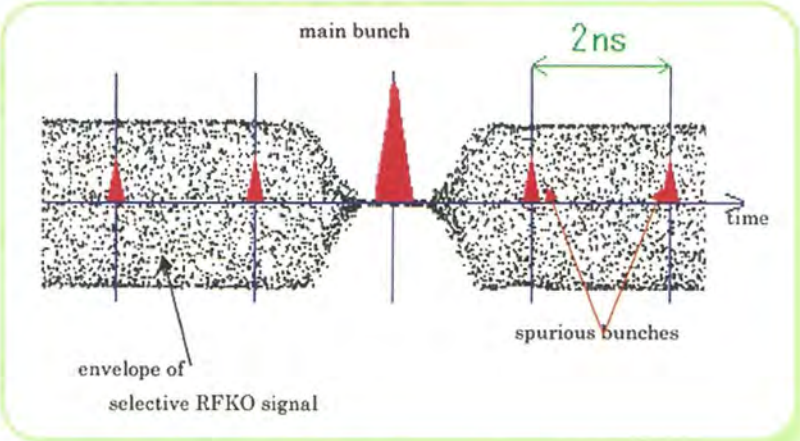

Figure 11.
Selective RF knockout method

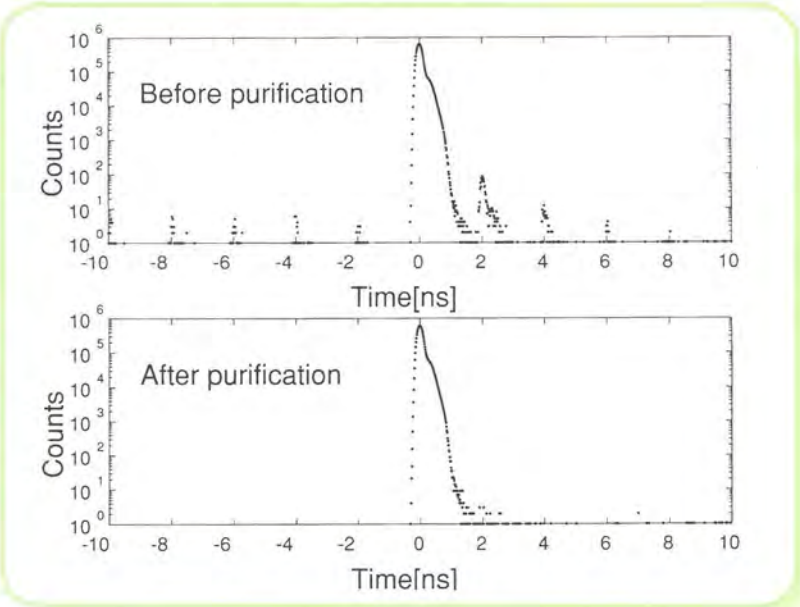

Figure 12.
Bunch population before (top) and after (bottom) purification.

Figure 12 shows the bunch population measured with the photon counting method. Several spurious bunches are recognizable in every 2 ns before the purification (top). It is clearly seen that the spurious bunches are removed with the purification procedure (bottom). The measured impurity of the 1st bunch was 8.3×10^{-5} and 5.6×10^{-7} before and after the purification, respectively. An impurity better than 1×10^{-6} was kept during user runs. The system works reliably as an indispensable tool for single-bunch operation in the PF.

1-2-2 Measurement of the beam emittances via SR interferometer

The beam emittances were estimated through beam-size measurements using the SR interferometer. Figures 13 and 14 show the absolute values of the complex degree of spatial coherence measured with wavelengths of λ=633 and 500 nm and best-fit results calculated under the assumption of a Gaussian distribution for the beam profile. From the fitting, the horizontal and vertical beam sizes

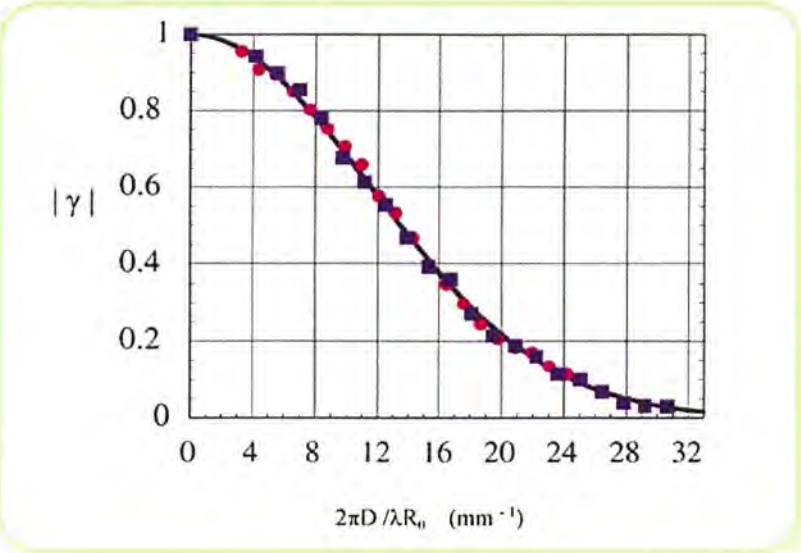

Figure 13.
Absolute value of the complex degree of spatial coherence for the vertical direction. The round and triangular spots denote the spatial coherence measured with λ=633 and 500 nm, respectively. The solid-line indicates the best-fit result under the assumption of a Gaussian distribution for the beam profile.

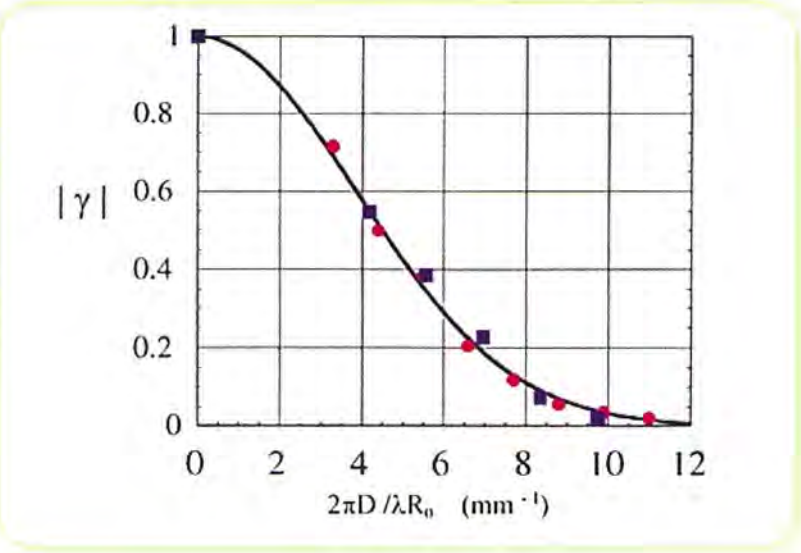

Figure 14.
Same as the Fig. 14, but the data were taken for the horizontal direction.

were evaluated to be 261.2 ± 2.6 and 87.3 ± 0.4 μm, respectively. The emittances are calculated using the measured beam sizes and the optical functions. As a result, the horizontal emittance was 29.5 nmrad, and the vertical one was 0.378 nmrad. Since the natural emittance for the optics at the measurement is designed to be 30 nmrad, the horizontal beam emittance has already reached the design value. The XY coupling obtained from the ratio between the horizontal and vertical emittance was calculated to be 1.28%.

1-2-3 Control System for the Insertion Device Beam lines

There are twenty-three synchrotron-radiation beam lines installed around the storage ring. The pressures in the storage ring and the beam lines are maintained at a UHV (Ultra-High Vacuum) of less than 10-8 Pa. A fast-closing valve system (FCV) in the beam line protects the UHV of the storage ring against an instantaneous vacuum failure by closing a guillotine blade (1.2-mm thick titanium-alloy) within ~0.01 seconds. There have been several vacuum failures at normal bending-magnet beam lines, which have been protected by FCVs.

Among twenty-three beam lines, there are five high-power ones (BL-2, BL-13, BL-16, BL-19 and BL-28) that have insertion devices (wiggler or undulator). The insertion devices can produce intense synchrotron radiation with a high power density, two orders of magnitude higher than that obtained with a bending-magnet source.

A thermal transient analysis was made for the FCV blades using a finite-element method (FEM). The calculated transient temperatures at the blades of the FCVs as a function of time show that the temperature exceeds the melting point within 100 ms at any high-power beam lines before the absorber closes at a normal beam current of 500 mA. Thus, the function of the FCV at all wiggler/undulator beam lines is ineffective. However, there has been no such protection system that allows five beam lines with high-power wigglers/undulators to protect UHV of the synchrotron radiation source. Thus, a UHV protection system has been developed and extended to each insertion-device beam line in each fiscal year.

Figure 15 shows a schematic diagram of the vacuum protection system. Each beam line is connected to four RF stations using optical transceivers and receivers. The beam line has an FCV controller, and two pairs of optical transmitters/receivers. The beam line is controlled by the Beam Line Control System. The Beam Line Control System is a distributed computer-controlled system that controls the backup valves, shutters and radiation safety interlocks. The FCV controller has a vacuum detector attached downstream of the beam line. The distance between the detector and the controller is approximately forty meters. There are also four RF stations, each of which comprises a

single-cell cavity and a klystron (500 MHz, 180 kW max) driven by a 10 W-power amplifier. The RF station has a PIN-diode RF switch and RF pickup antennas in each cavity at the RF stations. Using high-speed optical communication links, the high-power beam lines and the four RF stations constantly exchange these signals. Upon detecting a vacuum failure the FCV controller requests the RF stations to turn off the RF power in the klystrons, and simultaneously requests the Beam Line Control System to immediately close the backup vacuum valves as well as the absorber. At the station, the RF switch cuts off the RF output signal of the low-power amplifier. As a result, the RF power in each cavity can be dumped. Output RF signals of pickup antennas measuring the RF power in the cavities are used to allow the FCV controller, that is demanding the RF system to cut off the RF power, so to close its blade.

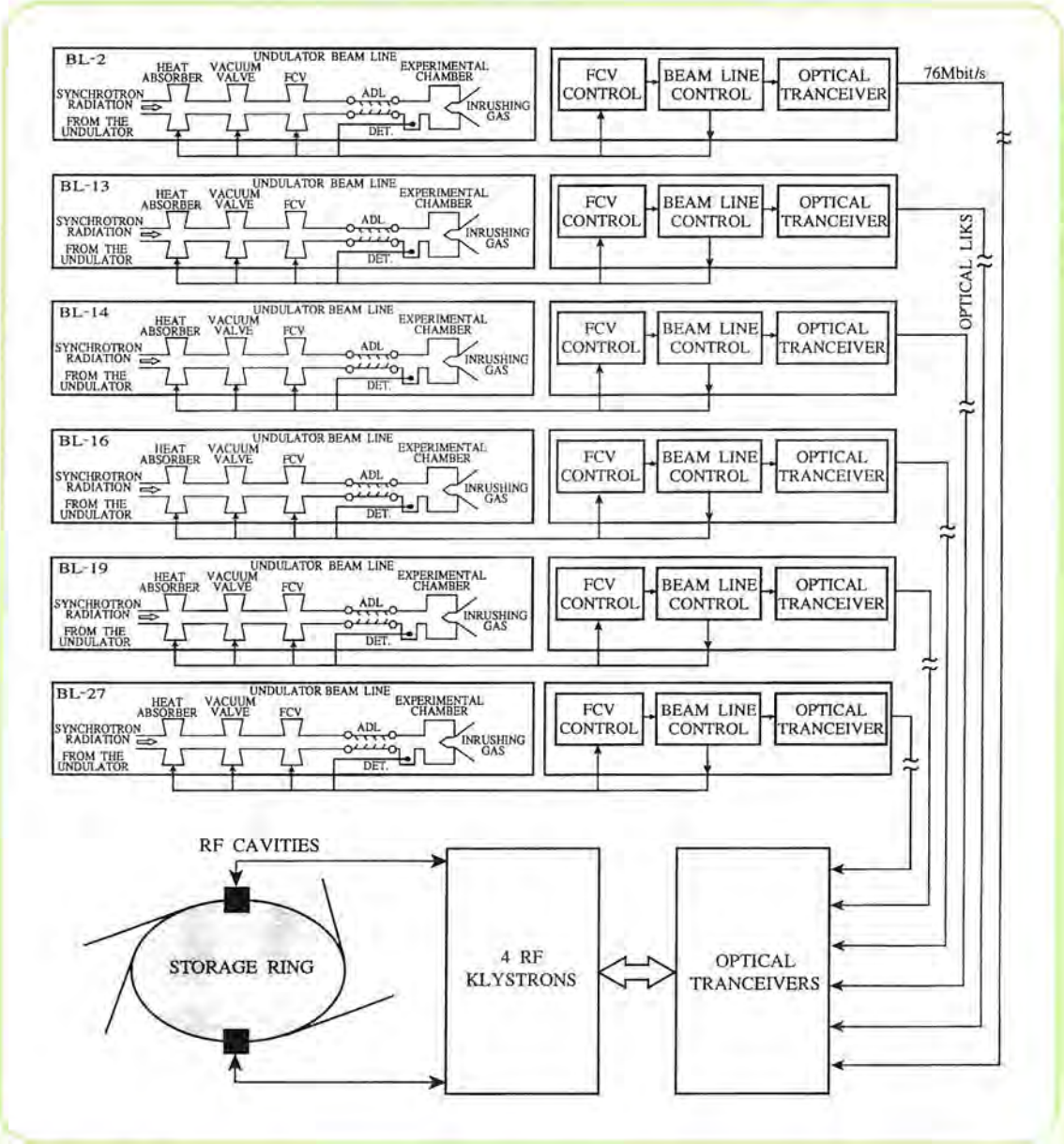

Figure 15.
Schematic diagram of the vacuum-protection system for the wiggler/undulator beam lines.

Figure 16 shows an actual accidental vacuum failure that occurred downstream of the high-power wiggler beam line BL-19 in the experimental hall. The protection system successfully protected the UHV of the storage ring and upstream of the beam line by closing the FCV after dumping the positron beam. The pressure downstream of the beam line at the experimental hall almost reached atmosphere, causing those ion pumps with an exhausting capacity of 500 litter/sec to break down. However, the pressures upstream of the beam line and the storage ring were successfully kept below 10-8 Pa by the protection system. It was found that the vacuum failure caused no damage at all to the storage ring or other beam lines; thus, the storage ring could resume operation for synchrotron-radiation experiments.

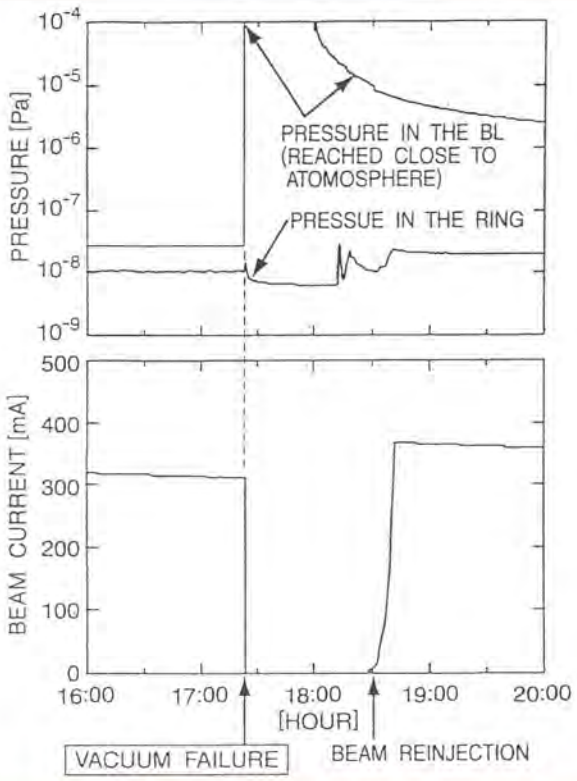

Figure 16.
Vacuum failure of the actual accident. The traces show the result of an actual vacuum failure successfully protected by the system. (Upper): The pressure rise at the downstream beam line, reaching atmospheric pressure. However, the pressure in the ring was successfully maintained below 10-8 Pa. (Lower): Beam current in the storage ring. The storage ring could resume its operation one-hour after the fatal vacuum deterioration.

1-2-4 Design of a HOM Coupler for a Damped Cavity

Four damped cavities have been operating in the PF ring. The damped cavity has a large-diameter beam duct. Higher order modes (HOMs) whose frequencies are above the cut-off frequency of the beam duct propagate out from the cavity to the beam duct, and the HOMs are damped by the SiC absorber which is placed inside wall of the beam duct. The several HOMs, with frequencies lower than the cut-off, still remain in the cavity with high Q values, and have the possibility to introduce coupled-bunch instabilities. These HOMs frequencies are detuned so as not to introduce any coupled bunch

instabilities using two fixed tuners of the cavity in the PF storage ring [1].

For a ring with larger circumference, however, frequency detuning becomes less effective, because of its low revolution frequency. We thus designed a HOM coupler with a rod-type antenna to reduce the HOMÅfs impedance of trapped modes in a damped cavity. The dangerous trapped HOMs are the TM011, TM020, TM021, TE111, TM110 and TM111 modes. These HOMÅfs frequencies are distributed from 0.7 to 1.4 GHz. Figure 17 shows a schematic cross-sectional view of the cavity with the HOM coupler. The rod antenna of the HOM coupler is located in the center of the cylindrical wall of the cavity. Therefore, the HOM coupler strongly couples with the TM011, TE111, TM021, and TM111 mode, and does not couple with the fundamental mode. The antenna is followed by a standard coaxial line. A tapered silicon carbide (SiC) load is fixed at the end of the coaxial line, and the trapped HOMs are absorbed by the SiC load. The HOM coupler is attached to an opening for the fixed tuner. The input reflection coefficient of the HOM coupler should be small enough over a wide frequency range of between 0.7 to 1.4 GHz. We set a design goal to achieve input VSWR of less than 1.7 (10% power reflection) in the frequency range. As for the load, we chose SiC (CERASIC-B, Toshiba Ceramics co. Ltd.), which is the same material as that used in the beam duct, since it has a high loss-tangent over a wide frequency range, a high thermal conductivity and a low outgassing rate.

The small-size HOM coupler is preferable for avoiding the interference with other ring components, such as synchrotron-radiation beam line. To satisfy this requirement, we designed the structure of the HOM coupler using computer simulation codes HFSS. Figure 18 shows an example of the simulation model. We set the basic design of the HOM coupler as follows. The diameters of the inner and outer conductors are 10mm and 20mm, respectively. The inner conductor is supported by a support disk and the SiC absorber, which is fixed between the outer and inner conductors at the end of the coaxial line. The end of the coaxial line is shorted by metal (short plate) to seal the vacuum. The SiC absorber is made in the shape of a taper to reduce reflections. We calculated the reflection characteristics of the taper of the SiC. Figure 19 shows the reflection characteristics versus frequency on the taper section length (La) of the SiC without support disk. The calculation conditions are as follows. The straight section length (Lb) of the SiC absorber is 80mm, which is long enough to completely absorb the incident power. The reflections from the short plate can be ignored. We assumed that the dielectric constants of the SiC are a permittivity $\varepsilon' = 25$ and $\tan\delta = 1.4$, which are approximate values of the beam duct SiC. The longer is the taper length (La), the lower is the reflection coefficient obtained, as expected. As shown in Fig. 19, the reflection power of the taper

section of the SiC become lower than 10% at a taper length La of 80mm. We thus adopted a taper length La of 80mm, and cut the thin part (below 2mm in thickness) of the taper, since a thin SiC is fragile.

Figure 20 shows our final design. The taper length (La) is 48mm and the minimum thickness of the SiC absorber is 2mm. The straight-section length (Lb = 10mm) of the SiC absorber is not long enough to

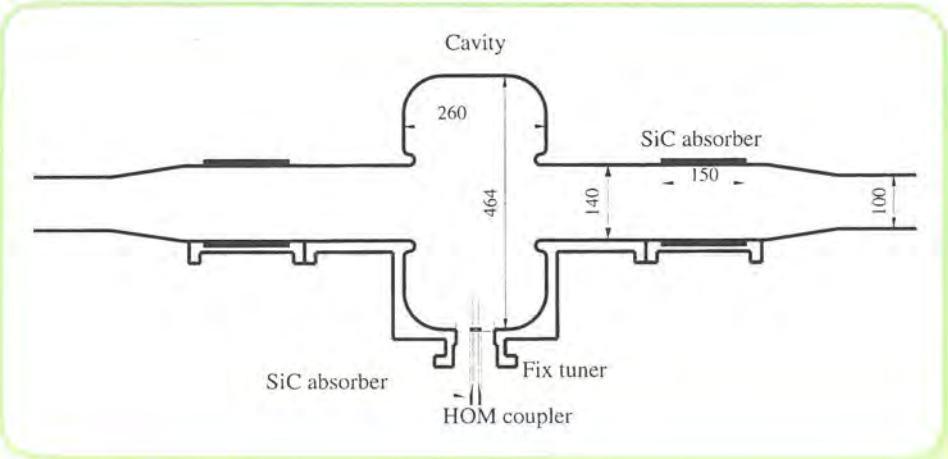

Figure 17.
Cross-sectional view of the cavity with the HOM coupler.

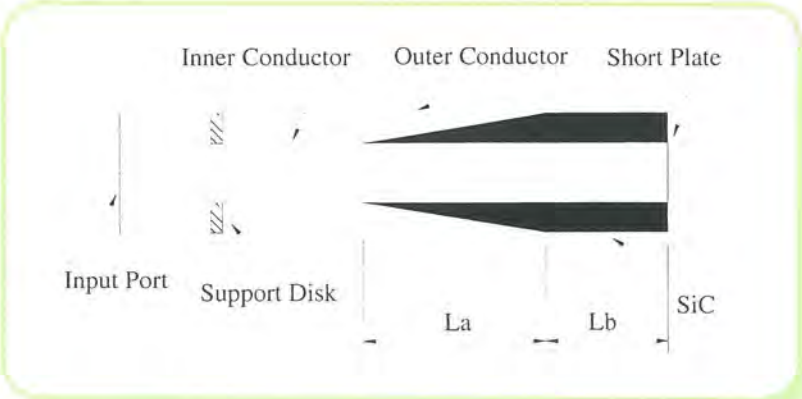

Figure 18.
Simulation model of the HOM load.

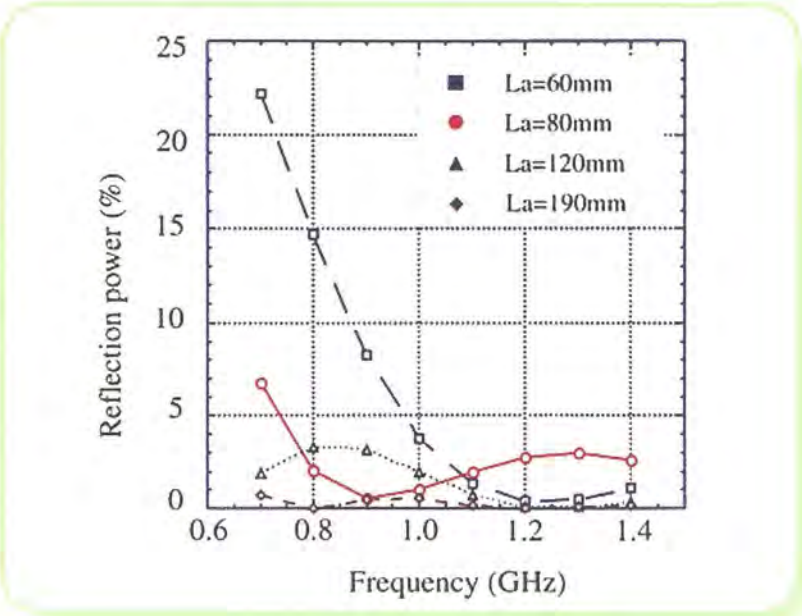

Figure 19.
Reflection characteristics of SiC absorber on some taper lengths (La = 60, 80, 120 and 190 mm).

completely absorb the incident power. However, the straight section length (Lb) and the distance between the support disk and the SiC absorber were adjusted, so that the reflection waves from the support disk, the SiC absorber, and the short plate (the end of the SiC absorber), would cancel each other. The SiC absorber is divided into four pieces, since they are easily brazed to the inner conductor. The inner and outer conductors have cooling-water channels. The SiC is cooled via the inner conductor. The support disk is located at 80mm from the cavity wall, where the electromagnetic field strength of the fundamental mode is weak enough. The influence of the support disk

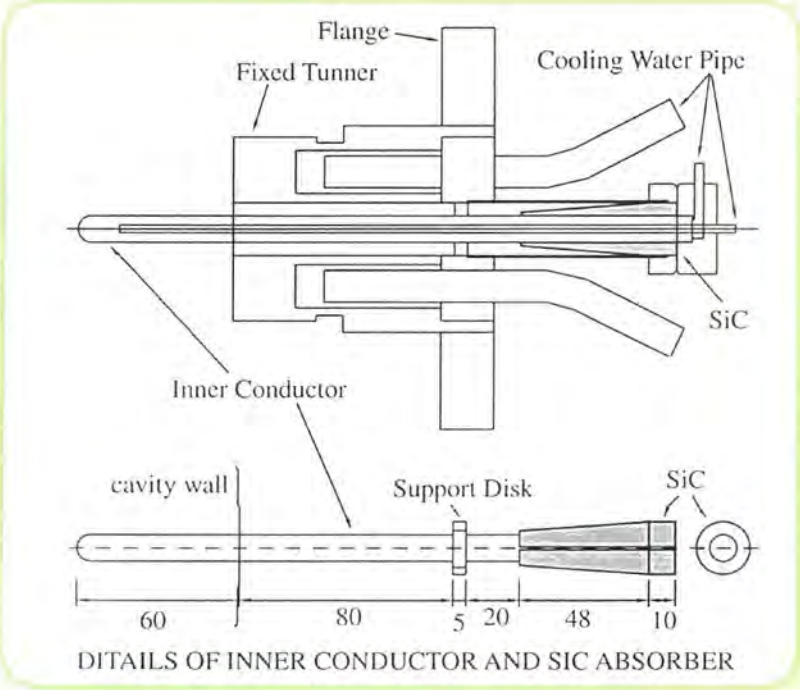

Figure 20.
Final design of the HOM absorber.

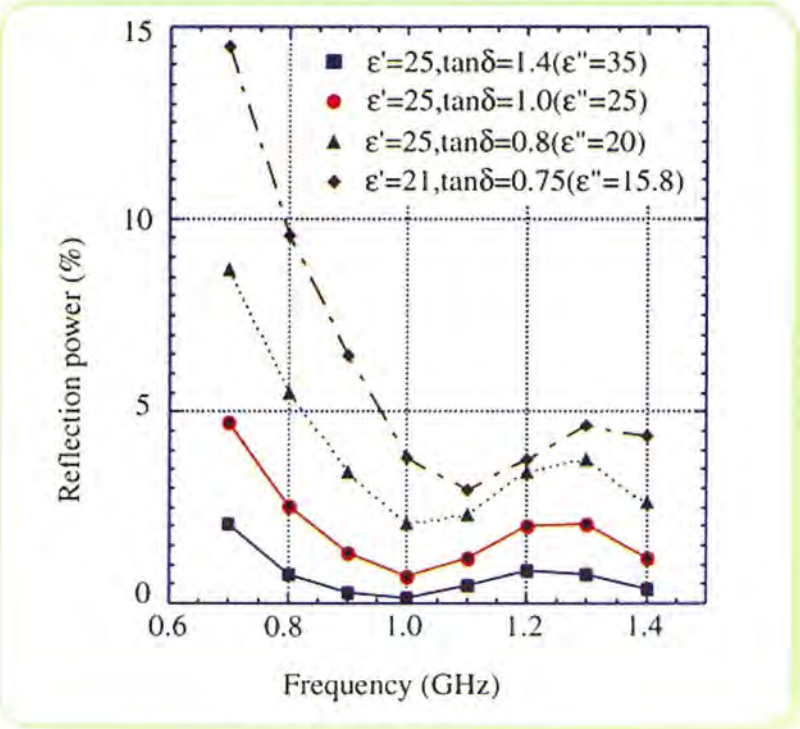

Figure 21.
Reflection characteristics of our final design of the HOM coupler for some different dielectric constants of the SiC.

on the reflection characteristics is very important in our design. We adopted the macor as a support-disk material, since the reflection coefficients become below 2%.

The reflection characteristics are also affected by the dielectric constant of SiC, which changes easily, depending on the fabrication condition. Figure 21 shows the effect of the dielectric constants of the SiC on the reflection characteristics. The required permittivity is about ε'' h = ~20 to satisfy our design goal, as shown in Fig. 21. We fabricated SiC samples to verify the process of manufacturing the SiC absorber and measured the complex dielectric constant. The measured values were ε' = 20 ~ 21, $\tan\delta$ = ~1.0 (ε'' = ~20) at 1 GHz. These dielectric constants are barely acceptable to achieve our design goal. The SiC absorber of our final design is being manufactured in Toshiba Corporation. The HOM coupler will be tested at the PF ring.

References

[1] Photon Factory Activity Report #15 PART A, p.137, 1997

1-2-5 Landau Damping of the Vertical Coherent Motion due to Lattice Nonlinearities

Systematic measurements of the vertical coherent motion were made with various chromaticities, octupole magnetic currents, beam currents and betatron tunes to study its damping mechanism. Recently we showed that the sign of the amplitude dependent tune shift produced by lattice nonlinearities play an important roll with the wake force in damping the horizontal coherent motion [1]. Landau damping is suppressed for the positive amplitude-dependent tune shift due to head-tail effects at higher beam currents, while it is amplified for a negative tune shift. This phenomenon is well understood through both the two-particle model and multi-particle-tracking simulation for comparing with the experimental results. We will next try to understand the damping mechanism of the vertical coherent motion. The experimental method was quite simple. The stored beam was deflected with a vertical fast kicker magnet, which can give just a single kick to the beam. The kicked beam begins to circulate in the ring with a large amplitude coherent betatron oscillation. The voltage supplied to the kicker magnet can control the amplitude. During measurements the voltage was fixed to make the initial vertical amplitude about 5 mm at a place of β_y=5 m. Then the beam position of the coherent betatron motion was detected with the turn-by-turn monitor system at a place of the ring [2]. Data were taken until 16384 turn (about 10 msec), which is longer than the radiation-damping time. The vertical chromaticity was controlled with defocus sextupole

magnets (SD). The amplitude-dependent tune shift was arranged with eight octupole magnetic currents; value is given by,

$$\Delta \nu_y = 3.3\times10^{-4} \cdot I_{oct}(A) \cdot y(mm)^2,$$

where y denotes the vertical amplitude. The sign of the tune shift can be changed by the polarity of the octupole magnetic currents.

First, we measured the dependence of the octupole magnetic currents. The vertical chromaticity and betatron tune were fixed at a ξ_y = -0.11 and ν_x = 3.30, respectively. Except for octupole-magnetic currents and the beam currents, other parameters were fixed. The measurements were made at seven different octupole magnetic currents (Ioct= +1.0, +0.5, +0.2, 0.0, -0.2, -0.5 and -1.0 A) to three beam currents (Ibeam=3.0, 5.0 and 10 mA). Figure 22 shows the measured results at a beam current of 5.0 mA. The damping behavior

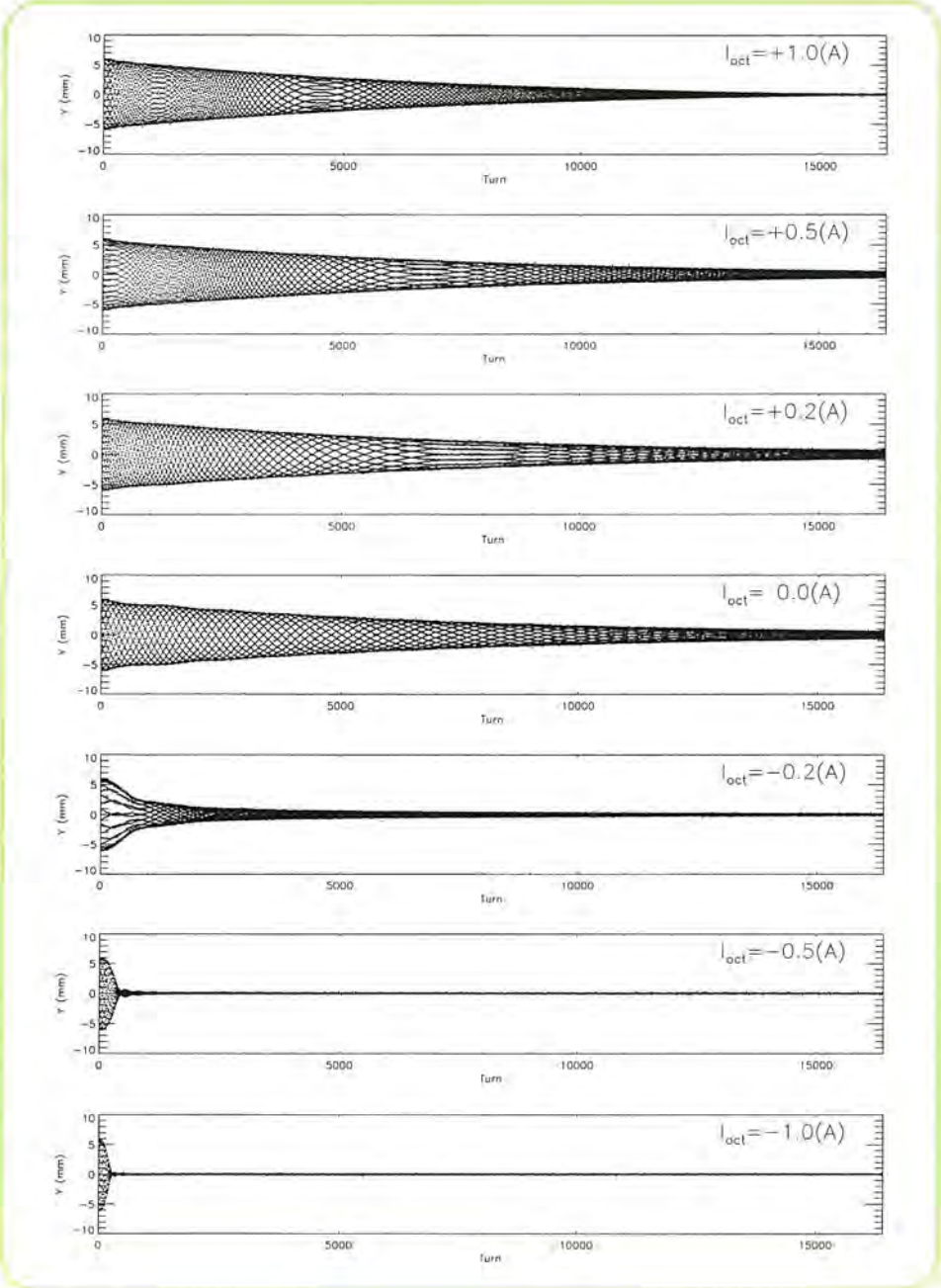

Figure 22.
Dependence of the octupole-magnetic currents in the damping behavior of the vertical coherent motions. Data were taken at a beam current of 5 mA; the vertical chromaticity, betatron tune and other parameters were fixed.

of the vertical coherent motion was changed rapidly when the magnetic currents obtained a negative value, which corresponds to the negative sign of the amplitude-dependent tune shift. When the magnetic currents have a positive value, the coherent motions damp exponentially. This phenomenon is the head-tail damping. On the other hand, the coherent motions damp very rapidly within 100 turn when the magnetic currents are negative. This is interpreted as Landau damping (nonlinear smear). It is thus seemed that the Landau damping of the vertical coherent motion is suppressed for the positive polarity of the octupole-magnetic currents in beam currents of 3-10 mA. This is the same situation as the horizontal coherent motion [1].

We next measured the dependence of the vertical chromaticities. The beam current and betatron tune were fixed at Ibeam = 5.0 mA

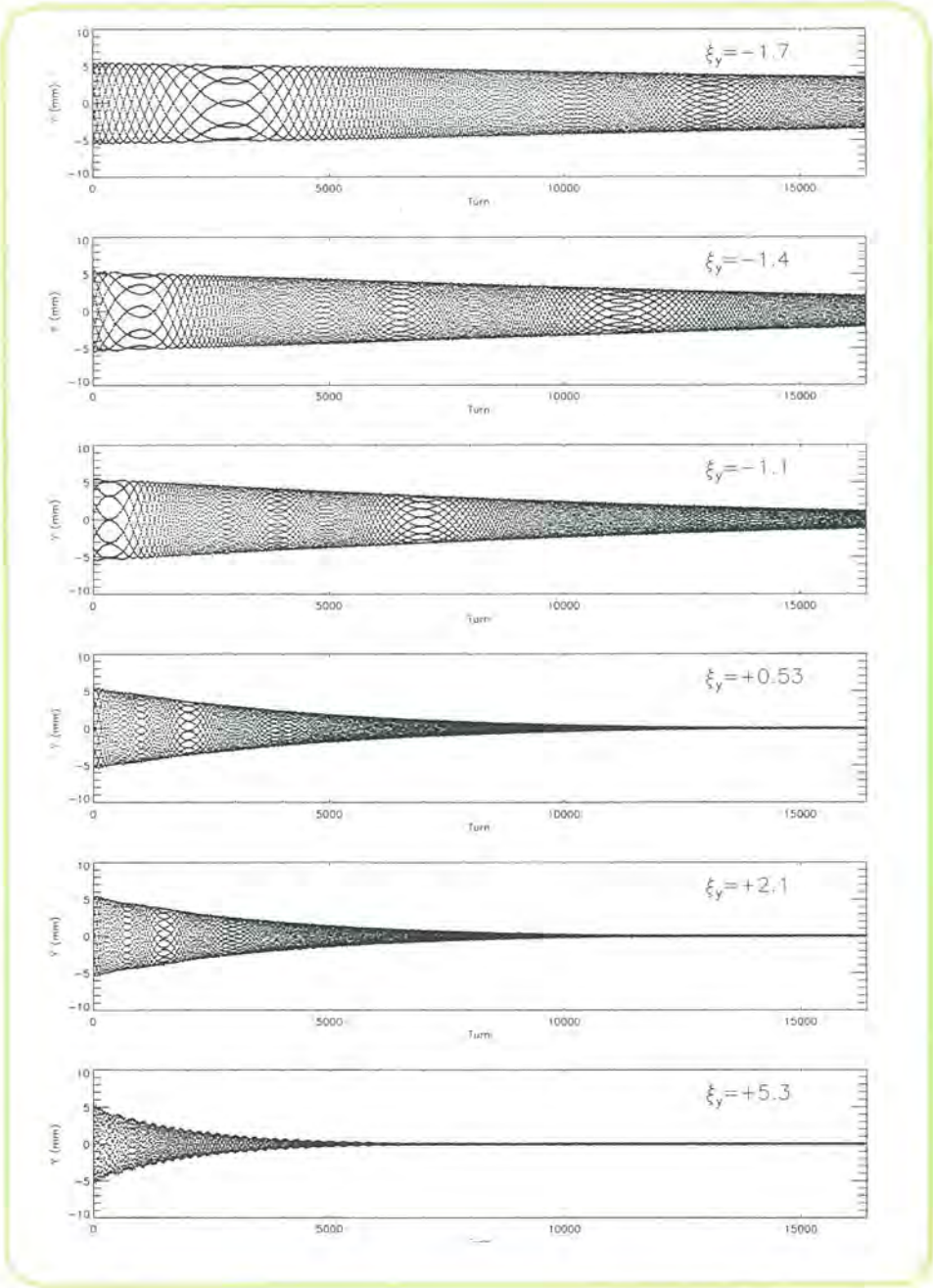

Figure 23.
Dependence of the vertical chromaticities in the damping behavior of the vertical coherent motions. Data were taken at an octupole-magnetic current of +1.0 A and a beam current of 5.0 mA; the betatron tune and other parameters were fixed.

and ν_x = 3.30, respectively. Except for octupole magnetic-currents and beam currents, other parameters were fixed. The measurements were made at six different vertical chromaticities (ξ_y = -1.7, -1.4, -1.1, +0.53, +2.1, and +5.3) to three octupole magnetic currents (Ioct= +1.0, 0.0 and -1.0 A), which were selected as the positive, zero and negative polarity of the currents. Figures 23 and 24 show the measured results at currents of +1.0 and -1.0 A, respectively. Only head-tail damping of the coherent motions was observed at a current of +1.0 A, although the damping time depended on the chromaticities. The situation of 0.0 A was almost the same as that of +1.0 A. On the other hand, only Landau damping was observed at a current of -1.0 A, and then the damping time never depended on the chromaticities.

We measured the systematic damping behaviors of the vertical

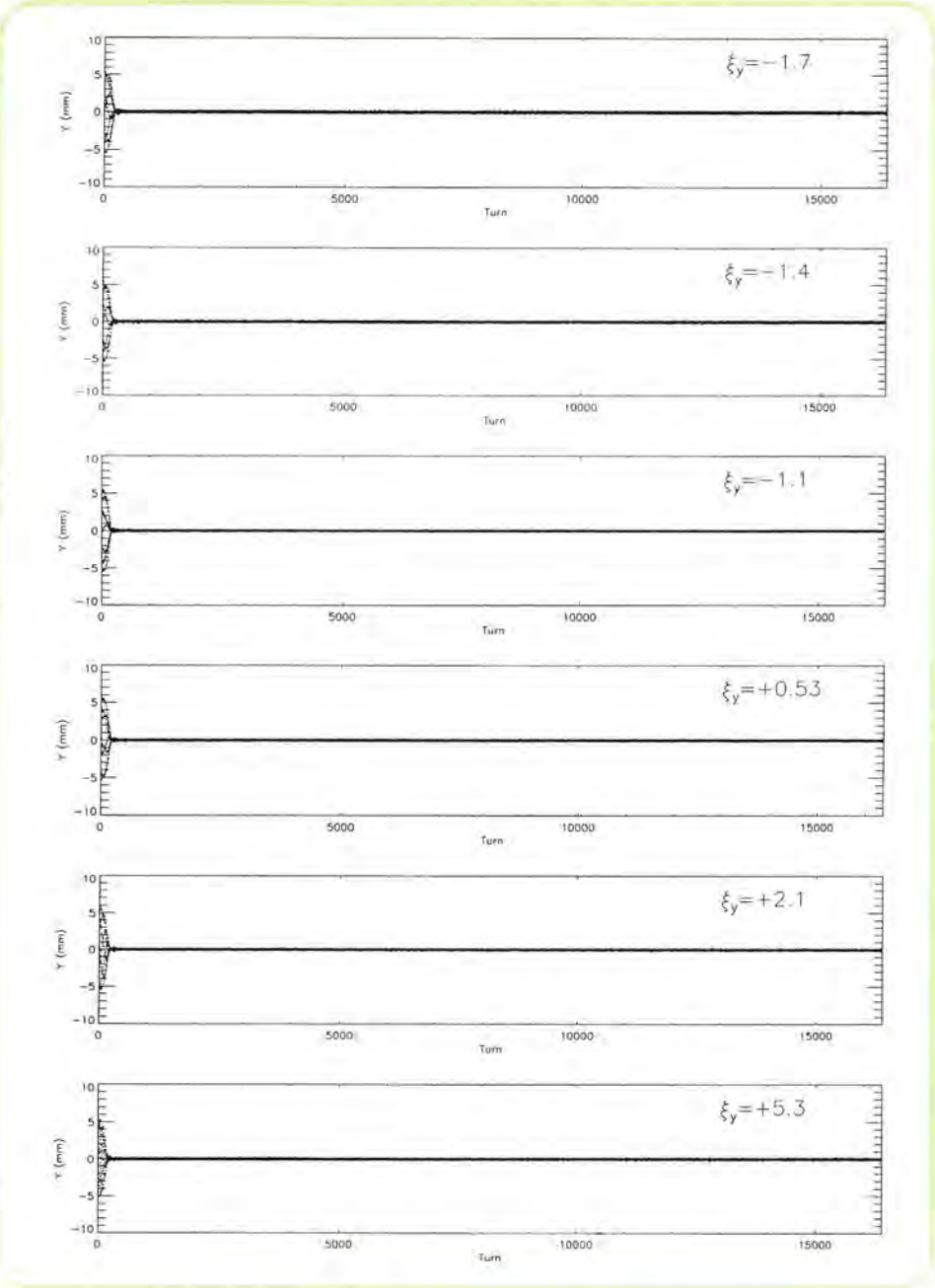

Figure 24.
Same as Fig. 24, but data were taken at an octupole magnetic current of -1.0 A.

coherent motion to various chromaticities, octupole magnetic, currents, beam currents and betatron tunes. In beam currents of between 0.5 and 10 mA, only head-tail damping was observed for the positive polarity of the octupole-magnetic currents, and the damping time depended on the vertical chromaticities. On the other hand, only Landau damping was observed for negative polarity, but the damping time never depended on the chromaticities. We are now going to make a multi-particle tracking simulation to compare the experimental results quantitatively.

References

[1] K. Ohmi and Y. Kobayashi, (Head-tail effect due to lattice nonlinearities in storage ring), Phys. Rev. E59, 1167 (1999)

[2] Y. Kobayashi et al., (Phase space monitor system at the Photon Factory storage ring), Proc. of EPAC 96

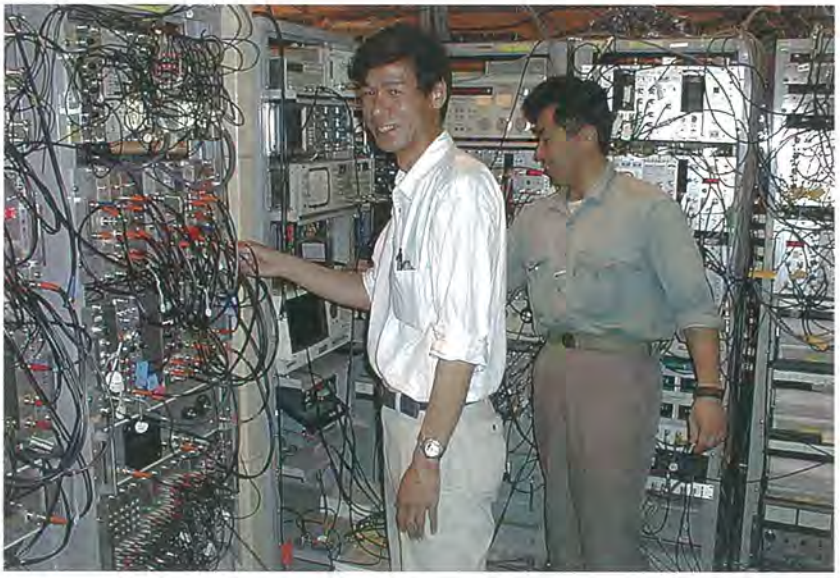

1-3 Storage Ring Specifications

This section contains principal specifications of the 2.5 GeV PF ring to provide quick and handy information for users and machine physicists. These parameters are under the new low-emittance lattice. Detail specifications and parameters are available through the World Wide Web (URL : http://pinecone.kek.jp/pfring.status.html).

Figure 25.
Beam transport line.

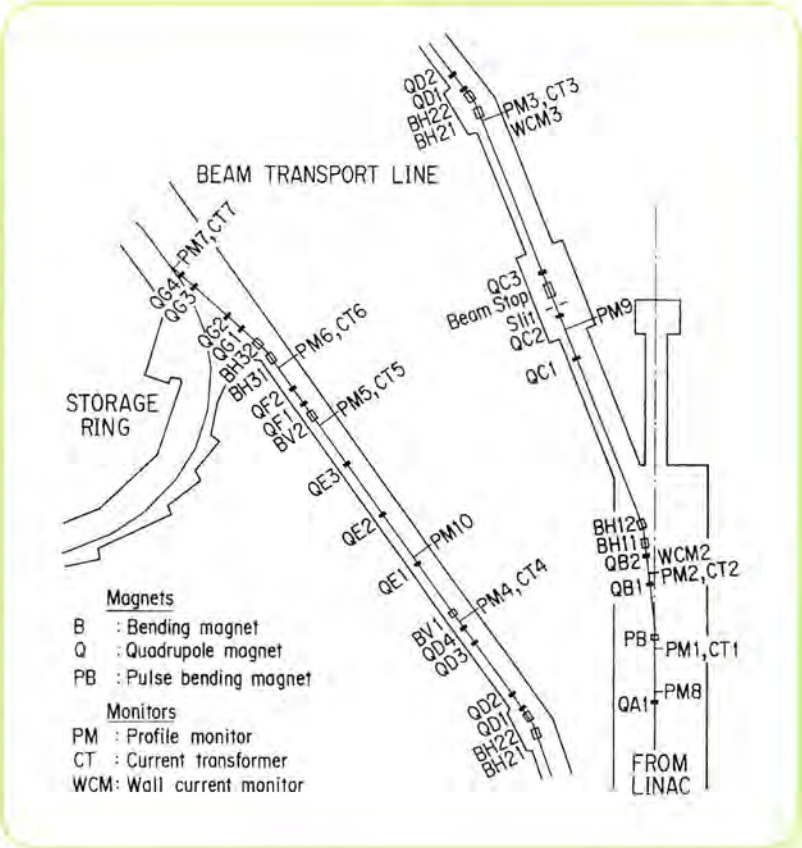

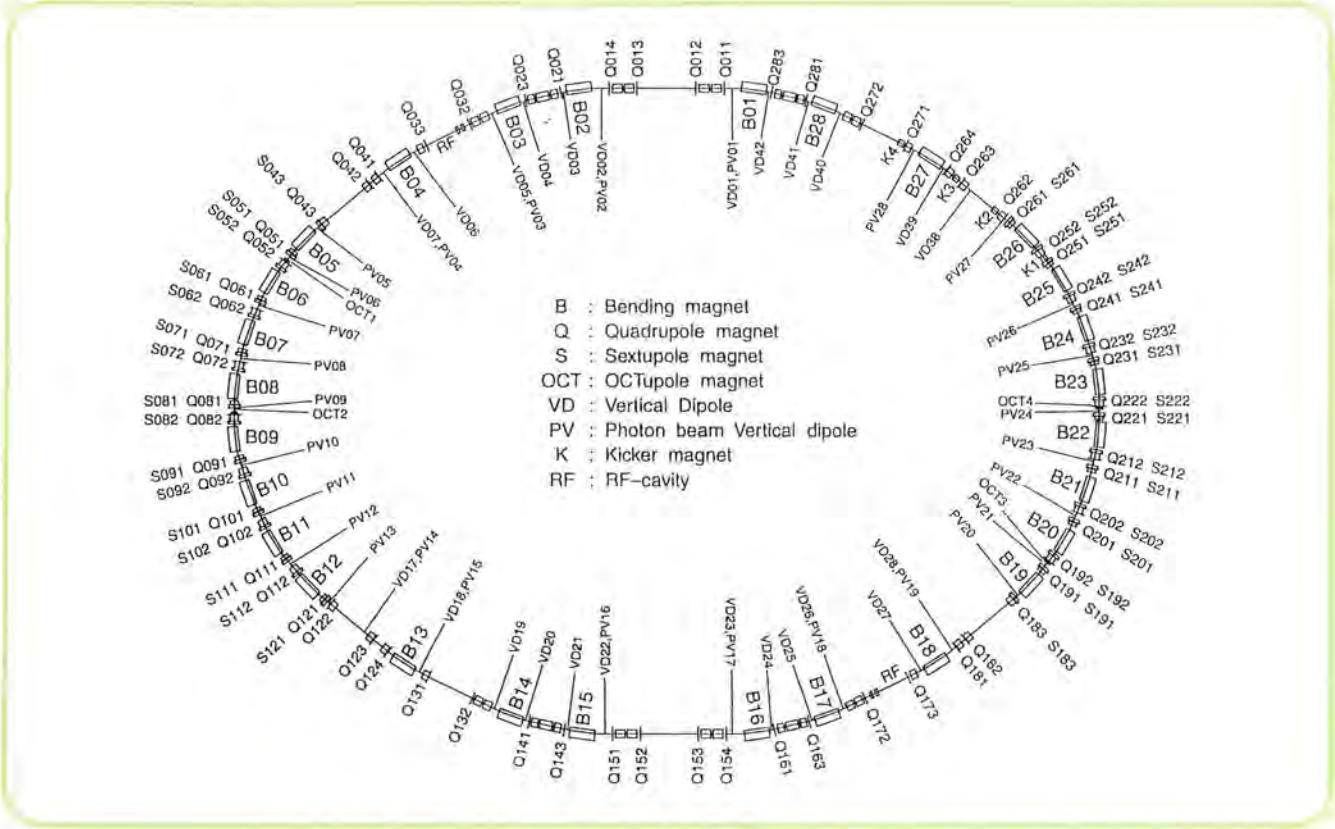

Figure 26.
Ring lattice components.

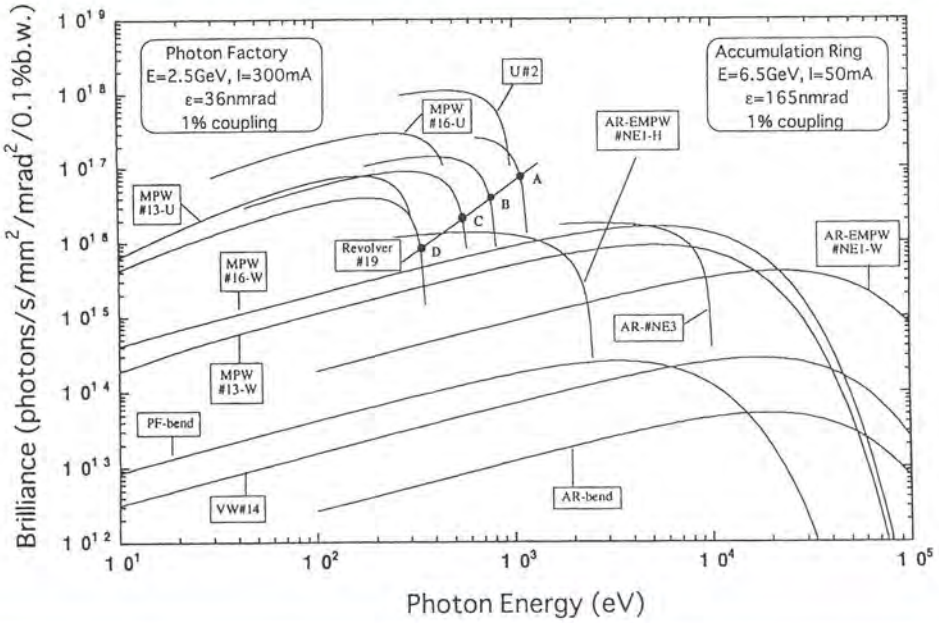

Figure27.

Synchrotron radiation spectra.

Brilliance of radiation vs. photon energy for the insertion devices (U#02, MPW#13, VW#14, MPW#16, Revolver#19 and EMPW#28) and the bending magnet (Bend) of the PF, and for the insertion device (EMPW#NE1 and MPW#NE3) of the AR. The name of each source is assigned in Table 10. Several insertion devices have both undulator and wiggler modes, which are denoted by U or W, respectively. The spectral curve of each undulator (or undulator mode of multipole wiggler) is a locus of the peak of the first harmonic within the allowable range of K-parameter. Spectra of Revolver#19 are shown for four kinds of period lengths.

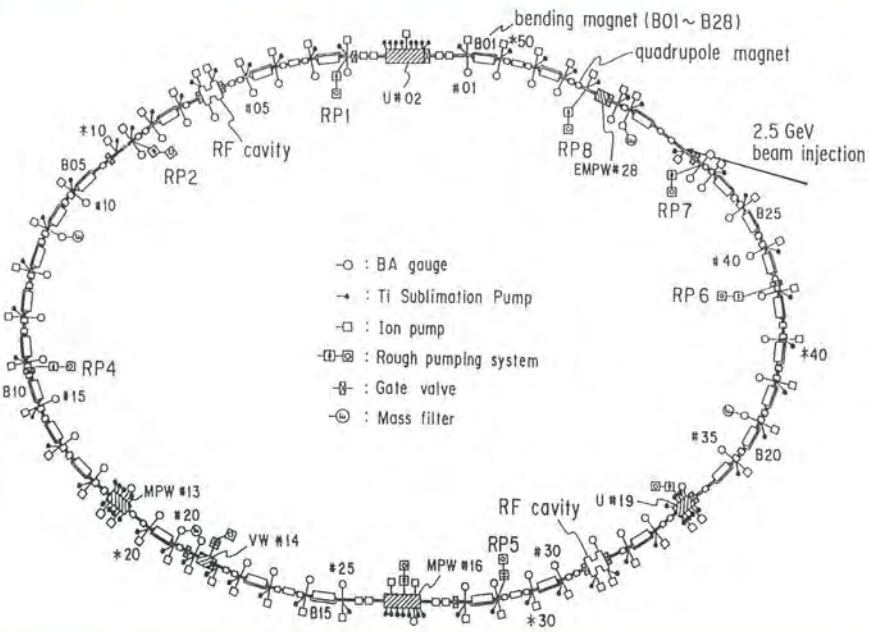

Figure 28.

Vacuum system components.

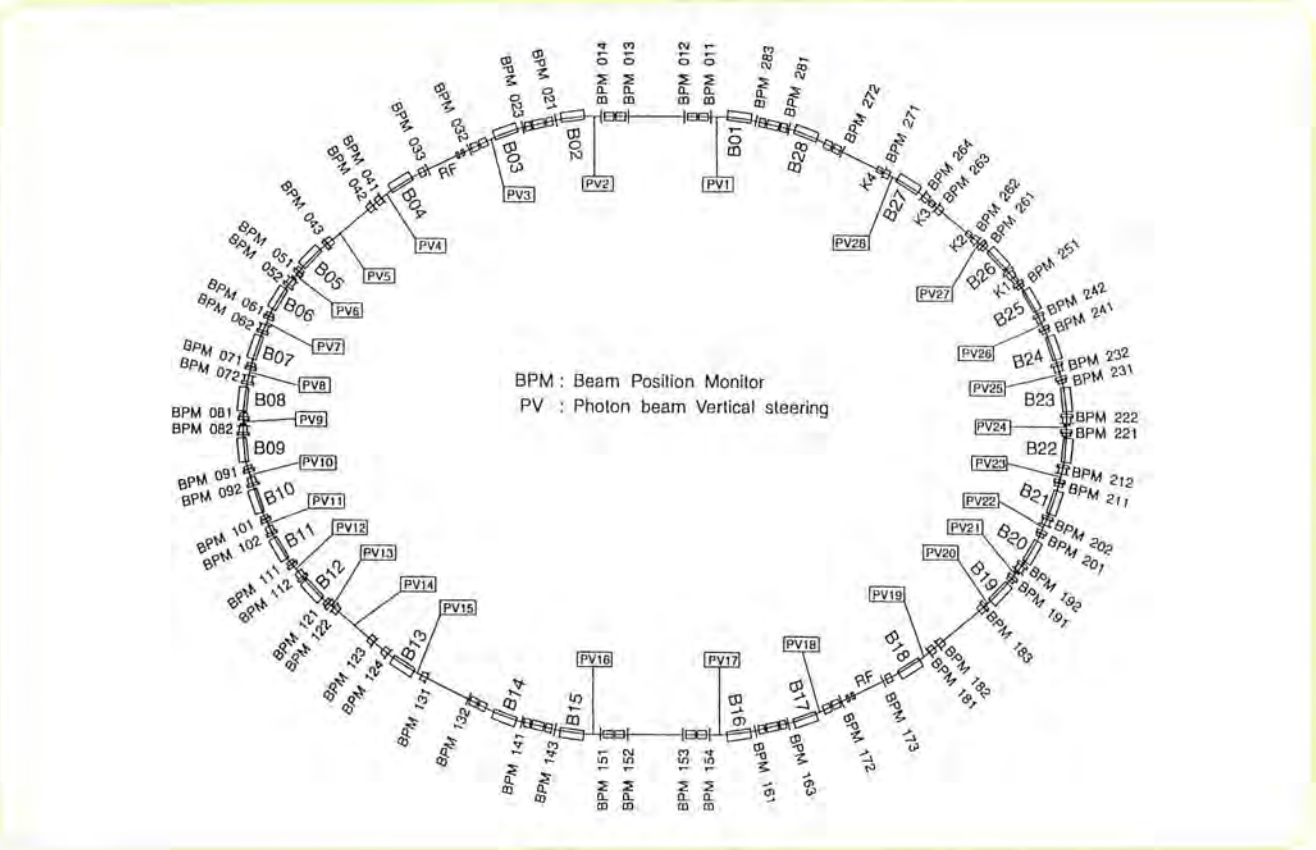

Figure 29.
Beam position monitors.

Table 2 Insertion devices

Caiculated spectral performances of the bend source and 6 insertion devices at the Photon Factory. E/I:beam energy and current, λ_u: period length, N: number of periods, L: length of undulator or wiggler, G_y (G_x) :minimum vertical (horizontal) gap height, B_y (B_x) maximum vertical (horizontal) magnetic field, P: pure configuration, H:hybrid configuration, S.C.: superconducting magnet, $\sigma_{x,y}$: horizontal or vertical beam size, $\sigma'_{x,y}$: horizontal or vertical beam divergence, K_n (K_v): horizontal (vertical) deflection parameter, $\varepsilon_1/\varepsilon c$: photon energy of the first harmonic (critical energy in the case of bend source or wiggler), D: photon flux in unit solid angle (photons/s・mrad²・0.1%b.w.), *B*:brilliance (photons/s・mm²・mrad²・0.1% b.w.), P_T: total radiated power, dP/dΩ: power in unit solid angle. Different operating modes of undulator and wiggler are denoted by-U and-W,respectively.

Name	E/I GeV/mA	λ_u cm	N	L m	$G_y(G_x)$ cm	$B_y(B_x)$ T	Type of magnet	σ_x mm	σ_y mm	σ'_x mrad	σ'_y mrad	$K_n(K_v)$	$\varepsilon_1/\varepsilon c$ keV	D	*B*	PT kW	dp/dΩ kW/mrad
Bend	2.5/300					0.96		0.39	0.059	0.186	0.013		4	3.60E+13	2.48E+14		0.061
U#02	2.5/300	6	60	3.6	2.8	0.4	H(NdFeB)	0.42	0.042	0.084	0.008	2.25	0.2	1.12E+17	9.73E+17	0.68	2.9
MPW#13-W	2.5/300	18	13	2.5	2.7	1.5	H(NdFeB)	0.86	0.019	0.117	0.018	25	6.2	9.70E+14	8.83E+15	6.48	2.53
MPW#13-U	2.5/300	18	13	2.5	2.7	1.5	H(NdFeB)	0.86	0.019	0.117	0.018	2	0.108	8.09E+15	6.94E+16	0.041	0.19
VW#14	2.5/300				5	5	S.C.	0.58	0.036	0.083	0.01		20.8	3.63E+13	2.75E+14		0.32
MPW#16-W	2.5/300	12	26	3.12	1.9	1.5	H(NdFeB)	0.42	0.042	0.084	0.008	16.8	6.2	7.69E+14	6.71E+15	8.17	4.84
MPW#16-U	2.5/300	12	26	3.12			H(NdFeB)	0.42	0.042	0.084	0.008	2	0.163	3.17E+16	2.72E+17	0.12	0.56
Revolver#19	2.5/300	5	46	2.3	3	0.28	H(NdFeB)	0.85	0.056	0.088	0.008	1.3	0.639	7.86E+16	2.60E+17	0.21	1.42
	2.5/300	7.2	32	2.3	3	0.4	H(NdFeB)	0.85	0.056	0.088	0.008	2.7	0.176	3.29E+16	1.08E+17	0.42	1.44
	2.5/300	10	23	2.3	3	0.54	H(NdFeB)	0.85	0.056	0.088	0.008	5	0.0437	9.63E+15	3.01E+16	0.77	1.52
	2.5/300	16.4	14	2.3	3	0.62	P(NdFeB)	0.85	0.056	0.088	0.008	9.5	0.0078	1.28E+15	3.22E+15	1.01	1.06
EMPW#28-W	2.5/300	16	12	1.92	3(11)	1(0.2)	P(NdFeB)	0.58	0.036	0.083	0.01	15(1)	4.1(90%)	2.30E+14	1.71E+15	2.13	0.35
EMPW#28-U	2.5/300	16	12	1.92			P(NdFeB)	0.58	0.036	0.083	0.01	1(1)	0.182(99%)	1.36E+16	9.98E+16	0.02	0.064

Table 3 General parameters of the storage ring.

Energy	2.5 GeV	(max 3 GeV)
Initial stored (multi-bunch) current	400mA	(max 500 mA at 2.5 GeV)
(single bunch)	65 mA	(max 100 mA)
Emittance	36 nm・rad (horizontal) ~0.4 nm・rad (vertical)	
Circumference	187 m	(bending radius=8.66m)
RF frequency	500.1 MHz	(harmonic number=312)
Injection	2.5-GeV Linac	(positron/electron)
Beam lifetime	30 h (at 300 mA)	$I \cdot \tau \gtrsim 9$ A・h (at 300 mA)
Vacuum pressure $\lesssim 5\times10^{-8}$ Pa (at 300 mA)		
	P/I×~2×~10^{-7} Pa/A (at 300 mA) ~6×~10^{-9} Pa (at 0 mA)	
Insertion devices	Superconducting vertical wiggler 5T 60 period undulator K=1.78~0.1 26 period multipole wiggler/undulator 1.5T~0.04T Four way revolver type undulator 14 period multipole wiggler Elliptically polarized multipole wiggler	
SR channels	SR experiment 22 Beam diagnosis 3	

Table 4 Beam parameters.

Horizontal tune ν_x	9.62
Vertical tune ν_y	4.29
Momentum compaction factor α	0.061
Natural chromaticity ξ_x	-12.5
ξ_y	-12.3
Bunch length σ_z	1.0 cm
Transverse damping time	7.8 msec
Longitudinal damping time	3.9 msec
Energy spread	7.3×10^{-4}
Radiation loss	400 keV

Table 5 Principal parameters of the accelerator system.

Magnet system

	number of magnets	number of power supplies
Bending	28	1
Quadrupole	74	15
Sextupole	32	3
Octupole	4	4
Vertical steerers	24	24
Fast vertical steerers for global orbit FB	30	30
Backleg windings		
on bendings for horizontal steerers	28	28
on sextupoles for vertical steerers	28	28
on sextupoles for skew quadrupoles	4	4
on sextupoles for field compensation	32	3
Electronic shunts on quadrupoles		
for optics matching and tune compensation	34	48

RF system

Number of RF stations	4
Number of klystrons	4 (180kW/klystron)
Number of RF cavities	4 (single cell cavity)
Shunt impedance	27.6MΩ (four cavities)
Unloaded Q	39000
Total power dissipated in cavity wall	105 kW
Total cavity gap voltage	1.7 MV
Synchrotron frequency	20 kHz

Vacuum system

Main pumping system		
pump	pumping speed	number
SIP(Sputter Ion Pump)	128 l/sec	54
DIP(Distributed Ion Pump)	150 l/sec	26
Ti sublimation	.....	71
NEG(Non-Evaporable Getter)	.....	2
total effective pumping speed $=2\times10^{4}$ l/sec(for CO)		
Rough pumping system	pumping speed	number
TMP(Turbo Molecular Pump)	300 l/sec	12
Measurement	number	
B-A gauge	48	
mass filter	4	
cold cathode gauge	16 (for baking)	
Sector gate valve	number	
all metal with RF shield	4	
viton seal with RF shield	11	

Injection system

Septum magnet		
name	Septum I (S1)	Septum II (S2)
core material	laminated silicon steel(passive type)	
length [mm]	1500	1000
maximum current [A]	6000	6000
deflection angle [degree]	7.0	5.0
pulse width [msec]	88	60

Kicker magnet	
name	K1, K2, K3, K4
core material	ferrite (window frame type)
core length [mm]	300
	3500
maximum deflection angle [mrad]	4.4
pulse width [msec]	5

Superconducting vertical wiggler

Maximum field strength on the beam orbit	5 Tesla
Magnet gap	66 mm
Magnet pole size (widthxhight)	40 mm×260 mm
Number of magnetic poles	5 poles (3 poles at nomal operation)
	arranged exery 200 mm
Rated exciting current	210 A at 4.8 Tesla
Superconducting wire	NbTi:Cu 1:1
	size 1.70×0.85mm^2
Cross section of coils	65 mm×70 mm
Number of turn	2520
Liquid helium consumption in the permanent current mode	0.7 L/h
Damping rate of the permanent current	1.4×10^{-5}/h
Inductance	1.31 H/coil

Monitor system

I . Orbiting Beam Monitors

PM (Position Monitor)	65
DCCT (Direct Current Current Transformer)	2
RFKO (Radio Frequency Knock-Out system)	1
WCM (Wall Current Monitor)	1
LS (Loss monitor)	30
Visible Light Monitor	
CCD TV camera	1
CCD profile monitor (H&V)	1
light profile monitor (H&V)	1
four-element photo diodes (for oscillation detection)	1
streak camera	1
photon counting system	1

II .Photon beam position monitors installed in beamlines

Beamline	Source	Upstream	Downstream	Ver./Hor.
BL2 U	DSPM	DSPM	V,H	
BL3A	B	SPM		V
BL3C	B	SPM	SPM	V
BL4C	B	SPM	SPM	V
BL6B	B	SLIT		V
BL6C	B	SLIT		V
BL6C	B	SPM	SPM	V
BL7C	B	SLIT	SPM	V
BL10A	B	SIC		V
BL10B	B	SLIT		V
BL12A	B	WM	WM	V
BL14C	SVW	SPM	SPM	H
BL15A	B	SPM		V
BL16	MPW	DSPM		V,H
BL21	B	WM		V
BL27	B	SPM		
BL28	EMPW	Under constr.		

Note:				
	SPM:	Split Photoemission Monitor	B:	Bending magnet
	SIC:	Split Ion Chamber	U:	Undulator
	WM:	Wire Monitor	SVW:	Superconducting Vertical Wiggler
	DSPM:	Dual SPM for insertion device line	MPW:	Multipole Wiggler
			EMPW:	Elliptical MPW

Control system

Computers	Serve	Workstation	PC	VME
Presentation/Console	—	3	13	—
Control/DB Engine	1	16	5	6
Equipment Control	—	—	3	9
Network Management	—	2	1	—

Network		Number	Port
ATM Switch (155Mbps)		1	single mode 12 multi-mode 4
ATM-Ethernet Switching Hub	12	10BASE-T 12/hub	

Table 6 Beam parameters.at source points.

B.L.	Source	σ_x[mm]	σ'_x[mrad]	σ_y[mm]	σ'_y[mrad]
BL01	B01(+2.5)	0.203	0.245	0.061	0.0125
BL02	U#02	0.422	0.084	0.042	0.0084
BL03	B02(-0.0)	0.238	0.263	0.066	0.0125
	B03(+0.0)	0.288	0.228	0.084	0.0066
BL04	B04(+2.5)	0.319	0.161	0.066	0.0173
BL06	B06(+2.5)	0.391	0.185	0.059	0.0129
BL07	B07(+2.5)	0.391	0.185	0.059	0.0129
BL08	B08(+2.5)	0.391	0.185	0.059	0.0129
BL09	B09(+2.5)	0.391	0.185	0.059	0.0129
BL10	B10(+2.5)	0.391	0.185	0.059	0.0129
BL11	B11(+2.5)	0.391	0.185	0.059	0.0129
BL12	B12(+2.5)	0.447	0.138	0.054	0.0092
BL13	MPW#13	0.859	0.115	0.020	0.0186
BL14	VW#14	0.580	0.083	0.036	0.0098
BL15	B15(+2.5)	0.203	0.245	0.061	0.0125
BL16	MPW#16	0.422	0.084	0.042	0.0084
BL17	B16(-0.0)	0.238	0.263	0.066	0.0125
	B17(+0.0)	0.288	0.228	0.084	0.0066
BL18	B18(+2.5)	0.319	0.161	0.066	0.0173
BL19	U#19	0.847	0.088	0.057	0.0078
BL20	B20(+2.5)	0.391	0.185	0.059	0.0129
BL21	B21(+2.5)	0.391	0.185	0.059	0.0129
BL27	B27(+1.2)	0.259	0.218	0.090	0.0176
BL28	EMPW#28	0.580	0.083	0.036	0.0098

Table 7. Summary of Beamline Front Ends in FY 1997.

Beamline	Affiliation	Source	Spectral	range Status
BL-1	KEK-PFandNTT	Bending magnet (B1)	VUV and soft X-ray	in operation
BL-2	KEK-PF	60-period undulator	soft X-ray	in operation
BL-3	KEK-PF	Bending magnet (B2&B3)	VUV and soft X-ray	in operation
BL-4	KEK-PF	Bending magnet (B4)	X-ray	in operation
BL-5	KEK-PF	Multipole wiggler/undulator	-	under installation
BL-6	KEK-PF	Bending magnet (B6)	X-ray	in operation
BL-7	KEK-PFand University of Tokyo	Bending magnet (B7)	VUV and X-ray	in operation
BL-8	Hitachi Ltd.	Bending magnet (B8)	VUV and X-ray	in operation
BL-9	Nippon Electrical Co. (NEC)	Bending magnet (B9)	VUV and X-ray	in operation
BL-10	KEK-PF	Bending magnet (B10)	X-ray	in operation
BL-11	KEK-PF	Bending magnet (B11)	VUV and soft X-ray	in operation
BL-12	KEK-PF	Bending magnet (B12)	VUV	in operation
BL-13	KEK-PF	27-pole wiggler/undulator	Soft and hard X-ray	in operation
BL-14	KEK-PF	Superconducting vertical wiggler	hard X-ray	in operation
BL-15	KEK-PF	Bending magnet (B15)	X-ray	in operation
BL-16	KEK-PF	53-pole wiggler/undulator	Soft and hard X-ray	in operation
BL-17	Fujitsu Ltd.	Bending magnet (B16&B17)	VUV and X-ray	in operation
BL-18	ISSP and KEK-PF	Bending magnet (B18)	VUV and X-ray	in operation
BL-19	ISSP and KEK-PF	Multi-undulator	VUV	in operation
BL-20	KEK-PF	Bending magnet (B20)	VUV and X-ray	in operation
BL-21	KEK-PF	Bending magnet (B21)	Beam diagnosis	in operation
BL-27	KEK-PF	Bending magnet (B27)	Soft X-ray and X-ray	in operation
BL-28	KEK-PF	25-pole wiggler/undulator	Circularly polarized VUV and soft X-ray	in operation

LIST OF PUBLICATIONS

2A

S.Tohno, J.Kawai, S.Chatani, M.Ohta, Y.Kitajima, K.Yamamoto, Y.Kitamura and M.Kasahara
Application of X-ray Absorption Fine Structure (XAFS) Spectrometry to Identify the Chemical States of Atmospheric Aerosols
J. Aersol Sci., **29** (1998) S235.

J.Adachi, Y.Takata, N.Kosugi, E.Shigemasa, A.Yagishita and Y.Kitajima
Kinetic Energy Dependence of Ionic Fragmentations Following S 1s Excitations of SO_2
Chem. Phys. Lett., **294** (1998) 559.

Y.Kitajima
Improved Performance of an Undulator Soft X-Ray Station BL-2A of the Photon Factory in its Reduced Emittance Operation
J. Synchrotron Rad., **6** (1999) 167.

2B

H.Ishii, T.Kimura, T.Miyahara, T.Hanyu, T.Iwasaki, S.Ueda, M.Tsunekawa, T.Nakatani, T.Matsushita, S.Imada, H.Daimon, S.Suga, A.Sekiyama, A.Fujimori, H.Namatame, M.Taniguchi, A.Kimura, H.Sugawara, Y.Aoki and H.Sato
Effects of Coster-Kronig Decay on Ce $3d$-$4f$ Resonant Photoemisseion Spectra of $CeOs_2$
J. Elec. Spec. Relat. Phenom., **88** (1998) 419.

M.Tanaka, M.Hasegawa, T.Higuchi, T.Tsukamoto, Y.Tezuka, S.Shin and H.Takei
Origin of the Metallic Conductivity in $PdCoO_2$ with Delafossite Structure
Physica B, **245** (1998) 157.

T.Higuchi, T.Tsukamoto, N.Sata, M.Ishigame, Y.Tezuka and S.Shin
Electronic Structure of p-type $SrTiO_3$ by Photoemission Spectroscopy
Phys. Rev. B, **57** (1998) 6978.

H.Sato, S.Senda, H.Okuda, M.Nakatake, A.Furuta, Y.Ueda, M.Taniguchi, A.Tanaka and T.Jo
Mn 2p-3d Resonant Photoemission Spectroscopy of MnY (Y = S, Se, Te)
J. Elec. Spec. Relat. Phenom., **88** (1998) 425.

T.Higuchi, T.Tsukamoto, N.Sata, M.Ishigame, Y.Tezuka and S.Shin
Photoemission Study of Protonic Conductor p-type $SrTiO_3$
Solid State Ionics, **108** (1998) 349.

T.Higuchi, T.Tsukamoto, M.Tanaka, H.Ishii, K.Kanai, Y.Tezuka, S.Shin and H.Takei
Photoemission Study on $PdCoO_2$
J. Elec. Spec. Relat. Phenom., **92** (1998) 71.

2C

Y.Harada, H.Ishii, M.Fujisawa, Y.Tezuka, S.Shin, M.Watanabe, Y.Kitajima and A.Yagishita
Spectrometer for Polarized Soft X-Ray Raman Scattering
J. Synchrotron Rad., **5** (1998) 1013.

3A

M.Yashima, S.Sasaki, Y.Yamaguchi, M.Kakihana, M.Yoshimura and T.Mori
Internal Distortion in ZrO_2-CeO_2 Solid Solutions: Neutron and High-Resolution Synchrotron X-Ray Diffraction Study
Appl. Phys. Lett., **72** (1998) 182.

J.Kokubun, K.Ishida and V.E.Dmitrieko
Forbidden Reflection Excited Owing to the Anisotropy of X-Ray Susceptibility. I. Interference with the Renninger Reflection
J. Phys. Soc. Jpn., **67** (1998) 1291.

A.Okita, F.Saito, S.Sasaki, T.Toyoda and H.Koinuma
Determination of Cation Distribution in Mn-Zn-Fe Ferrite by X-ray Anomalous Scattering
Jpn. J. Appl. Phys., **37** (1998) 3441.

N.Sugioka, K.Matsumoto, M.Tanaka, T.Mori and S.Sasaki
DAFS Measurements by the Imaging-Plate Weissenberg Method
J. Synchrotron Rad., **5** (1998) 908.

K.Kawasaki, M.Koizumi and H.Inagaki
Rapid Projection of Crystal Grain Orientation Distribution in Aluminium Alloy Sheets by Synchrotron X-ray Diffraction
J. Synchrotron Rad., **5** (1998) 1139.

J.Kokubun, T.Nagano, M.Kuribayashi and K.Ishida
Energy Dependence of the ATS Reflections of Iron Pyrite, FeS_2, Near the Fe K-Absorption Edge
J. Phys. Soc. Jpn., **67** (1998) 3114.

T.Ikeda, M.Tanaka, M.Sakata, J.Waliszewski, L.Dobrzynski, S.Porowski and J.Jun
Electron Density Distribution of Wurtzite-Type Gallium Nitride by Maximum Entropy Method
J. Phys. Soc. Jpn., **67** (1998) 4104.

M.Sakata
Structural Analyses of Biological Materials by SR 4. Crystal Structure Analysis by Maximum Entropy Method
Radioisotopes, **47** (1998) 883. (*in Japanese*).

T.Ikeda, T.Kobayashi, M.Takata, T.Takayama and M.Sakata
Charge Density Distributions of Strontium Titanate Obtained by the Maximum Entropy Method
Solid State Ionics, **108** (1998) 151.

S.Sasaki
A Potential of the X-ray Powder Diffraction Method for Determining the Valence in Crystals
KEK Proc., **97-22** (1998) 90. (*in Japanese*).

3B

T.M.Kojima, M.Oura, N.Watanabe, Y.Awaya, Y.Itoh, T.Koizumi, M.Sano and F.Koike
4 d Photoionization of Singly Charged Ions
J. Korean Phys. Soc., **32** (1998) 273.

T.M.Kojima, M.Oura, Y.Itoh, T.Koizumi, M.Sano, T.Sekioka, N.Watanabe, H.Yamaoka and Y.Awaya
Photoion Yield Spectroscopy in the 4d Photoionization of Eu^+
J. Phys. B: At. Mol. Opt. Phys., **31** (1998) 1463.

N.Watanabe, Y.Awaya, A.Fujino, Y.Itoh, M.Kitajima, T.M.Kojima, M.Oura, R.Okuma, M.Sano, T.Sekioka and T.Koizumi
Photoion-yield Spectra of Xe^{2+} in the 4d-threshold Energy Region
J. Phys. B: At. Mol. Opt. Phys., **31** (1998) 4137.

Y.Enta, Y.Miyanishi, H.Irimachi, M.Niwano, M.Suemitsu, N.Miyamoto, E.Shigemasa and H.Kato
Real-time Measurements of Si 2*p* Core Level during Dry Oxidation of Si(100)
Phys. Rev. B, **57** (1998) 6294.

Y.Enta, Y.Miyanishi, H.Irimachi, M.Niwano, M.Suemitsu, M.Miyamoto, E.Shigemasa and H.Kato
Real-time Core-level Spectroscopy of Initial Thermal Oxide on Si(100)
J. Vac. Sci. Tech. A, **16** (1998) 1716.

M.Sano, A.Ito and T.Koizumi
Photoionization and Giant Resonaces of Heavy Atomic Ions
Butsuri, **53** (1998) 278. (*in Japanese*).

4A

S.Homma-Takeda, Y.Kumagai, M.Shinyashiki and N.Shimojo
Application of Synchrotron Radiation X-ray Fluorescence Imaging Combined with Histochemical Staining to the Renal Section of Mercury-treated Rats
J. Synchrotron Rad., **5** (1998) 57.

I.Nakai, C.Numako, S.Hayakawa and A.Tsuchiyama
Chemical Speciation of Geological Samples by Micro-XANES Techniques
J. Trace & Electron Micro. Tech., **16(1)** (1998) 87.

I.Nakai
Synchrotron Radiation X-ray Fluorescence Analysis of Cultural Properties
Proceedings of International Symposium on the Coservartion and Restration of Cultural Properties, (1998) 125.

K.Okitsu, Y.Ueji, T.Oguchi, H.Maruyama, Y.Hasegawa and Y.Amemiya
Study on Dielectric Anisotropies in Crystals by Using the Energy-Tunable X-Ray Polarimeter with a Phase Retarder
J. Cryst. Soc. Jpn., **40** (1998) 341. (*in Japanese*).

K.Okitsu, T.Oguchi, H.Maruyama and Y.Amemiya
X-ray Linear Birefringence and Linear Dichroism in a Cobalt Crystal Measured with a Tunable X-ray Polarimeter
J. Synchrotron Rad., **5** (1998) 995.

K.Okitsu, Y.Ueji, T.Oguchi, Y.Hasegawa, Y.Ohashi and Y.Amemiya
X-ray Triple Refraction and Triple Absorption in a Cobalt-Complex Crystal
J. Synchorotron Rad., **5** (1998) 1055.

K.Hayashi, J.Kawai, S.Hayakawa, S.Goto, Y.Nihei and Y.Gohshi
X-ray Fluorescence Holography
J. Jpn. Soc. Synchrotron Rad. Res., **11** (1998) 361. (*in Japanese*).

K.Tsukamoto, I.Nakai and W-.V.Tesch
Do All Freshwater Eels Migrate?
Nature, **396** (1998) 635.

J.Kawai, K.Hayashi, T.Yamamoto, S.Hayakawa and Y.Gohshi
X-Ray Fluorescence Holography of $SrTiO_3$ Compared with X-ray Photoelectron Holography
Anal. Sci., **14** (1998) 903.

T.Yoshitomi, C.Nakayasu, S.Hasegawa, A.Iida and N.Okamoto
Site-Specific Lead Distribution in Scales of Lead-Administered Carp (*Cyprinus carpio*) by Non-Destructive SR-XRF Analysis
Chemosphere, **36** (1998) 2305.

T.Yoshitomi, J.Koyama, A.Iida, N.Okamoto and Y.Ikeda
Cadmium-Induced Scale Deformation in Carp (*Cyprinus carpio*)
Bull. Environ. Contam. Toxic., **60** (1998) 639.

I.Nakai
In situ XAFS Analysis of Secondary Lithium Battery Materials
Denki Kagaku, **66** (1998) 968. (*in Japanese*).

A.Iida, T.Noma and H.Miyata
Characterization of the Local Layer Structure at a Broad Wall in a Surface Stabilized Ferroelectric Liquid Crystal During Electric Field Application Using Synchrotron X-Ray Microdiffraction
Jpn. J. Appl. Phys., **38** (1999) 2845.

I.Nakai, R.Iwata and K.Tsukamoto
Ecological Study of the Migration of Eel by Synchrotron Radiation Induced X-ray Fluorescence Imaging of Otoliths
Spectrochim. Acta B, **54** (1999) 167.

4B2

H.Toraya
Crystal Structure Analysis of Ceramics Powders Using Synchrotron Radiation
Ceramics, **33** (1998) 625. (*in Japanese*).

4C

J.Kokubun, K.Ishida and V.E.Dmitrieko
Forbidden Reflection Excited Owing to the Anisotropy of X-Ray Susceptibility. I. Interference with the Renninger Reflection
J. Phys. Soc. Jpn., **67** (1998) 1291.

Y.Murakami, J.P.Hill, D.Gibbs, M.Blume, I.Koyama, M.Tanaka, H.Kawata, T.Arima, Y.Yokura, K.Hirota and Y.Endoh
Resonant X-ray Scattering from Orbital Ordering in $LaMnO_3$
Phys. Rev. Lett., **81** (1998) 582.

J.Kokubun, T.Nagano, M.Kuribayashi and K.Ishida
Energy Dependence of the ATS Reflections of Iron Pyrite, FeS_2, Near the Fe K-Absorption Edge
J. Phys. Soc. Jpn., **67** (1998) 3114.

H.Nakao, K.Ohwada, N.Takesue, Y.Fujii, M.Isobe, Y.Ueda, H.Sawa, H.Kawada, Y.Murakami, W.I.F.David and R.M.Ibberson
Lattice Dimerization and Strain in Inorganic Spin-Peierls Compound NaV_2O_5
Physica B, **241** (1998) 534.

I.Takahashi, S.Okita, N.Awaji, Y.Sugita and S.Komiya
Microcrystallinity at SiO_2/Si(001) Interfaces: An Effect of Annealing
Physica B, **245** (1998) 306.

Y.Murakami, H.Kawada, H.Kawata, M.Tanaka, T.Arima, Y.Moritomo and Y.Tokura
Direct Observation of Charge-and Orbital-Ordering in a Layered-Perovskite-Type Manganite
J. Jpn. Soc. Synchrotron Rad. Res., **11** (1998) 30. (*in Japanese*).

Y.Murakami
Study on Physical Property by Synchrotron Radiation a. Materials Structure Research by Synchrotron X-ray Diffraction
Radioisotopes, **48** (1999) 65. (*in Japanese*).

6A

S.Yoshikawa, K.Shinzawa-Itoh, R.Nakashima, R.Yaono, E.Yamashita, N.Inoue, M.Yao, M.J.Fei, C.P.Libeu, T.Mizushima, H.Yamaguchi, T.Tomizaki and T.Tsukihara
Redox-Coupled Crystal Structural Changes in Bovine Heart Cytochrome c Oxidase
Science, **280** (1998) 1723.

T.Oyama, M.Kusunoki, Y.Kishimoto, Y.Takasaki and Y.Nitta
Crystallization and Preliminary X-ray Analysis of β-Amylase from *Bacillus Cereus* var. *Mycoides*
Protein & Peptide Lett., **5** (1998) 349.

S.Fushinobu, K.Ito, M.Konno, T.Wakagi and H.Matsuzawa
Crystallographic and Mutational Analyses of an Extremely Acidophilic and Acid-stable Xylanase: Biased Distribution of Acidic Residues and Importance of Asp37 for the Catalysis at Low pH
Protein Engineering, **11** (1998) 1121.

T.Senda, K.Sugimoto, T.Nishizaki, M.Okano, T.Yamada, E.Masai, M.Fukuda and Y.Mitsui
Three-Dimensional Structure of an Extradiol-Type Catechol Ring Cleavage Dioxygenase BphC Derived from *Pseudomonas* sp. Strain KKS102: Structural Features Pertinent to Substrate Specificity and Reaction Mechanisms
Oxygen Homeostasis and Its Dynamics, (1998) 276.

T.Shirai
Alkaline Tolerance of Proteins
Seibutsubutsuri, **219** (1998) 211. (*in Japanese*).

M.Kataoka, K.Yamamoto, S.Shimizu, M.Ohta, A.Kita, Y.Higuchi and K.Miki
Crystallization and Preliminary X-ray Diffraction Study of Lactonohydrolase from *Fusarium Oxysporum*
Acta Cryst., **D54** (1998) 1432.

K.Kitano, K.Motohashi, M.Yoshida and K.Miki
A Novel Approach to Crystallizing Proteins with Temperature Induction Method: GrpE Protein from *Thermus thermophilus*
J. Cryst. Growth, **186** (1998) 456.

Y.Li, M.Takata and A.Nakamura
Size-dependent Enhancement of Nonlinear Optical Susceptibilities Due to Cofined Excitons in CuBr Nanocrystals
Phys. Rev. B, **57** (1998) 9193.

E.Nishibori, M.Takata, M.Sakata, M.Inakuma and H.Shinohara
Determination of the Cage Structure of $Sc@C_{82}$ by Synchrotron Powder Diffraction
Chem. Phys. Lett., **298** (1998) 79.

S.Murakami, K.Shinzawa-Itoh and S.Yoshikawa
Crystals of Bovine Heart Ubiquinol-cytochrome *c* Reductase Diffracting X-ray up to 2.8 ÅResolution at 276K
Acta Cryst., **D54** (1998) 146.

S.Fushinobu, K.Ito, M.Konno and H.Matsuzawa
X-ray Crystallography of Acid Xylanase C from *Aspergillus kawachii*
J. Appl. Glycosci., **45** (1998) 139. (*in Japanese*).

N.Sakabe
Studies on Millisecond Order Dynamics of Protein Crystal Structure Using Synchrotron Radiation
Jyuuten Ryoiki Houkokusho, (1998) (*in Japanese*).

H.K.Song and S.W Suh
Kunitz-type Soybean Trypsin Inhibitor Revisited: Refined Structure of its Complex with Porcine Trypsin Reveals an Insight into the Interaction between a Homologous Inhibitor from *Erythrina Caffra* and Tissue-type Plasminogen Activator
J. Mol. Biol., **275** (1998) 347.

Z.-X.Xia, Y.-N.He, W.-W.Dai, S.A.White, G.D.Boyd and F.S.Mathews
Detailed Active Site Configuration of a New Crystal Form of Methanol Dehydrogenase from *Methylophilus* W3A1 at 1.9ÅResolution
Biochem., **38** (1999) 1214.

A.Kita, S.Kita, K.Fujisawa, K.Inaka, T.Ishida, K.Horiike, M.Nozaki and K.Miki
An Archetypical Extradiol-Cleaving Cathecholic Dioxygenase: The Crystal Structure of Catechol 2,3-Dioxygenase (Metapyrocatechase) from *Pseudomonas Putida* mt-2
Structure, **7** (1999) 25.

T.Inoue, H.Sugawara, S.Hamanaka, H.Tsukui, E.Suzuki, T.Kohzuma and Y.Kai
Crystal Structure Determinations of Oxidized and Reduced Plastocyanin from the Cyanobacterium *Synechococcus* sp. PCC7942
Biochem., **38** (1999) 6063.

H.Komori, N.Sasai, F.Matsunaga, C.Wada and K.Miki
Crystallization and Preliminary X-ray Diffraction Studies of a Replication Intiator Protein (RepE54) of the Mini-F Plasmid Complexes with Iteron DNA
J. Biochem., **125** (1999) 24.

K.Sasaki, N.Watanabe, N.Sakabe and K.Sakabe
Computer Network System with Security for a Protein Data Collection System at the Photon Factory
J. Synchrotron Rad., **6** (1999) 116.

6B

S.Endo, A.Honda, K.Koto, O.Shimomura, T.Kikegawa and N.Hamaya
Crystal Structure of High-pressure Phase-IV Solid Hydrogen Sulfide
Phys. Rev. B, **57** (1998) 5699.

T.Kumagai, K.Muta, Y.Matoba, Y.Kawano, N.Kamiya, J.Davies and M.Sugiyama
Crystallization and Preliminary X-ray Diffraction Studies of Bleomycin-binding Protein from Bleomycin-producing *Streptomyces Verticillus*
Acta. Cryst., **D54** (1998) 127.

S.Nagashima, M.Nakasako, N.Dohmae, M.Tsujimura, K.Takio, M.Odaka, M.Yohda, N.Kamiya and I.Endo
Novel Non-heme Iron Center of Nitrile Hydratase with a Claw Setting of Oxygen Atoms
Nature Structural Biology, **5** (1998) 347.

Y.Yonehara and K.Yakushi
High-pressure Study of One-dimensional Phthalocyanine Conductor, $NiPc(AsF_6)_{0.5}$
Synthetic Metals, **94** (1998) 149.

Y.Izumi, H.Kurakata and K.Akika
Ethanol Synthesis from Carbon Dioxide on $[Rh_{10}Se/TiO_2]$ Catalyst Characterized by X-Ray Absorption Fine Structure Spectroscopy
J. Catal., **175** (1998) 236.

K.Fukumi, A.Chayahara, K.Kadono, H.Kageyama, T.Akai, N.Kitamura, M.Makihara, K.Fujii and J.Hayakawa
Structural Investigation on Implanted Copper Ions in Silica Glass by XAFS Spectroscopy
J. Non-Cryst. Solids, **238** (1998) 143.

N.Watanabe, M.Suzuki, Y.Higashi and N.Sakabe
Rotated-inclined Focusing Monochromator with Simultaneous Tuning of Asymmetry Factor and Radius of Curvature Over a Wide Wavelength Range
J. Synchrotron Rad., **6** (1999) 64.

K.Sasaki, N.Watanabe, N.Sakabe and K.Sakabe
Computer Network System with Security for a Protein Data Collection System at the Photon Factory
J. Synchrotron Rad., **6** (1999) 116.

6C

K.Maehata, K.Ishibashi, T.Noda, H.Nakagawa, H.Akoh, S.Takada, T.Nakajima, H.M.Shimizu, M.Yoshizawa and M.Katagiri
Detection of Synchrotron Radiation by Nb-Based Superconducting Tunnel Junctions
Jpn. J. Appl. Phys., **35** (1998) 78.

T.Tanimori, S.Aoki, Y.Nishi and A.Ochi
Development of a MicroStrip Gas Chamber as a Time-Resolved Area Detector
J. Synchrotron Rad., **5** (1998) 256.

7A

J.G.C.Shen and M.Ichikawa
Intrazeolite Anchoring of Co, Ru, and [Ru-Co] Carbonyl Clusters: Synthesis, Characterization and their Catalysis for CO Hydrogenation
J. Phys. Chem. B, **102** (1998) 5602.

J.G.C.Shen, A.M.Liu, T.Tanaka and M.Ichikawa
Intrazeolite Anchoring of Ruthenium Carbonyl Clusters: Synthesis, Characterization, and their Catalytic Performances
J. Phys. Chem. B, **102** (1998) 7782.

T.Yamamoto, T.Shido, S.Inagaki, Y.Fukushima and M.Ichikawa
A Robust Platinum Carbonyl Cluster Anion $[Pt_3(CO)_6]_5{}^{2-}$ Encapsulated in an Ordered Mesoporous Channel of FSM-16: FTIR/EXAFS/TEM Characterization and Catalytic Performance in the Hydrogenation of Ethene and 1,3-Butadiene
J. Phys. Chem. B, **102** (1998) 3866.

H.Yamashita, S.Kawasaki, Y.Ichihashi, M.Harada, M.Takeuchi, M.Anpo, G.Sterwart, M.A.Fox, C.Louis and M.Che
Characterization of Titanium-Silicon Binary Oxide Catalysts Prepared by the Sol-Gel Method and their Photocatalytic Reactivity for the Liquid-Phase Oxidation of 1-Octanol
J. Phys. Chem. B, **102** (1998) 5870.

S.G.Zhang, S.Higashimoto, H.Yamashita and M.Anpo
Characterization of Vanadium Oxide/ZSM-5 Zeolite Catalysts Prepared by the Solid-State Reaction and their Photocatalytic Reactivity: *In situ* Photoluminescence, XAFS, ESR, FT-IR, and UV-VIS Investigation
J. Phys. Chem. B, **102** (1998) 5590.

Y.Ito, A.M.Vlaicu, T.Tochio, T.Mukoyama, M.Takahashi, S.Emura and Y.Azuma
X-ray-absorption Features from Multielectron Excitations above Xe *L* Edges
Phys. Rev. A, **57** (1998) 873.

J.-H.Choy, Y.-S.Han, S.-H.Hwang, S.-H.Byeon and G.Demazeau
Citrate Route to Sn-Doped $BaTi_4O_9$ with Microwave Dielectric Properties
J. Am. Ceram. Soc., **81** (1998) 3197.

Y.Izumi
X-ray Absorption Fine Structure Spectroscopy as a Probe of Chemical State of Catalysts
Trends in Inorg. Chem., **5** (1998) 43.

Y.Izumi, H.Kurakata and K.Akika
Ethanol Synthesis from Carbon Dioxide on $[Rh_{10}Se/TiO_2]$ Catalyst Characterized by X-Ray Absorption Fine Structure Spectroscopy
J. Catal., **175** (1998) 236.

K.Fukumi, A.Chayahara, K.Kadono, H.Kageyama, T.Akai, N.Kitamura, M.Makihara, K.Fujii and J.Hayakawa
Structural Investigation on Implanted Copper Ions in Silica Glass by XAFS Spectroscopy
J. Non-Cryst. Solids, **238** (1998) 143.

A.Kozlov, A.K.Kozlova, K.Asakura and Y.Iwasawa
Zeolite-Encapsulated Vanadium Picolinate Peroxo Complexes Active for Catalytic Hydrocarbon Oxidations
J. Mol. Catal. A: Chemical., **137** (1999) 223.

M.Sakurai and M.Matsuura
Local Structure Analysis around Small Amount of Additives by Means of X-ray Absorption Fine Structure
Met. Technol., **69** (1999) 396. (*in Japanese*).

Y.-S.Hong, J.Darriet, J.-B.Yoon and J.-H.Choy
X-Ray Absorption Near Edge Structure and X-Ray Diffraction Studies of New Cubic $CsVTeO_5$ and $CsVTeO_6$ Compounds
Jpn. J. Appl. Phys., **38** (1999) 1506.

E.Yanase, I.Watanabe, M.Harada, M.Takahashi, Y.Dake and Y.Hiroshima
Probing Depth Study of Conversion Electron/He Ion Yield XAFS Spectroscopy on Strontium Titanate Thin Films
Anal. Sci., **15** (1999) 255.

J.-H.Choy, S.-J.Hwang and W.Lee
Anomalous Thermoelectric Power Behaviors of Lodine Intercalated $(Bi,Pb)_2Sr_2Ca_{n-1}Cu_nO_{2n+4+\delta}$ Superconductors ($n = 2$ and 3)
J. Solid State Chem., **142** (1999) 199.

T.Inoue, Y.Kubozono, K.Hiraoka, K.Mimura, H.Maeda, S.Kashino, S.Emura, T.Uruga and Y.Nakata
XAFS Study on $Eu@C_{60}$
J. Synchrotron Rad., **6** (1999) 779.

Y.Kubozono, K.Mimura, Y.Takabayashi, H.Maeda, S.Kashino, S.Emura, Y.Nishihata, T.Uruga, T.Tanaka and M.Takahashi
XAFS Study on RbC_{60}
J. Synchrotron Rad., **6** (1999) 564.

I.Nakai, Y.Shiraishi and F.Nishikawa
Development of a New *in situ* Cell for the X-ray Absorption Fine Structure Analysis of the Electrochemical Reaction in a Rechargeable Battery and its Application to the Lithium Battery Material, $Li_{1+y}Mn_{2-y}O_4$
Spectrochim. Acta B, **54** (1999) 143.

M.Shirai and M.Arai
Structure and Catalysis of Ion-Exchanged Nickel Species during Pyrolysis of Loy Yang Coal
Energy and Fuels, **13** (1999) 465.

S.Sugiyama, T.Yasutomi, T.Moriga, H.Hayashi and J.B.Moffat
Preparative Enhancement of the Thermal Stability of Calcium Hydroxyapatites
J. Solid State Chem., **142** (1999) 319.

J.-H.Choy, S.-J.Kwon, S.-J.Hwang, Y.-I.Kim and W.Lee
Intercalation Route to Nano-hybrids: Inorganic/organic-high T_c Cuprate Hybird Materials
J. Mater. Chem., **9** (1999) 129.

9A

M. Nomura and A. Koyama
Design of an XAFS Beamline at the Photon Factory: Possibilities of Bent Conical Mirrors
J. Synchrotron rad., **6** (1999) 182.

9C

K.Akimoto, M.Lijadi and A.Ichimiya
Interface Structure and Preferred Orientation of Ag/Si(111) Revealed by X-ray Diffraction
Surf. Rev. Lett., **5** (1998) 719.

10A

S.Sasaki, T.Toyoda, K.Yamawaki and K.Ohkubo
Valence-Difference Contrast Measurements Utilizing X-ray Anomalous Scattering
J. Synchrotron Rad., **5** (1998) 920.

A.Okita, F.Saito, S.Sasaki, T.Toyoda and H.Koinuma
Determination of Cation Distribution in Mn-Zn-Fe Ferrite by X-ray Anomalous Scattering
Jpn. J. Appl. Phys., **37** (1998) 3441.

N.Sugioka, K.Matsumoto, M.Tanaka, T.Mori and S.Sasaki
DAFS Measurements by the Imaging-Plate Weissenberg Method
J. Synchrotron Rad., **5** (1998) 908.

K.Yamasaki, Y.Soejima and K.F.Fischer
Superstructure Determination of $PbZrO_3$
Acta. Cryst., **B54** (1998) 524.

Y.Yamada, N.Ikeda and S.Nohdo
Valence Fluctuation and Polarization Fluctuation in Mixed Valence System
Kotaibutsuri, **33** (1998) 692. (*in Japanese*).

E.Takahashi and K.Kohn
Dielectric Dispersion and Charge Ordering of $LuFe_2O_4$
J. Korean Phys. Soc., **32** (1998) S44.

N.Ikeda, S.Nohdo and Y.Yamada
Charge Ordering of $LuFe_2O_4$ Observed by an Anomalous X-ray Dispersion
J. Korean Phys. Soc., **32** (1998) S165.

N.Ikeda, Y.Yamada, S.Nohdo, T.Inami and S.Katano
Incommensurate Charge Ordering in Mixed Valence System $LuFe_2O_4$
Physica B, **241** (1998) 820.

S.Sasaki
A Potential of the X-ray Powder Diffraction Method for Determining the Valence in Crystals
KEK Proc., **97-22** (1998) 90. (*in Japanese*).

T.Toyoda, S.Sasaki and M.Tanaka
Evidence of Charge Ordering of Fe^{2+} and Fe^{3+} in Magnetite Observed by Synchrotron X-ray Anomalous Scattering
Am. Mineralogist, **84** (1999) 294.

10B

T.Yokoyama
Path-Integral Effective-Potential Method Applied to Extended X-Ray-Absorption Fine-Structure Cumulants
Phys. Rev. B, **57** (1998) 3423.

S.Sugiyama, T.Minami, T.Moriga, H.Hayashi and J.B.Moffat
Calcium-Lead Hydroxyapatites: Thermal and Structural Properties and the Oxidation of Methane
J. Solid State Chem., **135** (1998) 86.

S.Sugiyama, Y.Iguchi, H.Nishioka, T.Minami, T.Moriga, H.Hayashi and J.B.Moffat
Effects of the Thermal Stability and the Fine Structure Changes of Strontium Hydroxyapatites Ion-Exchanged with Lead on Methane Oxidation in the Presence and Absence of Tetrachloromethane
J. Catal., **176** (1998) 25.

Y.Izumi, K.Oshihara and K.Aika
Characterization of Active Site on Cobalt-Magnesium Oxide by X-ray Absorption Fine Structure Spectroscopy
Chem. Lett., **8** (1998) 727.

K.Abe, O.Uemura, T.Usuki, Y.Kameda and M.Sakurai
The Local Atomic Arrangement in the Amorphous As-Te-I System
J. Non-Cryst. Solids., **232** (1998) 682.

I.Nakai and T.Nakagome
In situ Transmission X-Ray Absorption Fine Structure Analysis of the Li Deintercalation Process in $Li(Ni_{0.5}Co_{0.5})O_2$
Electrochem. Solid-State Lett., **1** (1998) 259.

T.Arikawa, Y.Takasu, Y.Murakami, K.Asakura and Y.Iwasawa
Characterization of the Structure of RuO_2-IrO_2/Ti Electrodes by EXAFS
J. Phys. Chem., **102** (1998) 3736.

S.Sugiyama, T.Yasutomi, T.Moriga, H.Hayashi and J.B.Moffat
Preparative Enhancement of the Thermal Stability of Calcium Hydroxyapatites
J. Solid State Chem., **142** (1999) 319.

J.-H.Choy, S.-J.Kwon, S.-J.Hwang, Y.-I.Kim and W.Lee
Intercalation Route to Nano-hybrids: Inorganic/organic-high T_c Cuprate Hybird Materials
J. Mater. Chem., **9** (1999) 129.

9A

M. Nomura and A. Koyama
Design of an XAFS Beamline at the Photon Factory: Possibilities of Bent Conical Mirrors
J. Synchrotron rad., **6** (1999) 182.

9C

K.Akimoto, M.Lijadi and A.Ichimiya
Interface Structure and Preferred Orientation of Ag/Si(111) Revealed by X-ray Diffraction
Surf. Rev. Lett., **5** (1998) 719.

10A

S.Sasaki, T.Toyoda, K.Yamawaki and K.Ohkubo
Valence-Difference Contrast Measurements Utilizing X-ray Anomalous Scattering
J. Synchrotron Rad., **5** (1998) 920.

A.Okita, F.Saito, S.Sasaki, T.Toyoda and H.Koinuma
Determination of Cation Distribution in Mn-Zn-Fe Ferrite by X-ray Anomalous Scattering
Jpn. J. Appl. Phys., **37** (1998) 3441.

N.Sugioka, K.Matsumoto, M.Tanaka, T.Mori and S.Sasaki
DAFS Measurements by the Imaging-Plate Weissenberg Method
J. Synchrotron Rad., **5** (1998) 908.

K.Yamasaki, Y.Soejima and K.F.Fischer
Superstructure Determination of $PbZrO_3$
Acta. Cryst., **B54** (1998) 524.

Y.Yamada, N.Ikeda and S.Nohdo
Valence Fluctuation and Polarization Fluctuation in Mixed Valence System
Kotaibutsuri, **33** (1998) 692. (*in Japanese*).

E.Takahashi and K.Kohn
Dielectric Dispersion and Charge Ordering of $LuFe_2O_4$
J. Korean Phys. Soc., **32** (1998) S44.

N.Ikeda, S.Nohdo and Y.Yamada
Charge Ordering of $LuFe_2O_4$ Observed by an Anomalous X-ray Dispersion
J. Korean Phys. Soc., **32** (1998) S165.

N.Ikeda, Y.Yamada, S.Nohdo, T.Inami and S.Katano
Incommensurate Charge Ordering in Mixed Valence System $LuFe_2O_4$
Physica B, **241** (1998) 820.

S.Sasaki
A Potential of the X-ray Powder Diffraction Method for Determining the Valence in Crystals
KEK Proc., **97-22** (1998) 90. (*in Japanese*).

T.Toyoda, S.Sasaki and M.Tanaka
Evidence of Charge Ordering of Fe^{2+} and Fe^{3+} in Magnetite Observed by Synchrotron X-ray Anomalous Scattering
Am. Mineralogist, **84** (1999) 294.

10B

T.Yokoyama
Path-Integral Effective-Potential Method Applied to Extended X-Ray-Absorption Fine-Structure Cumulants
Phys. Rev. B, **57** (1998) 3423.

S.Sugiyama, T.Minami, T.Moriga, H.Hayashi and J.B.Moffat
Calcium-Lead Hydroxyapatites: Thermal and Structural Properties and the Oxidation of Methane
J. Solid State Chem., **135** (1998) 86.

S.Sugiyama, Y.Iguchi, H.Nishioka, T.Minami, T.Moriga, H.Hayashi and J.B.Moffat
Effects of the Thermal Stability and the Fine Structure Changes of Strontium Hydroxyapatites Ion-Exchanged with Lead on Methane Oxidation in the Presence and Absence of Tetrachloromethane
J. Catal., **176** (1998) 25.

Y.Izumi, K.Oshihara and K.Aika
Characterization of Active Site on Cobalt-Magnesium Oxide by X-ray Absorption Fine Structure Spectroscopy
Chem. Lett., **8** (1998) 727.

K.Abe, O.Uemura, T.Usuki, Y.Kameda and M.Sakurai
The Local Atomic Arrangement in the Amorphous As-Te-I System
J. Non-Cryst. Solids., **232** (1998) 682.

I.Nakai and T.Nakagome
In situ Transmission X-Ray Absorption Fine Structure Analysis of the Li Deintercalation Process in $Li(Ni_{0.5}Co_{0.5})O_2$
Electrochem. Solid-State Lett., **1** (1998) 259.

T.Arikawa, Y.Takasu, Y.Murakami, K.Asakura and Y.Iwasawa
Characterization of the Structure of RuO_2-IrO_2/Ti Electrodes by EXAFS
J. Phys. Chem., **102** (1998) 3736.

M.Takemoto, H.Ikawa, N.Ohashi, T.Ohyama, T.Tsurumi, O.Fukunaga, J.Tanaka and A.Watanabe
Cu *K* Edge X-ray Absorption Spectra of $La_2SrCu_2O_6$-Type Superconductor
Physica C, **302** (1998) 151.

Y.Kawakita, R.Matsubara, H.Nakashima and S.Takeda
Structure of Liquid In-Te Mixtures
J. Non-Cryst. Solids, **232** (1998) 483.

H.Kageyama, K.Kadono, K.Fukumi, T.Saito and T.Kuji
Extended X-ray Absorption Fine Structure Study on Amorphous Nd-Fe-B Alloys
J. Mater. Res., **13** (1998) 2132.

S.Sugiyama, H.Nishioka, T.Moriga, H.Hayashi and J.B.Moffat
Ion-Exchange Properties of Strontium Hydroxyapatite under Acidic Conditions
Separation Sci. Tech., **33** (1998) 1992.

K.Kadono, M.Shojiya, H.Kageyama, N.Kamijo, Y.Kawamoto and H.Tanaka
Extended X-ray Absorption Fine Structure Study and Molecular Dynamics Simulation Studies on the Structure of CuX- and AgX-based Glasses (X=Cl, Br and I)
J. Phys. : Condens. Matter., **10** (1998) 5007.

K.Okumura, K.Asakura and Y.Iwasawa
Reversible Structure Change of One-Atomic Layer GeO_2 on SiO_2 Surface under the Interaction with Rh Particles by *in situ* XAFS Studies
Catal. Today, **39** (1998) 343.

Y.Tanaka, H.Shimada, N.Matsubayashi, A.Nishijima and M.Nomura
Accelerated Deactivation of Hydrotreating Catalysts: Comparison to Long-term Deactivation in a Commercial Plant
Catal. Today, **45** (1998) 319.

K.Nishi, K.Shimizu, M.Takamatsu, H.Yoshida, A.Satsuma, T.Tanaka, S.Yoshida and T.Hattori
Deconvolution Analysis of Ga K-edge XANES for Quantification of Gallium Coordinations in Oxide Evnironments
J. Phys. Chem. B, **102** (1998) 10190.

T.Yokoyama, Y.Murakami, M.Kiguchi, T.Komatsu and N.Kojima
Spin-crossover Phase Transition of a Chain Fe(II) Complex Studied by X-ray-absorption Fine-structure Spectroscopy
Phys. Rev. B, **58** (1998) 14238.

N.Matsubayashi, H.Yasuda, M.Imamura and Y.Yoshimura
EXAFS Study on Pd-Pt Catalyst Supported on USY Zeolite
Catal. Today, **45** (1998) 375.

J.G.C.Shen and M.Ichikawa
Intrazeolite Anchoring of Co, Ru, and [Ru-Co] Carbonyl Clusters: Synthesis, Characterization and their Catalysis for CO Hydrogenation
J. Phys. Chem. B, **102** (1998) 5602.

J.G.C.Shen, A.M.Liu, T.Tanaka and M.Ichikawa
Intrazeolite Anchoring of Ruthenium Carbonyl Clusters: Synthesis, Characterization, and their Catalytic Performances
J. Phys. Chem. B, **102** (1998) 7782.

T.Yamamoto, T.Shido, S.Inagaki, Y.Fukushima and M.Ichikawa
A Robust Platinum Carbonyl Cluster Anion $[Pt_3(CO)_6]_5^{2-}$ Encapsulated in an Ordered Mesoporous Channel of FSM-16: FTIR/EXAFS/TEM Characterization and Catalytic Performance in the Hydrogenation of Ethene and 1,3-Butadiene
J. Phys. Chem. B, **102** (1998) 3866.

S.D.Moreno, J.M.Martínez, A.M.Páez, H.Sakane and I.Watanabe
Molecular Structure Determination by EXAFS of $[Y(NCS)_6]^{3-}$ Units in Solid State and in Solution. A Comparison with Density Functional Theory Calculations
J. Phys. Chem. A, **102** (1998) 7435.

H.Yamashita, S.Kawasaki, Y.Ichihashi, M.Harada, M.Takeuchi, M.Anpo, G.Sterwart, M.A.Fox, C.Louis and M.Che
Characterization of Titanium-Silicon Binary Oxide Catalysts Prepared by the Sol-Gel Method and their Photocatalytic Reactivity for the Liquid-Phase Oxidation of 1-Octanol
J. Phys. Chem. B, **102** (1998) 5870.

S.G.Zhang, S.Higashimoto, H.Yamashita and M.Anpo
Characterization of Vanadium Oxide/ZSM-5 Zeolite Catalysts Prepared by the Solid-State Reaction and their Photocatalytic Reactivity: *In situ* Photoluminescence, XAFS, ESR, FT-IR, and UV-VIS Investigation
J. Phys. Chem. B, **102** (1998) 5590.

Y.Inada, Y.Sugimoto, Y.Nakano, Y.Itoh and S.Funahashi
Formation and Deprotonation Kinetics of the Sitting-Atop Complex of Copper(II) Ion with 5,10,15,20-Tetraphenylporphyrin Relevant to the Porphyrin Metalation Mechanism. Structure of Copper(II)-Pyridine Complexes in Acetonitrile As Determined by EXAFS Spectroscopy
Inorg. Chem., **37** (1998) 5519.

I.Nakai
In situ XAFS Analysis of Secondary Lithium Battery Materials
Denki Kagaku, **66** (1998) 968. (*in Japanese*).

J.-H.Choy, D.-H.Kim, D.-Y.Seung and A.Levasseur
X-Ray Absorption Spectroscopic Studies at the Arsenic K-Edge for New Ternary Li_2S-B_2S_3-As_2S_3 Glass Systems
J. Phys. Chem. Solids, **59** (1998) 1579.

L.Nagy, S.Yamaguchi, T.Mitsunaga, H.Wakita, M.J.-Bojczuk, M.Nomura and H.Kozlowski
Study of Local Structure of Cu^{II} Complex of 2-amino-1, 6-anhydro-2-deoxy-β-D-glucopyranose in Aqueous Solution by X-ray Absorption Spectroscopy
Acta Chem. Hung. -Models in Chem., **135** (1998) 941.

T.Nakagome and I.Nakai
Structure Analysis of $Li(Ni,Co)O_2$ Solid Solution by XAFS and X-ray Rietveld Methods
Denki Kagaku, **66** (1998) 727. (*in Japanese*).

Y.Izumi
X-ray Absorption Fine Structure Spectroscopy as a Probe of Chemical State of Catalysts
Trends in Inorg. Chem., **5** (1998) 43.

Y.Izumi, H.Kurakata and K.Akika
Ethanol Synthesis from Carbon Dioxide on $[Rh_{10}Se/TiO_2]$ Catalyst Characterized by X-Ray Absorption Fine Structure Spectroscopy
J. Catal., **175** (1998) 236.

S.Imamura, H.Sasaki, M.Shono and H.Kanai
Structure of Molybdenum Supported on α-, γ-, and χ-Aluminas in Relation to its Epoxidation Activity
J. Catal., **177** (1998) 72.

H.Yasuda, N.Matsubayashi, T.Sato and Y.Yoshimura
Confirmationof Sulfur Tolerance of Bimetallic Pd-Pt Supported o Highly Acidic USY Zeolite by EXAFS
Catal. Lett., **54** (1998) 23.

L.Nagy, S.Yamashita, T.Yamaguchi, P.Sipos, H.Wakita and M.Nomura
The Local Structures of Cu(II) and Zn(II) Complexes of Hyaluronate
J. Inorg. Biochem., **72** (1998) 49.

L.Nagy, T.Yamaguchi, M.Nomura, T.Páli and H.Ohtaki
The Structure of D-Ribose and D-Glucosamine Complexes of Copper (II). Electronic, EPR and EXAFS Spectral Studies
Acta Chem. Hung. -Models in Chem., **135** (1998) 129.

R.Kumashiro, Y.Kurada and M.Nagao
New Analysis of Oxidation State and Coordination Environment of Copper Ion-Exchanged in ZSM-5 Zeolite
J. Phys. Chem. B, **103** (1999) 89.

N.Kawamura, H.Maruyama, K.Kobayashi, S.Uemura, A.Urata and H.Yamazaki
Multielectron Excitations in $3d$ Transition Metal Compounds Probed by X-Ray Magnetic Circular Dichroism
J. Phys. Soc. Jpn., **68** (1999) 923.

I.Nakai, Y.Shiraishi and F.Nishikawa
Development of a New *in situ* Cell for the X-ray Absorption Fine Structure Analysis of the Electrochemical Reaction in a Rechargeable Battery and its Application to the Lithium Battery Material, $Li_{1+y}Mn_{2-y}O_4$
Spectrochim. Acta B, **54** (1999) 143.

J.-H.Choy, S.-J.Hwang and W.Lee
Anomalous Thermoelectric Power Behaviors of Lodine Intercalated $(Bi,Pb)_2Sr_2Ca_{n-1}Cu_nO_{2n+4+\delta}$ Superconductors ($n = 2$ and 3)
J. Solid State Chem., **142** (1999) 199.

M.Shirai and M.Arai
Structure and Catalysis of Ion-Exchanged Nickel Species during Pyrolysis of Loy Yang Coal
Energy and Fuels, **13** (1999) 465.

K.Asakura, T.Shido, Y.Noguchi and Y.Iwasawa
Synthesis of Mo Dimer Oxocarbide Species in NaY Supercages and its Catalytic Methanol Decomposition Reaction
Catal., **41** (1999) 116. (*in Japanese*).

Y.Kubozono, K.Mimura, Y.Takabayashi, H.Maeda, S.Kashino, S.Emura, Y.Nishihata, T.Uruga, T.Tanaka and M.Takahashi
XAFS Study on RbC_{60}
J. Synchrotron Rad., **6** (1999) 564.

K.Shimizu, M.Takamatsu, K.Nishi, H.Yoshida, A.Satsuma, T.Tanaka, S.Yoshida and T.Hattori
Alumina-Supported Gallium Oxide Catalysts for NO Selective Reduction: Influence of the Local Structure of Surface Gallium Oxide Species on the Catalytic Activity
J. Phys. Chem. B, **103** (1999) 1542.

Y.Kuroda, R.Kumashiro, T.Yoshimoto and M.Nagao
Characterization of Active Sites on Copper Ion-exchanged ZSM-5-type Zeolite for NO Decomposition Reaction
Phys. Chem. Chem. Phys., **1** (1999) 649.

D.Li, N.Ichikuni, S.Shimazu and T.Uematsu
Hydrogenation of CO_2 Over Sprayed Ru/TiO_2 Fine Particles and Strong Metal-Support Interaction
Appl. Catal. A: General, **180** (1999) 227.

K.Asakura, Y.Noguchi and Y.Iwasawa
Stepwise Synthesis and Structure Analysis of Mo Dimers in NaY Zeolite
J. Phys. Chem. B, **103** (1999) 1051.

K.Ebitani, Y.Fujie and K.Kaneda
Immobilization of Ligand-Preserved Giant Palladium Cluster on a Metal Oxide Surface and its Nobel Heterogenous Catalysis for Oxidation of Allylic Alcohols in the Presence of Molecular Oxygen
Langmuir, **15** (1999) 3557.

J.-H.Choy, S.-J.Kwon, S.-J.Hwang, Y.-I.Kim and W.Lee
Intercalation Route to Nano-hybrids: Inorganic/organic-high T_c Cuprate Hybird Materials
J. Mater. Chem., **9** (1999) 129.

C.Li, K.Lu, Y.Wang, K.Tamura, S.Hosokawa and M.Inui
Electronic Structure Study of Liquid Germanium Based on X-ray-absorption Near-edge Structure Spectroscopy
Phys. Rev. B, **59** (1999) 1571.

S.Sugiyama, T.Nakanishi, T.Ishimura, T.Moriga, H.Hayashi, N.Shigemoto and J.B.Moffa
Preparation, Characteization, and Thermal Stability of Lead Hydroxyapatite
J. Solid State Chem., **143** (1999) 296.

10C

M.Hirai
Synchrotron X-Ray Scattering Studies of Micellar Systems Composed of Biological Lipids
Membrame, **23** (1998) 8. (*in Japanese*).

M.Hirai, H.Iwase, S.Arai, T.Takizawa and K.Hayashi
Interaction of Gangliosides with Proteins Depending on Oligosaccharide Chain and Protein Surface Modification
Biophys. J., **74** (1998) 1380.

M.Hirai, S.Arai, H.Iwase and T.Takizawa
Small-Angle X-Ray Scattering and Calorimetric Studies of Thermal Conformational Change of Lysozyme Depending on pH.
J. Phys. Chem., **102** (1998) 1308.

M.Hirai, S.Arai, T.Takizawa, S.Yabuki and Y.Nakata
Characterisitics of Themotropic Phase Transition of Glycosphingolipid(ganglioside) Aggregates in Aqueous Solution
Thermochimica Acta, **308** (1998) 93.

Y.Izumi, H.Takezawa, N.Kikuta, S.Uemura and A.Tsutsumi
Two-Stage Melting in Dilute Gels of Poly(γ-benzyl L-glutamate)
Macromolecules, **31** (1998) 430.

M.Kato and T.Fujisawa
High-Pressure Solution X-ray Scattering of Protein Using a Hydrostatic Cell with Diamond Windows
J. Synchrotron Rad., **5** (1998) 1282.

H.Iijima, T.Kato, H.Yoshida and M.Imai
Small-Angle X-ray and Neutron Scattering from Dilute Solutions of Cesium Perfluorooctanoate. Micellar Growth along Two Dimensions
J. Phys. Chem., **102** (1998) 990.

Y.Hagihara, M.Hoshino, D.Hamada, M.Kataoka and Y.Goto
Chain-like Conformation of Heat-denatured Ribonuclease A and Cytochrome c as Evidenced by Solution X-ray Scattering
Folding & Design, **3** (1998) 195.

N.Matsushima, Y.Izumi and T.Aoba
Small-angle X-ray Scattering and Computer-Aided Molecular Modeling Studies of 20 kDa Fragment of Porcine Amelogenin: Does Amelogenin Adopt an Elongated Bundle Structure?
J. Biochem., **123** (1998) 150.

T.Oba, H.Furukawa, Z.-Y.Wang, T.Nozawa, M.Mimuro, H.Tamiaki and T.Watanabe
Supramolecular Structures of the Chlorophyll *a'* Aggregate and the Origin of the Diastereoselective Separation of Chlorophyll *a* and *a'*
J. Phys. Chem., **102** (1998) 7882.

S.Nojima, Y.Kanda and S.Sasaki
Time-Resolved Small-Angle X-Ray Scattering Studies on the Melting Behavior of Poly(ϵ-caprolactone)-*block*-Polybutadiene Copolymers
Polymer J., **30** (1998) 628.

K.Urayama, T.Kawamura, Y.Hirata and S.Kohjiya
SAXS Study on Poly(dimethylsiloxane) Networks with Controlled Distributions of Chain Lengths between Crosslinks
Polymer, **39** (1998) 3827.

H.Yoshida and M.Honma
Structure Formation of Syndiotactic Polystyrene From the Molthen State Observed by the Simultaneous DSC/SR-XRD Method
Rep. Prog. Polym. Phys. Jpn., **41** (1998) 303.

S.Sakurai, H.Umeda, C.Furukawa, H.Irie, S.Nomura, H.H.Lee and J.K.Kim
Thermally Induced Morphological Transition from Lamella to Gyroid in a Binary Blend of Diblock Copolymers
J. Chem. Phys., **108** (1998) 4333.

S.Sakurai, H.Irie, H.Umeda, S.Nomura, H.H.Lee and J.K.Kim
Gyroid Structure and Morphological Control in Binary Blends of Polystyrene-*block*-polyisoprene Diblock Copolymers
Macromolecules, **31** (1998) 336.

M.Hirai and T.Takizawa
Intensive Extrusion and Occlussion of Water in Ganglioside Micelle with Thermal Reversibility
Biophys. J., **74** (1998) 3010.

S.Arai and M.Hirai
Synchrotron Radiation Small-angle X-ray Scattering Study of Structural Transition and Gelation of Hen Egg-White Lysozyme Depending on pH and Ionic Strength under Isothermal Heating
Koubunshi Ronbunshu, **55** (1998) 654. (*in Japanese*).

Y.Hirata, S.Kohjiya, Y.Ikeda, H.Urakawa and K.Kajiwara
Time-Resolved Small-Angle X-ray Scattering Measurement of Organic/Inorganic Hybrid Gels During Drying Process
Proc. Polymer Network 98, (1998) 22.

H.Yoshida, K.Masaka, K.Baba and S.Nakamura
Liquid-Crystal Formation of Polyesters Containing Phenanthrene Moieties in the Main Chain Observed by the Simultaneous DSC/SR-XRD Method
Rep. Prog. Polym. Phys. Jpn., **41** (1998) 211.

H.Umeda, S.Sakurai, Y.Kitagawa, Y.Suda, J.Masamoto and S.Nomura
Studies on Morphologies and Mechanical Properties of Polystyrene-Block-Polyethylenebutylene-Block-Polystyrene Triblock Copolymers
J. Chem. Phys., **108** (1998) 4333.

H.Kanaya, K.Hara, A.Nakamura, N.Hiramatsu and E.Takushi
Time Resolved Small-Angle X-Ray Scattering Study on Gel-dehydration Processes of Heat-and Pressure-Treated Egg White
Proc. 2nd Tohwa Univ. Inter. Meeting, (1998) 184.

Y.Kamatari, S.Ohji, T.Konno, Y.Seki, K.Soda, M.Kataoka and K.Akasaka
The Compact and Expanded Denatured Conformations of Apomyoglobin in the Methanol-water Solvent
Protein Sci., **8** (1999) 873.

S.Arai and M.Hirai
Reversibility and Hierarchy of Themal Transition of Hen Egg-white Lysozyme Studied bu SR-SAXS
Biophys. J., **76** (1999) 2192.

S.Nojima, N.Kikuchi, A.Rohadi, S.Tanimoto and S.Sasaki
Melting Behavior of Poly(ϵ-caprolactone)-*block – PolybutadieneCopolymers*
Macromolecules, **32** (1999) 3727.

M.Hirai, S.Arai and H.Iwase
Complementary Analysis of Thermal Transition Multiplicity of Hen Egg-White Lysozyme at Low pH Using X-ray Scattering and Scanning Calorimetry
Phys. Chem. B, **103** (1999) 549.

M.Oosawa, S.Kuwamoto, Y.Izumi, K.L.Yap, M.Ikura, T.Shibanuma, H.Yokokura, H.Hidaka and N.Matsushima
Evidence for Calmodulin Inter-domain Compaction in Solution Induced by W-7 Binding
FEBS Lett., **442** (1999) 173.

11A

Y.Kitajima, K.Amemiya, Y.Yonamoto, T.Ohta, T.Kikuchi, T.Kosuge, A.Toyoshima and K.Ito
A Soft X-Ray (80 - 1500 eV) Grazing-Incidence Monochromator with Varied-Line-Spacing Plane Gratings at PF-BL-11A
J. Synchrotron Rad., **5** (1998) 729.

K.Amemiya, Y.Kitajima, Y.Yonamoto, S.Terada, H.Tsukabayash,T.Yokoyama and T.Ohta
Oxygen K-edge X-ray Absorption Fine Structure Study of Surface Methoxy Species on Cu(111) and Ni(111)
Phys. Rev. B, **59** (1999) 2307.

J.Kawai, K.Hayashi, H.Takahashi and Y.Kitajima
Micro-XANES by EPMA Spectrometer
J. Synchrotron Rad., **6** (1999) 356.

Y.Yamamoto, H.Ohara, I.Mori, K.Kajikawa, H.Ishii, Y.Kitajima, T.Imae, K.Seki and Y.Ouchi
NEXAFS Studies on the Structure of Perfluoroalkyl Carbonic Acid Langmuir Blodgett Films
J. Synchrotron Rad., **6** (1999) 796.

Y.Kitajima, Y.Yonamoto, K.Amemiya, H.Tsukabayashi, T.Ohta and K.Ito
Recent Performance of the Soft X-Ray (70 - 1900 eV) Bending Magnet Beamline 11A at the Photon Factory
J. Elec. Spec. Relat. Phenom., **101-103** (1999) 927.

11B

K.Akimoto, T.Kobayashi, T.Ogawa, W.Ohtsuka, T.Maruyama and Y.Kitajima
Configuration of Cl Atoms in ZnSe and ZnTe
J. Cryst. Growth, **184** (1998) 480.

J.Kawai, K.Hayashi, H.Amano, H.Takenaka and Y.Kitajima
Surface Analysis of Si/W Multilayer Using Total Reflaction X-ray Photoelectron Spectroscopy
J. Elec. Spec. Relat. Phenom, **88** (1998) 787.

S.Tohno, J.Kawai, S.Chatani, M.Ohta, Y.Kitajima, K.Yamamoto, Y.Kitamura and M.Kasahara
Application of X-ray Absorption Fine Structure (XAFS) Spectrometry to Identify the Chemical States of Atmospheric Aerosols
J. Aersol Sci., **29** (1998) S235.

A.Imanishi, T.Yokoyama, Y.Kitajima and T.Ohta
Structural and Electronic Properties of Adsorbed Thiophene on Cu(111) Studied by S K-Edge X-Ray Absorption Spectroscopy
Bull. Chem. Soc. Jpn., **71** (1998) 831.

A.Imanishi, K.Isawa, F.Matsui, T.Tsuduki,T.Yokoyama, H.Kondoh, Y.Kitajima and T.Ohta
Structural Studies of Adsorbed Alkanethiols on Cu(111) by Use of S and C K-edge X-ray Absorption Fine Structures
Surf. Sci., **407** (1998) 282.

Y.Hirata, S.Kohjiya, Y.Ikeda, H.Urakawa and K.Kajiwara
Time-Resolved Small-Angle X-ray Scattering Measurement of Organic/Inorganic Hybrid Gels During Drying Process
Proc. Polymer Network 98, (1998) 22.

H.Yoshida, K.Masaka, K.Baba and S.Nakamura
Liquid-Crystal Formation of Polyesters Containing Phenanthrene Moieties in the Main Chain Observed by the Simultaneous DSC/SR-XRD Method
Rep. Prog. Polym. Phys. Jpn., **41** (1998) 211.

H.Umeda, S.Sakurai, Y.Kitagawa, Y.Suda, J.Masamoto and S.Nomura
Studies on Morphologies and Mechanical Properties of Polystyrene-Block-Polyethylenebutylene-Block-Polystyrene Triblock Copolymers
J. Chem. Phys., **108** (1998) 4333.

H.Kanaya, K.Hara, A.Nakamura, N.Hiramatsu and E.Takushi
Time Resolved Small-Angle X-Ray Scattering Study on Gel-dehydration Processes of Heat-and Pressure-Treated Egg White
Proc. 2nd Tohwa Univ. Inter. Meeting, (1998) 184.

Y.Kamatari, S.Ohji, T.Konno, Y.Seki, K.Soda, M.Kataoka and K.Akasaka
The Compact and Expanded Denatured Conformations of Apomyoglobin in the Methanol-water Solvent
Protein Sci., **8** (1999) 873.

S.Arai and M.Hirai
Reversibility and Hierarchy of Themal Transition of Hen Egg-white Lysozyme Studied bu SR-SAXS
Biophys. J., **76** (1999) 2192.

S.Nojima, N.Kikuchi, A.Rohadi, S.Tanimoto and S.Sasaki
Melting Behavior of Poly(ϵ-caprolactone)-*block – PolybutadieneCopolymers*
Macromolecules, **32** (1999) 3727.

M.Hirai, S.Arai and H.Iwase
Complementary Analysis of Thermal Transition Multiplicity of Hen Egg-White Lysozyme at Low pH Using X-ray Scattering and Scanning Calorimetry
Phys. Chem. B, **103** (1999) 549.

M.Oosawa, S.Kuwamoto, Y.Izumi, K.L.Yap, M.Ikura, T.Shibanuma, H.Yokokura, H.Hidaka and N.Matsushima
Evidence for Calmodulin Inter-domain Compaction in Solution Induced by W-7 Binding
FEBS Lett., **442** (1999) 173.

11A

Y.Kitajima, K.Amemiya, Y.Yonamoto, T.Ohta, T.Kikuchi, T.Kosuge, A.Toyoshima and K.Ito
A Soft X-Ray (80 - 1500 eV) Grazing-Incidence Monochromator with Varied-Line-Spacing Plane Gratings at PF-BL-11A
J. Synchrotron Rad., **5** (1998) 729.

K.Amemiya, Y.Kitajima, Y.Yonamoto, S.Terada, H.Tsukabayash,T.Yokoyama and T.Ohta
Oxygen K-edge X-ray Absorption Fine Structure Study of Surface Methoxy Species on Cu(111) and Ni(111)
Phys. Rev. B, **59** (1999) 2307.

J.Kawai, K.Hayashi, H.Takahashi and Y.Kitajima
Micro-XANES by EPMA Spectrometer
J. Synchrotron Rad., **6** (1999) 356.

Y.Yamamoto, H.Ohara, I.Mori, K.Kajikawa, H.Ishii, Y.Kitajima, T.Imae, K.Seki and Y.Ouchi
NEXAFS Studies on the Structure of Perfluoroalkyl Carbonic Acid Langmuir Blodgett Films
J. Synchrotron Rad., **6** (1999) 796.

Y.Kitajima, Y.Yonamoto, K.Amemiya, H.Tsukabayashi, T.Ohta and K.Ito
Recent Performance of the Soft X-Ray (70 - 1900 eV) Bending Magnet Beamline 11A at the Photon Factory
J. Elec. Spec. Relat. Phenom., **101-103** (1999) 927.

11B

K.Akimoto, T.Kobayashi, T.Ogawa, W.Ohtsuka, T.Maruyama and Y.Kitajima
Configuration of Cl Atoms in ZnSe and ZnTe
J. Cryst. Growth, **184** (1998) 480.

J.Kawai, K.Hayashi, H.Amano, H.Takenaka and Y.Kitajima
Surface Analysis of Si/W Multilayer Using Total Reflaction X-ray Photoelectron Spectroscopy
J. Elec. Spec. Relat. Phenom, **88** (1998) 787.

S.Tohno, J.Kawai, S.Chatani, M.Ohta, Y.Kitajima, K.Yamamoto, Y.Kitamura and M.Kasahara
Application of X-ray Absorption Fine Structure (XAFS) Spectrometry to Identify the Chemical States of Atmospheric Aerosols
J. Aersol Sci., **29** (1998) S235.

A.Imanishi, T.Yokoyama, Y.Kitajima and T.Ohta
Structural and Electronic Properties of Adsorbed Thiophene on Cu(111) Studied by S K-Edge X-Ray Absorption Spectroscopy
Bull. Chem. Soc. Jpn., **71** (1998) 831.

A.Imanishi, K.Isawa, F.Matsui, T.Tsuduki,T.Yokoyama, H.Kondoh, Y.Kitajima and T.Ohta
Structural Studies of Adsorbed Alkanethiols on Cu(111) by Use of S and C K-edge X-ray Absorption Fine Structures
Surf. Sci., **407** (1998) 282.

S.Terada, T.Yokayama, M.Sakano, A.Imanishi, Y.Kitajima, M.Kiguchi, Y.Okamoto and T.Ohta
Thiophene Adsorption on Pd(111) and Pd(100) Surface Studied by Total-Reflection S K-edge X-ray Absorption Fine-structure Spectroscopy
Surf. Sci., **414** (1998) 107.

J.Kawai, S.Hayakawa, Y.Kitajima and Y.Gohshi
X-ray Absorption Fine Structure (XAFS) of Si Wafer Measured Using Total Reflection X-rays
Spectrochim. Acta B, **B54** (1999) 215.

T.Kubota, Y.Kitajima, K.Asakura and Y.Iwasawa
Pd L_3-Edge XANES Spectra of Supported Pd Particles Induced by the Adsorption and the Absorption of Hydrogen
Bull. Chem. Soc. Jpn., **72** (1999) 673.

M.Takemura, H.Satake, S.Yasuami, M.Yoshiki and Y.Kitajima
K-Edge X-Ray Absorption Spectra of Argon in Sputtered Aluminum Films
Spectrochim. Acta B, **54** (1999) 159.

S.Terada, T.Yokoyama, M.Sakano, M.Kiguchi, Y.Kitajima and T.Ohta
Asymmetric Surface Structure of SO_2 on Pd(111) Studied by Total-reflection X-ray Absorption Fine Structure Spectroscopy
Chem. Phys. Lett., **300** (1999) 645.

K.Hayashi, H.Amano, T.Yamamoto, J.Kawai, Y.Kitajima and H.Takenaka
Grazing Incidence X-ray Absorption Spectra of $(Si/W)_{100}/Si$ Multilayer
Spectrochim. Acta B, **B54** (1999) 223.

J. Kawai, T.Yamamoto, S.Tohno and Y.Kitajima
Comparison between X-ray Photoelectron and X-ray Absorption Spectra of an Enviromental Aerosol Sample Measured by Synchrotron Radiation
Spectrochim. Acta B, **B54** (1999) 241.

11C

M.Yoshikawa, N.Yamaguchi, T.Aota, K.Ikeda, Y.Okamoto, K.Yatsu and T.Tamano
Calibration of Space-Resolving VUV and Soft X-raySpectrographs for Plasma Diagnostics
J. Synchrotron Rad., **5** (1998) 762.

T.Maruyama, Y.Miyajima, K.Hata, S.H.Cho, K.Akimoto, H.Okumura, S.Yoshida and H.Kato
Electronic Structure of Wurtzite- and Zinc Blende-GaN Studied by Angle-Resolved Photoemission
J. Electronic Mater., **27** (1998) 200.

Y.Takakuwa, T.Yamaguchi, T.Hori, T.Horie, Y.Enta, H.Sakamoto, H.Kato and N.Miyamoto
In situ Observation of Thermal and Photon-induced Reaction on Si Surfaces by Ultraviolet Photoelectron Spectroscopy
J. Elec. Spec. Relat. Phenom., **88** (1998) 747.

Y.Takakuwa, Y.Endoh, H.Sakamoto and N.Miyamoto
Surface Electronic States during Si Gas Source Molecular Beam Epitaxy
Butsuri, **53** (1998) 758. (*in Japanese*).

Y.Haruyama, Y.Aiura, H.Bando, Y.Nishihara and H.Kato
Annealing Temperature Dependence on the Electronic Structure of the Reduced $SrTiO_3$ (111) Surface
J. Elec. Spec. Relat. Phenom., **88** (1998) 695.

Y.Takakuwa
In-situ Observation of Thermal and Photon-Induced Semiconductor Processes Using Time-Resolved Photoelectron Spectroscopy
Rep. Res. Inst. Sci. Meas., **47** (1999) 53. (*in Japanese*).

T.Noda, K.Ozawa, K.Edamoto and S.Otani
Angle-resolved Photoemission Study of the Surface Electronic Structure of HfC(111)
Solid State Commun., **110** (1999) 35.

11D

Y.Takegawa, Y.Enta, M.Suemitsu, N.Miyamoto and H.Kato
Growth Mode and Characteristics of the O_2-Oxidized Si(100) Surface Oxide Layer Observed by Real Time Photoemission Measurement
Jpn. J. Appl. Phys., **37** (1998) 261.

H.Sakamoto, Y.Takakuwa, T.Hori, Y.Enta, H.Kato and N.Miyamoto
Development of a Three-electrode-lens Drift Tube for Time-of-flight Mass Spectrometry
J. Synchrotron Rad., **5** (1998) 612.

T.Maruyama, Y.Miyajima, K.Hata, S.H.Cho, K.Akimoto, H.Okumura, S.Yoshida and H.Kato
Electronic Structure of Wurtzite- and Zinc Blende-GaN Studied by Angle-Resolved Photoemission
J. Electronic Mater., **27** (1998) 200.

Y.Takakuwa, T.Yamaguchi, T.Hori, T.Horie, Y.Enta, H.Sakamoto, H.Kato and N.Miyamoto
In situ Observation of Thermal and Photon-induced Reaction on Si Surfaces by Ultraviolet Photoelectron Spectroscopy
J. Elec. Spec. Relat. Phenom., **88** (1998) 747.

Y.Takakuwa, Y.Endoh, H.Sakamoto and N.Miyamoto
Surface Electronic States during Si Gas Source Molecular Beam Epitaxy
Butsuri, **53** (1998) 758. (*in Japanese*).

K.Ozawa, S.Ishikawa, K.Edamoto, H.Kato and S.Otani
Na Adsorption onthe Polar NbC(111) Surface
Surf. Sci., **419** (1999) 226.

Y.Takakuwa
In-situ Observation of Thermal and Photon-Induced Semiconductor Processes Using Time-Resolved Photoelectron Spectroscopy
Rep. Res. Inst. Sci. Meas., **47** (1999) 53. (*in Japanese*).

12B

P.C.Cosby, J.L.Price, R.A.Copeland, T.G.Slanger, A.P.Thorne, J.E.Murray and K.Yoshino
A Comparative High-resolution Study of Predissociation Linewidths in the Schumann-Runge Bands of O_2
J. Chem. Phys., **109** (1998) 3856.

K.Yoshino, J.R.Esmond, W.H.Parkinson A.P.Thorne, J.E.Murray, R.C.M.Leamer, G.Cox, A.S.-C.Cheung K.W.-S.Leung, K.Ito, T.Matsui and T.Imajo
The Application of a VUV Fourier Transform Spectrometer and Synchrotron Radiation Source to Measurements of: I. The $\beta(9,0)$ Band of NO
J. Chem. Phys., **109** (1998) 1751.

12C

K.Fukumi, A.Chayahara, K.Kadono, H.Kageyama, N.Kitamura, H.Mizoguchi, Y.Horino and M.Makihara
Formation of Metallic Ultrafine Particles in Silica Glass by Ion Implantation
J. Surf. Anal., **4(2)** (1998) 214.

J.M.Martínez, R.R.Pappalardo, E.S.Marcos, K.Refson, S.D.Moreno and A.M.Páez
Dynamics of a Highly Charged Ion in Aqueous Solutions: MD Simulations of Dilute $CrCl_3$ Aqueous Solutions Using Interaction Potentials Based on the Hydrated Ion Concept
J. Phys. Chem. B, **102** (1998) 3272.

H.Sakane, A.M.Páez, S.D.Moreno J.M.Martínez, R.R.Pappalardo and E.S.Marcos
Second Hydration Shell Single Scattering Versus First Hydration Shell Multiple Scattering in $M(H_2O)_6^{3+}$ EXAFS Spectra
J. Am. Chem. Soc., **120** (1998) 10397.

Y.Inada, Y.Sugimoto, Y.Nakano, Y.Itoh and S.Funahashi
Formation and Deprotonation Kinetics of the Sitting-Atop Complex of Copper(II) Ion with 5,10,15,20-Tetraphenylporphyrin Relevant to the Porphyrin Metalation Mechanism. Structure of Copper(II)-Pyridine Complexes in Acetonitrile As Determined by EXAFS Spectroscopy
Inorg. Chem., **37** (1998) 5519.

M.Nomura
Design and Performance of a Multi-element SSD for Fluorescent XAFS
KEK Report, **98-4** (1998)

Y.Izumi
X-ray Absorption Fine Structure Spectroscopy as a Probe of Chemical State of Catalysts
Trends in Inorg. Chem., **5** (1998) 43.

Y.Izumi, H.Kurakata and K.Akika
Ethanol Synthesis from Carbon Dioxide on $[Rh_{10}Se/TiO_2]$ Catalyst Characterized by X-Ray Absorption Fine Structure Spectroscopy
J. Catal., **175** (1998) 236.

M.Shirai and M.Arai
Structure and Catalysis of Ion-Exchanged Nickel Species during Pyrolysis of Loy Yang Coal
Energy and Fuels, **13** (1999) 465.

E.Yanase, I.Watanabe, M.Harada, M.Takahashi, Y.Dake and Y.Hiroshima
Probing Depth Study of Conversion Electron/He Ion Yield XAFS Spectroscopy on Strontium Titanate Thin Films
Anal. Sci., **15** (1999) 255.

13A

K.Nakayama, Y.Okada and H.Fujimoto
New Beamline Optics for the Effective Use of a Wiggler Beam
J. Synchrotron Rad., **5** (1998) 527.

13B2

A.Yoshiasa, T.Nagai, K.Murai, T.Yamanaka, O.Kamishima and O.Shimomura
Effective Pair Potentials of NaCl- and CsCl-type KBr Determined by X-Ray Absorption Fine Structure under Pressure
Jpn. J. Appl. Phys., **37** (1998) 728.

A.Yoshiasa, T.Nagai, O.Ohtaka, O.Kamishima and O.Shimomura
Pressure and Temperature Dependence of EXAFS Debye-Waller Factors in Diamond-type and White-tin-type Germanium
J. Synchrotron Rad., **6** (1999) 43.

13C

T.Saito, F.Esaka, Y.Kudo, K.Furuya, T.Kikuchi, M.Imamura, N.Matsubayashi and H.Shimada
XAS and XPS Studies on Molecular and Dissociative Adsorption of Nitric Oxide on Rh
J. Elec. Spec. Relat. Phenom., **88** (1998) 763.

T.Saito, F.Esaka, H.Shimada, M.Imamura, N.Matsubayashi, T.Sato, A.Nishijima, T.Kikuchi and K.Furuya
XPS Study on Dissociative Adsorption of NO on Polycrystalline Rh
Hyomen Kagaku, **19** (1998) 43. (*in Japanese*).

14A

T.Toda, T.Nogami, K.Yamasaki and Y.Soejima
Diffraction Anomalous Fine Structure on Forbidden and Superlattice Reflections
J. Appl. Cryst., **31** (1998) 423.

T.Inoue, Y.Kubozono, K.Hiraoka, K.Mimura, H.Maeda, S.Kashino, S.Emura, T.Uruga and Y.Nakata
XAFS Study on Eu@C_{60}
J. Synchrotron Rad., **6** (1999) 779.

14B

K.Hirano and A.Momose
Investigation of the Phase Shift in X-ray Forward Diffraction Using an X-ray Interferometer
J. Synchrotron Rad., **5** (1998) 967.

A.Takase, M.Kuribayashi, K.Ishida, K.Kimura, L-H.Kuo, T.Yasuda, S.Miwa, T.Yao, H.Tomita and S.Komiya
Characterization of ZnSe/GaAs(001) Heteroepitaxial Interfaces by X-Ray Reflectivity Measurement
Jpn. J. Appl. Phys., **37** (1998) 3475.

O.Sakata, Y.Tanaka, A.M.Nikolaenko and H.Hashizume
Ultrahigh-Vacuum Facility for High-Resolution Grazing-Angle X-ray Diffraction at a Vertical Wiggler Source of Synchrotron Radiation
J. Synchrotron Rad., **5** (1998) 1222.

14C

S.Iida, Y.Aoki, K.Okitsu, Y.Sugita, H.Kawata and T.Abe
Microdefects in an As-Grown Czochralski Silicon Crystal Studied by Synchrotron Radiation Section Topography with Aid of Computer Simulation
Jpn. J. Appl. Phys., **37** (1998) 241.

O.Ohtaka, T.Nagai, T.Yagi and O.Shimomura
In situ Observation of ZrO_2 Phase at High Pressure and Temperature
Properties of Earth and Planetary Materials at High Pressure and Temperature, **101** (1998) 429.

T.Kubo, E.Ohtani, T.Kato, H.Morishima, D.Yamazaki, A.Suzuki, K.Mibe, T.Kikegawa and O.Shimomura
An *in situ* X ray Diffraction Study of the α-β Transformation Kinetics of Mg_2SiO_4
Geophys. Res. Lett., **25** (1998) 695.

K.Kusaba, Y.Syono, T.Kikegawa and O.Shimomura
Compression Behavior and Phase Equilibria of FeS
Rev. High Pressure Sci. Tech., **7** (1998) 257.

S.Urakawa, N.Igawa, K.Kusaba, H.Ohno and O.Shimomura
Structure of Molten Iron Sulfide under Pressure
Rev. High Pressure Sci. Tech., **7** (1998) 286.

S.Saiki, S.Takei, Y.Ookubo, M.Tsubokawa, T.Yamaguchi and T.Kikegawa
Pressure Dependence of Melting Temperatures in Brached Polythylene up to 2 GPa
Polymer, **39** (1998) 4267.

Y.Matsumoto, O.Ohtaka, M.Kikuchi, T.Nagai, T.Yamanaka and O.Shimomura
Pressure Induced Structural Phase Transition of CdI_2-type PbI_2
Rev. High Pressure Sci. Tech., **7** (1998) 341.

K.Kusaba, Y.Syono and T.Kikegawa
Phase Transition of ZnO under High Pressure and Temperature
Proc. Jpn. Acad, **B75** (1999) 1.

15A

K.Fukuyama, T.Nishizawa and K.Nishikawa
Small Angle X-ray Scattering from Glass-like Carbon and Its Graphitization Behavior
Tanso, **182** (1998) 85. (*in Japanese*).

M.Arai, T.Ikura, G.V.Semisotnov, H.Kihara, Y.Amemiya and K.Kuwajima
Kinetic Refolding of β-Lactoglobulin. Studies by Synchrotron X-ray Scattering, and Circular Dichroism, Absorption and Fluorescence Spectroscopy
J. Mol. Biol., **275** (1998) 149.

K.Nishikawa, K.Fukuyama and T.Nishizawa
Structure Change of Glass-like Carbon with Heat Treatment, Studied by Small Angle X-Ray Scattering: I. Glass-like Carbon Prepared from Phenolic Resin
Jpn. J. Appl. Phys., **37** (1998) 6486.

T.Kobayashi, S.Kosuge, K.Narushima and H.Sugi
Evidence for Two Distinct Cross-Bridge Populations in Tetanized Frog Muscle Fibers Stretched with Moderate Velocities
Biochem. Biolog. Res. Commun., **249** (1998) 161.

T.Kobayashi, S.Kosuge and H.Sugi
Evidence for Two Cross-bridge Populations in Tetanized Frog Muscle Fibers Stretched with Moderate Velocities
Adv. Exp. Med. Biol., **453** (1998) 353.

Y.Takezawa, Y.Sugimoto and K.Wakabayashi
Structural Analyses of Biological Materials by SR 1. X-Ray Diffraction Scattering Studies of Muscle Contraction Using Sychrotron Radiation
Radioisotopes, **47** (1998) 776. (*in Japanese*).

J.Yano, S.Ueno, F.Kaneko and K.Sato
Polymorphic Transformation and Molecular Interactions of Mixed-Acid Lipids
Hyomen, **36** (1998) 242. (*in Japanese*).

S.Ueno, A.Minato, J.Yano, Y.Amemiya and K.Sato
Time-resolved Synchrotron Radiation X-Ray Diffraction Study of Polymorphic Crystallizatoin of a Single System and Binary Mixtures Systems in Triacylglycerols
J. Jpn. Soc. Synchrotron Rad. Res., **11** (1998) 208. (*in Japanese*).

T.Morita, H.Miyagi, Y.Shimokawa, H.Matsuo and K.Nishikawa
Construction of the Sample Holder and Small-Angle X-ray Scattering Measurement for Supercritical Water
Jpn. J. Appl. Phys., **37** (1998) 768.

S.Ueno, J.Yano and K.Sato
Physical Properties of Fats – Molecular Structures and Kinetics –
Nippon Shokuhin Kagaku Kogaku Kaishi, **45** (1998) 579. (*in Japanese*).

K.Sato, S.Ueno and J.Yano
A New Development of Physical Analysis for Fat Crystals
Nippon Yukagaku Kaishi, **47** (1998) 1099. (*in Japanese*).

D-S.Kim, Y.Takezawa, M.Ogino, T.Kobayashi, T.Arata and K.Wakabayashi
X-Ray Diffraction Studies on the Structural Changes of Rigor Muscles Induced by Binding of Phosphate Analogs in the Presence of MgATP
Biophys. Chem., **74** (1998) 71.

T.Ujihara, K.Osamura and Y.Amemiya
Shape Anisotropy of GP Zone in Early Decompositoin Preocess of Al-Zn Binary Alloy
J. Jpn. Inst. Met., **62** (1998) 117. (*in Japanese*).

K.Nishikawa and T.Morita
Fluid Behavior at Supercritical States Studied by Small-angle X-ray Scattering
J. Supercritical Fluids, **13** (1998) 143.

A.Minato
Physical Study on Molecular Interactions and Phase Behavior on Binary Mixtures of Triacylglycerols
J. Jpn. Soc. Synchrotron Rad. Res., **11** (1998) 50. (*in Japanese*).

H.Seto, D.Okuhara, M.Nagao, S.Komura and T.Takeda
A Pressure-Induced Phase Transition in a Ternary Microemulsion with an Assembly of a New High-Pressure Cell and Small-Angle X-ray Scattering Apparatus
Jpn. J. Appl. Phys., **38** (1999) 951.

Y.Tajima, K.Makino, T.Hanyuu, K.Wakabayashi and Y.Amemiya
The Overlap between the Thin- and Thick-filament Reflections in the Small-angle X-ray Diffraction Pattern from a Molluscan Smooth Muscle
J. Sychrotron Rad., **6** (1999) 93.

S.Ueno, A.Minato, J.Yano and K.Sato
Synchrotron Radiation X-Ray Diffraction Study of Polymorphic Crystallization of SOS from Liquid Phase
J. Cryst. Growth, **198** (1999) 1326.

T.Morita and K.Nishikawa
Study on Fluctuation of Supercritical Fluids by Small-Angle X-ray Scattering
J. Cryst. Soc. Jpn., **41** (1999) 66. (*in Japanese*).

H.Takahashi, M.Watanabe, P.J.Quinn and I.Hatta
Simultaneous X-ray Diffraction and Calorimetric Study of Metastable-to-stable Solid Phase Transformation of 1,2-dipalmitoyl-*sn*-glycerol
Biol. Chem., **77** (1999) 173.

H.Takahashi, M.Watanabe, S.Kato, S.Murayama, K.Ohki, P.J.Quinn and I.Hatta
Effect of Diacylglycerol on the Structure and Phase Behavior of Non-bilayer Forming Phospholipid
Biol. Chem., **77** (1999) 37.

15B1

K.Mizuno, S.Nagai, A.Tamiya, E.Hashimoto, K.ITo and T.Kino
Synchrotron Radiation Topographic Camera for Continuous Observation
Jpn. J. Appl. Phys., **37** (1998) 4209.

15C

J.Kohagura, T.Cho, M.Hirata, T.Okamura, T.Tamano, K.Yatsu, S.Miyoshi, K.Hirano and H.Maezawa
New Methods for Semiconductor Charge-Diffusion-Length Measurements Using Synchrotron Radiation
J. Synchrotron Rad., **5** (1998) 874.

T.Cho, M.Hirata, J.Kohagura, Y.Sakamoto, T.Okamura, T.Numakura, R.Minami, Y.Nishizawa, T.Sasuga, T.Tamano, K.Yatsu, S.Miyoshi, S.Tanaka, K.Sato, Y.Saitoh, K.Hirano and H.Maezawa
Characterization and Interpretation of the Quantum Efficiencies of Multilayer Semiconductor Detectors Using a New Theory
J. Synchrotron Rad., **5** (1998) 877.

K.Okitsu, Y.Ueji, T.Oguchi, H.Maruyama, Y.Hasegawa and Y.Amemiya
Study on Dielectric Anisotropies in Crystals by Using the Energy-Tunable X-Ray Polarimeter with a Phase Retarder
J. Cryst. Soc. Jpn., **40** (1998) 341. (*in Japanese*).

K.Okitsu, T.Oguchi, H.Maruyama and Y.Amemiya
X-ray Linear Birefringence and Linear Dichroism in a Cobalt Crystal Measured with a Tunable X-ray Polarimeter
J. Synchrotron Rad., **5** (1998) 995.

K.Okitsu, Y.Ueji, T.Oguchi, Y.Hasegawa, Y.Ohashi and Y.Amemiya
X-ray Triple Refraction and Triple Absorption in a Cobalt-Complex Crystal
J. Synchorotron Rad., **5** (1998) 1055.

J.Kohagura, T.Cho, M.Hirata, S.Kanke, K.Takahashi, T.Okamura, T.Tamano, K.Yatsu and S.Miyoshi
International Collaboration Researches on the Effects of a New Theory on the Plasma X-ray Diagnostics Using Semiconductor X-ray Detectors
Plasma Phys., **24** (1998) 218.

S.Kimura, T.Matsumura K.Kinoshita, K.Hirano and H.Kihara
High-resolution X-ray Topographic Images of Dislocations in a Silicon Crystal Recorded Using an X-ray Zooming Tube
J. Synchrotron Rad., **5** (1998) 1079.

K.Akimoto, T.Emoto and A.Ichimiya
Surface and Interface Strains Studied by X-ray Diffraction
Mat. Res. Soc. Symp., **505** (1998) 409.

T.Emoto, K.Akimoto and A.Ichimiya
Observation on the Strain Field Near the Si(111)7×7 Surface with a New X-ray Diffraction Technique
J. Synchrotron Rad., **5** (1998) 964.

J.Kohagura, T.Cho, M.Hirata, R.Minami, T.Numakura, T.Okamura, Y.Sakamoto, T.Tamano, K.Yatsu, S.Miyoshi, S.Tanaka, K.Sato, M.Inoue, Y.Saitoh and S.Yamamoto
Newly Developed Matrix-Type Semiconductor Detector for Temporally and Spatially Resolved X-Ray Analyses Ranging Down to a Few Tens eV Using a Single Plasma Shot
Rev. Sci. Instrum., **70** (1999) 633.

Y.Sakamoto, T.Cho, M.Hirata, J.Kohagura, T.Sasuga, Y.Nishizawa, T.Numakura, R.Minami, Y.Nakashima, T.Tamano, K.Yatsu and S.Miyoshi
Characterization of a Semiconductor Detector and Its Application for Ion Diagnostics Using a Novel Ion Energy Spectrometer
Rev. Sci. Instrum., **70** (1999) 857.

T.Cho, J.Kohagura, M.Hirata, Y.Sakamoto, T.Numakura, R.Minami, T.Sasuga, Y.Nishizawa, T.Okamura, T.Tamano, K.Yatsu, S.Miyoshi, K.Hirano and H.Maezawa
Effects of Neutrons on Semiconductor X-Ray Detectors Including *n*-Type Joint European Torus and *p*-Type GAMMA 10 Tomography Detectors
Rev. Sci. Instrum., **70** (1999) 577.

16A1

H.Hayashi, N.Watanabe and Y.Udagawa
Inelastic X-ray Scattering in Molecular Liquid and Electron Correlation Effects
J. Synchrotron Rad., **5** (1998) 1052.

N.Watanabe, H.Hayashi, Y.Udagawa, S.Ten-no and S.Iwata
Static Structure Factor and Electron Correlation Effects Studied by Inelastic X-ray Scattering Spectroscopy
J. Chem. Phys., **108** (1998) 4545.

S.Yamamura, M.Takata, M.Sakata and Y.Sugawara
Nature of the Hydrogen Bond in Teragonal KDP(KH_2PO_4) Observed by Maximum Entropy Method
J. Phys. Soc. Jpn., **67** (1998) 4124.

16A2

Y.Murakami, J.P.Hill, D.Gibbs, M.Blume, I.Koyama, M.Tanaka, H.Kawata, T.Arima, Y.Yokura, K.Hirota and Y.Endoh
Resonant X-ray Scattering from Orbital Ordering in $LaMnO_3$
Phys. Rev. Lett., **81** (1998) 582.

Y.Murakami, H.Kawada, H.Kawata, M.Tanaka, T.Arima, Y.Moritomo and Y.Tokura
Direct Observation of Charge-and Orbital-Ordering in a Layered-Perovskite-Type Manganite
J. Jpn. Soc. Synchrotron Rad. Res., **11** (1998) 30. (*in Japanese*).

Y.Murakami
Study on Physical Property by Synchrotron Radiation a. Materials Structure Research by Synchrotron X-ray Diffraction
Radioisotopes, **48** (1999) 65. (*in Japanese*).

17A

M.Koike, I.H.Suzuki and S.Komiya
X-ray Microfocusing by Ti/Al Multilayer Zone Plate and Bragg-Fresnel Lens
Proc. SPIE, **3449** (1999) 129.

17C

A.Takase, M.Kuribayashi, K.Ishida, K.Kimura, L-H.Kuo, T.Yasuda, S.Miwa, T.Yao, H.Tomita and S.Komiya
Characterization of ZnSe/GaAs(001) Heteroepitaxial Interfaces by X-Ray Reflectivity Measurement
Jpn. J. Appl. Phys., **37** (1998) 3475.

18A

T.Okane, M.Yamada, S.Suzuki, S.Sato, A.Kakizaki, T.Kobayashi, S.Shimoda, M.Iwaki and M.Aono
Atomic Diffusion and Electronic Structures of Ce/Ni(110) and Ce/Cu(110) Systems
J. Phys. Soc. Jpn., **67** (1998) 194.

W.R.A.Huff, M.Shimomura, N.Sanada, G.Kaneda, T.Takeuchi, Y.Suzuki, H.W.Yeom, T.Abukawa, S.Kono and Y.Fukuda
InP(001)-(2×4) Surface Electronic Structure Studied by Angle-resolved Photoelectron Spectroscopy
J. Elec, Spec. Relat. Phenom., **88** (1998) 609.

H.W.Yeom, T.Abukawa, Y.Takakuwa, S.Fujimori, T.Okane, Y.Ogura, T.Miura, S.Sato, A.Kakizaki and S.Kono
Anisotropy of Spin-orbit Branching Ratio in Angle-resolved Photoemission from Adsorbate Layers
Surf. Sci., **395** (1998) L236.

K.Sakamoto, M.Harada, D.Kondo, A.Kimura, A.Kakizaki and S.Suto
Bonding State of the C_{60} Molecule Adsorbed on a Si(111)-(7 × 7) Surface
Phys. Rev. B, **58** (1998) 13951.

A.Tanaka, K.Tamura, H.Tsunematsu, K.Takahashi, M.Hatano, S.Suzuki, S.Sato and S.Kunii
Angle-resolved Photoemission Study of the Surface Electronic Structure on NdB_6(110) Clean Surface
J. Elec. Spec. Relat. Phenom., **88** (1998) 637.

M.Shimomura, N.Sanada, G.Kaneda, T.Takeuchi, Y.Suzuki, Y.Fukuda, W.R.A.Huff, T.Abukawa, S.Kono, H.W.Yeom and A.Kakizaki
X-ray Photoelectron Diffraction and Surface Core-level Shift Study of Clean InP(001)
Surf. Sci., **412** (1998) 625.

18B

S.Nagashima, M.Nakasako, N.Dohmae, M.Tsujimura, K.Takio, M.Odaka, M.Yohda, N.Kamiya and I.Endo
Novel Non-heme Iron Center of Nitrile Hydratase with a Claw Setting of Oxygen Atoms
Nature Structural Biology, **5** (1998) 347.

Y.Katsuya, Y.Mezaki, M.Kubota and Y.Matsuura
Three-dimensional Structure of *Pseudomonas* Isoamylase at 2.2 ÅResolution
J. Mol. Biol., **281** (1998) 885.

M.Kato, T.Mizuno and T.Hakoshima
Crystallization of a Complex between a Novel C-terminal Transmitter, Hpt Domain, of the Anaerobic Sensor Kinase ArcB and the Chemotaxis Response Regulator CheY
Acta. Cryst., **D54** (1998) 140.

M.Kataoka, K.Yamamoto, S.Shimizu, M.Ohta, A.Kita, Y.Higuchi and K.Miki
Crystallization and Preliminary X-ray Diffraction Study of Lactonohydrolase from *Fusarium Oxysporum*
Acta Cryst., **D54** (1998) 1432.

K.Kitano, K.Motohashi, M.Yoshida and K.Miki
A Novel Approach to Crystallizing Proteins with Temperature Induction Method: GrpE Protein from *Thermus thermophilus*
J. Cryst. Growth, **186** (1998) 456.

N.Sakabe
Studies on Millisecond Order Dynamics of Protein Crystal Structure Using Synchrotron Radiation
Jyuuten Ryoiki Houkokusho, (1998) (*in Japanese*).

K.Sasaki, N.Watanabe, N.Sakabe and K.Sakabe
Computer Network System with Security for a Protein Data Collection System at the Photon Factory
J. Synchrotron Rad., **6** (1999) 116.

T.Inoue, H.Sugawara, S.Hamanaka, H.Tsukui, E.Suzuki, T.Kohzuma and Y.Kai
Crystal Structure Determinations of Oxidized and Reduced Plastocyanin from the Cyanobacterium *Synechococcus* sp. PCC7942
Biochem., **38** (1999) 6063.

A.Kita, S.Kita, K.Fujisawa, K.Inaka, T.Ishida, K.Horiike, M.Nozaki and K.Miki
An Archetypical Extradiol-Cleaving Cathecholic Dioxygenase: The Crystal Structure of Catechol 2,3-Dioxygenase (Metapyrocatechase) from *Pseudomonas Putida* mt-2
Structure, **7** (1999) 25.

H.Komori, N.Sasai, F.Matsunaga, C.Wada and K.Miki
Crystallization and Preliminary X-ray Diffraction Studies of a Replication Intiator Protein (RepE54) of the Mini-F Plasmid Complexes with Iteron DNA
J. Biochem., **125** (1999) 24.

18C

K.Takemura, K.Kobayashi and M.Arai
High-pressure bct-fcc Phase Transition in Ga
Phys. Rev. B, **58** (1998) 2482.

S.Endo, A.Honda, K.Koto, O.Shimomura, T.Kikegawa and N.Hamaya
Crystal Structure of High-pressure Phase-IV Solid Hydrogen Sulfide
Phys. Rev. B, **57** (1998) 5699.

Y.Yoshida, Y.Kubozono, T.Urakawa, H.Maeda, S.Kashino, Y.Murakami, T.Ohta, F.Izumi, K.Yamada and Y.Furukawa
Temperature Dependence of Atomic Displacements in Superconductor K_2RbC_{60}
Solid State Commun., **105** (1998) 557.

T.Hashimoto, N.Matsushita, Y.Murakami, N.Kojima, K.Yoshida, H.Tagawa, M.Dokiyo and T.Kikegawa
Pressure-induced Structural Phase Transition of $LaCrO_3$
Solid State Commun., **108** (1998) 691.

H.Yusa and K.Takemura
Laser Heating System with a Diamond Anvil Cell at NIRIM and the Topics of Experiments
Proceeding of the 5th NIRIM International Symposium on Advanced Materials, (1998) 9.

K.Takemura
Structural Change of Elemental Metals at High Pressures
Proceeding of the 5th NIRIM International Symposium on Advanced Materials, (1998) 13.

M.Takumi, Y.Koshio and K.Nagata
X-Ray, Raman and Photoluminescence Study of Vacancy Ordered β-Ga_2Se_3 under High Pressure
Physica Status Solidi(b), **211** (1999) 123.

K.Ishii, T.Watanuki, A.Fujiwara, H.Suematsu, Y.Iwase, H.Shimoda, T.Mitani, H.Nakao, Y.Fujii, Y.Murakami and H.Kawada
Structural Phase Transition in the Ammoniated Alkali C_{60} Compound $(NH_3)K_3C_{60}$
Phys. Rev. B, **59** (1999) 3956.

M.Takumi, Y.Koshio, A.Hirata, T.Ueda and K.Nagata
X-ray and Photoluminescence Measurements of β-Ga_2Se_3 under High Pressure
Fukuoka Univ. Sci. Rep., **29** (1999) 85. (*in Japanese*).

A.Onodera, M.Mimasaka, I.Sakamoto, J.Okumura, K.Sakamoto, S.Uehara, O.Shimomura, T.Ohtani and Y.Fujii
Structural and Electrical Properties of NiAs-type Compounds under Pressure
J. Phys. Chem. Solids, **60** (1999) 167.

19A

O.Rader, A.Kimura, N.Kamakura, K.An, A.Kakizaki, S.Miyanishi, H.Akinaga, M.Shirai, K.Shimada and A.Fujimori
Exchange Splittings of Mn- and Sb-Drived States by Spin Resolved Valence-band Photoemission of MnSb
Phys. Rev. B, **57** (1998) R689.

K.Shimada, T.Mizokawa, K.Mamiya, T.Saitoh, A.Fujimori, K.Ono, A.Kakizaki, T.Ishii, M.Shirai and T.Kamimura
Spin-integratd and Spin-resolved Photoemission Study of Fe Chalcogenides
Phys. Rev. B, **57** (1998) 8845.

K.Shimada, O.Rader, A.Fujimori, A.Kimura, K.Ono, N.Kamakura, A.Kakizaki, M.Tanaka and M.Shirai
Spin- and Angle-resolved Photoemission Spectroscopy of Ferromagnetic MnAs
J. Elec. Spec. Relat. Phenom., **88** (1998) 207.

K.Ono, A.Kakizaki, K.Tanaka, K.Shimada, Y.Saitoh and T.Sendohda
Resonant Enhancement of Valence Band Satellites of Ni: A Spin-Resolved Photoemission Study
Solid State Commun., **101** (1998) 739.

A.Kakizaki
Electronic Structure Observed by Spin-Resolved Photoemission
Shinkuu, **41** (1998) 561. (*in Japanese*).

J.Okamoto, T.Konishi, T.Mizokawa, A.Fujimori, N.Nakajima, T.Koide, H.Miyauchi, T.Miyahara, I.Hase, Y.Takeda and M.Takano
Photoemisssion Magnetic Circular Dichroism Study of the Ferromagnetic Transition-metal Oxide $SrRuO_3$
J. Elec. Spec. Relat. Phenom., **92** (1998) 41.

A.Kakizaki, A.Kimura, M.Sawada, K.Ono and S.Qiao
Valence Band Structure of Ferromagnetic Ni Observed by Spin- and Angle-resolved Phtoemission
J. Elect. Spec. Relat. Phenom., **92** (1998) 25.

19B

J.Kawai, T.Yamamoto, Y.Harada and S.Shin
Fluorine K_α X-Ray Fluorescence Spectra of MnF_2 Excited at Threshold
Solid State Commun., **105** (1998) 387.

M.Tanaka, M.Hasegawa, T.Higuchi, T.Tsukamoto, Y.Tezuka, S.Shin and H.Takei
Origin of the Metallic Conductivity in $PdCoO_2$ with Delafossite Structure
Physica B, **245** (1998) 157.

S.Shin, M.Fujisawa, H.Ishii, Y.Harada, M.Watanabe, M.M.Grush, T.A.Callcott, R.C.C.Perera, E.Z.Kurmaev, A.Moewes, R.Winarski, S.Stadler and D.L.Ederer
Soft X-ray Emission Spectroscopy of Early Transition Metal Compounds
J. Elec. Spec. Relat. Phenom., **92** (1998) 197.

E.Z.Kumaev, S.Stadler, D.L.Ederer, Y.Harada, S.Shin, M.M.Grushi, T.A.Callcott, R.C.C.Perera, D.A.Zatsepin, N.Overchkina, M.Kasai, Y.Tokura, T.Takahashi, K.Chandrasekaran, R.Vijayharaghavan and U.V.Varadaraju
Electronic Structure of Sr_2RuO_4: X-ray Fluorescence Emission Study
Phys. Rev. B, **57** (1998) 1558.

T.Higuchi, T.Tsukamoto, N.Sata, M.Ishigame, Y.Tezuka and S.Shin
Electronic Structure of *p*-type $SrTiO_3$ by Photoemission Spectroscopy
Phys. Rev. B, **57** (1998) 6978.

T.Kotsugi, H.Sato, S.Senda, H.Okuda, Y.Ueda, M.Taniguchi, Y.Harada, S.Shin, A.Tanaka and T.Jo
Soft X-ray Emission Spectroscopy of NiAs-type MnTe at the Mn 2p Core Threshold
J. Elec. Spec. Relat. Phenom., **88** (1998) 293.

J.Kawai, T.Yamamoto, Y.Harada and S.Shin
Mn $L_{\alpha,\beta}$ and F K_α Resonant X-ray Fluorescence Spectroscopy of MnF_2
J. Synchorotron Rad., **5** (1998) 1067.

S.Suga and S.Imada
Magnetic Dichroism in Core Absorption and Photoemission
J. Elec. Spec. Relat. Phenom., **92** (1998) 1.

T.Higuchi, T.Tsukamoto, N.Sata, M.Ishigame, Y.Tezuka and S.Shin
Photoemission Study of Protonic Conductor p-type $SrTiO_3$
Solid State Ionics, **108** (1998) 349.

T.Higuchi, T.Tsukamoto, M.Tanaka, H.Ishii, K.Kanai, Y.Tezuka, S.Shin and H.Takei
Photoemission Study on $PdCoO_2$
J. Elec. Spec. Relat. Phenom., **92** (1998) 71.

27A

Y.Baba
Auger Electron Spectyrometry
Radioisotopes, **47** (1998) 240. (*in Japanese*).

Y.Baba, K.Yoshii and T.A.Sasaki
Desorption of Fragment Ions from Mono- and Multilayered CCl_4 on Cu(100) by Inner-shell Photoexcitation
Surf. Sci., **402** (1998) 115.

27B

M.Akabori, T.Ogawa, A.Itoh, H.Motohashi and H.Shiwaku
Local Structure of $(U,Zr)Pd_3$ by EXAFS
J. Alloys Compounds, **271** (1998) 363.

T.Yaita, H.Narita, S.Suzuki, S.Tachimori, H.Shiwaku and H.Motohashi
Structural Study of Holmium (III) and Uranium (VI) Organic Ligand Complexes by Extended X-ray Absorption Fine-structure Spectroscopy
J. Alloys Compounds, **271** (1998) 184.

H.Maeta, T.Kato, H.Ohtsuka, H.Yuya, H.Sugai, H.Motohashi, K.Yamakawa and F.Ono
X-Ray Diffuse Scattering Study of Defect Cluster by Heavy Ion-Irradiated Ni Crystals at Low Temperature
JAERI Rev., **98-017** (1998) 87.

H.Yuya, T.Matsui, H.Maeta, H.Ohtsuka and H.Sugai
Defect Clusters in High-energy Ion-irradiated Ni and Dilute Ni Alloys Investigated by Diffuse X-ray Scattering
Nucl. Instrum. Meth. Phys. Res., **B148** (1999) 891.

28A

Y.Takayama, T.Hatano, T.Miyahara and W.Okamoto
Relationship Between Spatial Coherence of Sychrotron Radiation and Emittance
J. Sychrotron Rad., **5** (1998) 1187.

S.Suga and S.Imada
Magnetic Dichroism in Core Absorption and Photoemission
J. Elec. Spec. Relat. Phenom., **92** (1998) 1.

Y.Takayama, R.Z.Tai, T.Hatano, T.Miyahara and W.Okamoto and Y.Kagoshima
Measurement of the Coherenceof Synchrotron Radiation
J. Sychrotron Rad., **5** (1998) 456.

28B

T.Nakamura, M.Mizumaki, Y.Watanabe and S.Nanao
Distribution of Spin Polarization in Ferrimagnetic $DyFe_2$ by a Novel Analysis of Magnetic EXAFS
J. Phys. Soc. Jpn., **67** (1998) 3964.

T.Nakamura, S.Nanao, T.Iwazumi, K.Kobayashi, S.Kishimoto, D.Ohsawa, R.Katano and Y.Isozumi
X-ray Magnetic Circular Dichroism of Multielectron Excitation by Fluorescence Spectroscopy
J. Elec. Spec. Relat. Phenom., **92** (1998) 261.

N.Kawamura, H.Maruyama, K.Kobayashi, S.Uemura, A.Urata and H.Yamazaki
Multielectron Excitations in $3d$ Transition Metal Compounds Probed by X-Ray Magnetic Circular Dichroism
J. Phys. Soc. Jpn., **68** (1999) 923.

T.Nakamura and S.Nanao
Study of Magnetic Structures in Magnetic Materials by Magnetic EXAFS
Nihon Ohyohjiki Gakkaishi, **23** (1999) 906. (*in Japanese*).

NE1A1

H.Hashimoto, H.Sakurai, H.Oike, F.Itoh, A.Ochiai, H.Aoki and T.Suzuki
Magnetic Compton Study of a Use Single Crystal
J. Phys. Condens Matter, **10** (1998) 6333.

NE1A3

S.Ohtsuka, Y.Sugishita, T.Takeda, Y.Itai, J.Tada, K.Hyodo and M.Ando
Dynamic Intravenous Coronary Angiography Using 2D Monochromatic synchrotron Radiation
British J. Radiology, **72** (1999) 24.

NE1B

S.Suga and S.Imada
Magnetic Dichroism in Core Absorption and Photoemission
J. Elec. Spec. Relat. Phenom., **92** (1998) 1.

NE3A

J.Y.Zhao, X.-W.Zhang, M.Ando, Y.Yoda, S.Kikuta and H.Takei
X-ray Characterization of α-Fe_2O_3 Single Crystals Containing 2.2% and 95% ^{57}Fe
J. Synchrotron Rad., **5** (1998) 952.

NE5A

H.Mori, E.Tanaka, K.Hyodo, M.U.Mohammed, T.Sekka, K.Ito, Y.Shinozaki, A.Tanaka, H.Nakazawa, S.Abe, S.Handa, M.Kubota, K.Tanioka, K.Umetani and M.Ando
Synchrotron Microangiography Reveals Configurational Changes and To-and-fro Flow in Intramyocardial Vessels
Am. Phys. Soc., (1999) H429.

NE5C

O.Ohtaka, T.Nagai, T.Yagi and O.Shimomura
In situ Observation of ZrO_2 Phase at High Pressure and Temperature
Properties of Earth and Planetary Materials at High Pressure and Temperature, **101** (1998) 429.

T.Kubo, E.Ohtani, T.Kato, H.Morishima, D.Yamazaki, A.Suzuki, K.Mibe, T.Kikegawa and O.Shimomura
An *in situ* X ray Diffraction Study of the α-β Transformation Kinetics of Mg_2SiO_4
Geophys. Res. Lett., **25** (1998) 695.

M.Imai, T.Hirano, T.Kikegawa and O.Shimomura
Phase Transitions of $BaSi_2$ at High Pressures and High Temperatures
Phys. Rev. B, **58** (1998) 11922.

J.Tang, M.Kai, Y.Kobayashi, S.Endo O.Shimomura, T.Kikegawa and T.Ashida
A High-pressure High-temperature X Ray Study of Phase Relations and Polymorphism of HfO_2
Am. Geophys. Union, (1998) 401.

K.Kusaba, Y.Syono, T.Kikegawa and O.Shimomura
Compression Behavior and Phase Equilibria of FeS
Rev. High Pressure Sci. Tech., **7** (1998) 257.

S.Saiki, S.Takei, Y.Ookubo, M.Tsubokawa, T.Yamaguchi and T.Kikegawa
Pressure Dependence of Melting Temperatures in Brached Polythylene up to 2 GPa
Polymer, **39** (1998) 4267.

K.Kusaba, Y.Syono, T.Kikegawa and O.Shimomura
Structures an Phase Equilibria of FeS Under High Pressure and Temperature
Geophys. Monograph 101, (1998) 297.

K.Kusaba, Y.Syono and T.Kikegawa
Phase Transition of ZnO under High Pressure and Temperature
Proc. Jpn. Acad, **B75** (1999) 1.

MR

F.Sato, N.Saito, J.Kusano, K.Takizawa, H.Sugiyama, Y.Kagoshima, M.Ando, S.Kawado and T.Kato
Inner-Shell Electron Excitation Effect on the Structural Change in Amorphous and Crystalline GaAs with Brilliant X-Ray Irradiation Using Synchrotron Radiation
J. Electrochem. Soc., **145** (1998) 3063.

F.Sato, N.Saito, Y.Hirano, A.H.Jayatissa, K.Takizawa, S.Kawado, T.Kato, H.Sugiyama, Y.Kagoshma and M.Ando
Diamond-like Bonds in Amorphous Hydrogenated Carbon Films Induced by X-ray Irradiation
J. Vac. Sci. Technol., **A16(4)** (1998) 2553.

K.Wakabayashi, H.Sugiyama, N.Yagi, T.C.Irving, H.Iwamoto, K.Horiuti, Y.Takezawa, Y.Sugimoto, M.Ogino, S.Iino, D-S.Kim, T.Majima, Y.Amemiya, S.Yamamoto and M.Ando
High-Resolution X-ray Diffraction of Muscle Using Undulator Radiation from the Tristan Main Ring at KEK
J. Synchrotron Rad., **5** (1998) 280.

Others

M.Nomura
Structure Analysis of Materials by Means of XAFS
Houshasen, **24** (1998) 31. (*in Japanese*).

T.Kinoshita, Y.Takata, T.Matsukawa, H.Aritani, S.Matsuo, T.Yamamoto, M.Takahashi, H.Yoshida, T.Yoshida, Y.Ufuktepe, K.G.Nath, S.Kimura and Y.Kitajima
Performance of the YB_{66} Soft X-Ray Monochromator Crystal at the Wiggler Beam Line of the UVSOR Facility
J. Synchrotron Rad., **5** (1998) 726.

Other

M.Chiba, R.Hamatsu, T.Hirose, M.Irako, T.Kumita, T.Matsumoto, S.Matsuo, T.Nishimura and J.Yang
Four and Five Photon Decay from Positronium and the Lifetime Problem
Nucl. Instr. Meth., **B143** (1998) 121.

S.Tamura, K.Ohtani, M.Yasumoto, K.Murai, N.Kamijo, H.Kihara, K.Yoshida and Y.Suzuki
Synchrotron Radiation Hard X-Ray Microprobe by Multilayer Fresnel Zone Plate
Mat. Res. Soc. Proc., **524** (1998) 31.

ISSN 1344-6320

PHOTON FACTORY ACTIVITY REPORT

1998

PART A

HIGH LIGHTS AND FACILITY REPORT

#16

High Energy Accelerator Research Organization, KEK

PHOTON FACTORY ACTIVITY REPORT 1998 #16 PART A